NEAR-ANNUAL HISTORY OF SUBTROPICAL NORTH ATLANTIC HURRICANE ACTIVITY RECORDED IN BLUE HOLE SUCCESSIONS

A Dissertation

by

TYLER SCOTT WINKLER

Submitted to the Office of Graduate and Professional Studies of
Texas A&M University
in partial fulfillment of the requirements for the degree of

DOCTOR OF PHILOSOPHY

Chair of Committee,	Peter J. van Hengstum
Committee Members,	Jeffrey P. Donnelly
	Robert L. Korty
	Niall Slowey
Head of Department,	Shari Yvon-Lewis

August 2021

Major Subject: Oceanography

ABSTRACT

The year 2020 Common Era (CE) observed the highest number of named tropical cyclone events since the instrumental record began in 1850 CE. Most downscaled models suggest that the frequency and destructive potential of major hurricanes in the Atlantic will increase in response to Anthropogenic climate change over the next century. Problematically, it is difficult to ascertain if recent high activity levels are unprecedented over longer-time scales due to the short instrumental record. To extend this record, I have produced four near-annual resolution stratigraphic paleohurricane archives using sediment successions from blue holes across the northern Bahamas. These individual reconstructions archive hurricane passage within a 50-115 km radius over the last 600 to 1700 years, and document dramatic multidecadal and centennial scale variability in local hurricane frequency. They also reveal multiple 50 to 150 yearlong intervals in which hurricane frequency was significantly higher than it has been over the last 100 years. However, substantial significant inter-island spatial heterogeneity in hurricane frequency suggests that a single-site reconstruction may not always reflect broader regional climatology. Based on this, these four reconstructions and three others from across the Bahamian Archipelago have been statistically merged into a two different 1500 to 1600-year compilations. These Bahamian Hurricane compilations observe sustained higher frequency in the subtropical North Atlantic during the Little Ice Age (LIA) from 1300 to 1850 CE relative to lower frequency the prior millennium as well as the last 170 years. The US Eastern Seaboard also experienced

heightened hurricane activity during LIA, whereas the Gulf of Mexico and southern Caribbean were inactive. This suggests that despite globally cooler climate, regional ocean/climate conditions during the LIA remained favorable for cyclogenesis and intensification along specific hurricane pathways in the northern Bahamas and US East Coast.

DEDICATION

This dissertation is dedicated to the victims of Hurricane Dorian, which devastated the Abaco Islands and Grand Bahama in September 2019 CE. May this research into the past help us anticipate and prepare for storms of the future.

ACKNOWLEDGEMENTS

I would like to thank my committee chair, Dr. Pete van Hengstum. Pete sparked my interest in learning what mud at the bottom of caves and blue holes can tell us about the past and led me on my journey to gain the knowledge and skills that I needed to interpret these records. I also want to thank my committee members, Dr. Jeff Donnelly, Dr. Rob Korty, and Dr. Niall Slowey for their guidance and support throughout the course of this research. I look forward to continuing to collaborate and learn from each of these exceptional scientists as I continue my career.

I thank my past and current lab mates, Richard Sullivan, Shawna Little, Dr. Annie Tamalavage, Dr. David Brankovits, Jake Emmert, and Dr. Jacque Cresswell. I could not have asked for a better team to collaborate with and learn from, nor a better group of friends. Thanks also to my departmental colleagues and staff at both TAMU and TAMUG, including Dr. Sergey Molodtsov, Dr. Tatiana Williford, Andrew McGuffin, Andrew Pekowski, Dr. Shari Yvon-Lewis, Dr. Patrick Louchouarn, Dr. Kyeong Park, Dr. Laramie Jensen, Grace Townsend, and too many others to name. These individuals helped my time at Texas A&M University a great experience.

Thanks to my friends and collaborators at institutions around the world including Nicole D'Entremont, Dr. Elizabeth Wallace, Nancy Albury, Dr. Chris Maio, Dr. Jon Woodruff, Dr. Andrea Hawkes, Dana MacDonald, Dr. Sam Muñoz, Jeori Reinders, Dr. Michael Toomey, Kelly McKeon, Dr. Patricia Beddows, Victoria Keeton, Oscar Cavazos, Dr. Jimmy Bramante, Dr. Katie Castagno, Dr. Vittorio Maselli, and so many

others. I will forever cherish the memories we made in the field and look forward to more adventures in science to come!

I thank my teachers from Temple Independent School District, with a special mention to Dr. Chris Tutt, DDS. These individuals helped inspire me to seek a career in learning and gave me the tools I needed to succeed in higher education.

I also must thank Dan Torres and Eric Walker of Devil and the Deep Brewery in Galveston for offering us tired graduate students a place to unwind before we all inevitably started talking about science again, but this time over a beer.

Thanks to my mother, Lisa Winkler, father, Jr Winkler, and brother, Brett Winkler for their encouragement, patience, and love. I also extend special thanks to my grandparents, Flo and Marvin Winkler, and Dennis and Cleo (*in memory*) Roy for their endless love and support. The endless love of my family has always helped me endure, no matter the hardships I faced.

Finally, to my wife and partner in life, Shawna Little, whose name bears repeating. This would not have been possible without your constant love and support. I learn from you every day and look forward to facing all that lies ahead with you.

CONTRIBUTORS AND FUNDING SOURCES

Contributors

This work was supervised by a dissertation committee consisting of Dr. Peter van Hengstum of the Department of Oceanography at Texas A&M University (TAMU) and Marine and Coastal Environmental Science at Texas A&M University at Galveston (TAMUG) [advisor], Dr. Robert Korty of the Department of Atmospheric Sciences at TAMU, Dr. Niall Slowey of the Department of Oceanography at TAMU, and Dr. Jeffrey Donnelly of the Department of Geology and Geophysics at Woods Hole Oceanographic Institution (WHOI).

Dana McDonald of the Department of Geoscience at the University of Massachusetts-Amherst performed pollen analysis used in CHAPTER 2. The habitat and bathymetric data used to develop the map of Cay Sal Bank CHAPTER 3 Figure 3.2a was provided at the courtesy of the Khaled bin Sultan Living Ocean Foundation. The sedimentology and radiocarbon dating of the Turtle Pond (TURT) used in CHAPTER 4 was performed and shared by Dr. Christopher Maio and Jared Roberts of the Department of Geosciences at the University of Alaska Fairbanks. Portions of the compilation methodology that we used in CHAPTER 4 were originally published in 2019 by Dr. Elizabeth Wallace of the Massachusetts Institute of Technology/Woods Hole Oceanographic Institution Joint Program in Oceanography. All radiocarbon dating analysis was performed by staff of the National Ocean Sciences Accelerator Mass

Spectrometry (NOSAMS) facility at WHOI. All x-ray fluorescence (XRF) scans and gamma radiation analysis were performed by staff of the Coastal Geology Lab at WHOI.

Field and technical support was provided by Dr. Peter van Hengstum, Dr. Jeffrey Donnelly, Dr. Elizabeth Wallace, Nicole D'Entremont of the Department of Geology and Geophysics at WHOI, Dr. Andrea D. Hawkes of the Department of Earth and Ocean Sciences at the University of North Carolina Wilmington, Dr. Christopher Maio, Richard M. Sullivan of the Department of Oceanography at TAMU, Dr. Jonathan Woodruff of the Department of Geoscience at the University of Massachusetts-Amherst, Victoria Keeton of the Department of Marine Sciences at TAMUG, Stephanie Madsen of the Department of Geology and Geophysics at WHOI, Nancy Albury of the National Museum of The Bahamas, Jody Albury and the staff of Friends of the Environment in Abaco, The Bahamas, as well as Stuart McLoughlin (Science Officer) and the rest of crew of the M/V Alucia, the R/V Kate, and the R/V Endsley. Additional laboratory support was provided by National Science Foundation (NSF) Research Experience for Undergraduates fellows Sarah Swierz and Grace Kim, along with Texas A&M University at Galveston (TAMUG) undergraduate research interns Meghan Horgan, Kate Bricken, Laura Hurt, Jamie Lilly Garland, and Olivia Shipley.

All other work conducted for the thesis (or) dissertation was completed by the student independently.

Funding Sources

Graduate study was supported by a fellowship from Texas A&M University, the Texas A&M University at Galveston 2-Year Fellowship and the Texas A&M University at Galveston Boost Scholarship (to TSW).

This work was also made possible in part by funding from the National Science Foundation Awards OCE-1356509, OCE-1356708, OCE-1854917, OCE-1903616, and ICER-1854980 (to JPD and PJvH.), the Dalio Explore Foundation (to JPD and PJvH.), two Geological Society of America Student Research Grants (to TSW), Texas Sea Grant: Grant in Aid of Graduate Research (to T.S.W), and a Sigma Xi Grant in Aid of Graduate Research (to TSW). Its contents are solely the responsibility of the authors and do not necessarily represent the official views of the awarding agencies listed above.

NOMENCLATURE

$BHAC_{pdf\text{-}5}$	*Bahamas 5 site Paleo-Hurricane Frequency Compilation*
$BHAC_{stand\text{-}6}$	*Bahamas 6 site standardized Paleo-Hurricane Compilation*
BLWD	*Blackwood Sinkhole*
CSA	*Coarse Sediment Anomaly*
CE	*Common Era*
GBAM-TRA	*Grand Bahama Total Range and Average Composite*
GBAM-Stack	*Grand Bahama Coarse Sediment Anomaly Stacked Composite*
GoM	*Gulf of Mexico*
GIS	*Geographic Information System*
ENSO	*El Niño Southern Oscillation*
$FGoM_{comp}$	*Florida GoM Paleo-Hurricane Frequency Compilation*
IBTRrACS	*International Best Track Archive for Climate Stewardship*
ITCZ	*Intertropical Convergence Zone*
LDBH	*Lane's Delight Blue Hole*
LIA	*Little Ice Age*
mbsl	*Meters below sea level*
MDR	*Main Development Region*
MWP	*Medieval Warm Period*
NAO	*North Atlantic Oscillation*
NASH	*North Atlantic Subtropical High*
NAT_{comp}	*North Atlantic Standardized Paleo-Hurricane Compilation*

NE_{comp}	*New England Paleo-Hurricane Frequency Compilation*
NOAA	*National Oceanic and Atmospheric Administration*
NOSAMS	*National Ocean Sciences Accelerator Mass Spectrometry*
NSF	*National Science Foundation*
SST	*Sea Surface Temperature*
TAMUG	*Texas A&M University at Galveston*
TURT	*Turtle Pond*
TPBH	*Thatchpoint Blue Hole*
VWS	*Vertical Wind Sheer*
WHOI	*Woods Hole Oceanographic Institution*
yr(s) BP	*Year(s) Before Present (1950 CE)*

TABLE OF CONTENTS

Page

ABSTRACT ii

DEDICATION iv

ACKNOWLEDGEMENTS v

CONTRIBUTORS AND FUNDING SOURCES vii

NOMENCLATURE x

TABLE OF CONTENTS xii

LIST OF FIGURES xv

1. DISSERTATION INTRODUCTION 1

1.1. Background and Motivation 1
1.1.1. Atlantic hurricane impacts and climatology 1
1.1.2. Paleo-hurricane studies 6
1.1.1. Caribbean Blue Holes and Sinkholes 7
1.2. Research Design 11
1.2.1. Dissertation Structure 15
1.3. References 19

2. REVISING EVIDENCE OF HURRICANE STRIKES ON ABACO ISLAND (THE BAHAMAS) OVER THE LAST 700 YEARS* 30

2.1. Introduction 30
2.2. Study Site: Thatchpoint Blue Hole 34
2.2.1. Regional Setting 34
2.2.2. Previous Hurricane Record from Thatchpoint Blue Hole 36
2.3. Methods 37
2.3.1. Sediment Collection and Analysis 37
2.3.2. Age Control 39
2.3.3. Event Threshold Attribution and Frequency 42
2.3.4. Determining Active Hurricane Periods 43
2.3.5. Compilation of South Andros Paleo-Hurricane Records 44
2.4. Results: Sediment Record and Age Control 45

2.5. Discussion 49
2.5.1. Historical Hurricane Strikes: Calibrating the Record 49
2.5.2. Northern Bahamas Hurricane Frequency 55
2.5.3. Comparison to North Atlantic Paleo-Hurricane Reconstructions 62
2.6. Conclusions and Implications 67
2.7. References 69

3. OCEANIC PASSAGE OF HURRICANES ACROSS CAY SAL BANK IN THE BAHAMAS OVER THE LAST 550 YEARS 77

3.1. Introduction 77
3.2. Regional Setting: Hine's Hole on Cay Sal Bank 81
3.3. Methods 84
3.3.1. Sediment Collection and Analysis 84
3.3.2. Age Control 86
3.3.3. Event Attribution and Frequency Calculation 88
3.4. Results 92
3.4.1. Geophysical and Hydrographic Survey 92
3.4.2. Sedimentology and Age Control 94
3.5. Discussion 100
3.5.1. Age Model Limitations and Implications 100
3.5.2. Calibrating the Record to Historical Hurricanes 102
3.5.3. Changing Event Frequency 111
3.5.4. Regional Hurricane Patterns 114
3.6. Conclusions 125
3.7. References 127

4. ELEVATED HURRICANE ACTIVITY DURING THE LITTLE ICE AGE 135

4.1. Introduction 135
4.2. Regional Setting and Study Site 140
4.3. Methods 142
4.3.1. Field Methods 142
4.3.2. Sediment Textural Analysis 143
4.3.3. Sediment Elemental Analysis 146
4.3.4. Age-Control 146
4.3.5. Event Attribution and Frequency Calculation 148
4.4. Results 151
4.4.1. Geophysics and Hydrography 151
4.4.2. Sedimentology and Age-Control 153
4.5. Discussion 158
4.5.1. Event Bed Drivers and Attribution 158
4.5.2. Grand Bahama Hurricane Variability 170
4.5.3. Bahamian Hurricane Frequency 174

4.5.4. North Atlantic Regional Compilations....179
4.5.5. Climatic Forcing....186
4.6. Conclusions....195
4.7. References....197

5. DISSERTATION CONCLUSIONS....212

5.1. Scientific Contributions and Societal Implications....212
5.2. Future Directions....217
5.3. References....218

APPENDIX A BLUE HOLE DISTRIBUTION METHODS AND DETAILS....221

APPENDIX B CHAPTER 2 SUPPLEMENTAL INFORMATION....232

APPENDIX C CHAPTER 3 SUPPLEMENTAL INFORMATION....248

APPENDIX D CHAPTER 4 SUPPLEMENTAL INFORMATION....262

LIST OF FIGURES

Page

Figure 1.1. Frequency of ≥Category 2 hurricanes passing with 50 km from 1850-2019 CE and study site locations in the North Atlantic (adapted from Winkler et al., 2020 Fig. 1). 2

Figure 1.2. Land area normalized blue hole density in across the Bahamian Archipelago. 9

Figure 1.3. Location and photographs of blue hole study sites on the Little Bahama Bank (a, c, d) and Cay Sal Bank (b, e). 12

Figure 1.4. Conceptual model of a modern near-shore blue hole and the sedimentary process within and around the basin as well as representative hydrographic and geologic features and methods used to develop in sedimentary hurricane reconstructions (figure developed by Peter van Hengstum). 14

Figure 2.1. Frequency of ≥Category 2 hurricanes (Saffir-Simpson scale) within a 50 km radius from 1850 to 2019 CE in the North Atlantic. 31

Figure 2.2. Thatchpoint Blue Hole regional context. 35

Figure 2.3. Preserved sedimentary archives, stratigraphic correlation, and sedimentary age-model. 47

Figure 2.4. Sediment record sensitivity calibration/attribution to IBTrACS observational hurricane record from 1850 to 2014 CE. 50

Figure 2.5. Hurricane events per century recorded in Thatchpoint Blue Hole from 1330 to 2014 CE. 57

Figure 2.6. Comparison of paleo-hurricane records from Abaco. 60

Figure 2.7. Comparison of high-resolution paleo-hurricane records from throughout the North Atlantic. 66

Figure 3.1. Location of Cay Sal Bank in the North Atlantic. 79

Figure 3.2. Map of Cay Sal Bank and Hine's Hole bathymetry. 82

Figure 3.3. Hine's Hole Chirp and hydrography. 93

Figure 3.4. Hine's Hole sediment textural variability 96

Figure 3.5. Hine's Hole sedimentary age model and coarse sediment anomalies. 98

Figure 3.6. Calibration of Hine's Hole Composite to the instrumental record. 105

Figure 3.7. Hurricanes/century calculated from the Hine's Hole Composite. 112

Figure 3.8. Comparison of Hine's Hole Composite to Florida Keys reconstructions. ... 116

Figure 3.9. Near-annually resolved hurricane reconstructions from The Bahamas. 119

Figure 3.10. Comparison of Hine's Hole Composite to Bahamian Compilation. 123

Figure 4.1. (a) Map of ≥Category 2 hurricane frequency within a 50 km radius from 1850 to 2019 CE using storm track and intensity data is from the International Best Track Archive for Climate Stewardship (IBTrACS) v041,2 dataset (map modified from Fig. 1 in Winkler et al. (2020)). 137

Figure 4.2. LDBH geophysics and hydrography. 152

Figure 4.3. Downcore sediment textural data for cores from LDBH and TURT. 154

Figure 4.4. LDBH Composite and TURT textural varibility and age-models. 156

Figure 4.5. LDBH Composite event bed attributions to observed hurricanes. 164

Figure 4.6. Hurricanes/century for LDBH Composite and TURT. 171

Figure 4.7. Grand Bahama composite records. 173

Figure 4.8. Hurricanes/century from near annually resolved reconstructions across the Bahamian Archipelago (see Fig. 4.1 for site locations). 178

Figure 4.9.Points of origin, transition into hurricane strength, and last location of hurricane strength of all storms that passed within the approximate site-specific sensitivity radius of the six hurricane reconstructions in Fig. 8 from 1850 to 2019 CE as a ≥Category 1 hurricane. 181

Figure 4.10. Regional paleohurricane compilations. 184

Figure 4.11. Standardized regional paleo-hurricane compilations and climate reconstructions. 190

1. DISSERTATION INTRODUCTION

1.1. Background and Motivation

1.1.1. Atlantic hurricane impacts and climatology

On August 25th, 2017, Hurricane Harvey rapidly intensified into a Category 4 (Saffir-Simpson Scale) hurricane with up to 178 km/hr winds before making landfall near Rockport, TX. Harvey then crawled along the Texas Gulf Coast for over 36 hours, delivering rainfall that was as high as 154.4 cm near Houston, which is the highest rainfall for a tropical cyclone in the US to date (Blake and Zelinsky, 2018). The resultant flooding was responsible for at least 68 direct deaths and $125 billion USD in damage, making it the second most costly hurricane in US history, and the deadliest Texas hurricane since 1919 (Blake and Zelinsky, 2018). In fact, 4 of the 5 most destructive modern Atlantic hurricanes (Harvey included) have occurred since 2013 (Blake et al., 2011). Islands across the Bahamian Archipelago have been devastated by five major hurricanes from 2010-2020 CE, including Category 5 Hurricane Dorian in 2019 that inundated parts of Abaco and Grand Bahama with up to 4 m of surge, killing 84 people and leaving >245 others missing (Zegarra et al., 2020). Up to 1 m relative sea-level rise is estimated for The Bahamas by 2100 CE that could result in a 12% loss of land area (Dasgupta et al., 2009), which could enhance flooding from weaker storms (<Category 3) in low-lying coastal areas.

This trend is expected to continue as rising global temperatures may cause up to 1 m of global mean sea level rise by 2100 CE, making coastal zones more susceptible to

devastating hurricane storm surge (Miller et al., 2013, Wong et al., 2014, Woodruff et al., 2013), along with rising coastal populations and infrastructure (Pielke Jr et al., 2008), Furthermore, most models suggest that warming sea surface temperature (SST) may increase the frequency of intense hurricanes (Emanuel, 2005, Emanuel, 2013, Knutson et al., 2010, Korty et al., 2017, Sobel et al., 2016, Wong et al., 2014), although less storms overall are expected. This is further supported by analysis of datasets based on observations of hurricanes throughout the last ~150 years (Webster, 2005).

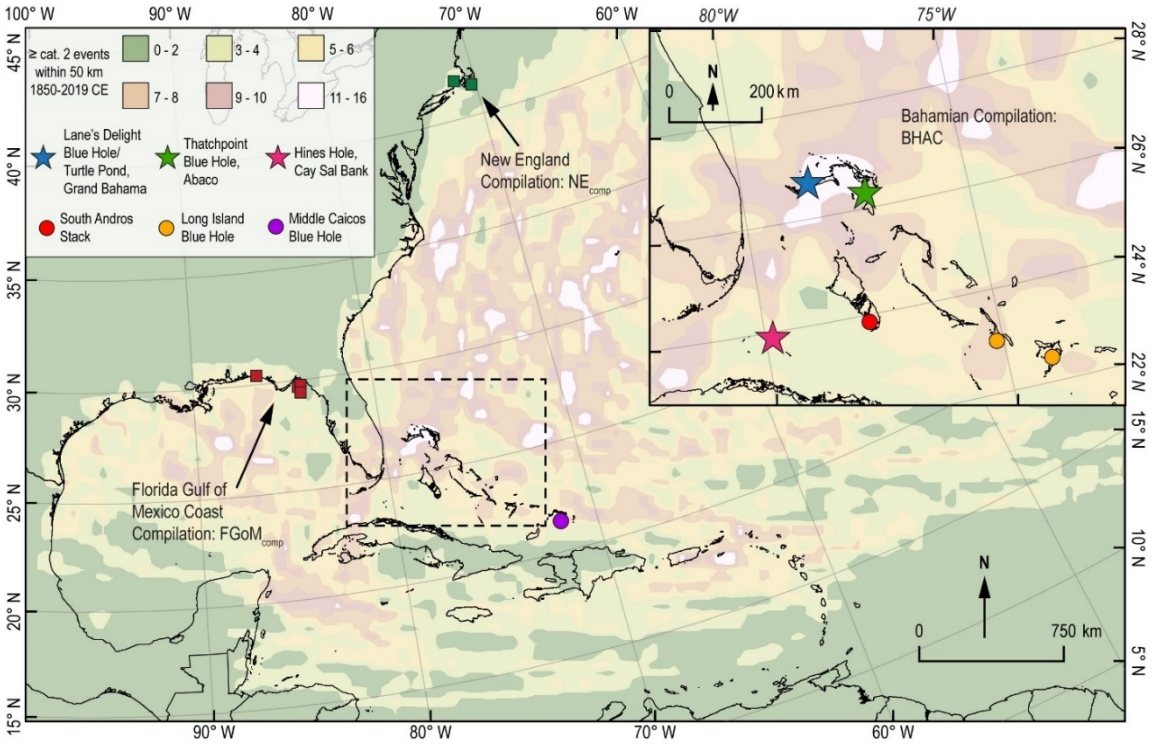

Figure 1.1. Frequency of ≥Category 2 hurricanes passing with 50 km from 1850-2019 CE and study site locations in the North Atlantic (adapted from Winkler et al., 2020 Fig. 1).
Storm track and intensity data is from the International Best Track Archive for Climate Stewardship (IBTrACS) v04 dataset (Knapp et al., 2018, Knapp et al., 2010). Stars indicate location of paleo-hurricane records developed for this dissertation, and circles represent other similar near-annually resolved reconstructions from the Bahamina Archipelago. Red (green) squares are the locations of paleo-hurricane records from the Florida GoM (New England) regional compilations (see CHAPTER 4).

Problematically, the International Best Track Archive for Climate Stewardship (IBTrACS; Knapp et al., 2018, Knapp et al., 2010) observational record of Atlantic hurricane landfalls only extends back to ~1851 CE, and significant uncertainty exists within this dataset prior to the development of satellite monitoring around 1970 CE (Vecchi and Knutson, 2011, Landsea and Franklin, 2013, Frappier et al., 2007). This relatively short instrumental record reveals substantial spatial heterogeneity in hurricane activity over the last 170 years (Fig. 1.1), which promotes uncertainty regarding long-term regional susceptibility to hurricanes and how this could be impacted by long-term climate variability (Donnelly et al., 2015, Landsea et al., 2006).

As proposed by Emanuel (1986), hurricane energy is derived from convective heat transfer from the ocean, and can therefore be modeled as a steady-state Carnot Heat Engine. In this model, hurricanes intensify and maintain themselves by extracting heat from the ocean and exporting into the troposphere (15-20 km above sea level). The formation and sustainability of the hurricane convective heat engine requires:

1) Hurricanes must form at least 500 km away from the equator so that Coriolis force is sufficient to cause the cyclonic (counterclockwise) rotation needed to maintain low pressure disturbance (Palmen, 1956). The MDR for hurricanes in the North Atlantic is off the West coast of Africa between 9°N to 20°N (Gray, 1968).

2) Warm (>26°C), deep seawater (≥ 50 m) to supply heated, moist air that rises to the troposphere (Palmen, 1956). Rapid cooling of this warm moist air creates thermal instability in the troposphere, thus fueling the low-pressure convection cell (Gray, 1968). This thermal instability in the troposphere is enhanced during periods of

reduced solar radiative influx that can cool the upper atmosphere (Cohen and Sweetser, 1975, Korty et al., 2012). Still further, recent research indicates that warmer SSTs can significantly enhance the rate of precipitation associated with the hurricane (Lin et al., 2015), increasing the potential for flooding. Studies have shown that warmer relative SSTs (difference between local SST and tropical mean SST) can also systematically increase the total area of hurricanes in the tropics (Chavas et al., 2016), which has the potential to greatly enhance the risk of coastal flooding via surge and rainfall exposure. This is problematic considering that the Intergovernmental Panel on Climate Change (IPCC) AR5 report in 2014 noted with certainty that the upper 70 m of the global ocean had warmed at a rate of ~0.11 °C per decade from 1971 to 2010 (Pachauri et al., 2014), and this trend is only expected to continue or increase moving forward.

3) Low vertical wind shear (<10 m/s) between the ocean surface and the upper troposphere, as high wind shear will decrease angular momentum needed to preserve cyclonic rotation around the eye wall. Long-term patterns in the intensity and provenance of vertical wind shear are modulated by multiple drivers including the El Niño Southern Oscillation ENSO) and latitudinal displacement of the Intertropical Convergence Zone (ITCZ). The ITCZ is a region of lower level trade wind convection that promotes high levels of precipitation and atmospheric instability. which migrates between 9°N to 2°N in response to regional SST (Schneider et al., 2014). When the ITCZ is shifted northward, cyclogenesis is promoted in the Main Development Region (MDR) (Kossin and Vimont, 2007).

4) If the above conditions exist, a pre-existing weather disturbance like African Easterly Waves can intensify into a hurricane (Riehl, 1954). Further, existing tropical storms and depressions passing over the warm shallow waters of the Bahamian Archipelago, western Caribbean, and Gulf of Mexico often intensify into hurricanes.

Based on the current understanding of hurricane climatology discussed above, research indicates that there are multiple mechanisms of climatic forcing that can influence Atlantic hurricane frequency, storm-track, and intensity at intra-seasonal, interdecadal, and centennial scale windows including: ENSO (Gray, 1984, Klotzbach, 2011a, Klotzbach, 2011b, Kossin et al., 2010) migration of the mean position of the summer ITCZ (van Hengstum et al., 2016, Wallace et al., 2019, Baldini et al., 2016), extent of the North Atlantic Subtropical High (NASH) as it relates to the North Atlantic Oscillation (NAO) (Elsner, 2003, Vecchi et al., 2017, Kossin et al., 2010, Baldini et al., 2016, Liu and Fearn, 2000), Hadley cell expansion/contraction (Sharmila and Walsh, 2018, Studholme and Gulev, 2018), and rate of Atlantic Meridional Overturning Circulation (AMOC) as it pertains to regional SSTs (Donnelly et al., 2015, Yang et al., 2020). However, disentangling the influence of these ocean/climate variables on modern hurricanes is challenged by the short instrumental record of hurricane activity, which is considerably less reliable and complete prior the widespread implementation of satellite monitoring after 1960 CE (Vecchi and Knutson, 2011, McAdie et al., 2009).

1.1.2. Paleo-hurricane studies

Knowledge of Atlantic cyclone activity can be extended using historical accounts, but these records are inherently limited to areas with dense populations with preserved recorded histories (Trouet et al., 2016, Chenoweth and Divine, 2008). Pre-historic tropical cyclone activity in the Atlantic has been reconstructed using numerous proxies (Frappier et al., 2007, Oliva et al., 2017, Wallace et al., 2014) including an array of sedimentary archives from salt-marshes (Donnelly et al., 2001, McCloskey and Liu, 2012), back-barrier coastal ponds and sinkholes (Brandon et al., 2013, Brandon et al., 2014, Donnelly, 2005, Donnelly et al., 2015, Donnelly and Woodruff, 2007, Lane et al., 2011, Oliva et al., 2017, van Hengstum et al., 2016, Woodruff et al., 2008), flooded offshore sinkholes known as blue holes (Denomee et al., 2014, Gischler et al., 2008, van Hengstum et al., 2014, Wallace et al., 2019, Wallace et al., Sub. March 2021, Wallace et al., 2021b, Winkler et al., Submitted 2021, Winkler et al., 2020, Schmitt et al., 2020a), and deep marine sediments along the continental shelf margins (Toomey et al., 2013, Yang et al., 2020). These reconstructions have expanded our temporal understanding of hurricane landfall variability, revealing that there are significant local and regional variations in landfall frequency at millennial, centennial, and multi-decadal scales; however, significant geospatial and temporal gaps remain. Further, weaker Category 1-2 events that are less-likely to be detected by most sediment-based paleo-hurricane reconstructions, so a substantial percentage of overall hurricane activity is largely undocumented beyond the instrumental record. As such, it remains unclear whether variance in the timing of active intervals throughout the western Atlantic is a function of

geography, climate modulation, resolution of captured archives, site sensitivity to storm induced wave climate, or stochastic variability (Wallace et al., 2021a). Subtidal blue holes are abundant throughout the Caribbean (Fig. 1.2), and studies indicate that they can have high-sedimentation rates (0.5-1.5 cm/yr), thus offering the potential to produce near-annually resolved reconstructions to resolve this uncertainty in regional multi-decal to centennial scale variability in regional hurricane activity.

Motivated by this, my primary research objectives are to (i) generate high-resolution reconstructions of hurricane activity spanning the last ~1700 years using sediment cores (up to 18 m) from three flooded sinkholes (blue holes) in The Bahamas (Fig. 1.1 and 1.3), and (ii) investigate the potential ocean and atmospheric drivers of observed variability in intense hurricane activity in the subtropical North Atlantic Ocean. We find that the selected blue holes have a continuous and near-annual sedimentation rate, thus providing high-resolution sedimentary records that are ideal for assessing the interdecadal to centennial scale impacts of climate variability on regional hurricane landfall frequency.

1.1.1. Caribbean Blue Holes and Sinkholes

The Bahamian Archipelago (The Bahamas and Turks and Caicos) began forming during the Jurassic (Mullins and Lynts, 1977), and the modern islands are made up of thick accumulations of Pleistocene marine limestones and aeolianite that overlay dolomite strata (Kaldi and Gidman, 1982, Melim et al., 1997, Whitaker and Smart, 1997). Karst dissolution landforms like blue holes, banana holes, pit caves, and flank caves are abundant throughout the eogenetic carbonate islands of the Bahamian

Archipelago. Blue holes have ignited the imagination of the earliest European explorers in the Caribbean, but were already places of worship, drinking water, and potentially interment to indigenous peoples of The Bahamas. The term blue hole originated in the Bahamas to describe fully or partially inundated coastal or offshore sinkhole-like voids in the Pleistocene marine eogenetic-limestones and aeolianite that dominate Bahamian surface geology (Kaldi and Gidman, 1982, Melim et al., 1997, Whitaker and Smart, 1997). The predominant hypothesis for blue hole and sinkhole development is that these features form when dissolution of underlying carbonate bedrock during lower sea levels forms a void that is so large that the ceiling cannot sustain its own weight and collapses (Cole, 1910, Mylroie et al., 1995).

Dissolution of eogenetic limestones is dependent on localized groundwater undersaturation with respect to calcite (Gulley et al., 2013, Mylroie and Carew, 1990, Ford and Ewers, 1978, Palmer, 1991). The Flank Margin Model for Dissolution Development proposed by Mylroie and Carew (1990) posits that the mixing of discharging freshwater and tide-pulsed marine water at the distal end of the freshwater lens creates a water mass undersaturated with respect to calcite, and is the dominant zone of dissolution. Others suggest that dissolution of eogenetic limestone is primarily mediated by spatial heterogeneity of pCO_2 along groundwater flow paths caused by oxidation of dissolved organic carbon (DOC) in the upper 1-2 m of the water table that leads to degassing (Whitaker and Smart, 2007b, Whitaker and Smart, 2007a) and subsurface microbial respiration (Gulley et al., 2015, Gulley et al., 2020, McClain et al., 1992). What is generally agreed upon is that dissolution rates are highest at the distal

margins of the freshwater lens where tidal pumping promotes mixing and ventilation (Gulley et al., 2020, Gulley et al., 2015, Mylroie and Carew, 1990) and specific discharge is highest (Vacher, 1988). Given the relatively consistent quaternary sea-level forcing and limestone geology across Bahamian Archipelago, these mechanisms alone would result in (i) largely uniform distribution of blue hole features across the Bahamian Archipelago given consistent Quaternary sea-level forcing and carbonate geology that is (ii) concentrated along coastal flank margins.

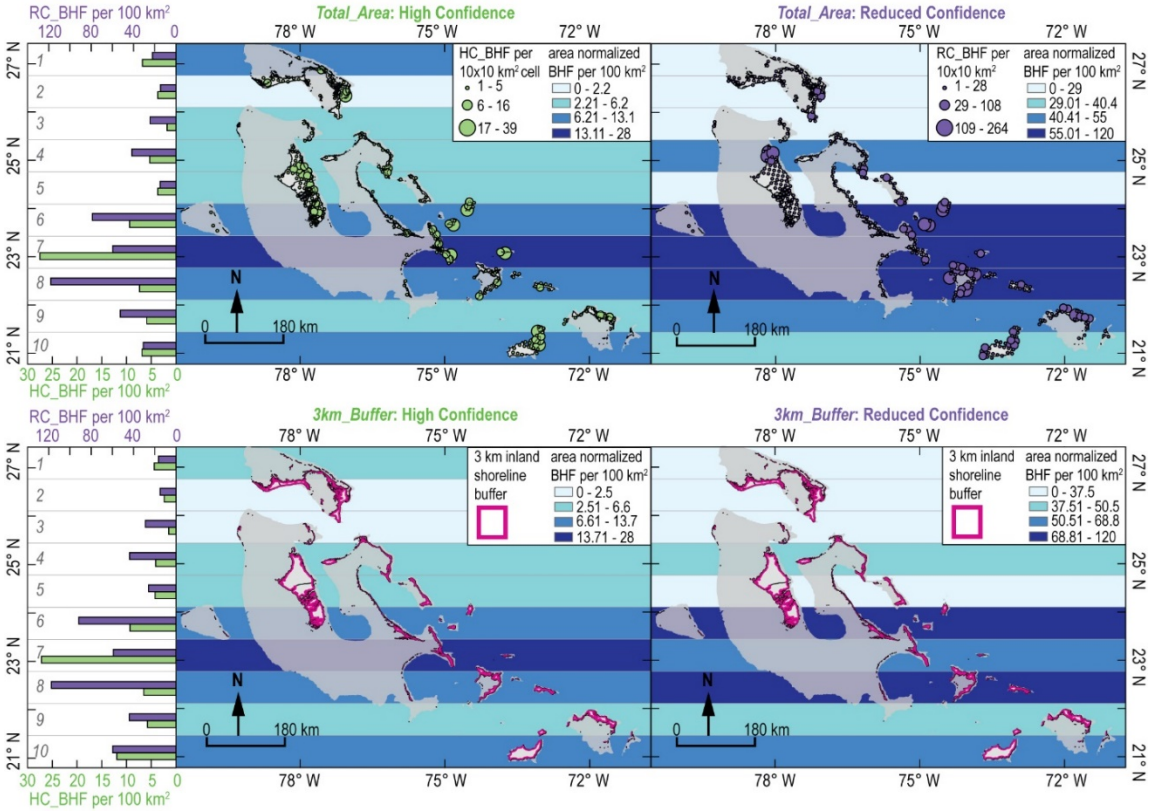

Figure 1.2. Land area normalized blue hole density in across the Bahamian Archipelago.
Top row panels show blue hole density normalized to land area in each latitudinal band for high-confidence (green) and low confidence (purple) data sets. Bottom row panels show the same, but only count blue holes and land area within 3 km of the modern shoreline (pink). Darker blue bands have higher blue hole density. See Appendix A* for methods and details.

Using satellite imagery, we observe significantly higher blue hole feature (BHF) density in the southern--central portion of the Bahamian archipelago (Fig. 1.2; Appendix A*; Winkler et al., In prep., 2021). We hypothesize that karst dissolution was enhanced in the southern archipelago during glacial periods when rainbelts currently positioned over the northern Bahamas (Jury et al., 2007) shifted south alongside the Intertropical Convergence Zone (ITCZ) during the glacial periods (Arbuszewski et al., 2013, Arienzo et al., 2017, Arienzo et al., 2015). Lower rainfall in the southern archipelago relative to the north throughout the late Holocene interglacial period coupled with increased bedrock porosity related to glacial period dissolution results in thin, fractured meteoric lenses in the southern islands. Winkler et al. (In prep., 2021) hypothesize that this positive feedback loop may also play a role in the southward bias in BHF distribution.

While the distribution of blue holes appears to have important palaeoclimatological implications (Winkler et al., In prep., 2021), sediment in blue holes is often exceptionally well preserved as these depressions are sheltered from surface wind-induced waves and currents, preventing sediment resuspension. Additionally, blue hole bottom-water is often dysoxic or anoxic which prevents bioturbation and decomposition of organic matter and faunal remains. As such, sedimentary archives from these karst depressions are extremely valuable in the study of paleohurricane activity (Denomee et al., 2014, Lane et al., 2011, van Hengstum et al., 2016, van Hengstum et al., 2014, Wallace et al., 2019, Gischler et al., 2008, Wallace et al., Sub. March 2021, Wallace et al., 2021b, Winkler et al., Submitted 2021, Winkler et al., 2020, Schmitt et al., 2020a, Rodysill et al., 2020, Shinn et al., 1996), hydroclimate and

groundwater variability (Alverez Zarikian et al., 2005, Crotty and Teeter, 1984, Kovacs et al., 2013, Tamalavage et al., 2018, van Hengstum et al., 2018, Schmitt et al., 2020b, Sullivan et al., Submitted, van Hengstum et al., 2020), and shifts in regional flora/fauna and anthropology (Hearty et al., 2004, Kjellmark, 1996, Steadman et al., 2007, Sullivan et al., 2020, Fall et al., 2021).

1.2. Research Design

This study will generate near-annual reconstructions of hurricane activity spanning the last ~2000 years using sediment cores (up to 18 m) from three blue holes in the Northern Bahamas (Fig. 1.3): Thatchpoint Bluehole (TPBH) on Great Abaco Island (CHAPTER 2), Hine's Hole on Cay Sal Bank (CHAPTER 3), and Lane's Delight Bluehole (LDBH) and Turtle Pond (TURT) on Grand Bahama (CHAPTER 4; sites discussed in *1.2.1 Dissertation Structure*). Based on radiocarbon results, similar blue holes have linear sedimentation rates of 0.5-1.5 cm/year over the last 2000 years, thus providing high-resolution sedimentary archives. During the last 168 years, at least 11 ≥Category 2 hurricanes passed within a 50 km radius of any given point near the Little Bahama Bank (Abaco and Grand Bahama), making the northern Bahamas one of the most vulnerable regions in the tropical western North Atlantic (Fig. 1.1). Contrarily, Cay Sal Bank (~400 km southwest of the Little Bahama Bank) is in a less active zone where only three to six ≥Category 2 hurricanes passed within a 75 km radius of any given point during the last 170 years. Developing paleo-hurricane reconstructions for each of these locales will help elucidate whether these geographic patterns are persistent through time.

Further, these reconstructions will be compiled with recent near-annually resolved paleo-hurricane reconstructions from the southern Bahamian Archipelago (Wallace et al., 2019, Wallace et al., Sub. March 2021, Wallace et al., 2021b) to develop a broader understanding of long-term regional hurricane variability and potential climate influence (CHAPTER 4).

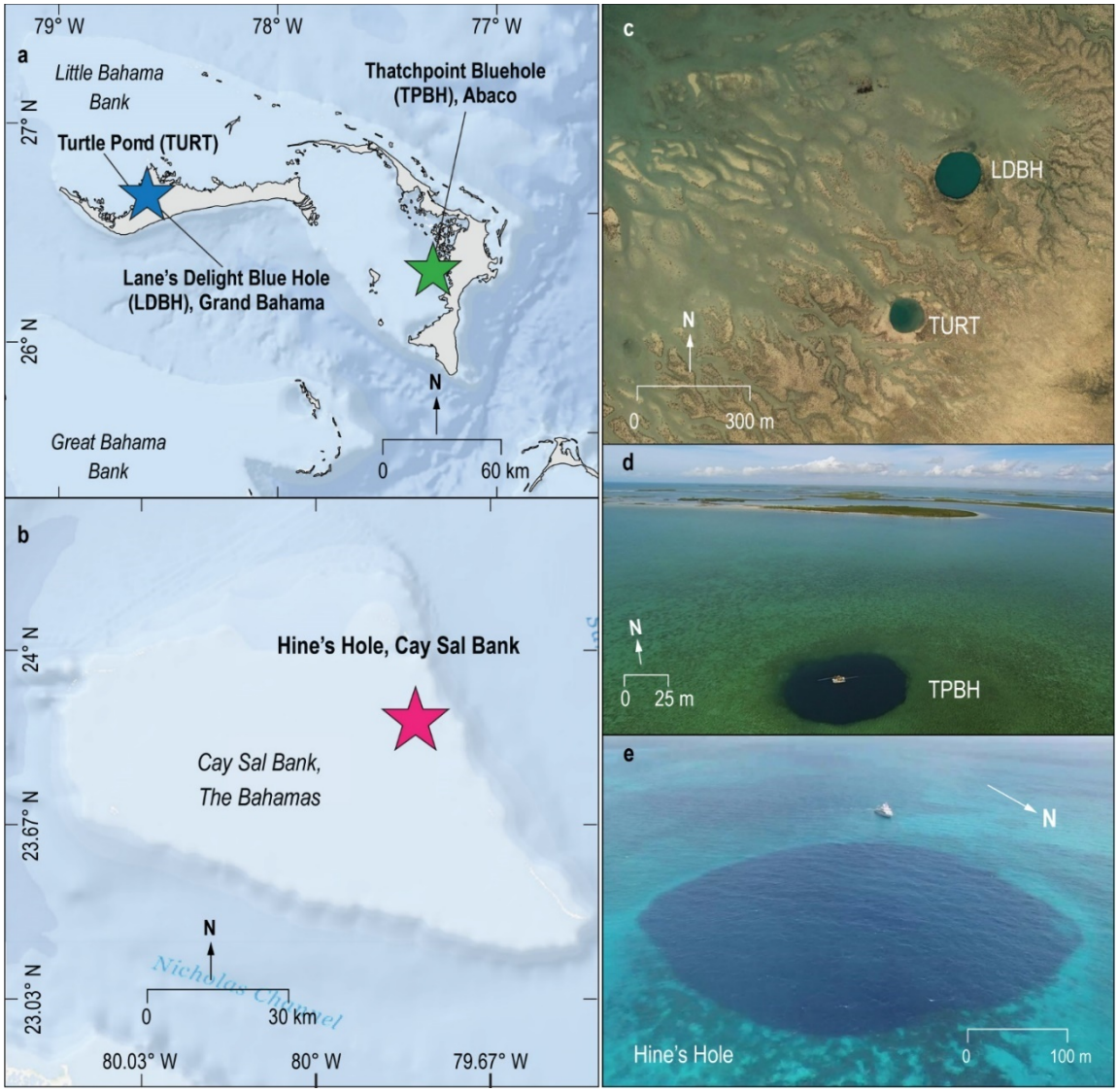

Figure 1.3. Location and photographs of blue hole study sites on the Little Bahama Bank (a, c, d) and Cay Sal Bank (b, e).

Methods and site-specific details will be discussed in detail for in CHAPTERS 2-4, but a general overview is summarized by Figure 1.4: (**1**) Sites were selected following hydrographic and geophysical surveying to assess whether the blue hole conditions are suitable for archiving sediment deposits (**2**) Sediment cores were collected using submersible vibracoring. (**3**) Textural variability is assessed using techniques such as sieving coupled with loss on ignition to assess the fraction of coarse-sediment (van Hengstum et al., 2016) or laser particle size analysis. Sediment that accumulates in most blue holes is fine grained aragonitic mud produced through the breakdown of biogenic carbonates as well as inorganic precipitation in the water column (Milliman et al., 1993, Trower et al., 2019, Neumann, 1987). Coarser sediments comprised of bioclastic sand and weathered antecedent karst can accumulate as tidal sand bars. The finer sediments can be transported in low-energy conditions related to tidal flux and less intense storms; however, the coarser-sediment is only mobilized during high-energy hydrodynamic conditions associated with hurricanes and therefore can serve as a proxy for proximal hurricane passage. (**4**) Chronological control points were established for each record using radiocarbon (^{14}C) dating and downcore ^{137}Cs activity, and a sedimentary age-model with 95% confidence intervals was developed from these control points using Bayesian statistical freeware R-program BACON (Blaauw and Christen, 2011). (**5**) Sediment textural data was plotted against time, and the last 170-years was compared with the timing of proximal hurricanes based on the IBTrACS instrumental record to assess the suitability of textural data a proxy for hurricanes and determine the archival sensitivity of the record (i.e., storm intensity, proximity, orientation). (**6**) Once a

threshold for defining coarse sediment beds was established following the calibration stage, significant event beds per century were counted using a 100-year sliding window. (**7**) Once hurricanes reconstructions are developed, these individual records from the Bahamian Archipelago will be statistically compiled to form a single regional composite record. Similar regional compilations will be made using existing multi-decadal resolution paleo-hurricane reconstructions from New England and the Florida Gulf of Mexico region. These three regional compilations will reflect a more unified regional signals that is less likely to be skewed by stochastic variations in hurricane activity that can significantly influence local hurricane frequency that is documented by single site records (Wallace et al., 2021a).

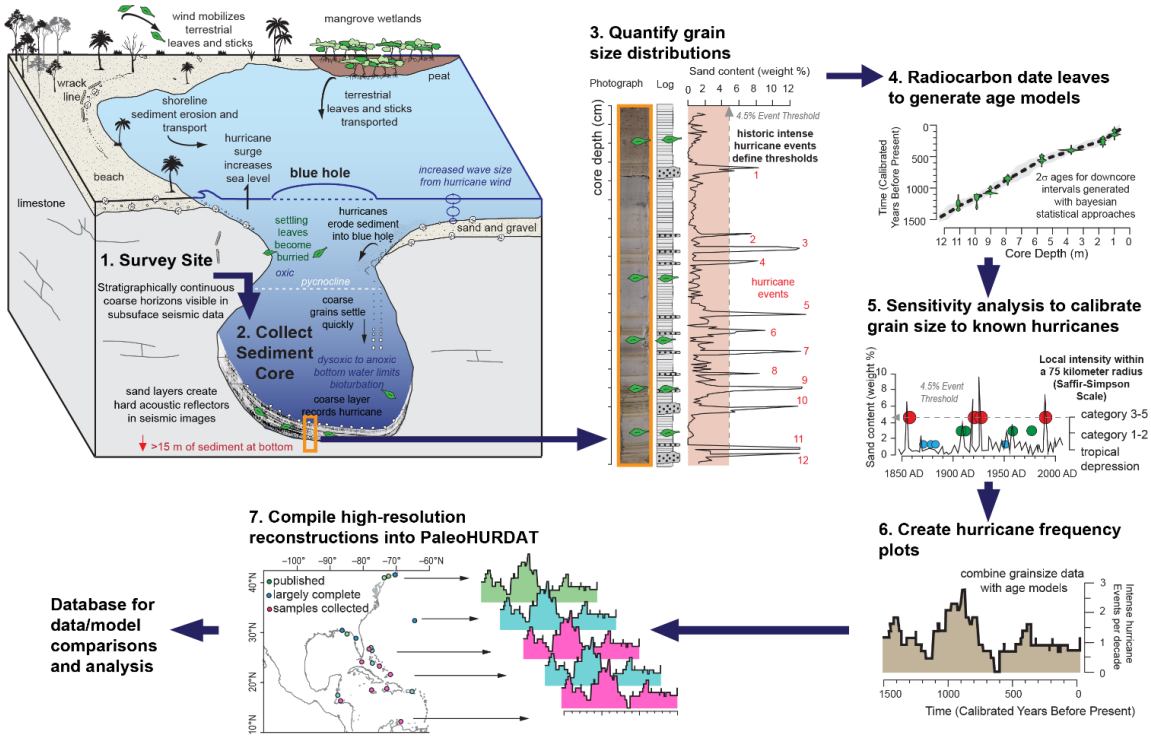

Figure 1.4. Conceptual model of a modern near-shore blue hole and the sedimentary process within and around the basin as well as representative hydrographic and geologic features and methods used to develop in sedimentary hurricane reconstructions (figure developed by Peter van Hengstum).

1.2.1. Dissertation Structure

Following this introductory chapter, CHAPTERS 2-4 of this dissertation are manuscripts that detail three nearly-annually resolved paleo-hurricane records from The Bahamas developed to investigate the following research questions:

Question 1: Do the selected blue holes in The Bahamas document sedimentary evidence of significant multidecadal to centennial-scale variability in local hurricane frequency throughout the last two-millennia??

Hypothesis 1*: Hurricane induced waves and currents are the most likely emplacement mechanism of coarse sediment beds in blue hole sediment stratigraphy. High sedimentation rates (0.5 to 1.5 cm/year) suggest that blue hole stratigraphy can be used to develop near-annually resolved records of local hurricane frequency.*

Question 2: Are active intervals for more frequent hurricane impacts temporally consistent across reconstructions from the Bahamian Archipelago?

Hypothesis2*: Paleohurricane reconstructions from Abaco and Grand Bahama sites are likely highly correlated given the proximity of these sites on the Little Bahama Bank. Sites that are further away like Hine's Hole on Cay Sal Bank are more likely to vary from the sites to the north..*

Question 3: How does the onset of regional active intervals across the Bahamian Archipelago (i.e., Bahamian paleo-hurricane compilations) compare those noted elsewhere in the North Atlantic (e.g., New England-NE_{comp}, Florida GoM-$FGoM_{comp}$), and do these patterns broadly match the regional variations in hurricane susceptibility demonstrated in Figure 1.1?

Hypothesis 3*: Bahamian active intervals will correlate temporally with active intervals along the US eastern coast, as hurricanes that impact these locales often form or intensify in the Main Development Region (MDR) and subtropical North Atlantic based on the instrumental record. Periods of more frequent hurricanes identified from reconstructions further to the south or west (Yucatan Peninsula, Gulf Coast, Puerto Rico, Andros) are likely to differ from the northern Bahamas as these locales are likely impacted more by storms that form in the GoM or southern tropics.*

Question 4: Is hurricane frequency across the Bahamian Archipelago impacted by climate variability during the last 2000 years? If so, are the impacts consistent throughout the North Atlantic?

Hypothesis 4*: While stochastic variability can have a significant impact on active intervals in individual records, the regional compilations will demonstrate that hurricane landfall frequency in the northern Bahamas and elsewhere in the Atlantic has been modulated throughout the last 2000 years by variability in SSTs, VWS and atmospheric steering features like the NASH that can vary both at the point of cyclogenesis and locally near the reconstruction site.*

CHAPTERS 2-4 each address specific research questions and localized implications of the records, and the regional compilations and climatic assessment is discussed in CHAPTER 4. We summarize each individual chapter below.

CHAPTER 2 details a 700-year reconstruction from TPBH on the western side of Abaco Island on the Little Bahama Bank. Using longer sediment cores (888 cm) and more reliable age-control, this study revises and temporally expands a previous study

from TPBH that underestimated the sedimentation rate (van Hengstum et al., 2014). We quantify coarse-sediment (>63 μm) fraction variability and develop a sedimentary age model for this site using more reliable terrestrial material for radiocarbon dating. By comparing the timing of proximal hurricane events in instrumental record, we find that coarse-sediment beds in TPBH document hurricane passage over the last 700-years, demonstrating substantial variability frequency in the past relative to observations since 1850 CE (**Question 1**). We compare this record to existing paleo-hurricane records from the North Atlantic to assess spatiotemporal variability in past frequency (**Question 2**).

CHAPTER 3 presents a 550-year paleo-hurricane record from an 18 m sediment core from Hine's Hole on Cay Sal Bank. Located in the center of the Florida Straits between Florida and the north coast of Cuba, Cay Sal Bank is a nearly-fully drowned carbonate platform (Fig. 1.3). As such, Hine's Hole is surrounded by ~10 m of water and is completely exposed to winds and currents from all directions meaning that is does not. Hine's Hole has a cumulative sedimentation rate of ~3.2 cm/yr, and documents 19 coarse sediment anomalies since 1850 CE that are each within age-model uncertainty at least one of 23 ≥Category hurricanes that passed thin 100 km of Hine's Hole since 1850 CE (**Question 1**), making one of the highest resolution paleo-hurricane archives from the North Atlantic. This reconstruction documents three multi-decadal scale intervals with significantly higher hurricane frequency than what has been observed since 1850 CE, with varying levels of similarity in timing to other individual reconstructions from The Bahamas (**Question 2**). The Hine's Hole record does show very strong correlation to a preliminary compilation of regional records, suggesting that the wide sampling radius

and ability to consistently archive weaker Category 1 hurricanes may allow this single site to reflect regional paleo-hurricane patterns (**Question 3**).

CHAPTER 4 provides a composite hurricane reconstruction from two blue holes within 300 m of one another on the northern coast of Grand Bahama on the Little Bahama Bank (LDBH and TURT, Fig. 1.3). This composite record spans from 350-1970 CE, making the longest near-annually resolved record from a Bahamian Blue Hole. It shows strong similarities to TPBH reconstruction in terms of the timing of active intervals (**Questions 1 and 2**). I compile this record along with TPBH, Hine's Hole, and three others near annually resolved Bahamian hurricane reconstructions from South Andros (Wallace et al., 2019), Long Island (Wallace et al., 2021b), and Middle Caicos (Wallace et al., Sub. March 2021) to update the Bahamian Regional Compilation first produced by (Wallace et al., 2021b) and extend regional compilations for New England and Florida GoM back to 200 CE (**Question 3**). I also produce new Bahamian and North Atlantic paleo-hurricane compilations that reflect relative changes in hurricane frequency by standardizing and averaging individual/regional records. These new multisite compilations demonstrate substantial regional shifts in hurricane frequency patterns, including a sustained period of elevated hurricane activity in the northern Caribbean throughout the entire Little Ice Age (**Question 3**). These compilations document regional hurricane patterns with unprecedented confidence, minimize the expression of inherent stochastic variability in storm tracks that impacts individual records, and allow me to interpret the influence of long-term climate variability on regional hurricane patterns (**Question 4**).

1.3. References

ALVEREZ ZARIKIAN, C. A., SWART, P. K., GIFFORD, J. A. & BLACKWELDER, P. L. 2005. Holocene paleohydrology of Little Salt Spring, Florida, based on ostracod assemblages and stable isotopes. *Palaeogeography, Palaeoclimatology, Palaeoecology,* 225**,** 134-156.

ARBUSZEWSKI, J. A., DEMENOCAL, P. B., CLÉROUX, C., BRADTMILLER, L. & MIX, A. J. N. G. 2013. Meridional shifts of the Atlantic intertropical convergence zone since the Last Glacial Maximum. 6**,** 959-962.

ARIENZO, M. M., SWART, P. K., BROAD, K., CLEMENT, A. C., POURMAND, A. & KAKUK, B. 2017. Multi-proxy evidence of millennial climate variability from multiple Bahamian speleothems. *Quaternary Science Reviews,* 161**,** 18-29.

ARIENZO, M. M., SWART, P. K., POURMAND, A., BROAD, K., CLEMENT, A. C., MURPHY, L. N., VONHOF, H. B. & KAKUK, B. 2015. Bahamian speleothem reveals temperature decrease associated with Heinrich stadials. *Earth and Planetary Science Letters,* 430**,** 377-386.

BALDINI, L. M., BALDINI, J. U., MCELWAINE, J. N., FRAPPIER, A. B., ASMEROM, Y., LIU, K.-B., PRUFER, K. M., RIDLEY, H. E., POLYAK, V. & KENNETT, D. J. 2016. Persistent northward North Atlantic tropical cyclone track migration over the past five centuries. *Scientific reports,* 6**,** 37522.

BLAAUW, M. & CHRISTEN, A. 2011. Flexible paleoclimate age-depth models using an autoregressive gamma process. *Bayesian Analysis,* 6**,** 457-474.

BLAKE, E. S., LANDSEA, C. W. & GIBNEY, E. J. 2011. The deadliest, costliest, and most intense United States tropical cyclones from 1851 to 2010 (and other frequently requested hurricane facts). *In:* CENTER, N. H. (ed.) *NOAA Technical Memorandum.* National Hurricane Center Miami.

BLAKE, E. S. & ZELINSKY, D. A. 2018. Hurricane Harvey. *In:* CENTER, N. H. (ed.) *National Hurricane Center Tropical Cyclone Report.* National Hurricane Center.

BRANDON, C. M., WOODRUFF, J. D., DONNELLY, J. P. & SULLIVAN, R. M. 2014. How unique was Hurricane Sandy? Sedimentary reconstructions of extreme flooding from New York Harbor. *Scientific reports,* 4**,** 7366.

BRANDON, C. M., WOODRUFF, J. D., LANE, P. & DONNELLY, J. P. 2013. Constraining flooding conditions for prehistoric hurricanes from resultant

deposits preserved in Florida sinkholes. *Geochemistry Geophysics Geosystems,* 14**,** 2993-3008.

CHAVAS, D. R., LIN, N., DONG, W. & LIN, Y. 2016. Observed tropical cyclone size revisited. *Journal of Climate,* 29**,** 2923-2939.

COHEN, T. J. & SWEETSER, E. I. 1975. The 'spectra'of the solar cycle and of data for Atlantic tropical cyclones. *Nature,* 256**,** 295-296.

COLE, L. G. 1910. The caverns and people of the northern Yucatan. *Bulletin of the American Geographical Society,* 42**,** 321-336.

CROTTY, K. & TEETER, J. Post Pleistocene salinity variations in a blue hole, San Salvador Island, Bahamas, as interpreted from the ostracode fauna. Proceedings of the Second Symposium on the Geology of the Bahamas, 1984. 3-16.

DASGUPTA, S., LAPLANTE, B., MEISNER, C., WHEELER, D. & YAN, J. 2009. The impact of sea level rise on developing countries: a comparative analysis. *Climatic change,* 93**,** 379-388.

DENOMEE, K. C., BENTLEY, S. J. & DROXLER, A. W. 2014. Climatic control on hurricane patterns: a 1200-y near-annual record from Lighthouse Reef, Belize. *Scientific Reports,* 4**,** 7.

DONNELLY, J. P. 2005. Evidence of past intense tropical cyclones from backbarrier salt pond sediments: a case study from Isla de Culebrita, Puerto Rico, USA. *Journal of Coastal Resarch,* 42**,** 201-210.

DONNELLY, J. P., HAWKES, A. D., LANE, P., MACDONALD, D., SHUMAN, B. N., TOOMEY, M. R., VAN HENGSTUM, P. J. & WOODRUFF, J. D. 2015. Climate forcing of unprecedented intense-hurricane activity in the last 2000 years. *Earth's Future,* 3**,** 49-65.

DONNELLY, J. P., SMITH BRYANT, S., BUTLER, J., DOWLING, J., FAN, L., HAUSMANN, N., NEWBY, P., SHUMAN, B., STERN, J., WESTHOVER, K. & WEBB, T. I. 2001. 700 yr sedimentary record of intense hurricane landfalls in southern New England. *Geological Society of America Bulletin,* 113**,** 715-727.

DONNELLY, J. P. & WOODRUFF, J. D. 2007. Intense hurricane activity over the past 5,000 years controlled by El Niño and the West African Monsoon. *Nature,* 447**,** 465-468.

ELSNER, J. B. 2003. Tracking hurricanes. *Bulletin of the American Meterorological Society,* 84**,** 353-356.

EMANUEL, K. 2005. Increasing destructiveness of tropical cyclones over the past 30 years. *Nature,* 436**,** 686-688.

EMANUEL, K. A. 1986. An air-sea interaction theory for tropical cyclones. Part I: Steady-state maintenance. *Journal of the Atmospheric Sciences,* 43**,** 585-605.

EMANUEL, K. A. 2013. Downscaling CMIP5 climate models shows increased tropical cyclone activity over the 21st century. *Proceedings of the National Academy of Sciences of the United States of America,* 110**,** 12219-12224.

FALL, P. L., VAN HENGSTUM, P. J., LAVOLD-FOOTE, L., DONNELLY, J. P., ALBURY, N. A. & TAMALAVAGE, A. E. 2021. Human arrival and landscape dynamics in the northern Bahamas. *Proceedings of the National Academy of Sciences,* 118.

FORD, D. C. & EWERS, R. O. 1978. The development of limestone cave systems in the dimensions of length and depth. *Canadian Journal of Earth Sciences,* 15**,** 1783-1798.

FRAPPIER, A., KNUTSON, T., LIU, K. B. & EMANUEL, K. 2007. Perspective: coordinating paleoclimate research on tropical cyclones with hurricane-climate theory and modelling. *Tellus A,* 59**,** 529-537.

GISCHLER, E., SHINN, E. A., OSCHMANN, W., FIEBIG, J. & BUSTER, N. A. 2008. A 1500-year Holocene Caribbean climate archive from the Blue Hole, Lighthouse Reef, Belize. *Journal of Coastal Resarch,* 24**,** 1495-1505.

GRAY, W. M. 1968. Global view of the origin of tropical disturbances and storms. *Monthly Weather Review,* 96**,** 669-700.

GRAY, W. M. 1984. Atlantic seasonal hurricane frequency. Part I: El Niño and 30 mb quasi-biennial oscillation influences. *Monthly Weather Review,* 112**,** 1649-1668.

GULLEY, J., BREECKER, D., COVINGTON, M., COOPERDOCK, S., BANNER, J., MOORE, P., NORONHA, A., BREITHAUPT, C., MARTIN, J. & JENSON, J. 2020. Tidal pumping and biogeochemical processes: dissolution within the tidal capillary fringe of eogenetic coastal carbonates. *Earth Surface Processes and Landforms*.

GULLEY, J. D., MARTIN, J. B., MOORE, P. J., BROWN, A., SPELLMAN, P. D. & EZELL, J. 2015. Heterogeneous distributions of CO2 may be more important for dissolution and karstification in coastal eogenetic limestone than mixing dissolution. *Earth Surface Processes and Landforms,* 40**,** 1057-1071.

GULLEY, J. D., MARTIN, J. B., MOORE, P. J. & MURPHY, J. 2013. Formation of phreatic caves in an eogenetic karst aquifer by CO2 enrichment at lower water tables and subsequent flooding by sea level rise. *Earth Surface Processes and Landforms,* 38**,** 1210-1224.

HEARTY, P. J., OLSON, S. L., KAUFMAN, D. S., EDWARDS, R. L. & CHENG, H. 2004. Stratigraphy and geochronology of pitfall accumulations in caves and fissures, Bermuda. *Quaternary Science Reviews,* 23**,** 1151-1171.

KALDI, J. & GIDMAN, J. 1982. Early diagenetic dolomite cements; examples from the Permian Lower Magnesian Limestone of England and the Pleistocene carbonates of the Bahamas. *Journal of Sedimentary Research,* 52**,** 1073-1085.

KJELLMARK, E. 1996. Late Holocene climate change and human disturbance on Andros Island, Bahamas. *Journal of Paleolimnology,* 15**,** 133-145.

KLOTZBACH, P. J. 2011a. El Niño–Southern Oscillation's impact on Atlantic basin hurricanes and US landfalls. *Journal of Climate,* 24**,** 1252-1263.

KLOTZBACH, P. J. 2011b. The influence of El Niño–Southern Oscillation and the Atlantic multidecadal oscillation on Caribbean tropical cyclone activity. *Journal of Climate,* 24**,** 721-731.

KNAPP, K. R., DIAMOND, H. J., KOSSIN, J. P., KRUK, M. C. & SCHRECK, C. J. 2018. International Best Track Archive for Climate Stewardship (IBTrACS) Project, Version 4, [North Atlantic Subset]. *In:* INFORMATION, N. N. C. F. E. (ed.).

KNAPP, K. R., KRUK, M. C., LEVINSON, D. H., DIAMOND, H. J. & NEUMANN, C. J. 2010. The international best track archive for climate stewardship (IBTrACS) unifying tropical cyclone data. *Bulletin of the American Meteorological Society,* 91**,** 363-376.

KNUTSON, T. R., MCBRIDE, J. L., CHAN, J., EMMANUEL, K., HOLLAND, G., LANDSEA, C., HELD, I., KOSSIN, J. P., SRIVASTAVA, A. K. & SUGI, M. 2010. Tropical cyclone and climate changes. *Nature Geoscience,* 3**,** 157-163.

KORTY, R. L., CAMARGO, S. J. & GALEWSKY, J. 2012. Variations in tropical cyclone genesis factors in simulations of the Holocene epoch. *Journal of Climate,* 25**,** 8196-8211.

KORTY, R. L., EMANUEL, K. A., HUBER, M. & ZAMORA, R. A. 2017. Tropical cyclones downscaled from simulations with very high carbon dioxide levels. *Journal of Climate,* 30**,** 649-667.

KOSSIN, J. P., CAMARGO, S. J. & SITKOWSKI, M. 2010. Climate modulation of North Atlantic hurricane tracks. *Journal of Climate,* 23**,** 3057-3076.

KOSSIN, J. P. & VIMONT, D. J. 2007. Understanding Altantic Hurricane variability and trends. *Bulletin of American Meteorological Society,* 88**,** 1767-1781.

KOVACS, S. E., VAN HENGSTUM, P. J., REINHARDT, E. G., DONNELLY, J. P. & ALBURY, N. A. 2013. The late Holocene flooding history of Runway Sinkhole: a partially flooded coastal karst basin in the northern Bahamas. *Quaternary International,* 317**,** 118-132.

LANDSEA, C. W. & FRANKLIN, J. L. 2013. Atlantic hurricane database uncertainty and presentation of a new database format. *Monthly Weather Review,* 141**,** 3576-3592.

LANDSEA, C. W., HARPER, B. A., HOARAU, K. & KNAFF, J. A. 2006. Can we detect trends in extreme tropical cyclones? *Science,* 313**,** 452-454.

LANE, P., DONNELLY, J. P., WOODRUFF, J. D. & HAWKES, A. D. 2011. A decadally-resolved paleohurricane record archived in the late Holocene sediments of a Florida sinkhole. *Marine Geology,* 287**,** 14-30.

LIN, Y., ZHAO, M. & ZHANG, M. 2015. Tropical cyclone rainfall area controlled by relative sea surface temperature. *Nature Communications,* 6**,** 6591.

LIU, K. & FEARN, M. L. 2000. Reconstruction of prehistoric landfall frequencies of catastrophic hurricanes in NW Florida from lake sediment records. *Quaternary Research,* 52**,** 238-245.

MCADIE, C., LANDSEA, C., NEUMANN, C. J., DAVID, J. E. & BLAKE, E. S. 2009. *Tropical Cyclones of the North Atlantic Ocean, 1851-2006: With 2007 and 2008 Track Maps Included*, US Department of Commerce, National Oceanic and Atmospheric Administration.

MCCLAIN, M. E., SWART, P. K. & VACHER, H. L. 1992. The hydrogeochemistry of early meteoric diagenesis in a Holocene deposit of biogenic carbonates. *Journal of Sedimentary Research,* 62**,** 1008-1022.

MCCLOSKEY, T. A. & LIU, K. B. 2012. *A 7000 year record of paleohurricane activity from a coastal weland in Belize*.

MELIM, L. A., MASAFERRO, J. L., VACHER, H. & QUINN, T. 1997. Geology of the Bahamas: subsurface geology of the Bahamas banks. *Geology and Hydrogeology of Carbonate Islands. Elsevier, Amsterdam. Dev. Sedimentol,* 54**,** 161-182.

MILLER, K. G., KOPP, R. E., HORTON, B. P., BROWNING, J. V. & KEMP, A. C. 2013. A geological perspective on sea-level rise and its impacts along the US mid-Atlantic coast. *Earth's Future,* 1**,** 3-18.

MILLIMAN, J. D., FREILE, D., STEINEN, R. P. & WILBER, R. J. 1993. Great Bahama Bank aragonitic muds; mostly inorganically precipitated, mostly exported. *Journal of Sedimentary Research,* 63**,** 589-595.

MULLINS, H. T. & LYNTS, G. W. 1977. Origin of the northwestern Bahama Platform: Review and reinterpretation. *Geological Society of America Bulletin,* 88**,** 1447-1461.

MYLROIE, J. E. & CAREW, J. L. 1990. The flank margin model for dissolution cave development in carbonate platforms. *Earth Surface Process Landforms,* 15**,** 413-424.

MYLROIE, J. E., CAREW, J. L. & MOORE, A. I. 1995. Blue holes: definitions and genesis. *Carbonates and Evaporites,* 10**,** 225-233.

NEUMANN, C. J. J. C. 1987. The national hurricane center risk analysis program (HURISK). 1**,** 5.

OLIVA, F., PEROS, M. & VIAU, A. 2017. A review of the spatial distribution of and analytical techniques used in paleotempestological studies in the western North Atlantic Basin. *Progress in Physical Geography***,** 171-190.

PACHAURI, R. K., MEYER, L. A. & TEAM, C. W. 2014. Climate change 2014: synthesis report. Contribution of Working Groups I, II and III to the fifth assessment report of the Intergovernmental Panel on Climate Change. *In:* PACHAURI, R. K. & MEYER, L. A. (eds.). Geneva, Switzerland: IPCC.

PALMEN, E. Formation and development of tropical cyclones. Proceedings of tropical cyclone symposium, Brisbane, 1956. 213-231.

PALMER, A. N. 1991. Origin and morphology of limestone caves. *Geological Society of America Bulletin,* 103**,** 1-21.

PIELKE JR, R. A., GRATZ, J., LANDSEA, C. W., COLLINS, D., SAUNDERS, M. A. & MUSULIN, R. 2008. Normalized hurricane damage in the United States: 1900–2005. *Natural Hazards Review,* 9**,** 29-42.

RIEHL, H. 1954. Tropical Meterology, New York, McGraw-Hill Book Co.

RODYSILL, J. R., DONNELLY, J. P., SULLIVAN, R., LANE, P. D., TOOMEY, M., WOODRUFF, J. D., HAWKES, A. D., MACDONALD, D., D'ENTREMONT, N. & MCKEON, K. 2020. Historically unprecedented Northern Gulf of Mexico hurricane activity from 650 to 1250 CE. *Scientific reports,* 10**,** 1-17.

SCHMITT, D., GISCHLER, E., ANSELMETTI, F. S. & VOGEL, H. 2020a. Caribbean cyclone activity: an annually-resolved Common Era record. *Scientific reports,* 10**,** 1-17.

SCHMITT, D., GISCHLER, E., BIRGEL, D., PECKMANN, J., ANSELMETTI, F. S. & VOGEL, H. 2020b. Great Blue Hole (Lighthouse Reef, Belize): A continuous, annually-resolved record of Common Era sea surface temperature, Atlantic Multidecadal Oscillation and cyclone-controlled run-off. *Quaternary science reviews,* 247**,** 106570.

SCHNEIDER, T., BISCHOFF, T. & HAUG, G. H. 2014. Migrations and dynamics of the intertropical convergence zone. *Nature,* 513**,** 45-53.

SHARMILA, S. & WALSH, K. 2018. Recent poleward shift of tropical cyclone formation linked to Hadley cell expansion. *Nature Climate Change,* 8**,** 730.

SHINN, E. A., REICH, C. D., LOCKER, S. D. & HINE, A. C. 1996. A giant sediment trap in the Florida Keys. *Journal of Coastal Research,* 12**,** 953-959.

SOBEL, A. H., CAMARGO, S. J., HALL, T. M., LEE, C.-Y., TIPPETT, M. K. & WING, A. A. 2016. Human influence on tropical cyclone intensity. *Science,* 353**,** 242-246.

STEADMAN, D. W., FRANZ, R., MORGAN, G. S., ALBURY, N. A., KAKUK, B., BROAD, K., FRANZ, S. E., TINKER, K., PATEMAN, M. P., LOTT, T. A., JARZEN, D. M. & DILCHER, D. L. 2007. Exceptionally well preserved late

Quaternary plant and vertebrate fossils from a blue hole on Abaco, The Bahamas. *Proceedings of the National Academy of Sciences,* 104**,** 19897-19902.

STUDHOLME, J. & GULEV, S. 2018. Concurrent changes to Hadley circulation and the meridional distribution of tropical cyclones. *Journal of Climate,* 31**,** 4367-4389.

SULLIVAN, R. M., VAN HENGSTUM, P. J., COATS, S. J., DONNELLY, J. P., TAMALAVAGE, A. E., WINKLER, T. S. & ALBURY, N. A. Submitted. Hydroclimate Dipole drive multi-centennial variability in the western Tropical North Atlantic Margin during the Middle and Late Holocene. *Paleoceanography and Paleoclimatology*.

SULLIVAN, R. M., VAN HENGSTUM, P. J., DONNELLY, J. P., WINKLER, T. S., MARK, S. E. & ALBURY, N. A. 2020. Absolute and relative dating of human remains in a Bahamian sinkhole (Great Cistern, Abaco). *Journal of Archaeological Science: Reports,* 32**,** 102441.

TAMALAVAGE, A. E., VAN HENGSTUM, P. J., LOUCHOUARN, P., MOLODTSOV, S., KAISER, K., DONNELLY, J. P., ALBURY, N. A. & FALL, P. L. 2018. Organic matter sources and lateral sedimentation in a Bahamian karst basin (sinkhole) over the late Holocene: Influence of local vegetation and climate. *Palaeogeography, Palaeoclimatology, Palaeoecology,* 506**,** 70-83.

TOOMEY, M. R., CURRY, W. B., DONNELLY, J. P. & VAN HENGSTUM, P. J. 2013. Reconstructing 7000 years of North Atlantic hurricane variability using deep-sea sediment cores from the western Great Bahama Bank. *Paleoceanography,* 28**,** 31-41.

TROWER, E. J., LAMB, M. P. & FISCHER, W. W. 2019. The origin of carbonate mud. *Geophysical Research Letters*.

VACHER, H. L. 1988. Dupuit-Ghyben-Herzberg analysis of strip island lenses. *Geological Society of America Bulletin,* 100**,** 580-591.

VAN HENGSTUM, P. J., DONNELLY, J. P., FALL, P. L., TOOMEY, M. R., ALBURY, N. A. & KAKUK, B. 2016. The intertropical convergence zone modulates intense hurricane strikes on the western North Atlantic margin. *Scientific reports,* 6.

VAN HENGSTUM, P. J., DONNELLY, J. P., TOOMEY, M. R., ALBURY, N. A., LANE, P. & KAKUK, B. 2014. Heightened hurricane activity on the Little Bahama Bank from 1350 to 1650 AD. *Continental Shelf Research,* 86**,** 103-115.

VAN HENGSTUM, P. J., MAALE, G., DONNELLY, J. P., ALBURY, N. A., ONAC, B. P., SULLIVAN, R. M., WINKLER, T. S., TAMALAVAGE, A. E. & MACDONALD, D. 2018. Drought in the northern Bahamas from 3300 to 2500 years ago. *Quaternary Science Reviews,* 186**,** 169-185.

VAN HENGSTUM, P. J., WINKLER, T. S., TAMALAVAGE, A. E., SULLIVAN, R. M., LITTLE, S. N., MACDONALD, D., DONNELLY, J. P. & ALBURY, N. A. 2020. Holocene sedimentation in a blue hole surrounded by carbonate tidal flats in The Bahamas: Autogenic versus allogenic processes. *Marine Geology,* 419**,** 106051.

VECCHI, G. A., DELWORTH, T. L. & BOOTH, B. 2017. Climate science: Origins of Atlantic decadal swings. *Nature,* 548**,** 284.

VECCHI, G. A. & KNUTSON, T. R. 2011. Estimating annual numbers of Atlantic hurricanes missing from the HURDAT database (1878–1965) using ship track density. *Journal of Climate,* 24**,** 1736-1746.

WALLACE, D. J., WOODRUFF, J. D., ANDERSON, J. B. & DONNELLY, J. P. 2014. Palaeohurricane reconstructions from sedimentary archives along the Gulf of Mexico, Caribbean Sea and western North Atlantic Ocean margins. *Geological Society, London, Special Publications,* 388**,** 481-501.

WALLACE, E., DONNELLY, J., VAN HENGSTUM, P., WIMAN, C., SULLIVAN, R., WINKLER, T., D'ENTREMONT, N., TOOMEY, M. & ALBURY, N. 2019. Intense hurricane activity over the past 1500 years at South Andros Island, The Bahamas. *Paleoceanography and Paleoclimatology,* 34.

WALLACE, E. J., COATS, S., EMANUEL, K. & DONNELLY, J. P. 2021a. Centennial-scale shifts in storm frequency captured in paleohurricane records from The Bahamas arise predominantly from random variability. *Geophysical Research Letters,* 48**,** e2020GL091145.

WALLACE, E. J., DONNELLY, J. P., VAN HENGSTUM, P. J., WINKLER, T. S., DIZON, C., LABELLA, A., LOPEZ, I., D'ENTREMONT, N. E., SULLIVAN, R. M., WOODRUFF, J. D., HAWKES, A. D. & MAIO, C. Sub. March 2021. Regional shifts in paleohurricane activity over the last 1500 years derived from blue hole sediments offshore of Middle Caicos Island. *Quaternary Science Reviews*.

WALLACE, E. J., DONNELLY, J. P., VAN HENGSTUM, P. J., WINKLER, T. S., MCKEON, K., MACDONALD, D., D'ENTREMONT, N. E., SULLIVAN, R. M., WOODRUFF, J. D., HAWKES, A. D. & MAIO, C. 2021b. 1050 years of

hurricane strikes on Long Island in The Bahamas. *Paleoceanography and Paleoclimatology,* 36**,** e2020PA004156.

WEBSTER, P. J., HOLLAND, G. J., CURRY, J. A., CHANG, H. -R. 2005. Changes in tropical cyclone number, duration, and intensity in a warming environment. *Science,* 1844**,** 1844-1846.

WHITAKER, F. F. & SMART, P. L. 1997. Hydrogeology of the Bahamian archipelago. *Geology and hydrogeology of carbonate islands: Amsterdam, Elsevier***,** 183-216.

WHITAKER, F. F. & SMART, P. L. 2007a. Geochemistry of meteoric diagenesis in carbonate islands of the northern Bahamas: 1. Evidence from field studies. *Hydrological Processes: An International Journal,* 21**,** 949-966.

WHITAKER, F. F. & SMART, P. L. 2007b. Geochemistry of meteoric diagenesis in carbonate islands of the northern Bahamas: 2. Geochemical modelling and budgeting of diagenesis. *Hydrological Processes: An International Journal,* 21**,** 967-982.

WINKLER, T. S., HENGSTUM, P. J. V., DONNELLY, J. P., WALLACE, E. J., D'ENTREMONT, N., HAWKES, A. D., SULLIVAN, R. M., WOODRUFF, J. D. & MAIO, C. V. Submitted 2021. Oceanic passage of hurricanes across Cay Sal Bank in The Bahamas over the last 550 years. *Marine Geology*.

WINKLER, T. S., VAN HENGSTUM, P. J., CAVAZOS, O., HIGHFIELD, W., DONNELLY, J. P. & COATS, S. In prep., 2021. Latitudinal rainfall mediates karst landform density across the Bahamian Archipelago. Texas A&M University.

WINKLER, T. S., VAN HENGSTUM, P. J., DONNELLY, J. P., WALLACE, E. J., SULLIVAN, R. M., MACDONALD, D. & ALBURY, N. A. 2020. Revising evidence of hurricane strikes on Abaco Island (The Bahamas) over the last 700 years. *Scientific Reports,* 10**,** 1-17.

WONG, P. P., LOSADA, I. J., GATTUSO, J., HINKEL, J., KHATTABI, A., MCINNES, K., SAITO, Y. & SALLENGER, A. 2014. Coastal systems and low-lying areas. *Climate Change***,** 361-409.

WOODRUFF, J. D., DONNELLY, J. P., MOHRIG, D. & GEYER, W. R. 2008. Reconstructing relative flooding intensities responsible for hurricane-induced deposits from Laguna Playa Grande, Vieques, Puerto Rico. *Geology,* 36**,** 391-394.

WOODRUFF, J. D., IRISH, J. L. & CAMARGO, S. J. 2013. Coastal flooding by tropical cyclones and sea-level rise. *Nature,* 504**,** 44.

YANG, Y., MASELLI, V., NORMANDEAU, A., PIPER, D. J., LI, M. Z., CAMPBELL, D. C., GREGORY, T. & GAO, S. 2020. Latitudinal response of storm activity to abrupt climate change during the last 6,500 years. *Geophysical Research Letters,* 47**,** e2020GL089859.

ZEGARRA, M. A., SCHMID, J. P., PALOMINO, L. & SEMINARIO, B. 2020. Impact of Hurricane Dorian in The Bahamas: A View from the Sky. Inter-American Development Bank.

2. REVISING EVIDENCE OF HURRICANE STRIKES ON ABACO ISLAND (THE BAHAMAS) OVER THE LAST 700 YEARS*

2.1. Introduction

The northern Bahamas has been a hurricane hotspot during the observational period (1850 CE to present) with some of the highest incidence of hurricane passage in the North Atlantic Ocean (~13 ≥Category 2 events within 50 km of any point in the northern Bahamas, Fig 1). These storms primarily formed in the Main Development region (MDR) before tracking westward to the northern Bahamas where they caused devastating wind and flood damage to Abaco Island and Grand Bahama Island, before recurving northwards into higher latitudes (Figs. 2, 4b-e; Knapp et al., 2018, Knapp et al., 2010, van Hengstum et al., 2016). On 26 August 2019, for example, Hurricane Dorian made landfall on Abaco Island at Category 5 strength (sustained winds up to 296 km hr^{-1}) and caused widespread economic and human loss. Future hurricane risk assessments mostly rely on observations taken over the last 170 years. However, it remains unclear whether the high rate of hurricane passage through the northern Bahamas has persisted through time or is simply an artifact of stochastic randomness from this short dataset.

*Reprinted with permission from WINKLER, T. S., VAN HENGSTUM, P. J., DONNELLY, J. P., WALLACE, E. J., SULLIVAN, R. M., MACDONALD, D. & ALBURY, N. A. 2020. Revising evidence of hurricane strikes on Abaco Island (The Bahamas) over the last 700 years. Scientific Reports, 10, 1-17.

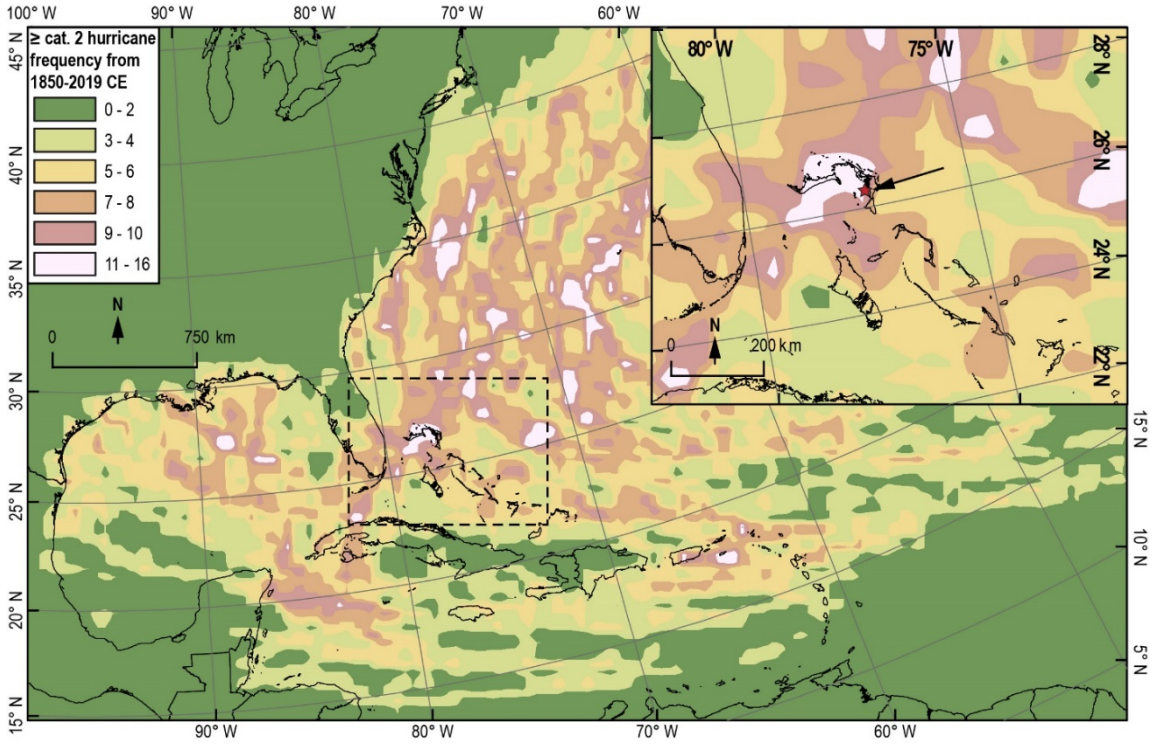

Figure 2.1. Frequency of ≥Category 2 hurricanes (Saffir-Simpson scale) within a 50 km radius from 1850 to 2019 CE in the North Atlantic.
Storm data is from the International Best Track Archive for Climate Stewardship (IBTrACS) v04 (Knapp et al., 2010, Knapp et al., 2018). Intensity is specifically derived from the IBTrACS v4 subset USA_Agency_SSHS, which is derived from HURDAT_ATL maximum wind speed data. TPBH is indicated with a red star pointed out by the black arrrow in the inset panel. The regions that we refer to as modern hurricane hotspots are pinkish-white in color (11-16 ≥Category 2 events within 50 km). The Little Bahama Bank is a hurricane hotspots. Basemaps were downloaded from *DIVA-GIS* by Hijmans et al., 2012). Map generation and associated spatial calculations were performed in ArcMap 10.7.1 software using North America Albers Equal Conic Area projected coordinate system (Snyder, 1978). See APPENDIX B Section S2.1 for detailed methods on how the map was created.

Models that evaluate hurricane activity in response to 2°C global warming indicate a medium-to-high confidence level that the global proportion of intense hurricanes (Category 4-5) will increase (Knutson et al., 2020, Emanuel et al., 2008, Emanuel, 2013, Walsh et al., 2015, Walsh et al., 2016, Sobel et al., 2016, Korty et al., 2017). This trend toward more frequent intense hurricanes has already been observed in

a statistical assessment of hurricanes recorded from 1979-2017 (Kossin et al., 2020). Four of the costliest Atlantic hurricanes during the last 170 years occurred between 2012 and 2019 CE (up to USD $336 billion in damage- Blake et al., 2011, 2018; Sandy-2012, Harvey-2017, Irma-2017, Maria-2017), demonstrating the socio-economic threats posed by more frequent intense hurricanes. Disentangling natural hurricane variability versus the impact of anthropogenic carbon dioxide loading of the atmosphere on future hurricane activity remains a significant climatological forecasting challenge for the 21st century. The northern Bahamas emerges as a key geographic locality to assess the natural hurricane patterns over the past millennium given the high occurrence of recent hurricane passage (Fig. 2.1), and the potential for local geological records to document meaningful change in long-term hurricane activity.

Paleo-hurricane studies can assess background levels of hurricane activity at a given location, at least for the more intense storms. Many of these studies have identified dramatic variability in hurricane activity over the past few thousand years with o centennial-scale active and quiet intervals. Furthermore, these reconstructions are useful for anticipating future hurricane activity because the simultaneous influence of climate on hurricane activity at multiple sites can be assessed. Prehistoric hurricane landfall frequency has been reconstructed using hurricane-induced sediment deposits in salt-marshes (Donnelly et al., 2001, McCloskey and Liu, 2012), back-barrier coastal ponds (Brandon et al., 2014, Donnelly, 2005, Donnelly et al., 2015, Donnelly and Woodruff, 2007, Woodruff et al., 2008b, Bregy et al., 2018), and deep-sea sediments (Toomey et al., 2013). In the last decade, stratigraphy preserved in blue holes and sinkholes on

carbonate platforms has emerged as providing faithful archives of paleo-hurricane passage (Denomee et al., 2014, van Hengstum et al., 2014, Wallace et al., 2019, Gischler et al., 2008, van Hengstum et al., 2016, Lane et al., 2011, Brandon et al., 2013, Brown et al., 2014). Blue holes form when dissolution of underlying carbonate bedrock forms a void or cave so large that the ceiling collapses under its own weight and (Mylroie et al., 1995a). The stratigraphy in a blue hole is often well preserved due to negligible exposure to waves or currents and bottom water dysoxia (Wallace et al., 2019).

Several paleo-hurricane reconstructions spanning the last several millennia at different resolutions (multi-decadal to annual), have linked latitudinal variability in Atlantic hurricane strikes to patterns of sea surface temperature variability in the tropical North Atlantic Ocean and the position of the Intertropical Convergence Zone (van Hengstum et al., 2016, Wallace et al., 2019). This result is consistent with some climate models (Merlis et al., 2013). In addition, paleo-hurricane activity in the sub-basins of the North Atlantic Ocean including the Gulf of Mexico (Brandon et al., 2013, Lane et al., 2011), Caribbean (Baldini et al., 2016, Denomee et al., 2014), and U.S. East Coast (Donnelly et al., 2015) exhibits spatial heterogeneity, based on the emerging array of high-resolution paleo-hurricane studies (<5-yr resolution per sample, spanning >500 years duration). Additional high-resolution paleo-hurricane studies are required to evaluate the degree to which this spatial heterogeneity is caused by stochastic variability versus the ocean-climate system.

Here we document that Great Abaco Island (Little Bahama Bank) experienced at least 18 intense hurricane strikes (*minimum* estimate, based on uncertainty) from 1500 to

1670 CE by developing a near annually-resolved record of hurricane passage from the sediment preserved in Thatchpoint Blue Hole (TPBH). This period from 1500 to 1670 CE (duration: 170 years), documents a minimum level of hurricane activity that exceeds the total number of ≥Category 2 observed events that passed near TPBH from 1850 to 2017 CE (duration: 169 years, 13 events in IBTrACS; Knapp et al., 2018, Knapp et al., 2010). This establishes a clear precedence for higher prehistorical hurricane activity in the northern Bahamas, and these results are critical to help diagnose climate influences on spatial patterns of intense hurricane activity through time.

2.2. Study Site: Thatchpoint Blue Hole

2.2.1. Regional Setting

TPBH is ~30 km southwest of Marsh Harbour on Great Abaco Island on the leeward margin of the Little Bahama Bank, which is the northernmost carbonate platform in the Bahamian Archipelago (26.32°N, 77.29°W, Fig. 2.2a, b). TPBH is currently 70 m deep and 50 m wide (van Hengstum et al., 2014). Antecedent lithology of this platform is ~10 km of mostly shallow-water carbonates that began accumulating in the Jurassic (Mullins and Lynts, 1977). Weathering and erosion have since dissolved these shallow-water carbonates into a mature karst landscape with abundant caves, terrestrial sinkholes, and flooded blue holes (Mylroie et al., 1995b, Mylroie et al., 1995a). TPBH is located at the transition between the Bight of Abaco (a shallow, subtidal lagoon) and the carbonate tidal flats on the western island margin (Fig. 2.2c). Temperature and salinity vary seasonally in the Bight of Abaco from 20 ºC to 30 ºC and

34 to 39 psu, with tidal pumping and wind-driven vertical mixing maintaining a stable tropical carbonate lagoon (Rasmussen and Neumann, 1988).

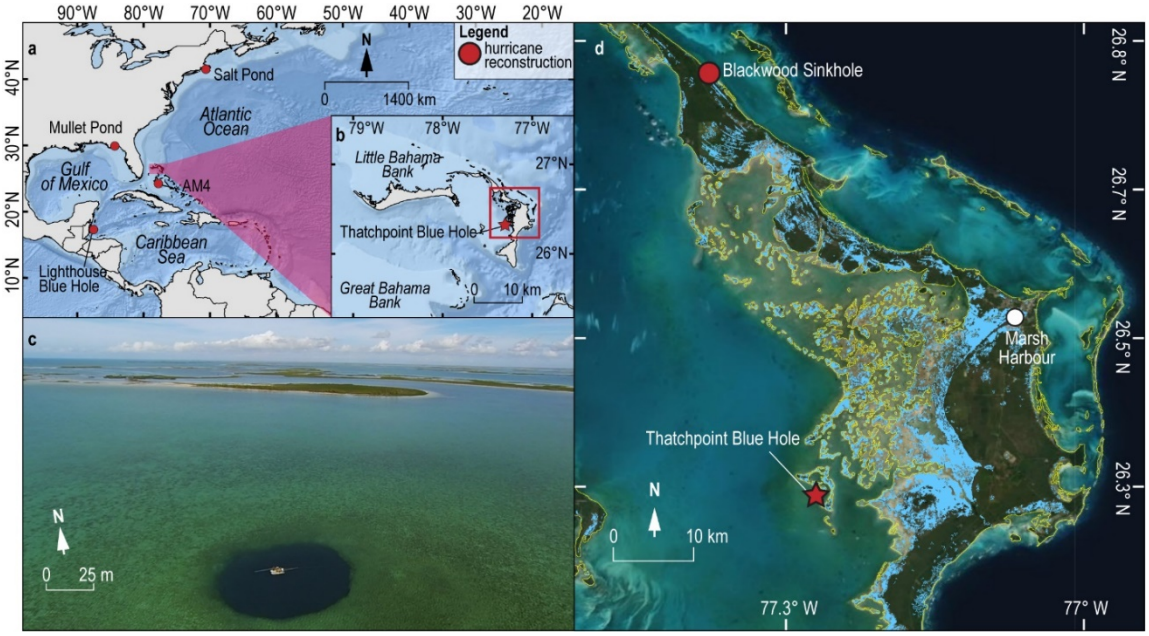

Figure 2.2. Thatchpoint Blue Hole regional context.
a, b) Location of TPBH (red star) in the North Atlantic, as well as the location of some huricane reconstructions cited in this study (red circles, Basemap source: *Esri Oceans*). c) Aerial photograph of TPBH collected by Pete van Hengstum in January 2015 using a DJI Phantom 3 with a mounted GoPro Hero3 digital camera. d) NASA ARIA satellite flood proxy map of Abaco Island on September 4th, 2019 during the peak flooding of Hurriane Dorian (Category 5, Saffir-Simpson scale; NASA-ARIA, 2019). The general terrestrial boundaries for Abaco are indicated in yellow (source: *DIVA-GIS* by Hijmans et al., 2012), and Dorian induced flooding is shown in light blue. Optical satelitte imagery was obtained from *ESRI* basemap compiled satellite imagery.

The benthos in the Bight of Abaco is covered with sandy-mud carbonate sediment that is mobilized during storm events, with the preferential off-bank export of finer particles as suspended load (Neumann and Land, 1975). Based on previous regional observations by Neumann and Land (1975), we expect that high waves, surge and current velocities during hurricane events mobilize and resuspend benthic sediment in the Bight of Abaco. Such physical processes are expected to naturally promote sand-

layer accumulation in a natural settling tube, like a blue hole, following hurricane passage (i.e., Thatchpoint Blue Hole). Local sedimentary environments have provided ample sediment supply for transport into TPBH during the last millennium, since the Bight of Abaco became a subtidal carbonate lagoon by ~5500 cal yrs BP (calibrated years before present; Rasmussen et al., 1990) and the carbonate tidal flats formed by ~2000 cal yrs BP (van Hengstum et al., 2020). Based on satellite imagery after Hurricane Dorian in September 2019 (NASA-ARIA, 2019), the western margin of Abaco Island where TPBH is located is vulnerable hurricane surge and flooding (Fig. 2.2d).

2.2.2. Previous Hurricane Record from Thatchpoint Blue Hole

In May 2011 (prior to Hurricane Irene in August 2011), SCUBA divers collected a 164 cm core (TPBH-C1, Fig. 2.3) from TPBH to evaluate the potential of its stratigraphy to document paleo-hurricane activity (van Hengstum et al., 2014). The core indicated that background sedimentation in TPBH was fine to medium carbonate silt (15-25 μm) juxtaposed with coarser-grained layers (mean grain size >45 μm). No terrestrial leaves were found in the stratigraphy, so radiocarbon dating of bivalves (i.e., *Barbatia domingensis*), ^{210}Pb, and ^{137}Cs provided age control. The radioisotopes indicated (^{14}C, ^{210}Pb, and ^{137}Cs) that the upper 60 cm of TPBH-C1 were deposited between 1950 and 2011 CE, with an average sedimentation rate of ~1.6 cm yr^{-1}. The uppermost coarse-grained (sand) sedimentary layers were attributed to Hurricane Jeanne in 2004 (Category 3) and Hurricane Floyd in 1999 (Category 3). Together, the sedimentary processes in the Bight of Abaco described by Neumann and Land (1975)

and the preserved stratigraphy in TPBH make this a suitable location to evaluate paleo hurricane passage.

Problematically, the radiocarbon dated *Barbatia domingensis* shells in the lower part of TPBH-C1 (61 to 164 cm) suggested that the sedimentation rate of 1.6 cm yr^{-1} (0 to 61 cm) abruptly decreased at ~1950 CE to ~0.1 cm yr^{-1} (61 to 164 cm). As discussed below, the new longer sediment cores collected from the center of TPBH do not contain *B. domingensis* shells, and the cores document a constant sedimentation rate in TPBH (1.3 cm yr^{-1}) spanning the last 700 years using an age model built with plant macrofossils. Elsewhere, *B. domingensis* lives attached to reefs and underwater cave walls, and the shell experiences post-mortem detachment and incorporation into the sediment record (van Hengstum et al., 2011, van Hengstum et al., 2019). Three relevant points emerge: (i) it is likely that TPBH-C1 was collected from a cave area (i.e., underneath a ceiling, APPENDIX B Fig. S2.2), (ii) the bivalves that were dated from lower in the core of TPBH-C1 became detached from the ceiling and incorporated into the sediment record long after their death, and (iii) the original 164 cm of stratigraphic sampled by TPBH-C1 actually preserves a continuous record of ~100 years (~1910 to 2011 CE), not 1000 years as previously reported by van Hengstum et al. (2014).

2.3. Methods

2.3.1. Sediment Collection and Analysis

Sediment vibracores (7.5 cm diameter) were collected in January 2015 (prior to Hurricane Dorian in 2019) by deploying a Rossfelder P3 submersible vibracoring system

from the surface on a portable raft that was positioned in the center of TPBH. The new cores collectively sampled the upper 888 cm of stratigraphy. The collected sediment-water interface was preserved in TPBH-C2 (615 cm; 26.3234° N, 77.2934° W) and TPBH-C5 (194 cm; 26.3233° N, 77.2934° W), but the Rossfelder P3 over-penetrated when collecting TPBH-C3 (836 cm, 26.32339° N, 77.29342° W) so the sediment-water interface was lost. TPBH-C3 and TPBH-C5 were taken within 1 m of each other, with TPBH-C2 taken within 5 m of these cores (APPENDIX B Fig. S2.2). The continuous sediment vibracores were sectioned into lengths up to 150 cm for transport back to the laboratory. During the sectioning of TPBH-C3, rapid sediment expansion caused by depressurizing hydrogen sulfide gas caused the loss of sediment from 410-447 cm core depth at a section break. A final composite and complete 888 cm stratigraphic record from TPBH was compiled by combining the preserved sediment-water interface from the upper 16 cm from TPBH-C5, the entirety of the longest core (TPBH-C3), and the stratigraphically-equivalent interval from TPBH-C2 (426-463 cm, established through correlative stratigraphy) that was lost during sectioning of TPBH-C3 (410-447 cm).

In the laboratory, all sediment core sections (TPBH-C2, TPBH-C3, TPBH-C5) were split lengthwise for photography, x-radiography, qualitative sediment description and quantitative textural analysis. Using similar methods as van Hengstum et al. (2014), sediment textural variability was analyzed in all cores using a standard loss on ignition procedure (LOI) combined with manual sieving over a 63 μm mesh (Fig. 2.3). Contiguous sediment subsamples (~2.5 cm^3) were obtained at 1 cm intervals downcore, desiccated overnight at 80°C, and then ignited at 550°C to re-mineralize organic carbon

(Heiri et al., 2001). The remaining carbonate sediment residue for each sample was manually wet sieved on a 63 μm mesh, re-desiccated at 80°C, and the reweighed to determine % mass (mg) of coarse particles >63 μm per total sampled mass of sediment ($\%D_{>63\mu m}$) content in each sample (Fig. 2.3).

2.3.2. Age Control

To independently constrain the upper portion of the TPBH record (top 510 cm) and the observational period in our record (1850 to 2015 CE) in particular, seven samples were analyzed downcore at 70 to 80 cm intervals (n = 7 from 1620 to 2015 CE) to identify any palynological evidence of colonial disturbance on the adjacent landscape from permanent settlements that were established as early as 1783 CE (Jasanoff, 2011). Pollen was processed following the methodology of Agosta G'meiner (2016), and counted to over 100 total grains per sample for all but one of the seven samples (*APPENDIX B Section 2 3 Opaque Spherules and Pollen*, APPENDIX B Table S2.2). Total fossil pollen concentrations ranged from 16,200 to 5,657 grains/cm^3 (APPENDIX B Table S2.2). The most substantial observation was a peak in opaque spherules at 140 cm, which are likely derived from the combustion of fossil fuels. Due east of TPBH, there was a short-lived settlement from 1906 to 1916 CE called "Wilson City" associated with the early 20th century Abaco pine logging industry (Craton and Saunders, 2002). This settlement included a rail system, logging town, and 300 ft. pier servicing ships that likely utilized coal. Therefore, 140 cm was assigned an age of 1911 ± 5 years in the sedimentary age-model. The stratigraphic position of the peak is consistent with the previous radioisotopic evidence from TPBH-C1 that the upper ~170 cm of sediment

dates to the within the last 100 years. ^{137}Cs activity was measured downcore in the top 140 cm of the core in 5-10 cm interval to constrain the chronohorizon associated with the onset and moratorium of nuclear weapons testing in 1954 CE and the 1963 CE, respectively. The results of this analysis were used as an independent test of the veracity of the sedimentary age-model for the TPBH composite record, and the precise methods used for this analysis are discussed in *APPENDIX B Section S2.3.2 Gamma Dating: Methods and Results*.

To develop age control for the older part of the record, available plant remains (e.g., mangrove leaves and unidentifiable organic matter) and two basal gastropods were submitted for radiocarbon dating from TPBH-C3 (n = 16) and TPBH-C2 (n = 2 dates, APPENDIX B Table S2.1). As previously mentioned, no *Barbatia domingensis* bivalves were found in any of the new cores extracted from the center of TPBH, and terrestrial plant macrofossils were rare. Samples submitted for radiocarbon dating did not originate from a stratigraphic level that was classified as a coarse sediment anomaly (see **2.3. Methods** subsection *2.3.3. Event Threshold Attribution and Frequency*), which helps limit the possibility of radiocarbon dating older material that was reworked during a high-energy event. The dates submitted from both TPBH-C3 and TPBH-C2 provided an independent assessment of sedimentation rate in two separate cores from TPBH, but all dates were subsequently used in developing the final downcore age-model for the 888 cm composite record.

Conventional radiocarbon results were calibrated into years before present (cal yrs BP) with consideration for the source of carbon incorporated into the analyzed

sample (i.e., marine vs. terrestrial reservoirs), and the fraction modern value ($F^{14}C$ exceeding 1.0 post-date 1950 CE). One mangrove leaf from 61.5 cm in TPBH-C3 was calibrated with the Northern Hemisphere Zone 2 dataset (NHZ2) in CALIbomb because its fraction modern carbon value ($F^{14}C$) exceeded 1.0000 (Reimer et al., 2004). Organic remains with a stable carbon isotopic value ($\delta^{13}C_{org}$) value more depleted than −18.0‰ were calibrated with IntCal13. However, the organic remains with more enriched $\delta^{13}C_{org}$ values of −17.0‰ and −8.8‰ were deemed as likely marine sourced organic remains (e.g., sea grass fragments), and the conventional radiocarbon results on these samples were subsequently calibrated using Marine13 (Reimer et al., 2013). Finally, two radiocarbon dates at the base of TPBH-C3 on intertidal gastropods (*Cerethium sp.*) were calibrated with a mixed 50/50% calibration curve to reflect their likely incorporation of both marine- and terrestrially-derived carbon into the production of their biogenic carbonate.

A final age-model with 95% confidence intervals for the 888 cm composite TPBH record was developed using Bayesian statistical approaches in the R package Bacon v2.2 (Blaauw and Christen, 2011) (Fig. 2.3). The final 15 control points used in the age-model were a core-top age of 2015 CE, the fossil fuel combustion spherule peak at 140 cm dated to 1906 to 1916 CE, and 13 radiocarbon dates (n = 11 from TPBH-C3, n = 2 from TPBH-C3). Dates from both TPBH-C3 and TPBH-C2 were included in the age-model for the composite 888 cm sedimentary record, with the depths in the composite record assigned to the dates from TPBH-C2 based on correlative stratigraphy. Coarse grained sedimentary layers that were thicker than 5 cm were assumed to have

been deposited instantaneously, based on their likely relationship to hurricane passage, so these coarse layers were treated as geologically instantaneous in the downcore age-model (indicated by orange bars in Fig. 2.3).

2.3.3. Event Threshold Attribution and Frequency

The methods of to identify the most likely intervals (i.e., event beds) where coarse-grained sedimentation substantially exceeds background sedimentary conditions were modified from Donnelly et al. (2015), Lane et al. (2011), Wallace et al. (2019). First, an 11-point moving average of data excluding those with a coarse fraction value >12% (upper 90th percentile of $\%D_{>63\mu m}$) was subtracted from all $\%D_{>63\mu m}$ data to establish a series of coarse sediment anomalies (CSA). Deposits were classified as hurricane events if the CSA exceeded the upper 90th percentile of the CSA cumulative distribution (CSA=4.39% $D_{>63\mu m}$). The suitability of this threshold was assessed by comparing the timing and number of deposits that exceed this threshold to the number of hurricanes that could have impacted TPBH during the last 164 years (1850-2014) based on the IBTrACS version 4 dataset that compiles observational records of hurricane activity since 1850 CE (Knapp et al., 2018, Knapp et al., 2010) (**2.5. Discussion** subsection *2.5.1. Historical Hurricane Strikes: Calibrating the Record*). Historical hurricanes were attributed to event beds by first determining the known hurricanes in the 2σ age-range of each event bed passed within or 50 and 115 km proximity thresholds. Starting with the most recent event bed (E1), we selected which hurricane(s) were most likely to leave a deposit in TPBH based on (i) how the date of the hurricane compared to the median age of the event deposit, (ii) intensity and proximity of the hurricane to

TPBH, (iii) which quadrant of the hurricane impacted the area around TPBH the most, and (iv) translational velocity of the hurricane (slower events are more likely to leave a deposit). Once a hurricane was attributed to an event deposit, this hurricane and any others that occurred more recently than that event were ruled out for attributions below. Similar to Lane et al. (2011), hurricane event beds per century were counted using a 100-year sliding window to assess centennial-scale hurricane variability, as well as a 50 year sliding window from which events per 50-years counts were multiplied by 2 to normalize units to events per century (Figs. 2.5, 2.6). The 50-year window counts emphasize shorter (multidecadal) periods of extremely high or low hurricane activity.

2.3.4. Determining Active Hurricane Periods

Independent of the climate system, simple stochastic variation in cyclogenesis and storm tracks can naturally create time intervals where hurricane activity at a given locale may be greater or less than average conditions. This random variability must be considered when assessing any potential periods of active hurricane activity at a given locality. Assuming hurricane frequency at a given location follows a Poisson process, we calculate cumulative Poisson probability (P) of hurricane frequency at value (k) based on expected frequency (λ) as follows in eq. 1:

$$\boldsymbol{P(k,\lambda) = 1 - \sum_{k=0}^{k} \frac{\lambda^k e^{-\lambda}}{k!}} \qquad \text{Eq. 1}$$

Values for expected hurricane event frequency (λ) were based on a regional estimate calculated by Wallace et al. (2019) (regional bounding 550 km radius circle centered over 24.08°N and 75.39°W). The expected regional frequency value (λ) of ≥Category 2 hurricanes passing within 50 km of any given point is 3.7 events per

century, resulting in upper 90th percentile cutoff threshold of 7.3 events per century and a lower 10th percentile cutoff threshold of 1.6 events per century. To calculate site-specific regional threshold, we examine the event frequency from 1900 to 2014 CE rather than the entire observational record back to 1850 CE due to increased uncertainty regarding storm intensity and track location in these older records. It was determined that there were 12 hurricane events that were likely to have induced coarse-sediment deposition in TPBH from 1900 to 2014 CE (see **2.5. Discussion** subsection: **2.5.1. Historical Hurricane Strikes: Calibrating the Record** for justification, Fig. 2.4). Of these twelve events, only nine coarse beds would be distinct in TPBH stratigraphy given the temporal resolution of this record (i.e., not counting multiple events within the same calendar year). This implies an average of 7.9 events per century which would result in an upper 90th percentile threshold of 13 events per century and a lower 10th percentile threshold of 4.7 events per century (Figs. 2.5, 2.6). As with the regionally derived thresholds, we calculated upper cutoff thresholds following the methods described by Ulm (1990). If the number of recorded storms per century exceeds (falls below) the upper (lower) threshold, there is a 90% probability that this increase (decrease) exceeds the influence of random variability and can be considered a period of active (quiescent) hurricane activity at a given locale.

2.3.5. Compilation of South Andros Paleo-Hurricane Records

The South Andros Stack compiles the three different blue hole sediment records (AM2, AM5, and AM4) presented in Wallace et al. (2019). These data are accessible online at the National Climatic Data Center (https://www.ncdc.noaa.gov/paleo-

search/study/27730). Wallace and others noted that these three different sediment records captured similar patterns of hurricane event frequency on South Andros while not capturing the exact same events. All three blue holes on South Andros were close enough to capture some, but not all, of the same events. Thus, when compiling these three records together, we sought to remove repeated representation of the same events among the three contributing records. To accomplish this, multiple events falling within the one sigma age-model uncertainties of each other were combined to represent a single landfall event on the island. We defined the date and one sigma age ranges for the combined events as the average of the dates and age ranges of the contributing events. When there was more than one event in a blue hole record falling within the age uncertainties of an event from another blue hole record, we consolidated the event in the first blue hole site that was closest in age to that captured in the second site. The main difference between the new South Andros Stack presented here and the solitary paleo-record from blue hole AM4 featured by Wallace et al. (2019) is a period of increased activity in the stacked record from ~1600 to 1780 CE.

2.4. Results: Sediment Record and Age Control

New sediment cores sampling the upper 888 cm of the sediment were collected from the center of TPBH (APPENDIX B Fig. S2.2). As with previous work, background sedimentation is marine carbonate mud (2.5Y 7/1, clay- to silt-sized particles) with fine-grained white, tan, and green laminations, with inclusions of small intertidal gastropods (e.g., *Cerethium* sp.) and subtidal marine benthic foraminifera (e.g., *Peneroplis sp.*). The

laminations and bedding indicate no mechanical mixing of the sediment by wave action or bioturbation. Interrupting the marine carbonate mud is coarse-grained carbonate sand (>63 um) deposits that are devoid of internal bedding and often dark grey (2.5Y 5/1). The mean coarse sediment fraction (%$D_{>63\mu m}$; % mass (mg) of >63 μm particles per sampled sediment mass) in TPBH-C3 is 6.84% (range: 0.36 to 44.18%, Fig. 2.3). Qualitative assessment of the particles in these coarse beds shows that they often contain fragmented macroinvertebrate skeletal material and larger (pebble-sized) clasts of weathered karst. Sediment surrounding TPBH in the subtidal carbonate lagoon have been characterized primarily as muddy sand (Neumann and Land, 1975), but karst fragments do occur on the proximal tidal sand bars (Rankey and Reeder, 2012).

TPBH-C3 and TPBH-C2 have overlapping stratigraphy for 612 cm for assessing the reproducibility of the sedimentary signals. By visually evaluating the coarse sediment anomalies (CSA) that exceed that event-bed definition threshold of 4.39% $D_{>63\mu m}$ CSA in TPBH-C3 and TPBH-C2 (see **2.3 Methods)**, it qualitatively appears that coarse-grained sedimentary bed incidence is replicated by each core (Fig. 2.3). TPBH-C3 records 34 events while TPBH-C2 records 33 events, when the same quantitative methodology for event threshold calculation is applied (described in **2.3 Methods**). The stratigraphic coherency of overlapping intervals of TPBH-C3 and TPBH-C2 lends confidence toward using the equivalent stratigraphic section from TPBH-C2 to “fill” the gap that occurred during sectioning of TPBH-C3 (426-463 cm, Fig. 2.3) to create a compiled composite record which records 53 total events in 888 cm.

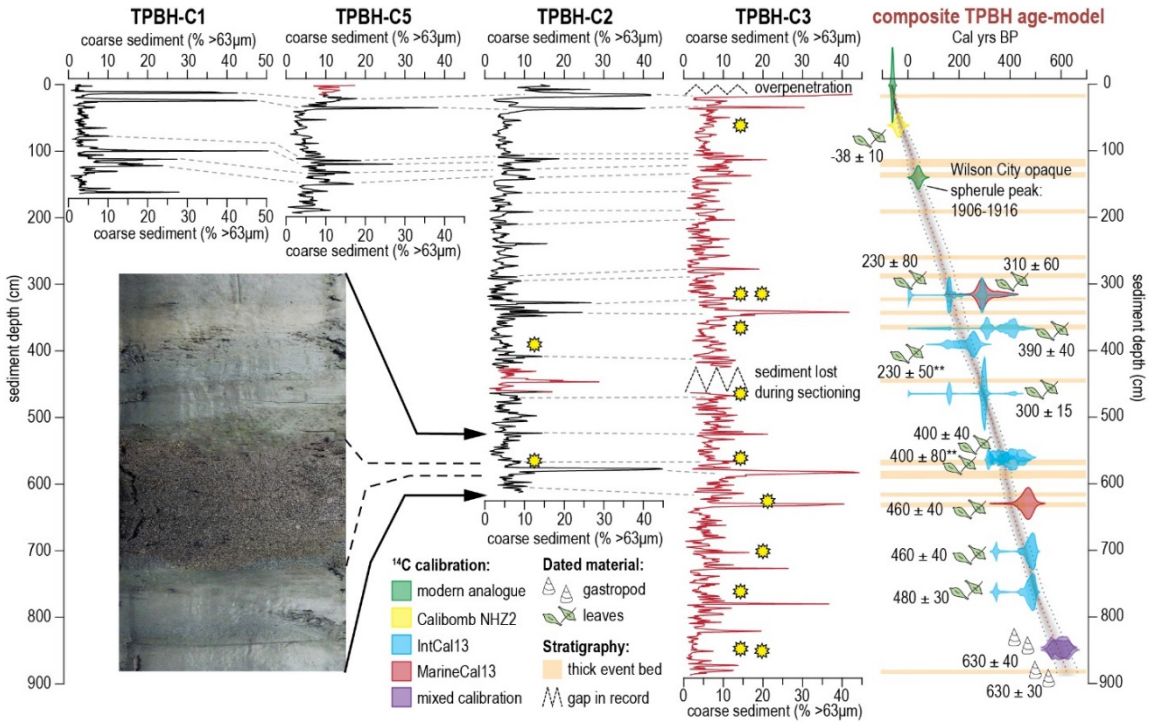

Figure 2.3. Preserved sedimentary archives, stratigraphic correlation, and sedimentary age-model.
Downcore sediment textural data (% $D_{>63\mu m}$) for all four cores from TPBH, with TPBH-C1 data derived from van Hengstum et al. (2014). The red lines are the portion of each individual core that was utilized in the composite TPBH record. Coarse sediment layers like the one in the photograph are generally considered to be hurricane event deposits. As indicated by the grey dashed lines, correlation of peaks is well maintained across the cores. The composite TPBH age-model was constructed using 15 points of age control including radiocarbon dated gastropods and terrestrial leaves from TPBH-C3 (*n* = 11 dates) and C2 (*n* = 2 dates), opaque spherule abundance, and modern core-top attribution of 2015 CE. The location of radiocarbon dates within each core is indicated by a yellow star.

The composite TPBH record has a near linear sedimentation rate of 1.3 cm yr^{-1} spanning the last ~700 years. This is based on an assessment of a fossil fuel combustion chronohorizon between 1906 and 1916 CE, and 13 radiocarbon dates calibrated into sidereal years from both TPBH-C3 (*n* = 11) and TPBH-C2 (*n* = 2) (see **2.3 Methods,** APPENDIX B Table S2.1, **APPENDIX B Section S2.3**). This means that each 1 cm sample represents ~0.77 years of time (i.e., sub-annual resolution), with an average age-

uncertainty of ±24.4 yrs cm^{-1}. This is within uncertainties of ~1.6 cm yr^{-1} estimate derived for the last 66 years based on post-1950 CE radiocarbon dates and ^{210}Pb activity in TPBH-C1 (van Hengstum et al., 2014). The basal dates for the composite record come from two radiocarbon dated *Cerethium sp.* gastropod shells from TPBH-C3, which were calibrated with a mixed 50/50% calibration curve (IntCal13 and Marine13; Reimer et al., 2013) to reflect the incorporation of both marine- and terrestrially-derived carbon into the production of their biogenic carbonate. This assumption produces a calibrated 2σ age range of 585 ± 50 cal yrs BP and 589 ± 50 cal yrs BP for these two shells. This is within uncertainties of the resultant stratigraphic age produced by a sedimentation rate of ~1.3 cm yr^{-1}, if only the first 13 points age-control are considered.

The top 60 cm of the composite record has the least age uncertainty, whereby each 1 cm of sediment deposition has an average age uncertainty of ±12 years. This interval is constrained by a post-bomb radiocarbon date from a leaf at 61.5 cm (1983 to 1992 CE) and the fossil fuel combustion chronohorizon at 140 cm (aged 1906 to 1916 CE) interpreted from a peak in opaque spherule concentration (370 spherules/cm^3, APPENDIX B Table S2.2). The age-model during the historic period is independently supported by downcore ^{137}Cs activity (see **APPENDIX B Section S2.3**, APPENDIX B Fig. S2.4). The highest age-uncertainties exist at the base of the composite record (800 to 888 cm), where each centimeter has an average 2σ uncertainty of ±50 years. The entire composite record (888 cm) spans ~1330 CE to 2014 CE, with the topmost 225 cm of sediment preserving the 164-year observational period (1850 to 2014 CE).

2.5. Discussion

2.5.1. Historical Hurricane Strikes: Calibrating the Record

An upper threshold of >4.39% $D_{>63\mu m}$ CSA in the quantitative textural data was calculated as indicating a coarse-grained sedimentary layer that is possibly anomalous and a disruption to background blue hole sedimentation. Eleven layers (or event beds) meet this threshold over the last 164 years (i.e., historical + instrumental period, E1 to E11), with 53 total event beds since 1330 CE. In paleotempestology, stratigraphic successions are evaluated for textural evidence of long term hurricane passage, with the highest quality reconstructions documenting only hurricane events. As such, other mechanisms that generate coarse sediment anomalies in the stratigraphic record like tsunamis or earthquakes must also be considered (Woodruff et al., 2009, Nanayama et al., 2000, Shanmugam, 2012). However, it is highly unlikely that tsunamis or earthquakes generated tempestites in TPBH because the northern Bahamas are positioned along a passive North American margin that has likely been tectonically stable during the Quaternary period (Carew and Mylroie, 1995), and there is no record of significant tsunami impacts in this region in recent history (Hearty, 1997, NOAA NCEI/WDS Global Historical Tsunami Database). For example, the maximum modelled wave runup during the 1755 CE earthquake in Lisbon, Portugal is only ~0.75 m in far field locations like on the eastern margin of the northern Bahamas (Barkan et al., 2009).

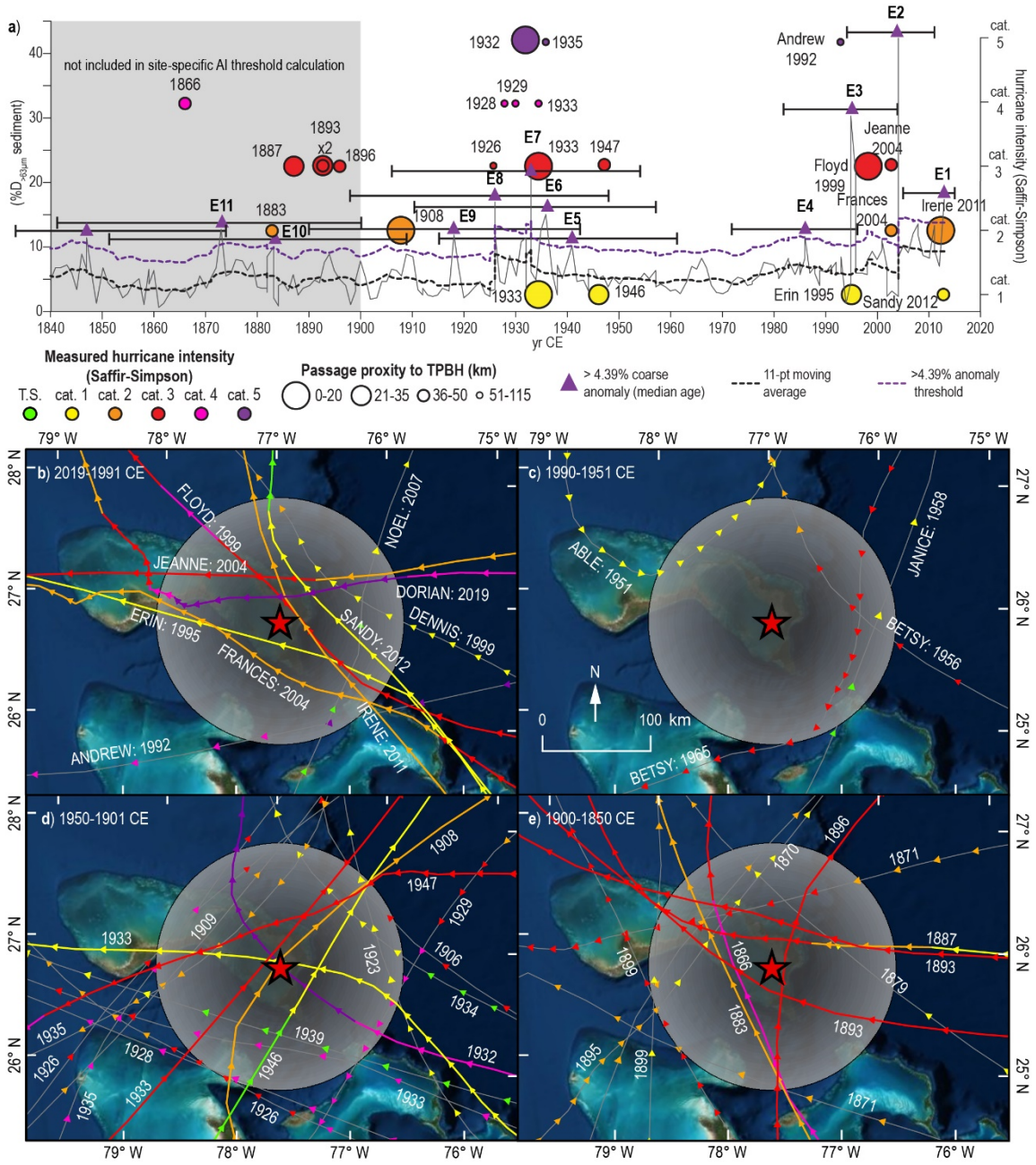

Figure 2.4. Sediment record sensitivity calibration/attribution to IBTrACS observational hurricane record from 1850 to 2014 CE.

a) Coarse sediment (%$D_{>63\mu m}$) plot (grey line) from TPBH composite record from 1850 to 2014 CE. The colored circles represent ≥Category 2 hurricanes that passed within 50 km of TPBH in the instrumental record, where larger (smaller) circles represent more proximal (distal) passage, and color represent Saffir-Simpson intensity. Coarse sediment anomalies (CSA) are peaks that exceed the 11-point moving average (dashed black line). The purple dashed line is the 4.39% $D_{>63\mu m}$ CSA threshold, and CSAs that exceed this threshold are marked with purple

triangles. b-e) Hurricane events from the IBTrACS v4 (Knapp et al., 2018, Knapp et al., 2010) within 115 km of TPBH from 1850 to 2019 CE in intervals from b) 2019 to 1991 CE, c) 1990 to 1951 CE, d) 1950 to 1901 CE, and e) 1900 to 1850 CE. Color of the storm segment denotes its Saffir-Simpson intensity category at the time of measurement based on the subset USA_Agency_SSHS, which is derived from HURDAT_ATL maximum wind speed data. The grey circle represents a 115 km radius around TPBH. Optical satellite imagery was obtained from ESRI compiled satellite imagery. Maps were made using the USA Contiguous Equidistant Conic projected coordinate system (Snyder, 1978) to accurately preserved track distanced from TPBH.

Several sources of uncertainty must be considered when attributing coarse-grained sedimentary deposits to individual hurricane events, including possible changes in hydrodynamics from individual storms and how those hydrodynamics interact with local sediment budgets and coastal landforms. It is likely that hurricanes of varying characteristics (i.e., intensity, track, size, translation speed) can generate event beds at TPBH. At Apalachee Bay in Florida, for example, hydrodynamical modeling indicates that although proximal Category 4 and 5 storms produced the most extreme storm surge, medium intensity Category 1-3 hurricanes are also capable of producing extensive local storm surge as a result of larger inner wind fields, storm track translational speed, or proximity (Lin et al., 2014). Sedimentologically, stratigraphic undercounting of hurricane events likely occurs during periods of frequent hurricane passage, where a single coarse grained layer may represent more than one hurricane (i.e., time averaging; Woodruff et al., 2008a). Advantageously, the high frequency of hurricane passage near TPBH since 1850 CE (Fig. 2.1) and archival of 11 event beds during the same period can be compared to evaluate the potential for different storm categories to generate event beds in TPBH.

First, as depicted in APPENDIX B Table S2.3 all hurricanes (Category 1-5) that passed within 115 km of TPBH from 2014 to 1850 CE were considered for their potential to generate the youngest event beds (E1 to E11, Fig. 2.4a, b). Layer E1 was deposited between 2015 and 2005 CE (median age 2013 CE, E1 in Fig. 2.4a) and is likely attributable to Hurricane Irene (Category 2), which passed ~15 km east of TPBH on 25 August 2011 CE or Hurricane Sandy, which passed ~45 km east of TPBH on 26 October 2012 CE. The only other hurricane that came within 115 km during this time was Hurricane Noel (Category 1), which passed ~80 km east on 1 November 2007, but this event was likely too weak and distal to create a tempestite. The deposit E1 was most likely Irene based on its intensity and proximity, but Hurricane Sandy cannot be ruled out given the inability of the sediment records to differentiate events within the same calendar year.

Events E2-E4 were deposited between 2015 to 1972 CE (2σ range), and seven hurricanes passed within 115 km of TPBH from 2012 and 1992 CE (Fig. 2.4a, b). Assuming we have correctly attributed E1 to Hurricanes Irene and/or Sandy, deposit E2 (median age 2004 CE, 2σ age-range: 2011 and 1995 CE) is likely attributable to Hurricane Frances (Category 2, ~40 km south on 24 September 2004 CE), or Hurricane Jeanne (Category 3, ~50 km north of TPBH on 25 September 2004 CE). Hurricane Floyd also passed just 15 km to the east of TPBH on 14 September 1999 CE as Category 3 hurricane, but it is more likely that Floyd deposited E3 (1995 CE median age, 2σ age-range: 1982 to 2004 CE). Category 1 Hurricane Dennis passed 60 km to the northeast on 28 August 1999, but was unlikely to deposit E3 because of its lower intensity and more

distal passage in relation to Hurricane Floyd. Deposit E4 (median age 1986 CE) dates to between 1996 and 1972 CE, and only Category 1 Hurricane Erin (22 km east; 1 August 1995 CE) and Category 4 Hurricane Andrew (112 km south; 23-24 August 1992 CE) occur during this time. Given that E4 narrowly meets the 4.39% $D_{>63\mu m}$ CSA threshold, it is reasonable to interpret that it is related to a weaker proximal storm like Erin (~25 km south of TPBH) or a more distal but intense storm like Andrew (~112 km south of TPBH). However, Erin (1995 CE) is barely within the upper 2σ age-limit, so Hurricane Andrew is more likely responsible for E4.

Equally important is the absence of coarse sediment anomalies with median ages that fall between 1990 to 1951 CE when there is little regional hurricane activity (i.e., no false positives). No hurricanes passed within 50 km of TPBH, but four storms passed within 115 km (Fig. 2.4c): (i) Hurricane Betsy (younger, Category 3) passed 70 km to the east on 6 September 1965 CE, (ii) Hurricane Janice (Category 1) passed 100 km east on 7 October 1958 CE, (iii) Hurricane Betsy (older, Category 3) passed 84 km to the east on 14 August 1956, and (iv) Hurricane Able (Category 1) passed 90 km to the northeast on 18 May 1951 CE. None of these storms caused meaningful coarse sediment deposition. The lack of false positives from 1951 to 1990 CE increases confidence that coarse sediment anomalies in the TPBH composite record can be reliably attributed to hurricane passage through time.

Observational uncertainty in the IBTrACS dataset increases prior to 1970 CE because this precedes the satellite era (Vecchi and Knutson, 2011). This uncertainty further increases prior to aircraft monitoring around 1945 CE (McAdie et al., 2009,

Vecchi and Knutson, 2011). Five coarse sediment anomalies were deposited at TPBH from 1901 to 1950 CE (E5-E9), when regional hurricane activity was elevated (6 hurricanes passed within 50 km and 14 passed within 150 km of TPBH). This includes a Category 5 unnamed hurricane whose center of circulation passed just 4 km to the east in 1932 CE (Fig. 2.4a, d). The uppermost event bed deposited in the first half of the 20th century is E5 with a median age of 1941 CE (2σ age-range: 1961 to 1915 CE, Fig. 2.4a). While this deposit could have been associated with one of the nine potential events between 1961 and 1915 CE, the most recent event after the ~40 year lull in activity between 1990 and 1950 CE is a Category 3 hurricane that passed 43 km northeast of TPBH on 21 September 1947 CE. A Category 1 hurricane passed 30 km to the southeast of TPBH on 12 September 1946 CE, so it is possible that both storms contributed to E5. Increasing uncertainty in track and intensity of hurricanes recorded prior to 1940 CE along with increasing age-uncertainty in the sedimentary age model limit confidence in the correlation between specific hurricanes and event beds. But, a qualitative assessment of this older time interval does reveal similar associations between event beds and hurricane magnitude as the post-1940 CE record (**APPENDIX B Section S2.4;** APPENDIX B Table S2.4**)**.

In summary, 4 of the 5 of event beds with median ages between 1940 and 2014 CE can be confidently attributed to ≥Category 2 hurricanes that pass within 50 km of TPBH (APPENDIX B Table S2.3), with event bed E4 also most likely caused by a Category ≥2 event. This encompasses all possible ≥Category 2 hurricanes that passed within 50 km of TPBH between 1940 and 2014 CE (not counting events occurring

within the same or adjacent years, like Francis and Jeanne in 2004). While it cannot be ruled out that a proximal Category 1 hurricane such as Erin (1995) could have deposited an event bed in TPBH, there is no deposit between 1850 and 2014 CE that is clearly attributable to this type of storm alone **(**APPENDIX B Tables S2.3 and S2.4). This would suggest that TPBH records most ≥Category 2 hurricanes that pass within a 50 km radius since 1940 CE, and may additionally archive more intense (Category 4-5) distal hurricanes (>50 km away from TPBH). As such, coarse event beds older than 1940 CE are likely emplaced by hurricanes with similar characteristics.

2.5.2. Northern Bahamas Hurricane Frequency

The new high-resolution record from TPBH revises and considerably expands upon previous paleo-hurricane records from the northern Bahamas (van Hengstum et al., 2016, van Hengstum et al., 2014). The previously published age-model for TPBH-C1 showed a dramatic reduction in sedimentation rate at 1950 CE from 1.6 cm yr^{-1} to 0.1 cm yr^{-1}. The new composite TPBH record has a mean sedimentation rate of ~1.3 cm yr^{-1} spanning the 888 cm record, and event beds can be visually correlated between TPBH-C1 (2014 core sample) and the upper 164 cm of the new TPBH-Composite (e.g., peak at 12, 24, 100 cm in TPBH-C1 to 15, 35, and 109 cm in TPBH composite record; Fig. 2.3). This suggests that the previous TPBH-C1 age-model is skewed too old prior to 1950 CE.

The age-model for the TPBH composite record was built largely from terrestrial plant macrofossils from two new cores with correlative stratigraphy (TPBH-C2 and TPBH-C3, Fig. 2.3). Terrestrial plant macrofossil dates are less likely to be influenced by the marine carbon reservoir, and therefore more reliable than the radiocarbon dated *B.*

domingensis bivalves from TPBH-C1. Given the increased confidence in the new TPBH composite record age-model, the original 164 cm stratigraphy sampled by TPBH-C1 actually represents only a continuous ~100 year record (~1910 to 2011 CE), in contrast to the ~1000 years originally reported (van Hengstum et al., 2014). This means, that while the original TPBH-C1 reconstruction does suggest that hurricane activity was increased between 1350 and 1650 CE, any similarity with the new TPBH composite record is coincidental. As such, only the new TPBH composite record should be used when assessing hurricane activity at TPBH prior to 1910 CE.

We define active intervals (AIs) using both a regionally-derived (grey boxes in Figs. 2.5, 2.6, 2.7) and site-specific (gold boxes in Figs. 2.5, 2.6, 2.7) upper-level significance threshold of 7.3 and 12.4 ≥Category 2 events per century generally within 50 km, respectively (see *2.3.4. Determining Active Hurricane Periods*). The most prolonged active period at TPBH occurs between 1500 to 1670 CE (AI-2), with a mean count of 11 hurricanes per century (AI-2, Fig. 2.5). Based on the regionally-derived upper threshold (7.34 ≥Category 2 events per century), there is a 90% statistical likelihood that stochastic forcing alone cannot explain the elevated hurricane frequency from 1500 to 1670 CE. Furthermore, the period from 1520 to 1600 CE also exceeds the site-specific upper threshold of 13 ≥Category 2 events per century, with an up to 14 events per century (average of 12.3 events per century, $n = 82$).

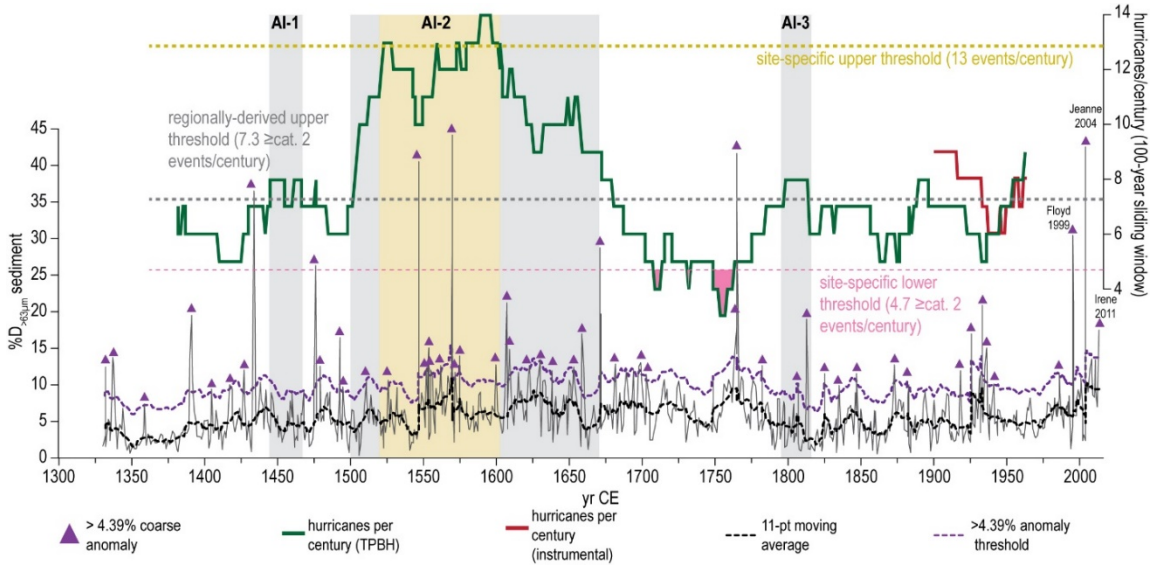

Figure 2.5. Hurricane events per century recorded in Thatchpoint Blue Hole from 1330 to 2014 CE.
Coarse sediment (%$D_{>63\mu m}$) plot (grey line) from TPBH composite record from 1330 to 2014 CE. Coarse sediment anomalies (CSA) are peaks that exceed the 11-point moving average (dashed black line). The purple dashed line is the 4.39% $D_{>63\mu m}$ CSA threshold, and CSAs that exceed this threshold are marked with purple triangles. The red line represents 100-year sliding window counts for events based on the IBTrACS v4 observational data (Knapp et al., 2018, Knapp et al., 2010), and the green line represents 100-year sliding window counts for significant peaks in the composite TPBH record. Event frequency significance thresholds are depicted as: gold dashed line is the site-specific upper 90th percentile threshold of 13 ≥Category 2 events per century, grey dashed line is the regionally derived upper 90th percentile threshold of 7.3 ≥Category 2 events per century, thin light-pink dashed line is the site-specific lower 10th percentile threshold of 4.7 ≥Category 2 events per century, thin red-pink dashed line is the regionally derived lower 10th percentile threshold of 1.6 ≥Category 2 events per century. The temporal windows where events per century exceed/fall-below these upper/lower thresholds are filled in with boxes that correspond to the color of the threshold lines.

Two other brief periods from ~1440 to 1470 CE exceed the regionally-derived upper 90% confidence interval of 7.3 ≥Category 2 events per century: (i) AI-1, average 7.7 events per century), and (ii) AI-3 from ~1795 to 1815 CE (average of 8 events per century), but these intervals do not reach activity levels that exceed the site specific upper threshold. It should be noted that the red line in Fig. 2.5 and 2.6 indicate the

number of hurricane events within 50 km between 1850 and 2014 CE expected to be detected by TPBH based on the sensitivity analysis, which means that deposits from Hurricanes Frances in 2004 (Category 2) and an unnamed Hurricane in 1933 (Category 3) were not counted as they occurred in the same or subsequent year as a more powerful or proximal hurricane. If these storms are included, the frequency counts throughout most of the last 164 years exceed the upper limits of the regionally derived threshold with an average of 13.2 events per century (n = 64 100-year windows).

These centennial-scale active intervals are also apparent at a multi-decadal scale (50-year sliding window counts, Fig. 2.6), short lived (multi-decadal) extremes in hurricane frequency are more pronounced when events per century is calculated based on 50 year sliding window counts. In the 50-year sliding window counts, AI-1 spans from 1400 to 1425 CE. When considering the regionally derived upper threshold of (7.3 ≥Category 2 events per century within 50 km), the length of AI-2 is extended to initiate around 1475 CE and end around 1700 CE. During the peak of AI-2 (1520 to 1600 CE), TPBH records up to 16 distinct event deposits per century (50-year sliding window) from 1547 to 1576 CE. The duration of AI-3 is extended by ~ 30 years, occurring from ~1780 to 1850 CE. Substantially lower hurricane frequency from 1700 to 1760 CE and 1960 to 1980 CE is emphasized in the 50-year sliding window counts, although events frequency per century briefly dips below the site-specific lower threshold (4.7 ≥Category 2 events per century) in the 100-year sliding window counts during the 1700 to 1760 CE interval (Fig. 2.6). Two additional periods from 1880 to 1940 CE and 1990 CE to present exceed the regional activity threshold in the 50-year sliding window counts, that

are not significant in the 100-year sliding window counts. However, given that average 2σ age-uncertainty throughout the TPBH composite record is ±24.4 years at each 1 cm interval, it is not clear if brief periods of enhanced activity that are only significant at the 50-year sliding window scale are driven by shorter lived (multi-decadal) external forcing (i.e., climate) or simply represent stochastic variability in hurricane activity.

A lower-resolution hurricane record (both: increased age uncertainty and lower capacity to observe storm passage) is available from Blackwood Sinkhole (van Hengstum et al., 2016), which is positioned 60 km northeast of TPBH on the eastern shoreline of Abaco. Blackwood Sinkhole only archived two intense hurricane events (≥Category 3 events) during the active interval from 1500 to 1675 CE (AI-2), but the age uncertainties for these events are large. In contrast to TPBH, Blackwood Sinkhole preserves the most event beds between 1790 and 1940 CE (five events recorded in Blackwood Sinkhole, Fig. 2.6), a period when TPBH records 12 events based only on the median age of coarse sediment anomalies, and up to 20 events during the maximum 1650 to 2000 2σ age-uncertainty for Blackwood Sinkhole during this period. Despite recording substantially more events than Blackwood Sinkhole record, there is no time between 1790 and 1940 CE in which the TPBH composite record centennial-scale event counts exceed the site-specific or regional statistical upper thresholds. TPBH centennial scale AI-3 (~1795 to 1815 CE) coincides with three events recorded in Blackwood Sinkhole (1771 CE ± 103 years, 1822 ± 134 years, and 1860 ± 116 years). Perhaps most interesting is that Blackwood Sinkhole archives no events beds with mean ages between ~1700 to 1780 CE when the composite record from TPBH has the fewest events per

century (average of 4.8 events per century, n = 76, three recorded events in 76 years, Figs. 2.5, 2.6).

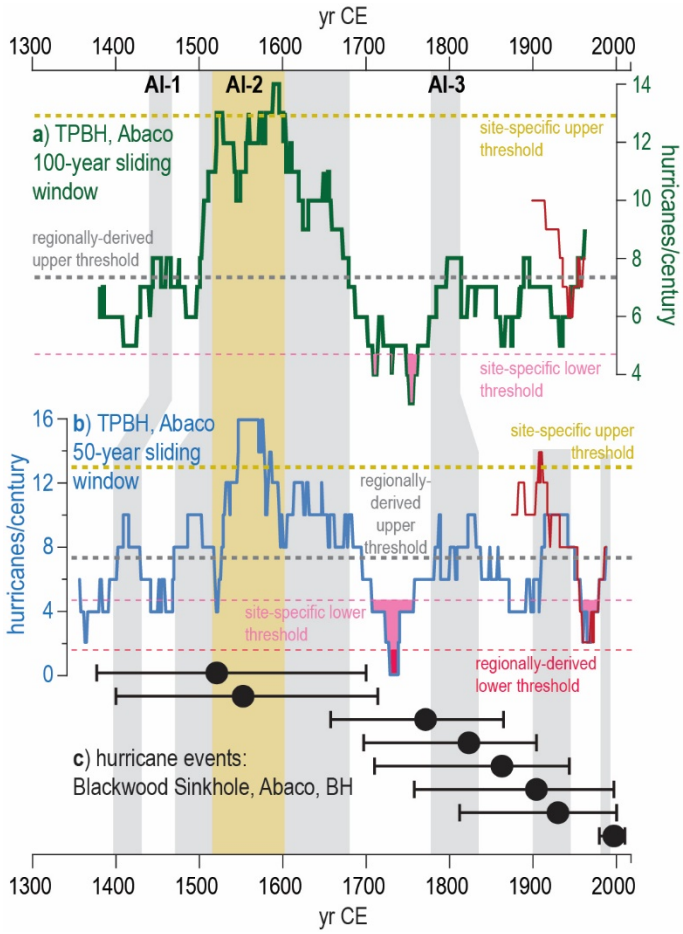

Figure 2.6. Comparison of paleo-hurricane records from Abaco. a) The solid red line represents 100-year sliding window counts for events based on IBTrACS v4 data (Knapp et al., 2018, Knapp et al., 2010), and the green line represents 100-year moving window counts for significant peaks in the composite TPBH record. b) The red line represents 50-year moving window counts for events based on IBTrACS v4 data, and the blue line represents events per century calculated from 50-year sliding window counts for significant peaks in the composite TPBH record. In a) and b), event frequency significance thresholds are depicted as: gold dashed line is the site-specific upper 90th percentile threshold of 13 ≥Category 2 events per century, grey dashed line is the regionally derived upper 90th percentile threshold of 7.3 ≥Category 2 events per century, thin light-pink dashed line is the site-specific lower 10th percentile threshold of 4.7 ≥Category 2 events per century, thin red-pink dashed line is the regionally derived lower 10th percentile threshold of 1.6 ≥Category 2 events per century. The temporal windows where events per century exceed/fall-below these upper/lower thresholds are filled

in with boxes that correspond to the color of the threshold lines. c) Black circles represent the mean age of hurricane events recorded in Blackwood Sinkhole in northern Abaco (van Hengstum et al., 2016) and the associated 2σ-age uncertainty is marked by the black lines extending from each circle.

It should be cautioned that one should not infer changes in storm *intensity* in the last 700 years based on the relative sensitivity of Blackwood Sinkhole (i.e., less sensitive) versus TPBH (i.e., more sensitive) to hurricane-induced sediment deposition. For example, it could be tempting to assume more intense hurricane strikes on Abaco based on more frequent events beds during the last 200 years in Blackwood Sinkhole (Fig. 2.6). However, Blackwood Sinkhole has an average 2σ age-uncertainty of ±110 years at each 0.5 cm interval from 1300 to 2013 CE, and a much lower overall sedimentation rate for the entirety of the record (0.3 to 0.6 mm yr^{-1}, last 3000 years) when compared to TPBH (~1.3 cm yr^{-1}, last 700 years). These differences in sedimentation rate and time averaging mean that TPBH records 53 events and Blackwood Sinkhole records 6 events during the same ~700-year span. The lower sedimentation rate, increased timing uncertainties, and fewer storm deposits during the instrumental period also mean that the types of hurricanes that produce favorable conditions for event bed deposition into Blackwood Sinkhole is less understood.

Sedimentary processes also significantly differ between each site: sedimentation in Blackwood Sinkhole on the terrestrial landscape versus TPBH in a subtidal marine setting with locally abundant sediment production and supply. The coarse-grained events beds in Blackwood Sinkhole comprise limestone fragments and brackish invertebrates, which are attributed to hurricane mobilization of particles from the adjacent terrestrial surface, wetlands, and vertical aquatic habitat on the sinkhole walls (Tamalavage et al.,

2018, van Hengstum et al., 2016). This means that the Blackwood Sinkhole hurricane signal is likely also linked to hurricane-induced flooding (surge-induced effects on the local groundwater table and rainfall). In contrast, TPBH in a subtidal lagoon setting is generating events beds from subaqueous sediment redistribution during elevated storm surge and local hydrodynamics during a hurricane event (Neumann and Land, 1975, Sahoo et al., 2019). In balance, the Blackwood Sinkhole record remains valuable because it extends deeper in time than the TPBH composite record (~2300 years longer, 3000 cal yrs BP total), the sedimentation rate is continuous with no hiatuses during the last 3000 years, and does provide a higher-resolution replication of evidence for intense hurricane activity at Puerto Rico (Donnelly and Woodruff, 2007). However, when considering the last 700 years, the dramatically increased sedimentary resolution and reduce temporal uncertainties means the composite record from TPBH vastly improves our understanding of hurricane activity in the northern Bahamas.

2.5.3. Comparison to North Atlantic Paleo-Hurricane Reconstructions

The northern Bahamas has experienced some of the highest levels of ≥Category 2 hurricane strikes within 50 km since 1850 CE (11-16 events) in the North Atlantic Ocean, along with the Gulf coast region (offshore Mississippi delta), northwestern Cuba, St. Johns and Puerto Rico, and just offshore of the Carolina Outer Banks (Fig. 2.1). In contrast, other areas experience much lower activity (3-4 ≥Category 2 hurricane strikes since within 50 km since 1850 CE), such as a lane between northern Cuba and Andros Island in the central Bahamas, the southern Gulf of Mexico, the southern Yucatan Peninsula, the northern coasts of Haiti and The Dominican Republic, the northern Gulf

Coast of Florida, Jamaica, and the southern coast of Cuba (Fig. 2.1). It is likely that geography plays a role in this spatial variability by creating a "shadow effect" that is observable behind larger landmasses in Figure 2.1, wherein storms weaken or dissipate while passing over land. For example, lower activity in the southern Gulf of Mexico likely results from hurricanes losing strength while passing over the Yucatan Peninsula. Similarly, Cuba likely shields the area south of Andros Island (The Bahamas) from many hurricanes that approach from the southern Caribbean.

High-resolution (near annual-scale) paleo-hurricane reconstructions can help assess if these recent spatial geographic relationships of hurricane activity persisted through prehistory. Indeed, increased hurricane strikes in the northern Bahamas between 1500 to 1670 CE is synchronous with evidence for elevated hurricane activity at higher latitudes on the U.S. eastern seaboard. For example, up to four ≥Category 2 hurricane strikes per century occurred at Salt Pond in Massachusetts from 1525 to 1600 CE (Donnelly et al., 2015), and increased hurricane event beds are preserved in subsurface sediments in Mattapoisett Marsh in Massachusetts from 1400 to 1650 CE (Boldt et al., 2010) (Fig. 2.7b). Increased frequency of barrier island inlet formation on the Outer Banks of North Carolina (Mallinson et al., 2011) along with enhanced salt marsh erosion in Connecticut (van de Plassche et al., 2006) from 1400 and 1600 CE also suggest more frequent hurricane strikes along the U.S. Eastern Seaboard during this time. Colonial-era shipwrecks increased during this interval, including 17 wrecked ships off Abaco during one event in 1595 CE (Craton, 1986) that could be archived as one of three event beds in TPBH whose age-uncertainties overlap this hurricane. A historical reconstruction of

tropical cyclone activity based on Spanish historical documents from the Archivo General de Indias (García-Herrera et al., 2005) provides further evidence of more hurricanes impacting naval activity during this time. Additionally, suppressed pine growth (based on tree ring data) from Florida indicates heightened activity between 1500 and 1650 CE (Trouet et al., 2016).

In contrast, the hurricane passage history in the northern Bahamas and eastern North America is different from the central Bahamas. For example, the near-annually resolved Common Era record of hurricane activity on South Andros (Wallace et al., 2019) (Fig. 2.7c, d) is largely anti-phased with the composite TPBH record over the last 684 years, yet these sites are only separated by ~280 km (northeast to southwest, Fig. 2.7d). Given that these sites document generally similar hurricane types (≥Category 2-3 passing within 50 km) and have similar sedimentation rates and age-uncertainties (1.3 cm yr^{-1} with ±24.4 yr 2σ uncertainty at each 1 cm interval at TPBH, ~1-1.4 cm yr^{-1} ± 38 yr 2σ uncertainty in South Andros records), they present as ideal case studies to assess long-term patterns of regional hurricane frequency (Fig. 2.1). When TPBH documents up to 14 events per century (mean 12.3 events per century, n = 82), the South Andros stack documents only 2 to 5 events per century (mean 3.2 events per century, n = 82). Throughout this entire active interval from ~1500 to 1670 CE when TPBH experiences an average 11 hurricane strikes per century (n = 178), the South Andros stack only documents a mean 4.3 events per century (n = 170, Fig. 2.7). In contrast, when the South Andros stack documents 6 events per century between 1700 CE to 1775 CE, TPBH experiences the lowest activity observed over the last the 684 years (mean 4.8 events per

century n = 76). It is also worth noting that TPBH (mean 7.7 events per century from 1330 to 2014 CE, n = 583 intervals) records more events overall than South Andros during the same time frame (average of 4.4 events per century, n = 590 intervals), which is consistent with spatial heterogeneity in regional storm frequencies during the instrumental period (Fig. 2.1).

At a broader geographic scale, the timing for enhanced paleo-hurricane activity in The Bahamas differs from paleo-hurricane records in the northeastern Gulf of Mexico and Yucatan Peninsula over the last millennium. Elevated activity recorded by TPBH from 1500 to 1670 CE (AI-2) corresponds with decreased activity both in the Gulf coast region of Florida (Lane et al., 2011, Brandon et al., 2013) and the eastern Yucatan Peninsula (Denomee et al., 2014). This interval documents a time in the past in which two sites that are relatively inactive during the observational record (3 to 4 ≥Category 2 events within 115 km since 1850 CE, Fig. 2.1) remain less active (Fig. 2.7). However, annual-scale hurricane reconstructions from these areas document that they have been much more active at times during the past, such as when Mullet Pond (Lane et al., 2011) and Spring Creek (Brandon et al., 2013) in Florida and Lighthouse Reef Blue Hole (Denomee et al., 2014) in Belize document more frequent hurricane strikes from ~1100 to 1400 CE (Fig. 2.7e, f).

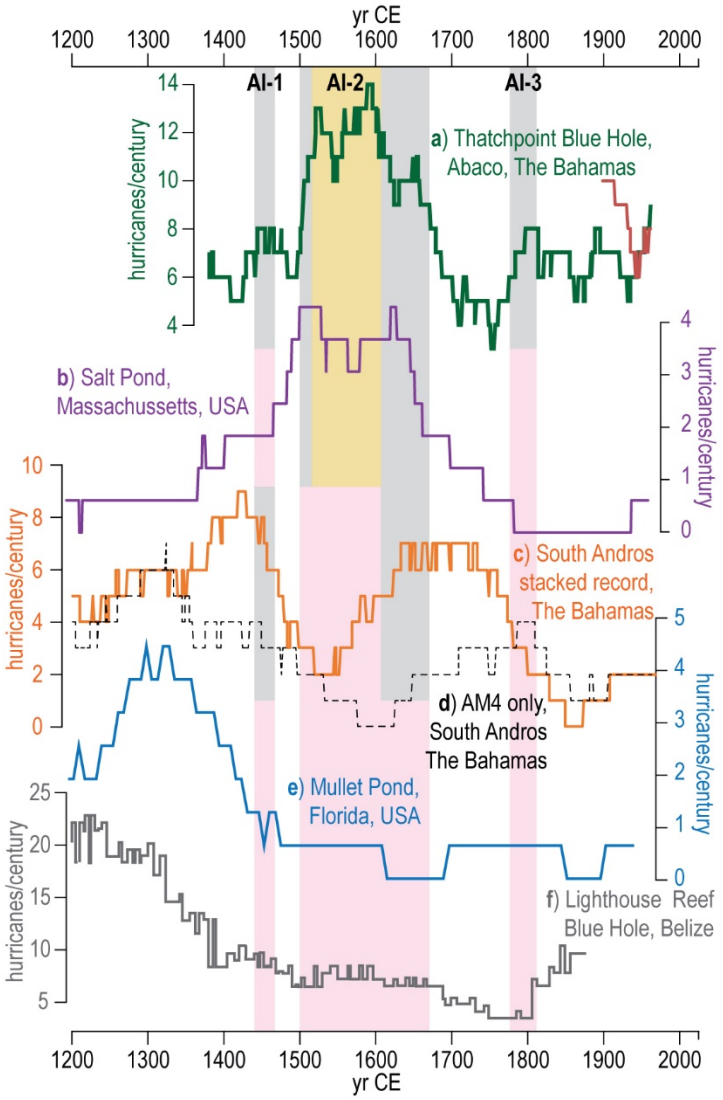

Figure 2.7. Comparison of high-resolution paleo-hurricane records from throughout the North Atlantic.

Hurricane events per century based on sedimentary reconstructions of regional hurricane frequency per century over the last 800 years at sites throughout the North Atlantic including: a) TPBH 100-year sliding window counts (green line), b) Salt Pond in Massachusetts (Donnelly et al., 2015, purple line), c) South Andros, The Bahamas stacked record presented in this study but derived from (Wallace et al., 2019; orange line) and d) AM4 (single record) in South Andros (Wallace et al., 2019; black dashed line). e) Mullet Pond on the Florida Gulf of Mexico Coast (Lane et al., 2011; blue line); f) Lighthouse Blue Hole, Belize (Denomee et al., 2014; grey line). The gold and grey boxes correspond to TPBH Composite record 100-year count statistical active intervals as defined in Fig. 2.5. The pink boxes match the temporal extent of these active intervals, but indicate lack of correlation between the timing/magnitude in the other records.

Confidence is emerging in evidence for regional and basin-wide paleo hurricane patterns based on the growing array of high-resolution paleo-hurricane studies. It is well established that climate impacts hurricane genesis, track, intensification, and overall Atlantic activity (see comprehensive reviews in Emanuel, 2003, Knutson et al., 2020, Knutson et al., 2010, Kossin et al., 2010). However, stochastic processes may partly explain spatiotemporal changes in paleo hurricane activity. This means that the recorded rate of hurricane landfalls over time at a given site can be driven by chance alone, and thus potentially mask an otherwise clear response to climatic forcing. Despite the potential for a stochastic component of the observed spatial-temporal patterns of paleo-hurricane activity, it should be noted that only 4 ≥Category 2 hurricanes passed within 50 km of South Andros between 1850 and 2019 CE compared to 14 such events in the northern Bahamas (Fig. 2.1). This would suggest that the spatial variability in the frequency of intense hurricane strikes over the last 169 years has persisted in some capacity throughout the last ~700 years. The high density of blue holes in the tropical North Atlantic Ocean, including on nearby Grand Bahama Island, provide promise for evaluating the results from TPBH both on the Little Bahama Bank and elsewhere.

2.6. Conclusions and Implications

The northern Bahamas (Abaco and Grand Bahama) have frequently experienced ≥Category 2 hurricane landfalls since 1850 CE, relative to most other places in the North Atlantic. Over the last ~700 years, however, a near-annually resolved record of prehistoric hurricane passage from Thatchpoint Blue Hole (TPBH) on Abaco Island

indicates that the northern Bahamas has experienced periods with statistically-significant *higher* frequencies of hurricane passage. From 1900 to 2014 CE, eight ≥Category 2 hurricanes passed within 50 km of TPBH, and an additional five ≥Category 4 events passed within 115 km. From 1900 to 2014 CE, the TPBH composite sediment record archived nine coarse sediment event beds within age-model uncertainties for passage of these hurricanes, providing unprecedented insight into the types of hurricane events that are most likely to cause event bed deposition in TPBH. Most ≥Category 2 events within 50 km and ≥Category 4 events within 115 km appear to be recorded within TPBH. This new record revises a previous study by van Hengstum et al. (2014) and demonstrates a nearly linear sedimentation rate at this blue hole of 1.3 cm yr^{-1} spanning the last ~700 years. Most importantly, the period from 1500 to 1670 CE was characterized by especially high levels of hurricane activity in the Northern Bahamas, similar to the eastern seaboard of North America. At TPBH, up to 14 ≥Category 2 hurricane strikes occurred per century, which represents a minimum estimate of the number of regional hurricane events. This active period is unlikely to be the result of stochastic variability alone because event counts exceed the upper 90^{th} percentile cutoff threshold based on calculated Poisson probability.

This study provides further evidence for spatial heterogeneity in hurricane strike frequency across the North Atlantic Basin over the last 700 years, which is apparent in observational data since 1850 CE. For example, while the northern Bahamas (TPBH) experienced enhanced hurricane passage from 1500 to 1670 CE, this is a period of relative quiescence in the Gulf of Mexico, central Bahamas (South Andros), and the

southern Caribbean (Belize). Spatial heterogeneity in paleo hurricane activity is further apparent when comparing the record of hurricane passage at TPBH to South Andros, where hurricane frequency is generally antiphased over the last ~700 years, despite being only ~280 km apart. This could suggest that The Bahamas is something of a crossroads for hurricane activity. Given this spatial heterogeneity, it is critical that (i) we continue to produce high-resolution paleo-hurricane records to better constrain the potential for multidecadal and centennial variations in Common Era hurricane activity, and (ii) that multiple sites from the same region are compiled and examined holistically before meaningful relationships between climate and hurricane activity can be fruitfully established in the broader areas of the north Atlantic. Nevertheless, multi-centennial regionally coherent patterns in hurricane activity are beginning to emerge across the Atlantic, such as the well replicated active interval along the North American Eastern Seaboard from 1450 to 1650 CE.

2.7. References

AGOSTA G'MEINER, A. 2016. *Holocene environmental change inferred from fossil pollen and microcharcoal at Cenote Jennifer, Cayo Coco, Cuba.* Masters, McGill University.

ANALYSIS, N. A. A. R. I. A. 2019. Hurricane Dorian Flood Proxy Map [ARIA_Sentinel-1_FPM_v0.2-Bahamas_Sep4.shp]. *NASA Jet Propulsion Laboratory.*

BALDINI, L. M., BALDINI, J. U., MCELWAINE, J. N., FRAPPIER, A. B., ASMEROM, Y., LIU, K.-B., PRUFER, K. M., RIDLEY, H. E., POLYAK, V. & KENNETT, D. J. 2016. Persistent northward North Atlantic tropical cyclone track migration over the past five centuries. *Scientific reports,* 6**,** 37522.

BARKAN, R., URI, S. & LIN, J. 2009. Far field tsunami simulations of the 1755 Lisbon earthquake: Implications for tsunami hazard to the US East Coast and the Caribbean. *Marine Geology,* 264**,** 109-122.

BLAAUW, M. & CHRISTEN, A. 2011. Flexible paleoclimate age-depth models using an autoregressive gamma process. *Bayesian Analysis,* 6**,** 457-474.

BLAKE, E. S., LANDSEA, C. W. & GIBNEY, E. J. 2011. The deadliest, costliest, and most intense United States tropical cyclones from 1851 to 2010 (and other frequently requested hurricane facts). *In:* CENTER, N. H. (ed.) *NOAA Technical Memorandum.* National Hurricane Center Miami.

BLAKE, E. S. National Hurricane Center. Costliest US tropical cyclones: 2018 Tables update. NOAA National Centers for Environmental Information. https://www.nhc.noaa.gov/news/UpdatedCostliest.pdf. access date: 24 Jan. 2020.

BOLDT, K. V., LANE, P., WOODRUFF, J. D. & DONNELLY, J. P. 2010. Calibrating a sedimentary record of overwash from Southeastern New England using modeled historic hurricane surges. *Marine Geology,* 275**,** 127-139.

BRANDON, C. M., WOODRUFF, J. D., DONNELLY, J. P. & SULLIVAN, R. M. 2014. How unique was Hurricane Sandy? Sedimentary reconstructions of extreme flooding from New York Harbor. *Scientific reports,* 4**,** 7366.

BRANDON, C. M., WOODRUFF, J. D., LANE, P. & DONNELLY, J. P. 2013. Constraining flooding conditions for prehistoric hurricanes from resultant deposits preserved in Florida sinkholes. *Geochemistry Geophysics Geosystems,* 14**,** 2993-3008.

BREGY, J. C., WALLACE, D. J., MINZONI, R. T. & CRUZ, V. J. 2018. 2500-year paleotempestological record of intense storms for the northern Gulf of Mexico, United States. *Marine Geology,* 396**,** 26-42.

BROWN, A. L., REINHARDT, E. G., VAN HENGSTUM, P. J. & PILARCZYK, J. E. 2014. A coastal Yucatan sinkhole records intense hurricane events. *Journal of Coastal Research,* 30**,** 418-428.

CAREW, J. L. & MYLROIE, J. E. 1995. Quaternary tectonic stability of the Bahamian Archipelago: Evidence from fossil coral reefs and flank margin caves. *Quaternary Science Reviews,* 14**,** 145-153.

CRATON, M. 1986. *A History of the Bahamas*, San Salvador Press.

CRATON, M. & SAUNDERS, G. 2002. *Islanders in the Stream: A History of the Bahamian People. Volume Two: From the Ending of Slavery to the Twenty-First Century*, JSTOR.

DENOMEE, K. C., BENTLEY, S. J. & DROXLER, A. W. 2014. Climatic control on hurricane patterns: a 1200-y near-annual record from Lighthouse Reef, Belize. *Scientific Reports,* 4**,** 7.

DONNELLY, J. P. 2005. Evidence of past intense tropical cyclones from backbarrier salt pond sediments: a case study from Isla de Culebrita, Puerto Rico, USA. *Journal of Coastal Resarch,* 42**,** 201-210.

DONNELLY, J. P., HAWKES, A. D., LANE, P., MACDONALD, D., SHUMAN, B. N., TOOMEY, M. R., VAN HENGSTUM, P. J. & WOODRUFF, J. D. 2015. Climate forcing of unprecedented intense-hurricane activity in the last 2000 years. *Earth's Future,* 3**,** 49-65.

DONNELLY, J. P., SMITH BRYANT, S., BUTLER, J., DOWLING, J., FAN, L., HAUSMANN, N., NEWBY, P., SHUMAN, B., STERN, J., WESTHOVER, K. & WEBB, T. I. 2001. 700 yr sedimentary record of intense hurricane landfalls in southern New England. *Geological Society of America Bulletin,* 113**,** 715-727.

DONNELLY, J. P. & WOODRUFF, J. D. 2007. Intense hurricane activity over the past 5,000 years controlled by El Niño and the West African Monsoon. *Nature,* 447**,** 465-468.

EMANUEL, K. 2003. Tropical cyclones. *Annual review of earth and planetary sciences,* 31**,** 75-104.

EMANUEL, K., SUNDARARAJAN, R. & WILLIAMS, J. 2008. Hurricanes and global warming: results from downscaling IPCC AR4 simulations. *Bulletin of the American Meterorological Society,* 89**,** 347-367.

EMANUEL, K. A. 2013. Downscaling CMIP5 climate models shows increased tropical cyclone activity over the 21st century. *Proceedings of the National Academy of Sciences of the United States of America,* 110**,** 12219-12224.

GARCÍA-HERRERA, R., GIMENO, L., RIBERA, P. & HERNÁNDEZ, E. 2005. New records of Atlantic hurricanes from Spanish documentary sources. *Journal of Geophysical Research,* 110**,** 7 p.

GISCHLER, E., SHINN, E. A., OSCHMANN, W., FIEBIG, J. & BUSTER, N. A. 2008. A 1500-year Holocene Caribbean climate archive from the Blue Hole, Lighthouse Reef, Belize. *Journal of Coastal Resarch,* 24**,** 1495-1505.

HEARTY, P. J. 1997. Boulder deposits from large waves during the last interglaciation on North Eleuthera Island, Bahamas. *Quaternary Research,* 48**,** 326-338.

HEIRI, O., LOTTER, A. F. & LEMCKE, G. 2001. Loss on ignition as a method for estimating organic and carbonate content in sediments: reproducibility and comparability of results. *Journal of Paleolimnology,* 25**,** 101-110.

HIJMANS, R. J., RIOJAS, E., O'BRIEN, R., CRUZ, M. DIVA-GIS Version 7.5:Countries- Administrative Boundaries. https://www.diva-gis.org/gdata. Accessed 24 Jan 2020.

JASANOFF, M. 2011. *Liberty's Exiles: The Loss of America and the Remaking of the British Empire*, HarperCollins UK.

KNAPP, K. R., DIAMOND, H. J., KOSSIN, J. P., KRUK, M. C. & SCHRECK, C. J. 2018. International Best Track Archive for Climate Stewardship (IBTrACS) Project, Version 4, [North Atlantic Subset]. *In:* INFORMATION, N. N. C. F. E. (ed.).

KNAPP, K. R., KRUK, M. C., LEVINSON, D. H., DIAMOND, H. J. & NEUMANN, C. J. 2010. The international best track archive for climate stewardship (IBTrACS) unifying tropical cyclone data. *Bulletin of the American Meteorological Society,* 91**,** 363-376.

KNUTSON, T., CAMARGO, S. J., CHAN, J. C., EMANUEL, K., HO, C.-H., KOSSIN, J., MOHAPATRA, M., SATOH, M., SUGI, M. & WALSH, K. 2020. Tropical cyclones and climate change assessment: Part II. Projected response to anthropogenic warming. *Bulletin of the American Meteorological Society*.

KNUTSON, T. R., MCBRIDE, J. L., CHAN, J., EMMANUEL, K., HOLLAND, G., LANDSEA, C., HELD, I., KOSSIN, J. P., SRIVASTAVA, A. K. & SUGI, M. 2010. Tropical cyclone and climate changes. *Nature Geoscience,* 3**,** 157-163.

KORTY, R. L., EMANUEL, K. A., HUBER, M. & ZAMORA, R. A. 2017. Tropical cyclones downscaled from simulations with very high carbon dioxide levels. *Journal of Climate,* 30**,** 649-667.

KOSSIN, J. P., CAMARGO, S. J. & SITKOWSKI, M. 2010. Climate modulation of North Atlantic hurricane tracks. *Journal of Climate,* 23**,** 3057-3076.

KOSSIN, J. P., KNAPP, K. R., OLANDER, T. L. & VELDEN, C. S. 2020. Global increase in major tropical cyclone exceedance probability over the past four decades. *Proceedings of the National Academy of Sciences*.

LANE, P., DONNELLY, J. P., WOODRUFF, J. D. & HAWKES, A. D. 2011. A decadally-resolved paleohurricane record archived in the late Holocene sediments of a Florida sinkhole. *Marine Geology,* 287**,** 14-30.

LIN, N., LANE, P., EMANUEL, K. A., SULLIVAN, R. M. & DONNELLY, J. P. 2014. Heightened hurricane surge risk in northwest Florida revealed from climatological-hydrodynamic modeling and paleorecord reconstruction. *Journal of Geophysical Research: Atmospheres,* 119**,** 8606-8623.

MALLINSON, D. J., SMITH, C. W., MAHAN, S., CULVER, S. J. & MCDOWELL, K. 2011. Barrier island response to late Holocene climate events, North Carolina, USA. *Quaternary Research,* 76**,** 46-57.

MCADIE, C., LANDSEA, C., NEUMANN, C. J., DAVID, J. E. & BLAKE, E. S. 2009. *Tropical Cyclones of the North Atlantic Ocean, 1851-2006: With 2007 and 2008 Track Maps Included*, US Department of Commerce, National Oceanic and Atmospheric Administration.

MCCLOSKEY, T. A. & LIU, K. B. 2012. *A 7000 year record of paleohurricane activity from a coastal weland in Belize*.

MERLIS, T. M., ZHAO, M. & HELD, I. M. 2013. The sensitivity of hurricane frequency to ITCZ changes and radiatively forced warming in aquaplanet simulations. *Geophysical Research Letters,* 40**,** 4109-4114.

MULLINS, H. T. & LYNTS, G. W. 1977. Origin of the northwestern Bahama Platform: Review and reinterpretation. *Geological Society of America Bulletin,* 88**,** 1447-1461.

MYLROIE, J. E., CAREW, J. L. & MOORE, A. I. 1995a. Blue holes: definitions and genesis. *Carbonates and Evaporites,* 10**,** 225-233.

MYLROIE, J. E., CAREW, J. L. & VACHER, H. L. 1995b. Karst development in the Bahamas and Bermuda. *In:* CURRAN, H. A. & WHITE, B. (eds.) *Terrestrial and Shallow Marine Geology of the Bahamas and Bermuda.*

NANAYAMA, F., SHIGENO, K., SATAKE, K., SHIMOKAWA, K., KOITABASHI, S., MIYASAKA, S. & ISHII, M. 2000. Sedimentary differences between the

1993 Hokkaido-nansei-oki tsunami and the 1959 Miyakojima typhoon at Taisei, southwestern Hokkaido, northern Japan. *Sedimentary Geology,* 135**,** 255-264.

NASA ARIA: Advanced Rapid Imaging and Analysis. Hurricane Dorian Flood Proxy Map [ARIA_Sentinel-1_FPM_v0.2-Bahamas_Sep4.shp]. NASA Jet Propulsion Laboratory. https://aria-share.jpl.nasa.gov/201909-Hurricane_Dorian_Bahamas/. Accessed 19 Dec 2019.

NEUMANN, C. A. & LAND, L. S. 1975. Lime mud deposition and calcareous algae in the Bight of Abaco, Bahamas; a budget. *Journal of Sedimentary Research,* 45**,** 763-786.

NOAA NATIONAL CENTERS FOR ENVIRONMENTAL INFORMATION (NCEI). National Geophysical Data Center / World Data Service: NCEI/WDS Global Historical Tsunami Database. [access date: 28 Feb. 2020]. https://doi.org/10.7289/V5PN93H7.

RANKEY, E. C. & REEDER, S. L. 2012. Tidal sands of the Bahamian Archipelago. *Principles of tidal sedimentology.* Springer.

RASMUSSEN, K. A., HADDAD, R. I. & NEUMANN, A. C. 1990. Stable-isotope record of organic carbon from an evolving carbonate banktop, Bight of Abaco, Bahamas. *Geology,* 18**,** 790-794.

RASMUSSEN, K. A. & NEUMANN, A. C. 1988. Holocene overprints of Pleistocene paleokarst: Bight of Abaco, Bahamas. *In:* JAMES, N. P. & CHOQUETTE, P. W. (eds.) *Paleokarst.* New York: Springer.

REIMER, P. J., BARD, E., BAYLISS, A., BECK, J. W., BLACKWELL, P. G., RAMSEY, C. B., BUCK, C. E., CHENG, H., EDWARDS, R. L. & FRIEDRICH, M. 2013. IntCal13 and Marine13 radiocarbon age calibration curves 0–50,000 years cal BP. *Radiocarbon,* 55**,** 1869-1887.

REIMER, P. J., BROWN, T. A. & REIMER, R. W. 2004. Discussion: reporting and calibration of post-bomb 14C data. *Radiocarbon,* 46**,** 1299-1304.

SAHOO, B., JOSE, F. & BHASKARAN, P. K. 2019. Hydrodynamic response of Bahamas archipelago to storm surge and hurricane generated waves–A case study for Hurricane Joaquin. *Ocean Engineering,* 184**,** 227-238.

SHANMUGAM, G. 2012. Process-sedimentological challenges in distinguishing paleo-tsunami deposits. *Natural Hazards,* 63**,** 5-30.

SNYDER, J. P. 1978. Equidistant conic map projections. *Annals of the Association of American Geographers,* 68**,** 373-383.

SOBEL, A. H., CAMARGO, S. J., HALL, T. M., LEE, C.-Y., TIPPETT, M. K. & WING, A. A. 2016. Human influence on tropical cyclone intensity. *Science,* 353**,** 242-246.

TAMALAVAGE, A. E., VAN HENGSTUM, P. J., LOUCHOUARN, P., MOLODTSOV, S., KAISER, K., DONNELLY, J. P., ALBURY, N. A. & FALL, P. L. 2018. Organic matter sources and lateral sedimentation in a Bahamian karst basin (sinkhole) over the late Holocene: Influence of local vegetation and climate. *Palaeogeography, Palaeoclimatology, Palaeoecology,* 506**,** 70-83.

TOOMEY, M. R., CURRY, W. B., DONNELLY, J. P. & VAN HENGSTUM, P. J. 2013. Reconstructing 7000 years of North Atlantic hurricane variability using deep-sea sediment cores from the western Great Bahama Bank. *Paleoceanography,* 28**,** 31-41.

TROUET, V., HARLEY, G. L. & DOMÍNGUEZ-DELMÁS, M. 2016. Shipwreck rates reveal Caribbean tropical cyclone response to past radiative forcing. *Proceedings of the National Academy of Sciences,* 113**,** 3169-3174.

ULM, K. 1990. Simple method to calculate the confidence interval of a standardized mortality ratio (SMR). *American journal of epidemiology,* 131**,** 373-375.

VAN DE PLASSCHE, O., ERKENS, G., VAN VLIET, F., BRANDSMA, J., VAN DER BORG, K. & DE JONG, A. F. 2006. Salt-marsh erosion associated with hurricane landfall in southern New England in the fifteenth and seventeenth centuries. *Geology,* 34**,** 829-832.

VAN HENGSTUM, P. J., CRESSWELL, J. N., MILNE, G. A. & ILIFFE, T. M. 2019. Development of anchialine cave habitats and karst subterranean estuaries since the last ice age. *Scientific reports,* 9**,** 1-10.

VAN HENGSTUM, P. J., DONNELLY, J. P., FALL, P. L., TOOMEY, M. R., ALBURY, N. A. & KAKUK, B. 2016. The intertropical convergence zone modulates intense hurricane strikes on the western North Atlantic margin. *Scientific reports,* 6.

VAN HENGSTUM, P. J., DONNELLY, J. P., TOOMEY, M. R., ALBURY, N. A., LANE, P. & KAKUK, B. 2014. Heightened hurricane activity on the Little Bahama Bank from 1350 to 1650 AD. *Continental Shelf Research,* 86**,** 103-115.

VAN HENGSTUM, P. J., SCOTT, D. B., GRÖCKE, D. R. & CHARETTE, M. A. 2011. Sea level controls sedimentation and environments in coastal caves and sinkholes. *Marine Geology,* 286**,** 35-50.

VAN HENGSTUM, P. J., WINKLER, T. S., TAMALAVAGE, A. E., SULLIVAN, R. M., LITTLE, S. N., MACDONALD, D., DONNELLY, J. P. & ALBURY, N. A. 2020. Holocene sedimentation in a blue hole surrounded by carbonate tidal flats in The Bahamas: Autogenic versus allogenic processes. *Marine Geology,* 419**,** 106051.

VECCHI, G. A. & KNUTSON, T. R. 2011. Estimating annual numbers of Atlantic hurricanes missing from the HURDAT database (1878–1965) using ship track density. *Journal of Climate,* 24**,** 1736-1746.

WALLACE, E., DONNELLY, J., VAN HENGSTUM, P., WIMAN, C., SULLIVAN, R., WINKLER, T., D'ENTREMONT, N., TOOMEY, M. & ALBURY, N. 2019. Intense hurricane activity over the past 1500 years at South Andros Island, The Bahamas. *Paleoceanography and Paleoclimatology,* 34.

WALSH, K. J., CAMARGO, S. J., VECCHI, G. A., DALOZ, A. S., ELSNER, J., EMANUEL, K., HORN, M., LIM, Y.-K., ROBERTS, M. & PATRICOLA, C. 2015. Hurricanes and climate: the US CLIVAR working group on hurricanes. *Bulletin of the American Meteorological Society,* 96**,** 997-1017.

WALSH, K. J., MCBRIDE, J. L., KLOTZBACH, P. J., BALACHANDRAN, S., CAMARGO, S. J., HOLLAND, G., KNUTSON, T. R., KOSSIN, J. P., LEE, T. C. & SOBEL, A. 2016. Tropical cyclones and climate change. *Wiley Interdisciplinary Reviews: Climate Change,* 7**,** 65-89.

WOODRUFF, J. D., DONNELLY, J. P., EMANUEL, K. & LANE, P. 2008a. Assessing sedimentary records of paleohurricane activity using modeled hurricane climatology. *Geochemistry, Geophysics, Geosystems,* 9.

WOODRUFF, J. D., DONNELLY, J. P., MOHRIG, D. & GEYER, W. R. 2008b. Reconstructing relative flooding intensities responsible for hurricane-induced deposits from Laguna Playa Grande, Vieques, Puerto Rico. *Geology,* 36**,** 391-394.

WOODRUFF, J. D., DONNELLY, J. P. & OKUSU, A. 2009. Exploring typhoon variability over the mid-to-late Holocene: evidence of extreme coastal flooding from Kamikoshiki, Japan. *Quaternary Science Reviews,* 28**,** 1774-1785.

3. OCEANIC PASSAGE OF HURRICANES ACROSS CAY SAL BANK IN THE BAHAMAS OVER THE LAST 550 YEARS

3.1. Introduction

The year 2020 Common Era (CE) observed the highest number of named Atlantic tropical cyclones (30) since the instrumental record began in 1850 CE. From 1980 to 2020 CE, 52 tropical cyclones have individually caused ≥$1 billion USD in damage (adjusting for inflation), collectively resulting in $997.3 billion USD in damages (Consumer Price Index adjusted) and 6,593 verified deaths in the United States alone (Smith, 2020). Growing coastal populations and development will continue to increase the vulnerability of coastal communities to deleterious impacts of extreme flooding events like tropical cyclones (Woodruff et al., 2013, Pielke Jr. et al., 2008), and Davenport et al. (2021) propose that anthropogenically facilitated climate change is directly responsible for a substantial portion of these flood related damages. Based on projected 2°C of global warming during the 21st century, tropical cyclone models and observations indicate: (i) an increase in the global proportion of intense hurricanes (Knutson et al., 2020, Emanuel et al., 2008, Emanuel, 2013, Walsh et al., 2015, Walsh et al., 2016, Sobel et al., 2016, Korty et al., 2017); (ii) an increase in the amount of precipitation delivered by hurricanes (Patricola and Wehner, 2018), (iii) an increase in hurricane size and rainfall area (Chavas et al., 2016, Lin et al., 2015); and (iv) reduced hurricane translational speed that can enhance landscape flooding from surge and rainfall (Kossin, 2018). Coupled with high-confidence projections of an additional ~1 m global

sea level-rise by 2100 CE (Oppenheimer and Hinkel, 2019), it is clear that coastal populations are increasingly threatened by hurricane storm surge amplification, winds, and flooding (Miller et al., 2013, Wong et al., 2014, Woodruff et al., 2013, Vacchi et al., 2018, Pielke Jr. et al., 2008).

Future tropical cyclone risk assessments mostly rely on the tropical cyclone instrumental record over the last 170 years (International Best Track Archive for Climate Stewardship-IBTrACS; Knapp et al., 2018, Knapp et al., 2010). The regional frequency of Atlantic tropical cyclones, referred to hereafter as hurricanes, is spatially-heterogenous throughout the Atlantic since 1850 CE, and significant variability in >Category 2 hurricane frequency can be observed at islands less than 300 km apart in the Bahamian Archipelago (Winkler et al., 2020). Problematically, the relatively short-temporal scale of the instrumental record makes it unclear if observed spatial heterogeneity of Atlantic hurricane frequency (see Fig. 2.1 in CHAPTER 2: Winkler et al., 2020) persists on longer timescales (i.e., centennial and millennial; (Donnelly et al., 2015, Landsea et al., 2006). Knowledge of Atlantic hurricane activity can be extended using historical accounts, but these records are incomplete and biased toward well populated regions with preserved recorded histories (Trouet et al., 2016, Chenoweth and Divine, 2008). Many lower resolution sedimentary and geochemical records of paleo-hurricane impacts have helped extend the record of Atlantic storms back thousands of years (Biguenet et al., 2021, Bregy et al., 2018, Donnelly and Woodruff, 2007, Liu and Fearn, 2000, Liu and Fearn, 1993, Mallinson et al., 2011, Oliva et al., 2018, van Hengstum et al., 2016, Yang et al., 2021). However, these records tend to have higher

age-uncertainties and typically archive only the most intense hurricane events. Further, significant spatial and temporal gaps remain in the coverage of existing records, thus limiting confidence in interpreting changes in hurricane climatology on centennial timescales.

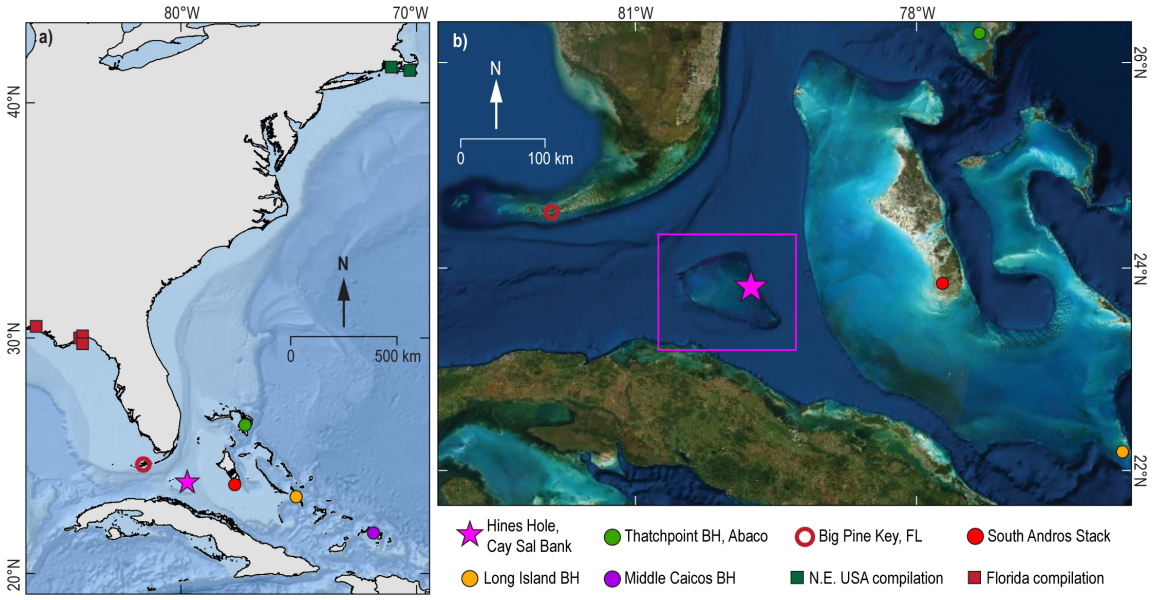

Figure 3.1. Location of Cay Sal Bank in the North Atlantic.
a) Location of Cay Sal Bank, The Bahamas in the northern Atlantic (pink star) as well as the location of high-resolution hurricane reconstructions from the Bahamian Archipelago (colored circles correspond to reconstructions in Figs. 3.8 and 3.9), the northeastern US (green squares), and Gulf of Mexico (red squares; basemap source: *Esri Oceans*). b) Optical satellite imagery from ESRI of Cay Sal Bank (pink box), which is emplaced between south Florida and Cuba in the center of the Florida Straits.

Over the last 10 years, an array of near-annually resolved sedimentary archives from deep coastal basins have expanded temporal understanding of regional hurricane variability throughout the North Atlantic, revealing significant variations in landfall frequency at centennial and multi-decadal scales (Brandon et al., 2013, Denomee et al., 2014, Donnelly et al., 2015, Lane et al., 2011, Schmitt et al., 2020, Wallace et al., 2019,

Winkler et al., 2020, Wallace et al., Sub. March 2021, Wallace et al., 2021b).These studies also reveal substantial spatial heterogeneity in hurricane activity throughout the last 2000 years, meaning that variability recorded by a single site may not necessarily reflect changing climatology throughout the entire Atlantic. Based on an assessment of downscaled hurricane model runs spanning the last millennium, Wallace et al. (2021a) suggest that much of the century-scale hurricane frequency variability in individual paleohurricane records from The Bahamas may be related to local-scale weather patterns rather than broader regional climate forcing. However, as more near-annually resolved studies emerge from the Bahamian Archipelago, synchronous periods of active/quiet hurricane activity persist through multiple records, and a statistical compilation of these records by Wallace et al. (2021b) that smooths out local-scale variations in storm frequency reveals robust centennial scale patterns (see Wallace et al. (Sub. March 2021) for updated compilation). Thus, a climate mediated signal may be emerging from the compiled regional hurricane reconstructions, but the global and regional climatic mechanisms and their relative influence remain an active area of study.

Here we present a 550-year, near annually-resolved sedimentary record from a drowned (subtidal), oceanic blue hole on Cay Sal Bank, The Bahamas. To date, this record is one of the highest resolution sedimentary reconstructions of paleohurricane activity from the North Atlantic Ocean owing to the high sedimentation rate in the site. This site is not sheltered from wave action by supratidal geomorphology, which enables most ≥Category 1 hurricane events (Saffir-Simpson Scale) within a 115 km radius to be archived in the stratigraphy. This is in contrast to previous locations where paleo

hurricane records have been developed that only record more intense hurricane strikes (≥Category 2) within a more proximal radius (e.g., Bregy et al., 2018, Lane et al., 2011, van Hengstum et al., 2016, Wallace et al., 2019, Winkler et al., 2020, Wallace et al., 2021b). This single record captures spatiotemporal trends in hurricane activity that emerge from a compilation of existing near-annually resolved hurricane activity (Wallace et al., 2021b, Wallace et al., Sub. March 2021).

3.2. Regional Setting: Hine's Hole on Cay Sal Bank

Hine's Hole is located on the eastern margin of Cay Sal Bank, The Bahamas (Figs. 3.1 and 3.2), so named after pioneering surveying efforts led by Dr. Albert Hine (Hine and Steinmetz, 1984). This slightly oblong blue hole is 340 m wide north to south, and 315 m wide east to west, with a gently sloping bathymetry from 80 to 95 meters below sea level (mbsl). The 6000 square km Cay Sal Bank is the westernmost carbonate platform in The Bahamas, and is considered partially drowned with an average bank-top depth of ~10 mbsl (Hine and Steinmetz, 1984). Cay Sal Bank's elevation is lower relative to other platforms in the Bahamian Archipelago, including the Little Bahama Bank and the Great Bahama Bank which both have well developed platform-edge reefs. As such, the platform-edge reef growth was outpaced by faster rates of relative sea-level rise during the mid-Holocene (Hine and Steinmetz, 1984), making Cay Sal Bank one of just two Bahamian platforms with non-aggraded margins (Purkis et al., 2014).

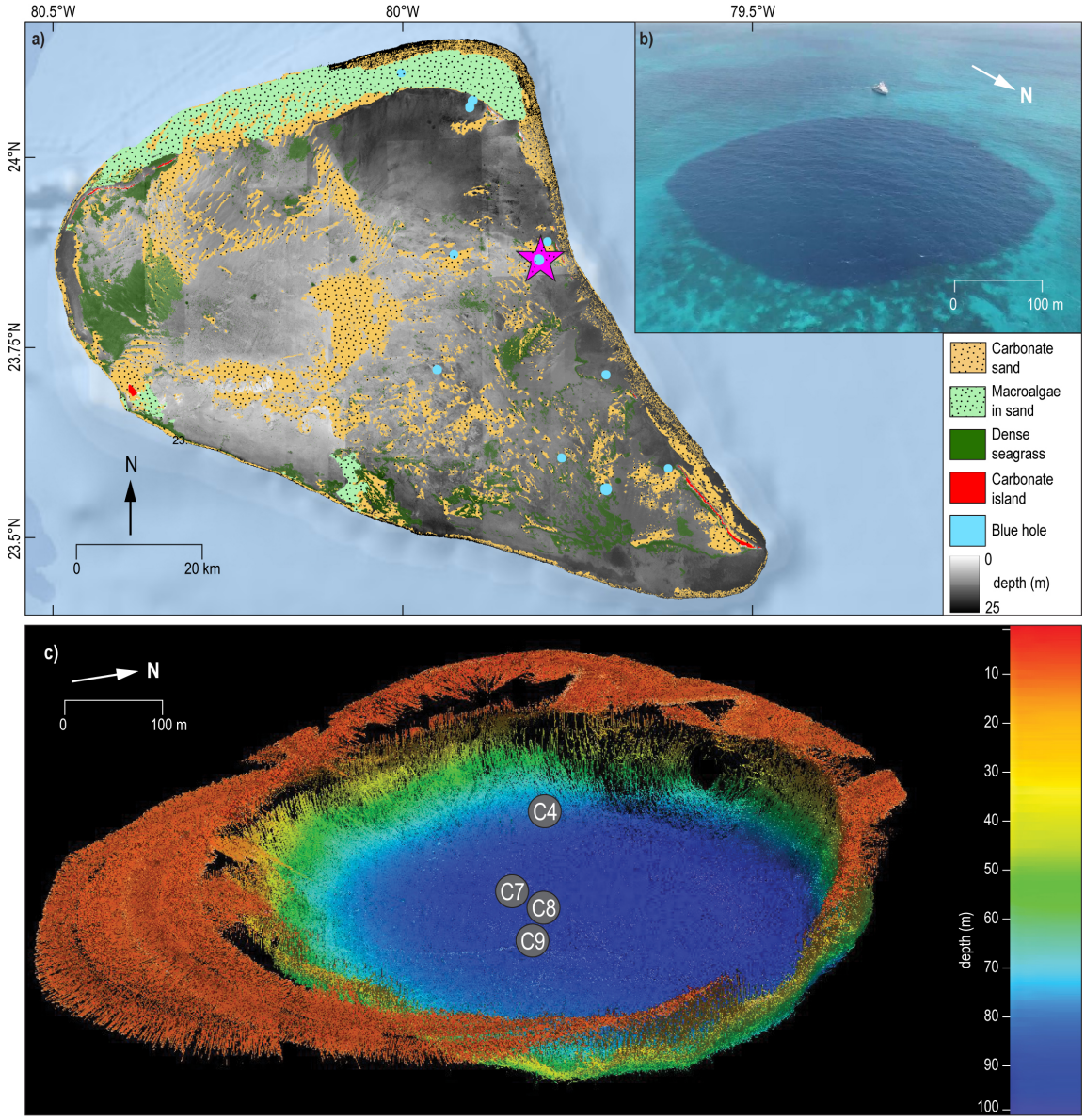

Figure 3.2. Map of Cay Sal Bank and Hine's Hole bathymetry.
a) **Location of Hine's Hole (pink star) on the northeastern flank of Cay Sal Bank, The Bahamas (basemap source: *Esri Oceans*). This map shows high resolution bathymetry (lighter=shallower, darker=deeper) as well as the location of large sand accumulations (dotted tan and light green areas) and habitat features on Cay Sal Bank. The bathymetric and habitat data is used courtesy of the Khaled Bin Sultan Living Oceans Foundation, and the collection methods and further discussion of the data can be found in (Purkis et al., 2014). b) Aerial photograph of Hine's Hole. c) 3D multibeam bathymetry of Hine's Hole with coring locations noted by grey circles. This survey was completed for this study onboard the MV Alucia in April 2016 using a Teledyne Reson SeaBat 7160 Multibeam Echo Sounder, and proprietary Teledyne PDS software was used to produce the image.**

Cay Sal Bank has limited biologic productivity at both a micro- and macro-scale, which limits biogenic carbonate sediment production (Goldberg, 1983, Purkis et al., 2014), and inorganic carbonate mud produced in the water column is winnowed-off the bank-top by strong currents and waves (Purkis et al., 2014). As such, average sediment cover on Cay Sal Bank is generally less than 10 cm (Goldberg, 1983). In comparison, the Holocene succession on the Little Bahama Bank is 2 m (Rasmussen et al., 1990), and the Holocene succession in some areas of Bermuda is ~5 m (Ashmore and Leatherman, 1984). Previous work by Hine and Steinmetz (1984) and Purkis et al. (2014) document scattered and thin (<2 m) deposits of sand-sized particles made up of intraclasts, peloids, and skeletal grains on the windward (eastern) portion, and gravels on the leeward (western and central) region (Fig. 3.2a). Sand samples contain less than 30% identifiable skeletal grains, and sand particles are mostly benthic foraminifera, echinoderms, corals, bryozoa, arthropods, and coralline algae. While bank-top sediment accumulation is scarce, geophysical surveys by Hine and Steinmetz (1984) documented thick sediment accumulation in Hine's Hole.

Since 1975 CE, seasonally averaged winds reveal that the easterly trade winds dominate the surface field across Cay Sal Bank throughout both the wet (April-September) and dry (October-March) seasons, with a slight secondary peak of northeasterly winds during the dry season. Using the Florida Keys Hybrid Coordinate Ocean Model (Kourafalou and Kang, 2012), Purkis et al. (2014) demonstrated that bank-top current velocity has minimal interannual variability. Purkis et al. (2014) found that annually averaged surface current velocity on Cay Sal Bank is ~0.1 m/sec,

approximately one order of magnitude slower than the Florida Current, thus signaling that surface flow over Cay Sal Bank is at least partially decoupled from the nearby Gulf Stream. Based on MODIS-Aqua sea-surface temperature (SST) observations from 2002 to 2011 CE, Cay Sal Bank has a mean annual SST of ~27.5 °C ± 2 °C, with highest monthly temperatures during most of the wet and peak hurricane season from June through October (~29.7 °C ± 0.5 °C), and lowest temperatures from November through May (~26 °C ± 0.9 °C) (Purkis et al., 2014).

3.3. Methods

3.3.1. Sediment Collection and Analysis

Visual, geophysical, hydrographic, and coring surveys were conducted aboard the *M/V Alucia* and *HOV Nadir* submersible in April 2016. A Teldyne RESON 7160 PDS2000 multibeam sonar system was used to map the bathymetry of the blue hole and surrounding rim along with the shape of the surrounding walls (Fig. 3.2c). Blue hole stratigraphy was mapped using an EdgeTech 3100 Chirp sub-bottom sonar system towed while sweeping at a 4-24 kHz bandwidth (Fig. 3.3, APPENDIX C Fig. S3.1). A YSI EXO1 portable sonde was deployed at a rate of 1 cm/second, with 2 measurements of temperature (± 0.01 °C), salinity (±0.1 Practical Salinity Units-PSU), dissolved oxygen (± 0.01 mg/L), and pH (± 0.01 pH units) collected each second (Fig. 3.3b).

Sediment cores (7.5 cm diameter) were collected using a Rossfelder-P3 submersible vibracorer (Figs. 3.3, 3.4a, and 3.5), and coring location, water depth, drive length, and recovery lengths are reported in APPENDIX C Table S3.1. These drives

collectively sampled up to 18 m of the stratigraphy within Hine's Hole. The sediment water interface was well preserved in Core-8 and Core-9, but the upper 110 cm of the longest recovered drive Core-7 was disturbed during the recovery process (1800 cm drive, 1627 cm recovery due to compaction and gas release). Prior to core sectioning, 3 mm diameter holes were drilled into the core pipe at ~1.45 m long increments down each core to facilitate release of interstitial hydrogen-sulfide gas for 24 hours. Following gas release, each contiguous core was cut into ~1.45 m sections at each drill point. A 1728 cm long composite record, which we hereafter refer to as the Hine's Hole Composite, was made by combining the upper 280 cm of Core-9 to the point of stratigraphic equivalence in Core-7 at 180 cm, thus including the 1447 cm of Core-7 below this point (Figs. 3.5 and 3.6). These methods have been used to assemble portions of separate coring drives into single continuous sediment records for other Bahamian blue holes (Wallace et al., Sub. March 2021, Wallace et al., 2021b, Winkler et al., 2020).

In the laboratory, sediment core sections were split lengthwise to undergo high resolution photography, radiographic imaging, and textural analysis. Textural analysis and visual sedimentary characteristics facilitated downcore stratigraphic correlation between the individual drives (Fig. 3.5, greater detail in APPENDIX C Fig. S3.3). Sediment textural analysis was completed for each drive using a procedure similar to the sieve-first loss on ignition method described by van Hengstum et al. (2016). This technique avoids potential bias introduced by aggregating and cementing together individual fine-sediment grains through desiccation or combustion. First, a standard sediment volume of 2.5 cm^3 was sampled at contiguous 1 cm intervals downcore, then

gently wet sieved over a >63 μm mesh to determine the volumetric mass of the fine-sand sized and greater particles in each subsample. The sieved residues were transferred into pre-weighed aluminum tins, then desiccated for 24 hours at 85°C. Fully dried residues were weighed to determine the mass of >63μm sediment per unit volume (mg/cm^3) of each 1 cm subsample (Fig. 3.5). While this procedure does not combust bulk organic matter content, there is little bias from coarse organic matter particles on the coarse carbonate sediment deposition downcore because the stratigraphy contained negligible coarse-grained organic matter fragments. Coarse-fraction sediment residues were stored in plastic vials for use in further analysis. Subsampled residues of all Core-7 sections (1627 cm) and the first three sections of Core-9 (346 cm), which encompass all stratigraphy included in the 1728 cm long Hine's Hole Composite, were re-sieved over a >250 μm mesh following the same methods described above to constrain the ≥ medium sand size particle mass per cm^3.

3.3.2. Age Control

Stratigraphic age-control was developed for the Hine's Hole record using 13 radiocarbon dates from Core-7 and 13 radiocarbon dates from Core-9 (Figs. 3.4 and 3.5; APPENDIX C Table S3.2). All dates were derived from the outer growth ring of articulated bivalve shells belonging to the *Tellinidae* family, save for one date derived from a gorgonian coral branch from the base of Core-7 (1627 cm). All dated material was extracted from the core then cleaned using ultrasonic vibrations in a deionized water bath. Samples were then rinsed over a >250 μm mesh to remove any remaining sediment, then dried overnight at 85°C. Bivalve shells were de-articulated using ethanol

sterilized tweezers, and ~2 mm wide sections of the outermost/youngest growth rings were cleaved away to be dated. All radiocarbon dating was completed by the National Ocean Sciences Accelerator Mass Spectrometry facility at Woods Hole Oceanographic Institution, where samples were hydrolyzed prior to measurement of radiocarbon abundance and $\delta^{13}C$ ratios using accelerated mass spectrometry.

Based on the high $\delta^{13}C$ measured for each mollusc and coral sample, conventional radiocarbon dates were calibrated into years before present (cal yr BP) using the Marine20 calibration curve (Heaton et al., 2020). This calibration provides a global mean correction of 550 years to address residence time of radiocarbon within marine reservoirs prior to bioassimiliation by marine organisms that build on the atmospheric correction provided by IntCal20 (Reimer et al., 2020). As discussed in detail in **APPENDIX C Section S3.4** No additional reservoir (ΔR) correction was applied to these samples as the marine reservoir variability on Cay Sal Bank has not been constrained given that no regional correction value has been established in the literature. Three samples from the upper 100 cm of Cores-7 and 9 with fraction modern carbon value ($F^{14}C$) in excess of 1 were calibrated using the Northern Hemisphere Zone 2 dataset (NHZ2) from the free online resource CALIbomb (Reimer et al., 2004).

Fifteen of these radiocarbon dates, 4 from Core-9 and 11 from Core 7, and a modern age of 2016 CE at the core-top were used as age-control points in a sedimentary age model (Fig. 3.5) that was developed using Bayesian statistical approaches in the R library Bacon v2.3 (Blaauw and Christen, 2011). The age model only includes age-control points from the core sections that were included in the Hine's Hole Composite

(i.e., upper 280 cm of Core 9 and lower 1447 cm of Core 7), and ages were estimate downcore for every 1 cm stratigraphic level for the Hine's Hole Composite. Based on the results (see below), we assume that thick (>2 cm), coarse grained stratigraphic units with >40 mg/cm^3 of 250 μm were deposited instantaneously, most likely by heightened hydrodynamic conditions related to severe weather events. As such, these coarse layers were designated as geologically instantaneous events using the SLUMP command in Bacon, which lumps the entire specified layer into a single year in the age model output (75 SLUMP entries, 580 cm total with an average thickness of 7.7 cm ± 5.1). Using the same parameters and control points, we also developed an alternate age model to test the temporal effects of using a reservoir correction of ΔR = –92 ± 111, which was found to be the weighted mean of the 40 most proximal ΔR values from the literature, which ranged from 150 to 360 km away from Hine's Hole (**APPENDIX C Section S3.4**, APPENDIX C Fig. S3.4; (Diaz et al., 2017, Druffel, 1997, Druffel and Linick, 1978, DiNapoli et al., 2021, Hadden and Schwadron, 2019, Lighty et al., 1982, Broecker and Olson, 1961). As discussed in APPENDIX C Section S3.4 this age model was not used because it introduced significant uncertainty regarding the reservoir correction. However, this alternate age model did indicate that even an aggressive reservoir correction of ΔR = –92 ± 111 would have minimal influence on the median/mean predicted ages (<50 years).

3.3.3. Event Attribution and Frequency Calculation

Coarse sediment anomalies that are likely indictive of high-energy event transport/deposition were identified as significant "event beds" if the fraction of coarse

sediment >250 μm mg/cm^3 exceeded a threshold of 40.9 mg/cm^3 derived following the Tukey rule of outlier detection for exponentially distributed data (Tukey, 1977). The Tukey rule states that outliers are values that fall above the third quartile (*Q3*) or below the first quartile (*Q1*) by at least 1.5 times the interquartile range (*IQR*) of the dataset (Eq. 3.1). This outlier threshold was calculated by determining the mean value of all >250 μm mg/cm^3 points that fell below 50 mg/cm^3, which is the *lower ~75th percentile* of the cumulatively distributed >250 μm fraction (n = 1257), to estimate the average composition of non-event sedimentation (16.46 mg/cm^3), resulting in a rate parameter of λ = 0.061.

$$Tukey\ rule\ for\ outliers\ = Q3 + 1.5IQR \qquad \textbf{(Eq. 3.1)}$$

$$Q1 = -\ln 0.75/\lambda;\ Q2 \text{ or } mean = 1/\lambda;\ Q3 = -\ln 0.25/\lambda;\ IQR = Q3 - Q1$$

The highest mg/cm^3 value from a single coarse event bed in excess of this threshold was counted as the event depth if the event bed was thicker than 1 cm. In the conservative event counting, event beds were considered independent from one another if they were separated by diminishing values for at least 2 cm provided at least one of these values either: (i) fell near or below the 40.9 mg/cm^3 threshold, (ii) was <50% of the value of the highest peaks on both sides of the bed, or (iii) could be visually distinguished by sedimentary characteristics in the core (i.e., coarse vs. fine grains and color; Figs. 3.5-3.7). In the more liberal event counts, beds were considered distinct if they were separated by more than 2 cm of sediment wherein mg/cm^3 values diminished by at least 30% of the highest value on either side. (Figs. 3.5-3.7).

Separate procedures were followed to calculate the >63 μm mg/cm^3 anomalies based on the methods of Donnelly et al. (2015). A 40-point moving average was calculated for >63 μm data, excluding values that exceeded 400 mg/cm^3. This moving average was subtracted from the >63 μm mg/cm^3 data to isolate coarse sediment anomalies. Similar to the liberal >250 μm event counts, only the highest value point from each coarse bed was counted, and beds were s considered distinct if they were separated by more than 2 cm of sediment wherein mg/cm^3 values diminished by ~30% of the highest value on either side. (Fig. 3.5b, APPENDIX C Fig. S3.6).

Following the methods of Winkler et al. (2020), hurricanes from 1850 to 2016 CE documented in the IBtRACS v4 dataset (Knapp et al., 2018, Knapp et al., 2010) were attributed to event beds in the upper portion of the Hine's Hole Composite where event beds median 2σ age was between 1850 and 2016 CE (Fig. 3.6, APPENDIX C Tables S3.3 and S3.4). Hurricanes within the 2σ age-range of the event bed were considered as potential depositional drivers if they passed within 115 km of Hine's Hole based on the geographic exposure of Hine's Hole as well as the recording sensitivity of other Bahamian blue hole records (Wallace et al., Sub. March 2021, Wallace et al., 2021b, Winkler et al., 2020). Starting with the most recent event bed, *E1*, we identified the event(s) that had the highest probability of generating each event bed based on factors such as the median age of the deposit, the intensity and proximity of the storm to Hine's Hole, the relative age/depth separation between sequential event beds vs the temporal window between historic storms, and which quadrant of the storm had the dominant impact during passage (Fig. 3.6, APPENDIX C Tables S3.3 and S3.44). This calibration

process was used to verify the accuracy of the event bed detection thresholds as well as providing context for what types of storms are most likely to be recorded by Hine's Hole throughout the paleo-record.

After calibrating the site sensitivity and verify thresholds, hurricane event beds were counted in both the >250 μm and >63 μm datasets using 50 and 100-year sliding windows following the methods of Lane et al. (2011), wherein the number of coarse sediment anomalies within 50 (25) years (before and after) each 1 cm interval is counted (Fig. 3.7, APPENDIX C Fig. S3.6). Both temporal windows were normalized to hurricanes/century to assess centennial-scale hurricane variability, but the 50-year sliding window counts likely emphasize shorter periods of extremely high or low hurricane activity that are variable at a multidecadal scale.

Active intervals with significantly elevated hurricane frequency are defined using the site-specific threshold calculations detailed by (Lane et al., 2011, Wallace et al., 2019), wherein we assume hurricane impact frequency follows a Poisson process. Based on the site sensitivity calibration, most of the 23 total ≥Category 1 hurricanes within 115 km since 1850 CE left a significant event deposit in the Hine's Hole Composite at a rate of 13.9 hurricanes/century (see *3.5.2. Changing Event Frequency*). Based on this rate, we calculate an upper 95% significance threshold of 21.9 hurricanes/century following the procedures of Ulm (1990), meaning that any activity levels above this threshold are unlikely to be driven by random variability in storm tracks alone (Fig. 3.7).

3.4. Results

3.4.1. Geophysical and Hydrographic Survey

The rim of Hine's Hole sits at an average depth of ~10 m (Fig. 3.2c) and is partially surrounded by a 0-2 m thick veneer of sandy sediment. Hine's Hole appears to have vertical karst walls around the North, East, and West flanks, and a ~45° downward slope along the south flank that extends ~100 m before flattening out to a ~5° deepening northward slope (Fig. 3.2c). No cave passages were observed during direct human observations aboard the HOV Nadir submersible. The water column is slightly stratified in Hine's Hole, with a moderate pycnocline from 50 to 60 m (salinity change: 40.4 to 41 psu), below which dissolved oxygen decreases to a minimum of 2 mg/L in the benthos (Fig. 3.3b). This suggests that the benthic water mass in the blue hole is at least partially sheltered wave-induced mixing and surface currents. However, the levels of dissolved oxygen are still sufficient to support a benthic ecosystem, as indicate by invertebrate burrows in the fine-grained benthic sediment (APPENDIX C Fig. S3.2).

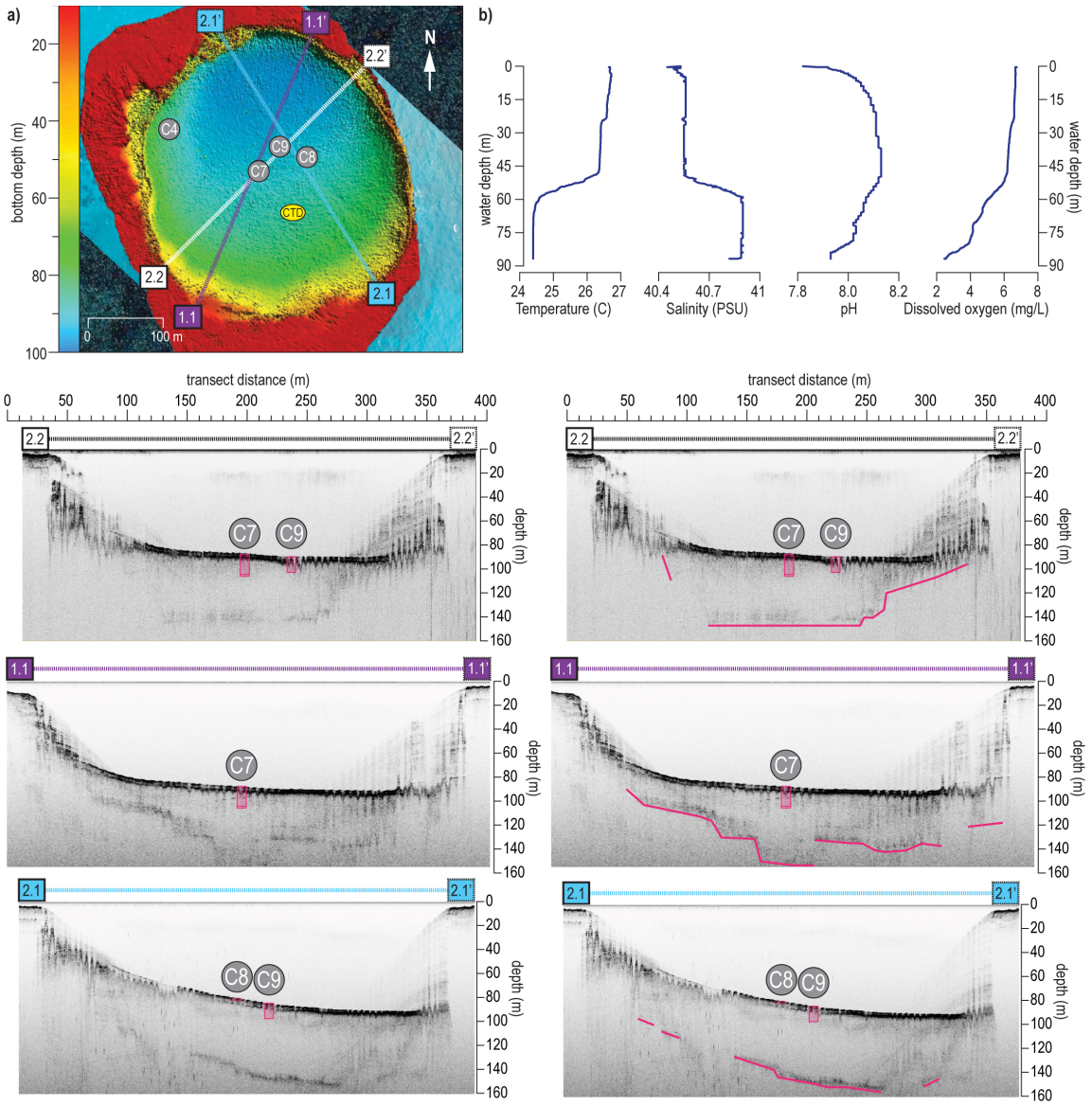

Figure 3.3. Hine's Hole Chirp and hydrography.
a) 2D depiction of multibeam bathymetry of Hine's Hole from along with coring locations noted by grey circles, the sample location of the water column profile in b) shown by a yellow oval, and 3 Chirp subbottom seismic transect paths. Images from each transect are shown below the map panel, with raw output to the left and interpreted subbottom features noted in pink in the identical images to the right. Core names and depths are added to each image where the transect line intersects core sampling location. Panel b) in the top right provides an 87 m water column profile (temperature, salinity, pH, and dissolved oxygen) for Hine's Hole measured on 23 April 2016 sampled at 23.8652°N and 79.8048°W.

Overall, the benthos of Hine's Hole gently slopes from ~80 m along the southern base to ~95 m along the northern margin (Figs. 3.2c and 3.3). Seismic subbottom surveys conducted in 2016 CE for this study confirm the observations of Hine and Steinmetz (1984) for thick sediment accumulations across the bottom of the blue hole, with internal acoustic reflectors visible in the top 5 m of the accumulation that likely indicate sediment density changes (Fig. 3.3, APPENDIX C Fig. S3.1). A sloping, relatively continuous hard reflector can be observed from 20-60 m below the sediment surface at the base of the hole. Strata between the upper and lower reflectors is obscured, likely because of high levels of interstitial hydrogen sulfide gas that attenuates the acoustic energy during transmission. These results suggest that the blue hole contains at least a 60 m stratigraphic succession, with the thickest accumulation in the deeper north-central area. Hine and Steinmetz (1984) observed higher levels of sediment deposition along the eastern flank of the blue hole. However, expanded sediment accumulation in the eastern portion of Hine's Hole is not supported by the relatively flat bathymetry across the base of Hine's Hole (Fig. 3.2c), nor is it evident in the new subbottom reflectors from the Chirp surveys (Fig. 3.3a, APPENDIX C Fig. S3.1). Therefore, it is likely that sediment is first well dispersed in the water column before settling out of suspension evenly across the benthos in this natural settling column.

3.4.2. Sedimentology and Age Control

Recovered sediments reveal that Hine's Hole predominantly traps carbonate mud and fine sands that are likely deposited during relatively quiescent hydrodynamic conditions. Fine-grained carbonate mud was not found in previous bank top

sedimentological surveys (Hine and Steinmetz, 1984, Purkis et al., 2014, Goldberg, 1983) or in the sediment grab samples collected from the periphery of Hine's Hole for this study. However, fine grained sediments were observed settling-out of suspension from the water column during an exploratory dive in the *HOV Nadir* submersible in 2016 CE (APPENDIX C Fig. S3.2c-f). Fine-grained carbonate mud intervals in Hine's Hole are not continuously laminated like the anoxic Great Blue Hole on Lighthouse Reef Atoll in Belize (Gischler et al., 2008), so they are not conducive to developing an independent, varve-based age model (e.g., Denomee et al., 2014, Schmitt et al., 2020). These finer-grained muds and fine sands are interrupted by numerous coarse-grained beds in the stratigraphy that are rich in skeletal material, pelloids, and weathered karst fragments (texture: medium to coarse-sand). While dissolved oxygen concentrations at the benthos are high enough to support some invertebrates (APPENDIX C Fig. S3.2h), sharp contacts between the coarse and fine stratigraphic layers indicate negligible bioturbation and homogenization of this primary textural signal. The coarser layers are visually distinct, and textural analysis quantifies the sharp contacts between sandy-mud background facies and these medium to coarse-sands (Fig. 3.4). These coarser sediments dominate the sand deposits currently found on the bank-top (Figs. 3.2, 3.4, and 3.5; Purkis et al., 2014). Overall, organic matter particles were visually scarce in both the fine and coarse lithofacies, but where observed, were composed of fragmented sea grass blades and small clusters of green macroalgae. Lastly, the presence of clear horizontal bedding and occasional laminations indicate that there is little evidence for post-depositional bioturbation or current driven reworking of sediments (Fig. 3.3b).

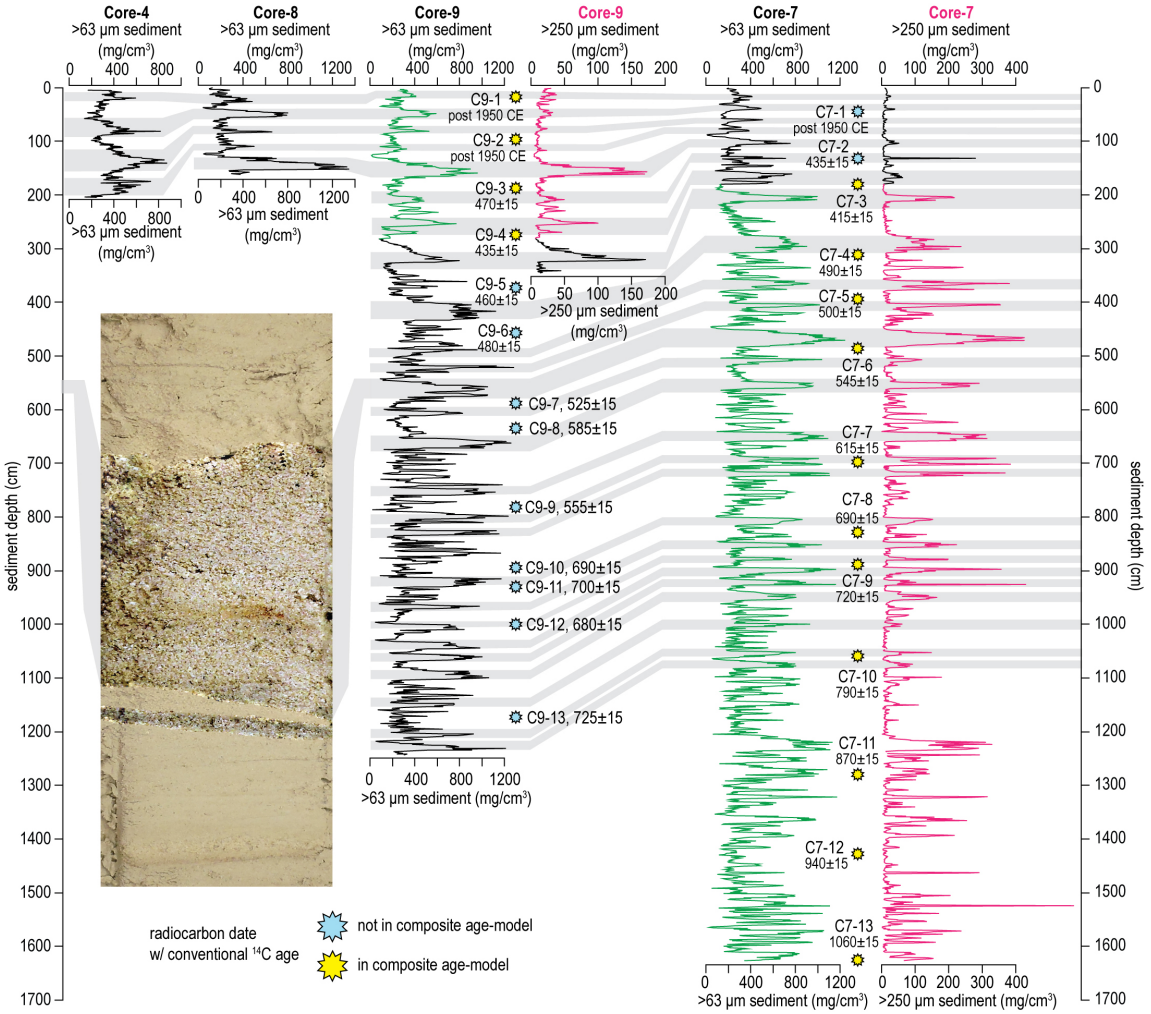

Figure 3.4. Hine's Hole sediment textural variability.
Downcore sediment textural data (>63 µm mg/cm^3) for four cores from Hine's Hole, along with medium sand textural variability (>250 µm mg/cm^3) for all of Core-7 and ~300 cm of Core-9. The pink and green lines are the portion of Cores-7 and 9 that respectively comprise the composite Hine's Hole record at the >250 µm and >63 size fractions. Coarse sediment layers like the one in the photograph are generally considered to be hurricane event deposits. As indicated by the grey bars, correlation of peaks is well maintained across the cores in both the >250 µm and >63 µm size fractions. See APPENDIX C Figure S3.3 for a detailed demonstration of the correlation of specific beds from 625 to 765 cm in Core-9 and 560 to 670 cm in Core-7. Yellow (blue) stars indicate the locations of radiocarbon dated articulated bivalves and gorgonian corals fragments that were (were not) used to develop the sedimentary age model for the Hine's Hole Composite reconstruction.

The coarse beds and other features like occasional laminations could be stratigraphically correlated between cores using high-resolution photographs and the textural data throughout the overlapping portions of each of the four cores (Fig. 3.4, APPENDIX C Fig. S3.3). Based on this correlation analysis, the 280 cm of Core-9 represent a complete and often expanded (i.e. thicker lithologic units) sequence that correlates to the first 180 cm of Core-7 (Fig. 3.4), with the length discrepancy likely resultant of sediment that was lost or highly disturbed during the recovery process of Core-7. Similarly, coarse bed stratigraphy in the 162 cm Core-8 (the best-preserved recovery of the upper meter of sediment) reproduces that of the first 190 cm of Core-9. Core-4 also shows many stratigraphic similarities to these three cores but was collected ~100 m westward of the other cores and appears to archive thicker coarse beds likely due to higher sediment accumulation given its proximity to the rim of the blue hole. As such, portions of each of Cores-7, 9, and 8 were compiled to assemble the 1728 cm long Hine's Hole Composite (Figs. 3.4 and 3.5a, b). The first 280 cm of Core-9 was used as the upper portion of the Hine's Hole Composite, with 180 to 1627 cm in Core-7 (1447 cm) representing the rest of the 1728 cm long composite record. This point of merging is supported by two radiocarbon dates from Cores-9 and 7 at depths of 273.5 cm (C9-4) and 179.5 (C7-3) cm in the Hine's Hole Composite, where the conventional radiocarbon ages are 435 yr BP ± 15 yr BP and 415 yr BP ± 15 yr BP (Fig. 3.5, APPENDIX C Table S3.2).

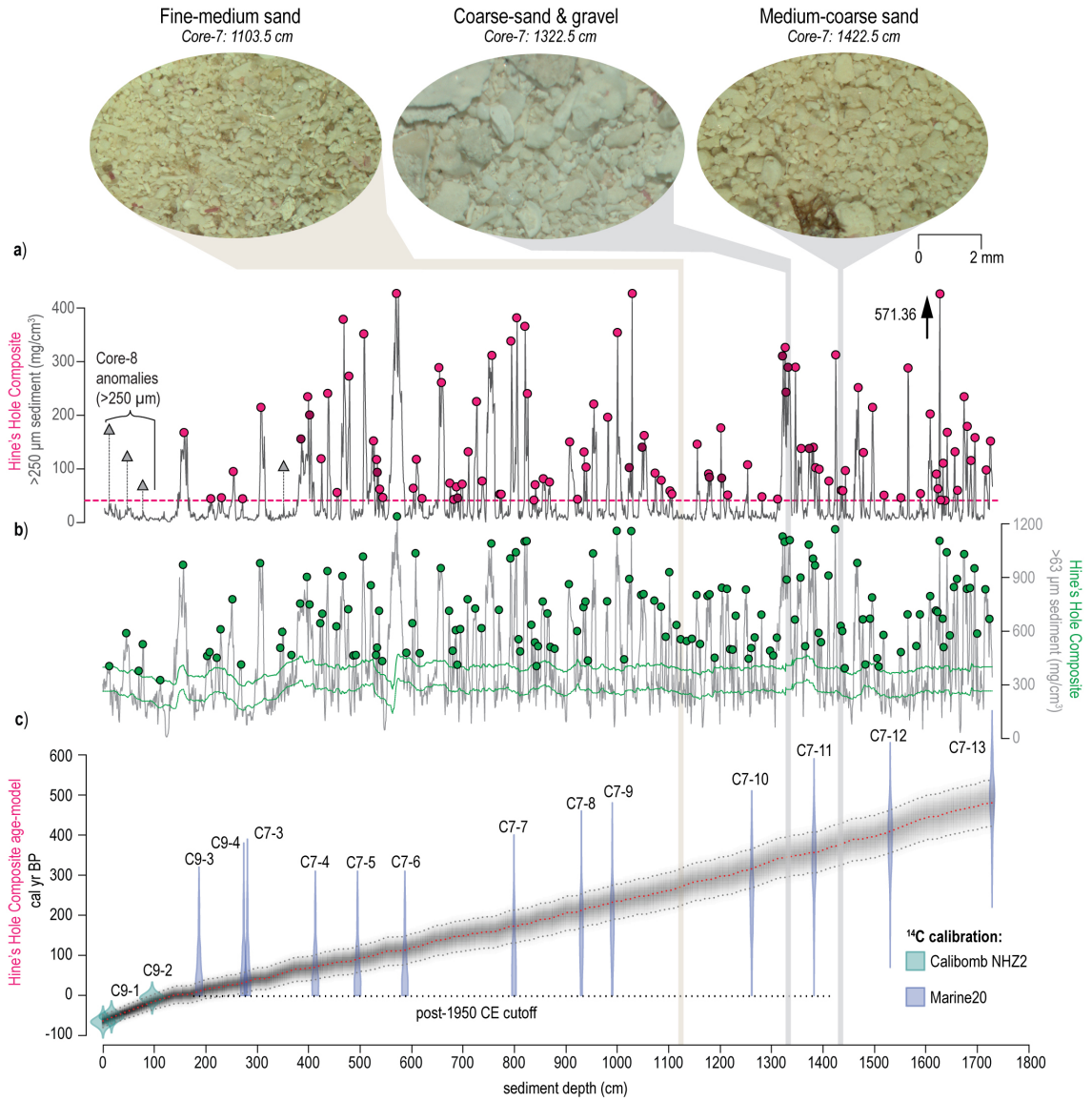

Figure 3.5. Hine's Hole sedimentary age model and coarse sediment anomalies. Downcore sediment textural data for the a) >250µm (dark grey) and b) light grey >63µm size fractions (mg/cm^3) of the Hine's Hole Composite. In a), Pink circles indicate statistically anomalous coarse event beds that exceed the 40.9 mg/cm^3 upper event bed threshold for >250 µm data. In b), green circles are statistically anomalous coarse event beds that exceed the 40-pt moving average (dark green line) + 150 mg/cm^3 upper event bed threshold for >63 µm data (light green line). Images above a) shows variability in particle size and composition in >63 µm sediment fractions found in Core-7. c) Sedimentary age model for the Hine's Hole Composite was constructed using 16 points of age control including 14 radiocarbon dated articulated bivalve shells leaves and 1 branch of a gorgonian soft coral from Core-7 (*n* = 11 dates) and Core-9 (*n* = 4 dates) along with a modern core-top date of 2016 CE. See APPENDIX C Table S3.2 for details on dated material.

Conventional radiocarbon dates in the deeper portions of Cores-9 and 7 support the accuracy of the visual stratigraphic correlations that were made between these two cores (Fig. 3.4, APPENDIX C Table S3.2). No age-control points were obtained for Core-8 so no continuous portions of it were used in the Hine's Hole Composite; however, >63 μm coarse peaks in Core-8 were re-sieved over a >250 μm mesh to determine the fractional mass of the coarse sediment in these beds. Core-8 is much shorter, so the coring process was much faster, meaning that it was not exposed to prolonged vibrations from the coring motor that can homogenize less-consolidated sediment for the same duration as Cores-7 and 9.

The >250 μm dataset had an average coarse sediment mass fraction of 48.6 $mg/cm^3 \pm 68.5$ mg/cm^3, and 99 (109) coarse sediment deposits exceeded the threshold of 40.9 mg/cm3 and were identified as coarse sediment anomalies using the conservative (liberal) counting methods (Fig. 3.5a). Four additional event beds were identified (E1 to E3) in Core-8 and Core-9 (E10) that exceeded the significance threshold, whereas stratigraphically correlated coarse-sediment beds in the Hine's Hole Composite were less pronounced and did not exceed the significance threshold (Figs. 3.4 and 3.5). These additional event beds bring the total to 103 and 113 for the conservative and liberal event counts, respectively. The >63 μm dataset had an average coarse sediment mass fraction of 422.2 $mg/cm^3 \pm 241.1$, and 148 event beds were identified as coarse sediment anomalies based on the thresholds discussed in *section 3.3 Event attribution and frequency calculation* (Fig. 3.5b). Anomalous coarse-bed thickness ranged from <1 cm

to up to ~35 cm in both the >250 μm and >63 μm size fractions, with an average thickness of ~6 cm in the >250 μm dataset.

Sedimentation in Hine's Hole is approximately linear with an average sedimentation rate of 2.1 cm/yr from 1460 to 2016 CE based on the Bayesian statistical age model (Fig. 3.5c). This sedimentation rate represents an estimate of the background, non-event driven sedimentation rate that was calculated by labelling all coarse deposits ≥4 cm in thickness as instantaneous events during age model development (background sedimentation accounts for ~1148 cm in >250 μm dataset). If these events are not excluded, the overall sedimentation rate of the 1728 cm Hine's Hole Composite is ~3.2 cm/yr. Age model uncertainty is lowest at from 0-500 cm (1850 to 2014 CE), where the average uncertainty was ±21.4 yr (standard deviation ± 4.1). Below this 500 cm, positive (younger) uncertainty increased linearly with depth and time, averaging 37.1 yr ± 5.9, whereas negative (older) uncertainty increased exponentially at a rate of $31.993^{0.0013x}$, with x being depth, to an average –78 yr ± 35 yr.

3.5. Discussion

3.5.1. Age Model Limitations and Implications

MarineCal20 calibrated median-ages of control points from Core-9 (C9-3, C9-4) and Core-7 (C7-3, C7-4, C7-5, C7-6) are more recent than 1950 CE when no ΔR correction is applied, despite none of these having fraction modern ^{14}C values >1. For dates C7-7 through C7-13 from Core-7, Marine20 calibrated median ages fall prior to 1950 CE and the average background sediment accumulation rate of 2.1 cm/yr (3.2

cm/yr including coarse beds) falls within higher confidence age- range estimates for these control points (Fig. 3.5c). The fact that the median age of the first six non-modern ^{14}C rich samples is calibrated beyond 1950 CE suggest that some additional negative ΔR correction is needed to correct for a local marine reservoir that is likely younger than the 550 year global marine reservoir used in the Marine20 calibration curve (Heaton et al., 2020). However, no ΔR correction values currently exist for Cay Sal Bank, and high-levels of interspecies and regional variability in ΔR corrections across the Caribbean means that applying any sort of regionally-averaged ΔR correction introduces additional uncertainty (**APPENDIX C Section S3.4**; DiNapoli et al., 2021, Toth et al., 2017). Further, based on the work of Kondo (1987), the pallial sinus index of the Tellinidae bivalve specimens we dated (~0.3 based on 10 measured specimens) suggests that these organisms burrow their approximate body length into the sediment, meaning that dated organisms are likely to be stratigraphically young relative to surrounding sediment at the burrow depth. As such, we assume that adding any additional ΔR correction presents greater uncertainty than just correcting to the global marine reservoir value alone.

Regardless of uncertainties, Hine's Hole sedimentation rate is exceptionally high relative to other Bahamian blue holes in subtidal settings, which tend to fall between 0.6-1.3 cm/yr (Wallace et al., 2019, Wallace et al., Sub. March 2021, Wallace et al., 2021b, Winkler et al., 2020). Given that the current depth of Cay Sal Bank around Hine's Hole is ~10 mbsl, Hine's Hole would have remained an inundated marine depositional environment until ~8000 yrs BP based on the Bahamas sea-level curve compiled by Khan et al. (2017). If we assume that: (i) the average sedimentation rate of ~3.2 cm/yr

calculated for the upper 18 m of stratigraphy (carbonate mud and multiple storm-driven carbonate sand layers) is constant through time, and (ii) sedimentary processes have remained similar throughout the inundated marine phase which likely persisted since the bank top flooded ~11,000 to 6000 years ago (Purkis et al., 2014), then the ~60 m of accumulation that is observable in the Chirp surveys (Fig. 3.3, APPENDIX C Fig. S3.1) could represent just ~1900 years of sediment accumulation in Hine's Hole.

3.5.2. Calibrating the Record to Historical Hurricanes

Based on the median date derived from the age model, the upper ~500 cm of the Hine's Hole Composite represents to the period from 1850 to ~2016 CE. During this time, there are 19 coarse sediment anomalies in the >250 μm size fraction that exceed the 40.9 mg/cm^3 significance threshold including the 4 additional anomalies that were only detected in correlated beds from Cores-8 or 9 (E1-E3 and E10, Figs. 3.4-3.6). Based on the punctuated nature of these coarse-sediment beds, it is likely that these anomalies were deposited by heightened currents or waves that are generated during extreme events like hurricanes and tsunamis. As discussed by Winkler et al. (2020), tectonic sources (i.e., tsunamis) are unlikely to play a major role in causing extreme waves in the region around The Bahamas. The Azores–Gibraltar plate boundary is the most likely tectonic origin of major tsunamis that could impact The northern Bahamas, such as with the 1755 CE Lisbon Earthquake, for which numerical models predict far-field wave heights of less than 1 m in the northern Caribbean (NCEI/WDS Global Historical Tsunami Database; (Barkan et al., 2009, Arcos et al., 2018). Further, it is likely that the Little Bahama Bank buffered these waves resulting in a diminished impact with

modelled wave amplitude of <0.2 m across Cay Sal Bank (Arcos et al., 2018). Even if a tsunami from a strong event like the 1755 CE Lisbon Earthquake could deposit a coarse sediment bed in Hine's Hole, the tsunami recurrence interval in The Bahamas is on the order of ~500 years (Parsons and Geist, 2008) compared to the decadal recurrence of intense hurricanes throughout the region. Given that we are interested most in long-term variability illuminated by high-resolution sediment records, as opposed to interpreting a single event bed as climatically deterministic, tsunami induced coarse deposits likely have negligible impacts on the derived temporal trends and interpretations in this study.

A relatively comprehensive instrumental record of North Atlantic hurricane activity(e.g., timing, track, wind speed, pressure) from 1850 to 2020 CE is compiled by the IBtRACS hurricane database, which is most reliable following widespread implementation of satellite observation in the 1960 CE and is considerably less reliable prior to the use of air-craft storm monitoring in the 1940s (Vecchi and Knutson, 2011, McAdie et al., 2009). As described in the methods, we initially assumed that hurricanes of at ≥Category 1 strength passing within 75 km of Hine's Hole may be capable of generating a coarse deposit in the sedimentary record. However, only 15 hurricanes since 1850 CE meet these criteria, and four of these events fall within separate two-year periods and are likely indistinguishable in the sedimentary record (Fig. 3.6, APPENDIX C Tables S3.3 and S3.4). As such, the proximity threshold was expanded to ≥Category 1 strength within 115 km since 1850 CE, which includes 23 possible storms, including at least 5 hurricanes separated by less than 2 years that may not be distinguishable in the sedimentary record based on how some hurricanes may impact coarse sediment supply

around Hine's Hole (18 total). Starting with the most recent deposits and working backward through time, these 18-23 historical hurricanes from 1850 to 2016 CE were assessed as emplacement mechanisms for each of the 19 >250 μm coarse-sediment anomalies based on age-range, proximity, wind-speed, and angle of approach (Fig. 3.6, APPENDIX C Tables S3.3 and S3.4). To understand this process, APPENDIX C Tables S3.3 (1900-2016 CE) and S3.4 (1850-1899 CE) list characteristics of all ≥Category 1 hurricanes passing within 115 km of Hine's Hole that fall within 2σ age range of each >250 μm coarse-sediment anomaly of the last ~170 years (Fig. 3.6a, b). In Figure 3.6b, the 95% (2σ) age probability distribution functions are plotted for each coarse anomaly, and the strength and timing of historical storms overlay this to demonstrate which events could be responsible for each deposit based on the sedimentary age model. Finally, Figure 3.6c shows the most proximal passage for each storm to Hine's Hole, and Figure 3.6d plots each historical event by passage distance vs wind speed to show what types of storm characteristics are most associated with attributed hurricanes.

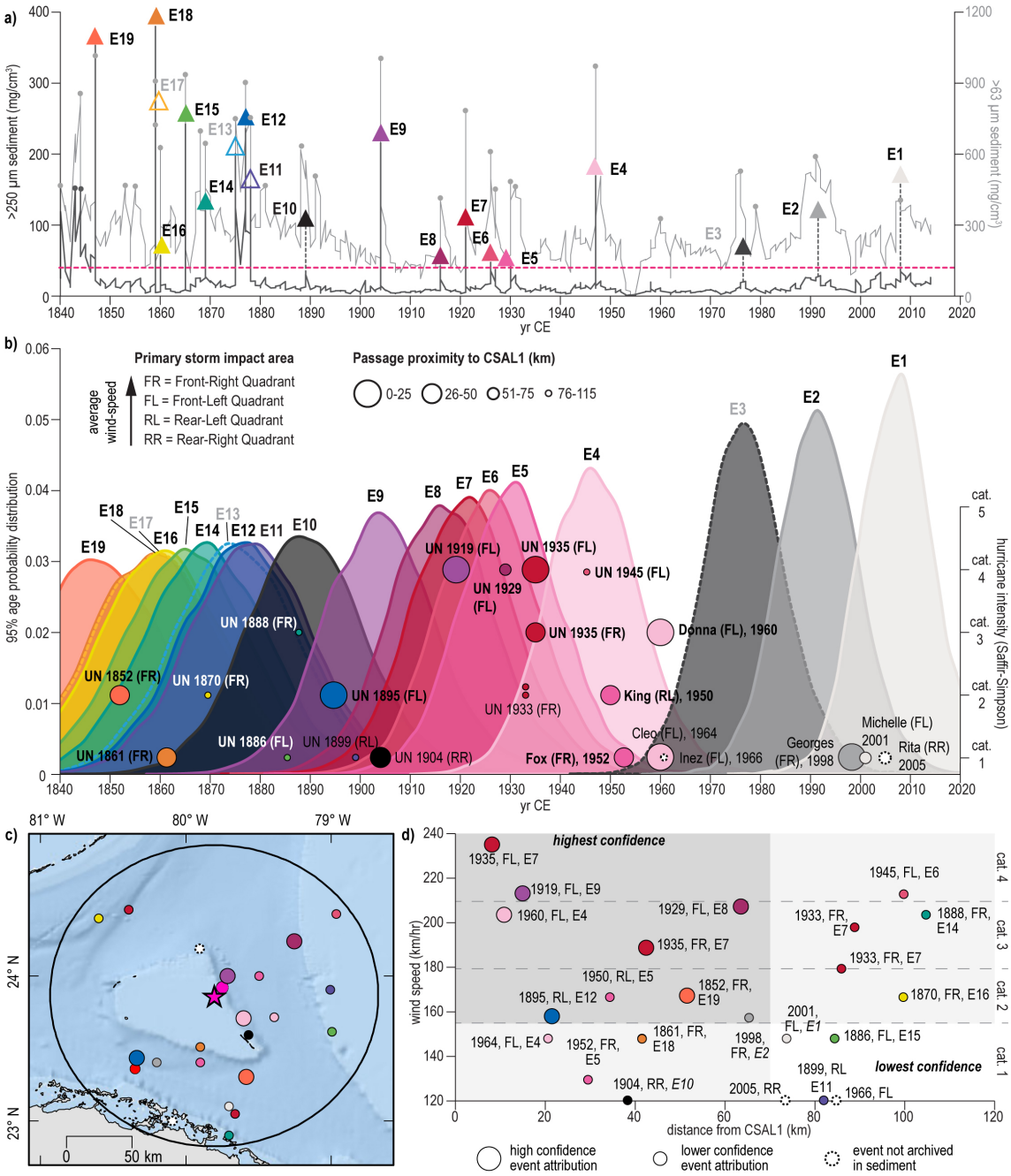

Figure 3.6. Calibration of Hine's Hole Composite to the instrumental record. a) Coarse sediment data (mg/cm^3 >250 µm, in dark grey and >63 µm in light grey) with >40.9 mg/cm^3 >250µm coarse anomaly event beds E-1, E2, E3, and E10 (from Cores-8 and 9) and E4-E19 indicated respectively by greyscale and colored triangles that correspond to the colors of 95% age probability distribution (95% PDF) plots in panel b). Only the >250 µm data was used to define hurricane event beds, but the most prominent peaks are also observed in the >63 µm data. Circles on panel b) correspond to the timing of hurricanes observed within 115 km of

Hine's Hole from 1850 to 2015 CE (*n = 23*), with the diameter being relative to the passage proximity (larger circle = closer passage), and the vertical position of the cores corresponding to the intensity of the storm on the Saffir-Simpson hurricane scale (right y-axis). The color of the circles corresponds to the color of the 95% PDF plot of the event bed that the observed hurricane event is most likely associated with (modern hurricanes with no associated event bed in the Hine's Hole Composite are solid black. Panel c) includes a map of the point of closest passage to Hine's Hole of all hurricanes from 1850 to 2015 CE depicted in panel b), with color associated with the coarse anomaly that is attributed to the hurricane event and the size and shape corresponding to the confidence in that attribution (see legend). Applying the same symbology, d) is a scatterplot of the wind speed of each of these hurricanes plotted against to the distance of closest passage to Hine's Hole. This diagram shows that over the last ~170 years, Hine's Hole: 1) reliably archives all ≥Category 2 hurricanes within 75 km; 2) records most ≥Category 1 hurricanes within 75 km or ≥Category 2 hurricanes within 115 km depending on the angle of approach; and 3) does not reliably record ≤Category 1 hurricanes passing further than 75 km away from Hine's Hole.

Deposit E1 has a median-age of 2007 CE and a 2σ range = 1993-2016 CE. The next deposit, *E2*, has a median age of 1991 CE and a 2σ range of 1976-2007 CE. The only hurricanes within 115 km of Hine's Hole during the age-uncertainty range of these two deposits are Rita in 2005 (Category 1, 26 km), Michelle in 2001 (Category 1, 73 km), and Georges in 1998 CE (Category 1-2, 65 km). Rita was a very weak Category 1 hurricane when is passed Hine's Hole (max wind speed ~120 km/hr), which was exposed to even weaker winds in the rear-right quadrant of the storm. As such, the most likely sources of E1 and E2 are, respectively, Hurricanes Michelle (2001 CE) and Georges (1998 CE) (Fig. 3.6, APPENDIX C Table S3.3).

Following this, E3 has a median date of 1977 CE with a 2σ age range of 1961-1994 CE, during which time two hurricanes, Cleo (1964 CE, Category 1) and Donna (1960 Category 3), and on tropical storm (Greta, 1970 CE) passed within 30 km of Hine's Hole with the site exposed to the front left quadrant of the storm. Additionally,

Hurricane Inez passed within 85 km of Hine's Hole in 1966 as a Category 1 storm. Based on the ~15-year separation between the median ages of E2 and E3 and the relatively small fractional mass of >250 μm sediment of E3 (~65 mg/cm^3), it is likely that one or both of the younger storms, weaker TS Greta (1970 CE) or more distal Hurricane Inez (1966 CE), was the source of E3. Proximal hurricane passage was generally more frequent prior to 1970 CE, so we will only discuss the most likely event deposit sources here; however, the comprehensive list of hurricanes since 1850 CE can be viewed in APPENDIX C Tables S3.3 and S3.4. Coarse anomaly E4 (median age 1947 CE; 2σ range 1929-1966 CE) is the most prominent-coarse deposit in the upper 300 cm of sediment. Based on the magnitude of the >250 μm sediment mass, with E3 likely attributed to TS Greta (1970 CE) or Hurricane Inez (1966 CE), deposit E4 is almost certainly attributable to Hurricane Donna, which passed within 11 km of Hine's Hole as a Category 3 event in 1960 CE. E3 has a maximum fractional mass of only 64 mg/cm^3 and ~3 cm thick, whereas the full coarse deposit for E4 has a maximum value of 169.4 mg/cm^3 and is 23 cm thick. This does not necessarily mean that the thickness or >250 μm coarse sediment mass of the hurricane deposit is always indicative of storm intensity or proximity; however, Hurricane Donna and TS Greta both passed to the north of Hine's Hole moving from east to west, but Donna was 20 km closer and had at least 120 km/hr faster winds. As such, Hurricane Donna was likely responsible for a more notable coarse sediment deposit. This high confidence attribution of E4 to Hurricane Donna suggests that there is likely a -10 to -20-year CE offset in median age estimates at this point in the record, which manifests in other attributions shown in Figure 3.6. This is

likely resultant of the greater age-uncertainty associated with the Marine20 calibration curve as well as the need for a slight ΔR correction.

Following this assignment, median ages of coarse anomalies E5-E8 are all clustered between 1930 and 1916 CE, and likely represent several decades of relatively high activity. The cumulative 2σ age uncertainty of these deposits is from 1951 to 1896 CE, during which time nine ≥Category 1 hurricanes passed within 115 km of Hine's Hole, including two strong hurricanes in both 1935 and 1933 CE. Based on this, E5 (median age 1930 CE; 2σ range 1911-1951 CE) is most likely attributed to one or both Category 2 Hurricane King which passed within 34 km in 1950 CE or Category 1 Hurricane Fox whose front right quadrant passed within 30 km of Hine's Hole in 1952 CE. Chronologically, E6 was most likely deposited by a Category 4 hurricane whose front left quadrant passed within 100 km of Hine's Hole in 1945. Deposit E7 was likely deposited by one or more of the two Category 4 and 3 hurricanes in passing within 8 and 43 km of Hine's Hole in 1935 CE, as well as the Category 3 and 2 hurricanes that passed within ~85-90 km in 1933 CE. Though the magnitude of the >250 μm sediment mass is relatively low given the strength and proximity of these storms, it is possible that the first of these major hurricanes washed sediment accumulations off the bank-top leaving minimal time for new sand banks to accumulate around Hine's Hole between each storm. Depleted bank-top coarse sediment supply following the two hurricanes in 1933 CE could explain why two distinct coarse sediment anomalies are not observed for both the 1933 CE and 1935 CE hurricane clusters, even though ~4 cm of carbonate mud should have accumulated between the 1933 and 1935 CE events based on the 2.1 cm/yr

background sediment accumulation rate. Finally, E8 has a median age of 1916 CE (1896-1938 CE), just 5 years before E7, meaning it was most likely deposited by a Category 3 hurricane on 27 September 1929 as it is the last major hurricane event in this 20-year cluster.

Following E8, only E9 and E10 had median ages more recent than 1900 CE (Fig. 3.6, APPENDIX C Table S3.3). The only hurricanes within 115 km during this time were a Category 4 hurricane within 15 km of Hine's Hole in 1919 CE, and a weak Category 1 hurricane within ~40 km in 1904. Deposit E9 has a median age of 1904 CE with 2σ range of 1883-1927 CE, meaning it occurred approximately 10 years prior to E8 which was attributed to a 1929 event. Based on the timing, the relatively high fractional mass of >250 μm sediment (216 mg/cm^3), and the lack of event beds within 10 years of the median age of E9 on either side, we are confident in attributing this deposit to the Category 4 hurricane in 1919. This means that the weak Category 1 event in 1904 CE is most likely attributed to the relatively less coarse E10, which was not significant in Core-7 section used in the Hine's Hole Composite but had a value of 106 mg/cm^3 in a correlated bed in Core-9.

Nine additional coarse anomalies were detected with mean ages the fell between ~1850 and 1899 CE (E11-E19), which had a cumulative 2σ age-range of 1822-1903 CE (Fig. 3.6, APPENDIX C Table S3.4). During this time, only seven ≥Category 1 hurricanes are recorded as passed within 115 km of Hine's Hole in the IBtRACS database. We attribute these 7 hurricanes to the coarse sediment anomalies on a mostly chronological basis, with the only confident attributions being: (i) E12 (median age 1877

CE) likely deposited by a Category 2 hurricane within 20 km in 1895, (ii) E18 (median age 1859 CE) being deposited by front right quadrant Category 1 winds within 42 km in 1861, and (iii) E19 (median age 1848 CE) being deposited by front right quadrant Category 2 winds within 42 km in 1852. Only E13 and E17 did not have clear attributions to hurricanes within 115 km of Hine's Hole. Given the technology prior to 1900 CE along with the remote nature of Cay Sal Bank, it is possible that an unrecorded event or a more distal event like Category 1 hurricane in 1891 CE passing within 175 km of Hine's Hole produced these deposits. It is also possible that these deposits represent overcounts as both E13 and E17 were identified using the liberal counting method (Fig. 3.5a, 3.6a; see **3.3 Methods**).

Collectively, this calibration reveals that 16 of the 19 >250 μm coarse sediment anomalies with median ages from 1850-2016 CE can be attributed to ≥Category 1 hurricanes that pass within 115 km of Hine's Hole throughout the instrumental record (Fig. 3.6). As demonstrated by Figure 3.6d, hurricanes that are: more intense (≥Category 2), more proximal, pass at an angle that subjects Hine's Hole to stronger winds from the front-right or left quadrant (relative to the intensity of the individual storm), and occur after 1940 CE all tend to result in higher confidence attributions. Based on this we have: (i) high-confidence that the Hine's Hole Composite archives all ≥Category 2 hurricanes within 75 km provided they are separated by at least 2 years, (ii) medium confidence that >Category 1 hurricanes within 75 km or >Category 2 events within 115 km are archived, and (iii) lower confidence that ≤Category 1 hurricanes that pass further than 75 km away are archived (Fig. 3.6a).

3.5.3. Changing Event Frequency

As discussed above, coarse sediment anomalies in the >250 µm data set that exceed the fractional mass threshold of >40.9 mg/cm^3 are all coevally timed with proximal passage of hurricanes from 1850-2016 CE (Fig. 3.6). This correlation is also observed for many of the >63 µm anomalies, but there are multiple anomalies in this smaller sediment size-fraction data that do not correspond with any proximal hurricanes in the instrumental record. As such, we focus on the >250 µm data for the reconstruction of paleo-hurricane activity near Hine's Hole. Specifically, we interpret this record from the liberal counting method as, by nature, sedimentary records of hurricanes represent a minimum-count of hurricane activity over time (Woodruff et al., 2008).

In the 100-yr moving window liberal counts (Fig. 3.7a), hurricane event frequency is heightened to just below the significance threshold in the oldest portion of the record from 1510-1610 CE, with an average of 21.4 hurricanes/century ± 1, with activity from 1510-1550 CE generally exceeding the 21.8 hurricanes/century threshold and has a maximum of 24 hurricanes/century. From 1610-1710 CE, activity diminished somewhat, with an average of 17.4 hurricanes/century ± 1.6 and a minimum value of 13 hurricanes/century. Following this less active period, event bed frequency reached maximum sustained levels and exceeded the site-specific event-frequency threshold of 21.8 hurricanes/century from 1710-1850 CE, with a maximum of 31 hurricanes/century and an average 26.6 hurricanes/century ± 2.6. Archived hurricane impact frequency was lowest from 1850-1964 CE, with a minimum of 7 hurricanes/century and an average 13.9 hurricanes/century ± 5.4.

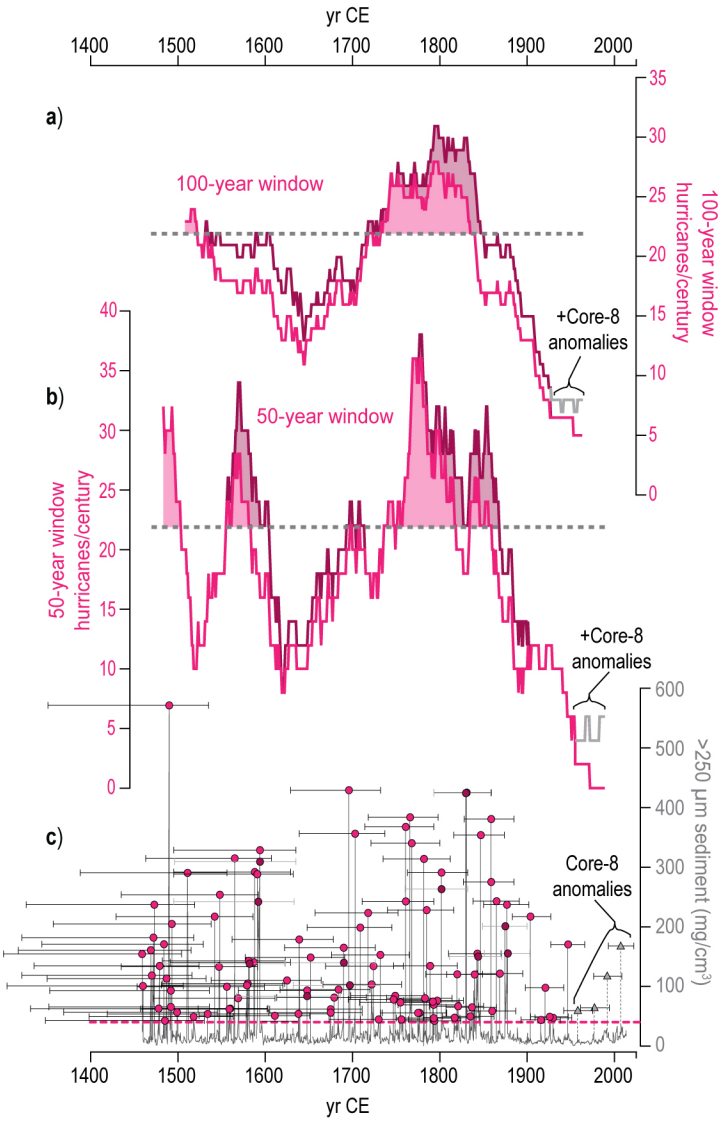

Figure 3.7. Hurricanes/century calculated from the Hine's Hole Composite. a) The pink/maroon lines represent 100-year moving window counts for >250 µm event beds per century in the Hine's Hole Composite at the conservative (pink) and liberal (maroon) counting methods. The pink conservative lines are plotted in front of the maroon liberal lines, so the conservative and liberal counts are in full agreement when only the pink line is seen. The site-specific upper threshold for a statistically active interval, >21.8 hurricanes/century (≥Category1 within 115 km), is marked by a dashed grey line in both the 100- and 50-year window counts. Temporal windows where hurricanes/century exceed this limit are shaded in pink (conservative) or maroon (liberal). b) Same as a), but lines represent the 50-year window counts which were doubled to normalize to hurricanes/century. c) >250 µm coarse sediment anomalies (grey line) from Hine's Hole Composite from 1460 to 2016 CE. The pink dashed line is the 40.9 mg/cm^3 anomaly threshold, and event

beds that exceed this threshold are marked with pink circles (maroon for liberal only bed). 2σ (95%) age-uncertainty windows for each coarse anomaly are shown by the horizontal black error bars.

The 50-year window counts (Fig. 3.7b), which were doubled to normalize to hurricanes/century, emphasize changes in hurricane frequency that occur at a multidecadal scale. In these counts, two early active intervals are observed from 1485-1505 CE (average 27.9 hurricanes/century ± 3.1) and from 1555-1605 CE (average 26.6 hurricanes/century ± 3.5). Hurricane frequency from 1505-1555 CE and 1605-1735 CE never exceeded the site-specific significance threshold of 21.8 hurricanes/century for sustained periods; however, these two-time windows had an average 16.9 hurricanes/century ± 3.7 which is higher than the average hurricane frequency from 1850-2016 CE. The longest and most active interval occurred from 1735-1870 CE, with an average rate of 27.8 hurricanes/century ± 4.2 and a maximum 38 hurricanes/century. In the 50-year window counts, activity is lowest from 1890-1990 CE, with an average of 8.4 hurricanes/century ± 3.4, which falls just below the site-specific frequency lower significance threshold of 8.5 events/century.

Overall, the 100-year and 50-year counts are very similar, especially from 1600-2016 CE. However, the 100-year window counts fail to capture the multidecadal variability from 1485-1600 CE, where the 50-year window counts document two statistically significant active intervals from 1485-1505 CE and 1555-1605 CE that are separated by a 50-year lull in activity. Instead, the 100-year window averages these two active periods together with the lull, resulting in a ~150-year period where archived hurricane impacts are relatively elevated but fall just below the upper significance

threshold of 21.8 hurricanes/century. As such, we suggest that the 50-year window better represents the multi-decadal variability in hurricane frequency that the Hine's Hole Composite is particularly well suited to archive given its high-sedimentation rate that enables clear distinction of multiple hurricane deposits within a relatively short temporal range (1-5 years). The 50-year window counts will therefore be the primary focus of the discussion hereafter.

3.5.4. Regional Hurricane Patterns

The evidence from Hine's Hole for significantly higher hurricane activity in the past than what has been observed throughout the ~170 year-long instrumental record has also been documented by other proxy-based and historical reconstructions. Near the Florida Keys, for example, Trouet et al. (2016) inferred that elevated periods of hurricane frequency suppressed growth in south Florida slash pine trees (*Pinus elliottii* var. *densa*, TC_{supp}). It is thought that high-winds and saltwater intrusion from hurricanes causes diminished growth in slash pines, which can be observed from annual tree ring thickness (Trouet et al., 2016). Given the nearly-annual sedimentation rate in Hine's Hole and annual-scale resolution of tree ring growth-based proxies, Hine's Hole and tree ring evidence of hurricane activity are highly comparable. Trouet et al. (2016) demonstrated that on a decadal basis, the percentage of the 38 sampled slash pine trees on Big Pine Key (Florida Keys; Fig. 3.1) that exhibited tree ring growth suppression correlates well with ≥ Category 1 hurricane frequency within ~160 km of Big Pine Key since 1850 CE (TC_{supp}; Fig. 3.8c). This record was extended to 1495 CE by compiling documentary evidence of 657 Spanish shipwrecks caused by storm activity from 1495 to

1825 CE (TC_{ship}), and a historical reconstruction of tropical cyclone activity based on storm observations in Spanish historical documents from the Archivo General de Indias ($TC_{archive}$; (García-Herrera et al., 2005). These records show decadal scale similarities to TC_{supp} during the ~110 years of overlap from 1710 to 1820 CE (Fig. 3.8c).

The Hine's Hole Composite and TC_{ship} (Trouet et al., 2016) each suggest a brief but significant active period for hurricane impacts in the Florida Straits from 1485 to 1505 CE (AI-1, Fig. 3.8b, c). After a 30 year lull, Hine's Hole Composite, TC ship, and $TC_{archive}$ (García-Herrera et al., 2005) all suggest a prolonged increase in regional hurricane impact frequency from 1550 to 1620 CE. Following this active period, TC_{ship}, $TC_{archive}$, and Hine's Hole Composite all suggest a relative less active period from 1630-1700 CE. Beginning around 1710 CE, Hine's Hole Composite, TC_{supp}, TC_{ship}, and $TC_{archive}$ all suggest a substantial increase in hurricane activity that spans until 1870 CE, which represents the interval in the Hine's Hole Record that record the most frequent hurricane event beds over the last 600 years (Fig.8). After 1870 CE, the Hine's Hole Composite and TC_{supp} both suggest an overall decrease in regional hurricane activity.

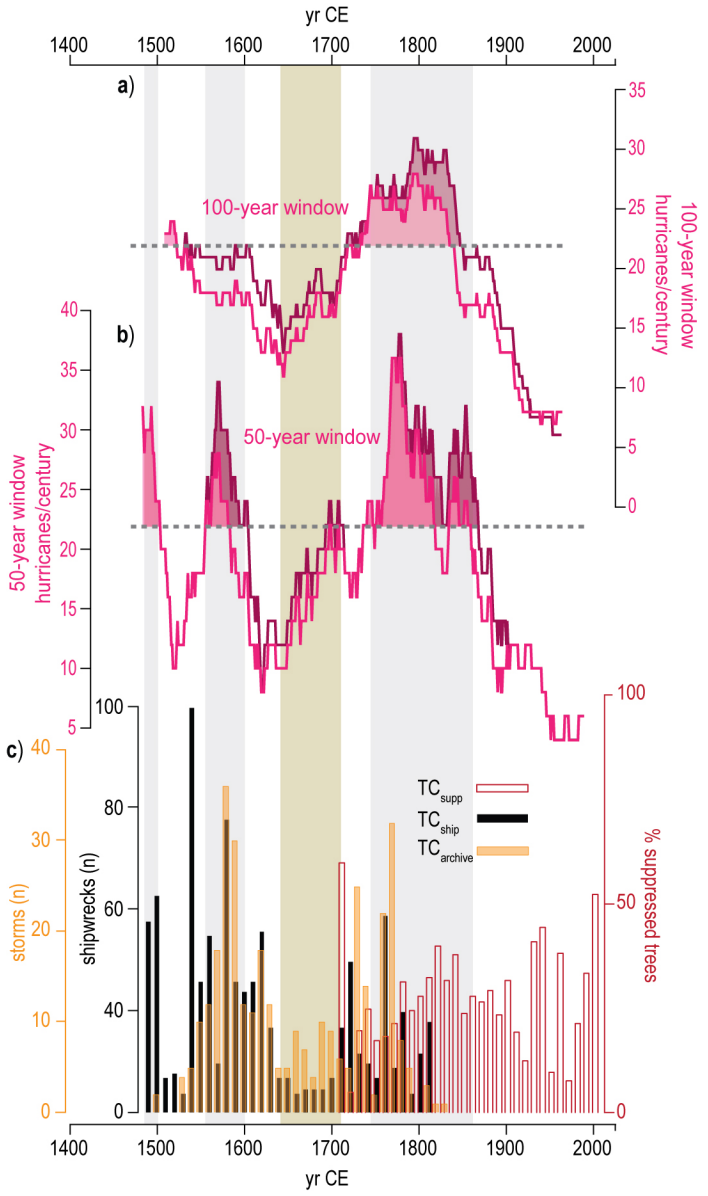

Figure 3.8. Comparison of Hine's Hole Composite to Florida Keys reconstructions. a) The 100-year and b) 50-year moving window counts of most ≥Category 1 hurricanes/century within 115 km of Hine's Hole on Cay Sal Bank (this study). c) and d) are modified from Figure 3A, B in Trouet et al. (2016), where TC_{supp} is the percentage of 38 examined south Florida slash pine (*Pinus elliottii* var. *densa*) trees whose rings record a period of suppressed growth related to hurricanes (red bars), TC_{ship} is a compilation of 657 Spanish shipwreck events in the Caribbean from 1495 to 1825 CE (black bars) based on Marx (1987), $TC_{archive}$ is a historical record of Caribbean tropical cyclones compiled from the ship log archives of the Spanish Armada (orange bars; (García-Herrera et al., 2005). Each of the datasets in c) are shown compiled into decadal bins as reported by (Trouet et al., 2016).

TC_{supp} does record spikes in hurricane activity from 1920-1940 CE, 1960-1970 CE, and 1990-2010 CE that are not detected in the 100-year or 50-year moving window counts of the Hine's Hole Composite. However, based on the attribution of hurricanes to >250 µm coarse sediment anomalies (section *5.2 Calibrating the Record to Historical Hurricanes*), up to 6 hurricanes from 1919-1940 CE could leave deposits in Hine's Hole. This suggests that the differences in the records over the last 120 years are most likely related to age model uncertainty and variability in the counting resolution of the records rather than spatial variance in hurricane frequency between the Cay Sal Bank and the Florida Keys. Winkler et al. (2020) demonstrated that the frequency of proximal ≥Category 2 hurricane passage can vary considerably over the ~200 km stretch from Hine's Hole to Big Pine Key over the last 170 years, so some variance is to be expected between these two records. That said, similarities in the (i) timing of active intervals, (ii) temporal resolution (near-annual), and (iii) record sensitivity (≥Category 1 hurricanes within 115-160 km radius) extend across the Hine's Hole Composite, Trouet et al. (2016) compiled records, and the García-Herrera et al. (2005) documentary record lend confidence to the Hine's Hole sedimentary age model. Collectively, these regional records suggest that significant multidecadal- to centennial-scale variations in hurricane frequency are archived over the last 600 years, and that these changes are temporally consistent in the region of Cay Sal Bank and the Florida Keys.

A series of near annually-resolved records of paleohurricane activity have been developed from across the eastern portion of the Bahamian Archipelago (Wallace et al., 2019, Wallace et al., Sub. March 2021, Wallace et al., 2021b, Winkler et al., 2020)

(Figs. 3.1 and 3.9). Comparisons must be tempered as the temporal length of the different sedimentary records plotted in Figure 3.9 and the individual site sensitivity of the different blue holes they come from is not constant (i.e., their individual potential to record hurricane passage). For example, Thatchpoint Blue Hole (Fig. 3.9a) is a ~700 year record from a ~2 m deep subtidal carbonate lagoon on the western margin of Great Abaco Island that records most ≥Category 2 hurricanes within 50 km and most ≥Category 4 hurricanes within 75 km (Winkler et al., 2020). The three blue holes that comprise the 1500 year-long South Andros Stack (Fig. 3.9b) are found in 0.5-1 m deep tidal inlet channels on the southern tip of Andros Island, and tend to only record ≥Category 3 hurricanes within 50 km (Wallace et al., 2019). The 1050 year Long Island Blue Hole reconstruction is from a blue hole in a 1-2 m deep subtidal lagoon on the northwest shore of Long Island in the central Bahamas (Fig. 3.9d), and is most likely to record ≥Category 3 hurricane passing within 75 km to the east or north of Long Island or ≥Category 4 hurricanes passing to the west or south (Wallace et al., 2021b). Finally, Middle Caicos Blue Hole (Fig. 3.9e) is a 1550 year record from a subtidal lagoon on the western side of Middle Caicos Island, and tends to record most ≥Category 2 hurricanes passing within 100 km to the south of the site (Wallace et al., Sub. March 2021). Despite the varying levels of consistency in the timing and magnitude of active/inactive intervals of hurricane impacts across these records, some consistent patterns between sites are beginning to emerge that are at times evident in the 550-year long Hine's Hole Composite (Fig. 3.10b).

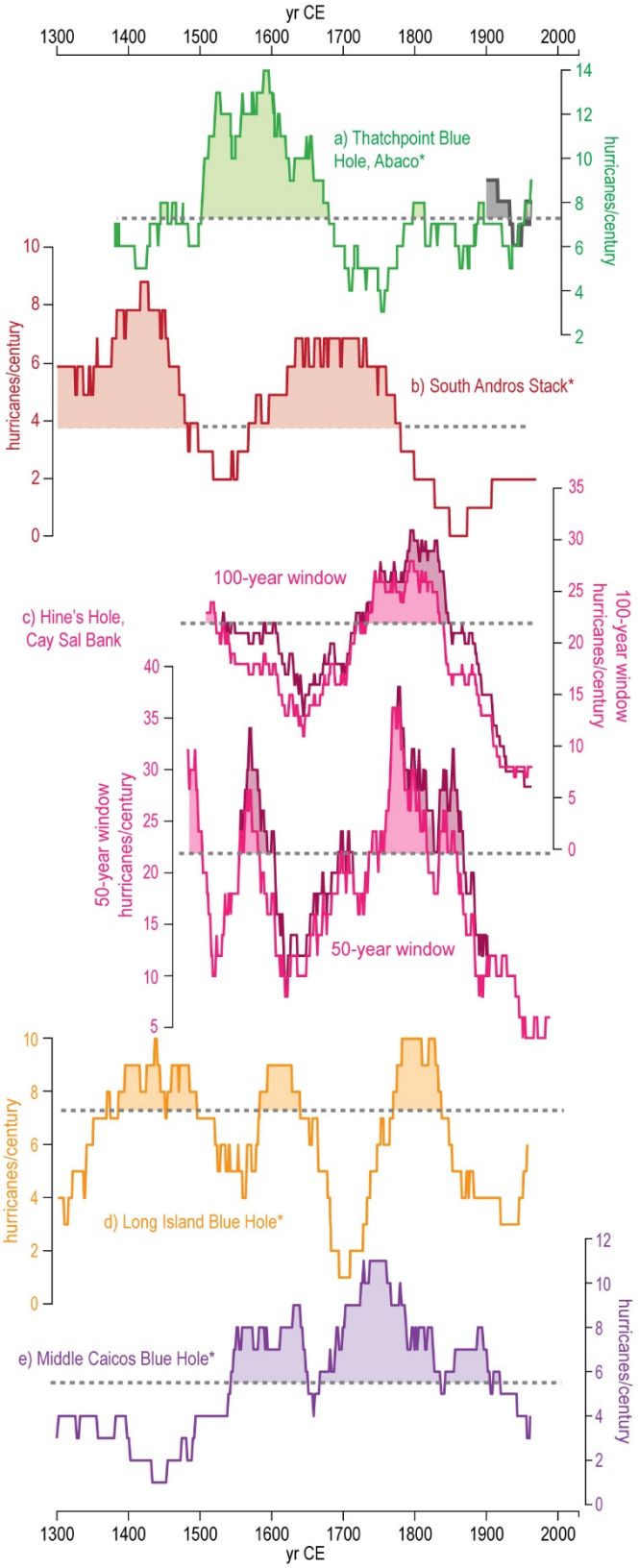

Figure 3.9. Near-annually resolved hurricane reconstructions from The Bahamas. Hurricanes/century from near annually resolved hurricane reconstructions across the Bahamian Archipelago (see Fig. 3.1 for site locations). Starting from northernmost locale: a) ≥Category 2 (3) hurricanes/century within 50 (75) km of Thatchpoint Blue Hole on Abaco Island (Winkler et al., 2020); b) ≥Category 3 hurricanes/century within 50 km of the Southern Andros region based on the stacked record of three blue hole archives (Wallace et al., 2019, Winkler et al., 2020); c) The 100-year and 50-year moving window counts of most ≥Category 1hurricanes/century within 115 km of Hine's Hole on Cay Sal Bank (this study); d) ≥Category 2 hurricanes/century within 100 km to the south of Long Island Blue Hole (Wallace et al., 2021b); and e) ≥Category2 hurricanes/century within 75 km of Middle Caicos Ocean Hole on Middle Caicos (Wallace et al., Sub. March 2021). For each reconstruction, the grey dashed line and the colored in portion above it represent the upper significance threshold for hurricane frequency used in each study.

The first statistically significant active interval in the Hine's Hole Composite is from 1485 to 1505 CE in the 50-year counts. While this active interval is only recorded for ~20 years at the base of the Hine's Hole Composite, it is unknown how far back in time it may extend. As demonstrated by Figure 3.9, it is possible that this active interval coincides with the onset of active periods observed from 1480-1510 CE in the 50-year window hurricanes/century counts from Thatchpoint Blue Hole in Abaco (Winkler et al., 2020), 1200-1480 CE in the South Andros Stack from (Wallace et al., 2019, Winkler et al., 2020), and from 1395-1500 CE in Long Island Blue Hole (Wallace et al., 2021b). The second active interval in the 50-year window counts from the Hine's Hole Composite from 1555-1605 CE occurs during the most prolonged active interval at Thatchpoint Blue Hole (1500-1655 CE), during which time the 50-year window counts from Thatchpoint Blue Hole record up to 16 hurricanes/century from 1525-1600 CE. Active intervals archived by Long Island Blue Hole from 1590-1650 CE and Middle Caicos Blue Hole (Wallace et al., Sub. March 2021) from 1550-1655 CE also partially overlap this active interval from Hine's Hole. The South Andros Stack record notably records a lull in activity from ~1500-1600 CE, making it anti-phased with the other near-annually resolved Bahamian records during this time. Notably, all of the near-annually resolved Bahamian records aside from the South Andros Stack observe 50-to-100-year period of diminished hurricane impact frequency during the activity lull from 1605-1740 CE in the Hine's Hole Composite and the historical and tree-ring compilations by Trouet et al. (2016) and García-Herrera et al. (2005).

The most prominent active interval in the Hine's Hole Composite extends from 1740-1870 CE in the 50-year window counts and an 1720-1850 CE in the 100-year window counts. During this 130-year period, brief spikes of increased activity are recorded by Thatchpoint Blue Hole from 1790-1810 CE, but hurricanes/century are otherwise relatively low. The tail end of most recent active interval in the South Andros Stack that began around 1600 CE overlaps active interval from 1720-1780 CE documented in the Hine's Hole Composite. Finally, both Long Island Blue Hole and Middle Caicos Blue Hole archive heightened hurricane activity from 1775-1845 CE and 1675-1910 CE respectively, each overlapping the majority of this Hine's Hole active interval. Interestingly, both Hine's Hole (50-year window) and Middle Caicos Blue Hole record a brief but substantial lull in activity from 1820-1840 CE that briefly drops the hurricanes/century below each record's active interval threshold. Aside from Thatchpoint Blue Hole, these records all document relatively low hurricane frequency throughout the instrumental record from 1850-2016 CE. Farther to the southeast, a 2000-year long lower-resolution sedimentary reconstruction from Scrub Island in the lesser Antilles records its most active period in hurricane strikes from 1750-1850 CE (Biguenet et al., 2021), which also indicates that the 1720-1870 CE period represents an active interval for hurricanes in the Caribbean.

Although the duration of the active intervals is never fully consistent across the five paleohurricane records in Figure 3.9, most records overlap for some portion of each of the three active intervals archived by the Hine's Hole Composite. The differences in the records is likely related to the variance in each site's recording sensitivity; however,

significant spatial gradients exist in the frequency of hurricane impacts across the Bahamian Archipelago throughout the instrumental record (Winkler et al., 2020)). For instance, islands like Great Abaco in the northern Bahamas experienced 11-16 ≥Category 2 hurricanes within 50 km since 1850 CE, whereas areas around Cay Sal Bank, Andros, and Long Island in the central Bahamas had 3 to 4 ≥Category 2 hurricanes within 50 km during the same time (Fig. 3.1b).

Analysis of over 50,000 downscaled storms from last-millennium simulations reveal that inherent stochastic variability in storm tracks alone are capable of producing significant centennial scale variability in Caribbean hurricane frequency (Wallace et al., 2021a). Therefore, caution should be exercised when using just one paleoclimate record to interpret broader regional climatic change. Motivated by this, recent studies have developed a 1500 year long near-annually resolved compilation of paleo-hurricane reconstructions from The Bahamas to develop more robust regional signals that increase probability of sampling the full scope of intra-regional spatial variations in storm tracks (Fig. 3.10b; see Wallace et al. (2021b) for detailed compilation methods and Wallace et al. (Sub. March 2021) for most recent data inclusion). This Bahamas Compilation includes all non-duplicate hurricane deposits identified from the records included for each island, which were then smoothed with a 100-year moving window. The included study sites are plotted in Figure 3.1a, and The Bahamas compilation includes all records from Figure 3.9 aside from Hine's Hole (Wallace et al., 2019, Wallace et al., Sub. March 2021, Wallace et al., 2021b, Winkler et al., 2020).

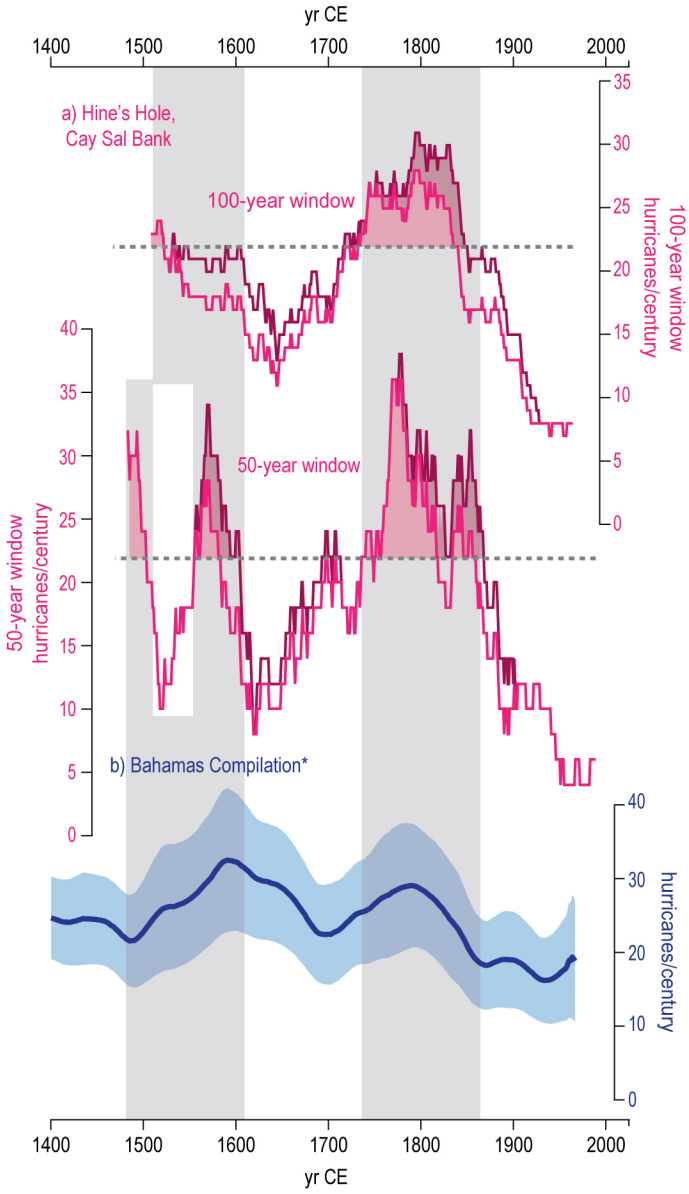

Figure 3.10. Comparison of Hine's Hole Composite to Bahamian Compilation. a) The 100-year and 50-year moving window counts of most ≥Category 1 hurricanes/century within 115 km of Hine's Hole on Cay Sal Bank (this study); b-d) Adapted from Figure 10 of Wallace et al. (Sub. March 2021). Compilations of paleohurricane records from b) the Bahamian Archipelago (all studies from Fig. 3.8 aside from Hine's Hole; blue). The compilation methods are detailed in (Wallace et al., Sub. March 2021, Wallace et al., 2021b). The shaded confidence intervals are calculated from the ages produced in Monte Carlo age-simulations run using the Bayesian age modelling program Bacon (Blaauw and Christen, 2011) for each of the contributing records. The compilations shown were smoothed with a 100-year moving window.

As seen in Figure 3.10a, b, both the 100-year and 50-year moving window hurricanes/century counts archived by the Hine's Hole Composite shows remarkable similarities to the Bahamas Compilation over the last 600 years. Aside from a lull in activity from 1505-1555 CE observe in the 50-year window counts, the Hine's Hole Composite archives evidence that regional hurricane activity was significantly higher from 1485-1605 CE and from 1720-1860 CE. The increased sampling radius and sensitivity of the Hine's Hole Composite allowed it to archive 109 potential hurricane deposits from 1450-2016 CE. During this time, the other 4 near-annually resolved Bahamian paleo-hurricane reconstructions collectively archived 134 distinct event beds (average 34 ± 10 per reconstruction) that were likely deposited by proximal ≥Category 2-3 hurricanes. Both the Hine's Hole Composite and Bahamas Compilation tend to record 10-40 hurricanes/century over the last 600 years. Of the 23 storms that passed within 115 km of Hine's Hole since 1850 CE, 9 formed in the Main Development Region in the Atlantic, 6 formed to the northeast of the Bahamian Archipelago, and 8 formed in the Southern Caribbean (APPENDIX C Fig. S3.5), meaning that the storms that are most likely to be archived in the Hine's Hole Composite are evenly distributed between the major regions of Atlantic cyclogenesis throughout the instrumental record. It is therefore possible that the wide variety of storms (i.e., point of origin, strength, track direction) and increased archival rate in the Hine's Hole Composite Record make it an exceptional record for recording broad regional trends in hurricane frequency. Regardless of the mechanisms, the Hine's Hole Composite provides substantial evidence in support of regional patterns that emerge from recent regional compilations of more

intense hurricane strikes across the Bahamian Archipelago. While the geographic area sampled by the Hine's Hole Composite is less than the cumulative scope of the Bahamas Compilation, the higher temporal resolution means it is less likely to undercount hurricanes in consecutive years as other sites in the Bahamas Compilation. Furthermore, the fact that it is a single, continuous record means that there is also less chance of overcounting duplicate storms that may have been recorded by multiple sites within the Bahamas Compilation.

3.6. Conclusions

Hine's Hole on Cay Sal Bank archives an exceptionally high-resolution record of hurricane frequency due to its high sediment accumulation rate. Cay Sal Bank is nearly fully drowned, with an average water depth of ~10 mbsl, meaning that Hine's Hole can be exposed to hurricane wind and waves regardless of passage direction and with minimal effects geomorphologic effects from other coastal and terrestrial systems. Indeed, we observe exceptional temporal correspondence of the 19 >250 μm coarse sediment anomalies in the Hine's Hole Composite from 1850-2016 CE, to the 23 ≥Category 1 hurricanes within 115 km of Hine's Hole throughout the instrumental record. Based on this modern calibration, we hypothesize that the Hine's Hole Composite archives sedimentary evidence of most ≥Category 1 hurricanes through the 550-year record In total, the Hine's Hole Composite documents 99 (conservative count) to 109 (liberal count) >250 μm coarse sediment anomalies that are interpreted as hurricane deposits between 1450 and 2016 CE, resulting in an average of 17.4 to 19.4

events/century based on 50-year sliding window counts. Only 19 >250 μm event beds were recorded from 1850 to 2016 CE, averaging to just ~10 hurricanes/century. However, up to three periods earlier in the record archive a significantly higher levels of hurricane activity: 1485 to 1505 CE (27.9 hurricanes/century ± 3.1); 1555-1605 CE (26.6 hurricanes/century ± 3.5; and 1735-1870 CE (27.8 hurricanes/century ± 4.2).

This reconstruction demonstrates further that centennial to multidecadal scale Bahamian hurricane frequency can vary significantly in response to climatic and stochastic forcing within the pre-industrial climate system (Wallace et al., 2019, Wallace et al., 2021a, Wallace et al., Sub. March 2021, Wallace et al., 2021b, Winkler et al., 2020). The most active century from 1760-1860 CE documents 29.2 hurricanes/century ± 3.7, which is ~21 hurricanes/century higher than the least active century from 1890 to 1990 CE (8.4 hurricanes/century ± 3.4), which consequently overlaps with the majority of the ~170-year instrumental record. This demonstrates that recurrence intervals based on the ~170-year instrumental record alone can severely underestimate the threat hurricanes pose certain localities. We emphasize that median-age estimates for the onset and offset of active intervals as well as the temporal extent of the record all have an average uncertainty of 33 (62) years younger (older), with an additional ± 20 years related ΔR correction uncertainties (**APPENDIX C Section S3.4**). However, these active periods are synchronous with frequent hurricane impacts documented by a high-resolution tree ring reconstruction in the Florida Keys (Trouet et al., 2016). The Hine's Hole Composite record further documents the substantial intra-island spatial heterogeneity in hurricane frequency across the Bahamian Archipelago that is observed

in instrumental and paleo-hurricane records (Wallace et al., 2019, Wallace et al., Sub. March 2021, Wallace et al., 2021b, Winkler et al., 2020). However, events/century derived from the 50-yr counts of the Hine's Hole Composite show strong correspondence with a regional compilation of 4 near-annually resolved reconstructions from across the Bahamian Archipelago (Wallace et al., Sub. March 2021, Wallace et al., 2021b), particularly with regard to decreasing hurricane frequency from 1850 CE to present, and heightened frequency from 1550-1650 CE and 1725-1825 CE. Given that only 18 m of the at least 60 m of accumulation in Hine's Hole is presented here, this site offers unprecedented potential for developing a near-annually resolved record of multidecadal hurricane frequency variability throughout the last 2000 years.

3.7. References

ARCOS, N., CHACON-BARRANTES, S., VARNER, J. & LOPEZ, A. 2018. Caribbean and Adjacent Regions Tsunami Sources and Models (CATSAM) Map Viewer.

ASHMORE, S. & LEATHERMAN, S. P. 1984. Holocene sedimentation in Port Royal Bay, Bermuda. *Marine geology,* 56**,** 289-298.

BARKAN, R., URI, S. & LIN, J. 2009. Far field tsunami simulations of the 1755 Lisbon earthquake: Implications for tsunami hazard to the US East Coast and the Caribbean. *Marine Geology,* 264**,** 109-122.

BIGUENET, M., SABATIER, P., CHAUMILLON, E., CHAGUÉ, C., ARNAUD, F., JORISSEN, F., COULOMBIER, T., GEBA, E., CORDRIE, L. & VACHER, P. 2021. A 1600 year-long sedimentary record of tsunamis and hurricanes in the Lesser Antilles (Scrub Island, Anguilla). *Sedimentary Geology,* 412**,** 105806.

BLAAUW, M. & CHRISTEN, A. 2011. Flexible paleoclimate age-depth models using an autoregressive gamma process. *Bayesian Analysis,* 6**,** 457-474.

BRANDON, C. M., WOODRUFF, J. D., LANE, P. & DONNELLY, J. P. 2013. Constraining flooding conditions for prehistoric hurricanes from resultant

deposits preserved in Florida sinkholes. *Geochemistry Geophysics Geosystems,* 14**,** 2993-3008.

BREGY, J. C., WALLACE, D. J., MINZONI, R. T. & CRUZ, V. J. 2018. 2500-year paleotempestological record of intense storms for the northern Gulf of Mexico, United States. *Marine Geology,* 396**,** 26-42.

BROECKER, W. S. & OLSON, E. A. 1961. Lamont radiocarbon measurements VIII. *Radiocarbon,* 3**,** 176-204.

CHAVAS, D. R., LIN, N., DONG, W. & LIN, Y. 2016. Observed tropical cyclone size revisited. *Journal of Climate,* 29**,** 2923-2939.

CHENOWETH, M. & DIVINE, D. 2008. A document-based 318-year record of tropical cyclones in the Lesser Antilles, 1690–2007. *Geochemistry, Geophysics, Geosystems,* 9.

DAVENPORT, F. V., BURKE, M. & DIFFENBAUGH, N. S. 2021. Contribution of historical precipitation change to US flood damages. *Proceedings of the National Academy of Sciences,* 118.

DENOMEE, K. C., BENTLEY, S. J. & DROXLER, A. W. 2014. Climatic control on hurricane patterns: a 1200-y near-annual record from Lighthouse Reef, Belize. *Scientific Reports,* 4**,** 7.

DIAZ, M., MACARIO, K., GOMES, P., ÁLVAREZ-LAJONCHERE, L., AGUILERA, O. & ALVES, E. 2017. Radiocarbon marine reservoir effect on the northwestern coast of Cuba. *Radiocarbon,* 59**,** 333.

DINAPOLI, R. J., FITZPATRICK, S. M., NAPOLITANO, M. F., RICK, T. C., STONE, J. H. & JEW, N. P. 2021. Marine reservoir corrections for the Caribbean demonstrate high intra-and inter-island variability in local reservoir offsets. *Quaternary Geochronology,* 61**,** 101126.

DONNELLY, J. P. 2016. *RE: Observations from HOV Nadir Submersible Dive in Hine's Hole on Cay Sal Bank.*

DONNELLY, J. P., HAWKES, A. D., LANE, P., MACDONALD, D., SHUMAN, B. N., TOOMEY, M. R., VAN HENGSTUM, P. J. & WOODRUFF, J. D. 2015. Climate forcing of unprecedented intense-hurricane activity in the last 2000 years. *Earth's Future,* 3**,** 49-65.

DONNELLY, J. P. & WOODRUFF, J. D. 2007. Intense hurricane activity over the past 5,000 years controlled by El Niño and the West African Monsoon. *Nature,* 447**,** 465-468.

DRUFFEL, E. M. & LINICK, T. W. 1978. Radiocarbon in annual coral rings of Florida. *Geophysical Research Letters,* 5**,** 913-916.

DRUFFEL, E. R. 1997. Pulses of rapid ventilation in the North Atlantic surface ocean during the past century. *Science,* 275**,** 1454-1457.

EMANUEL, K., SUNDARARAJAN, R. & WILLIAMS, J. 2008. Hurricanes and global warming: results from downscaling IPCC AR4 simulations. *Bulletin of the American Meterorological Society,* 89**,** 347-367.

EMANUEL, K. A. 2013. Downscaling CMIP5 climate models shows increased tropical cyclone activity over the 21st century. *Proceedings of the National Academy of Sciences of the United States of America,* 110**,** 12219-12224.

GARCÍA-HERRERA, R., GIMENO, L., RIBERA, P. & HERNÁNDEZ, E. 2005. New records of Atlantic hurricanes from Spanish documentary sources. *Journal of Geophysical Research,* 110**,** 7 p.

GISCHLER, E., SHINN, E. A., OSCHMANN, W., FIEBIG, J. & BUSTER, N. A. 2008. A 1500-year Holocene Caribbean climate archive from the Blue Hole, Lighthouse Reef, Belize. *Journal of Coastal Resarch,* 24**,** 1495-1505.

GOLDBERG, W. M. 1983. Cay Sal Bank, Bahamas: a biologically impoverished, physically controlled environment. *Atoll Research Bulletin*.

HADDEN, C. S. & SCHWADRON, M. 2019. Marine reservoir effects in eastern oyster (Crassostrea virginica) from southwestern Florida, USA. *Radiocarbon,* 61**,** 1501-1510.

HEATON, T. J., KÖHLER, P., BUTZIN, M., BARD, E., REIMER, R. W., AUSTIN, W. E., RAMSEY, C. B., GROOTES, P. M., HUGHEN, K. A. & KROMER, B. 2020. Marine20—the marine radiocarbon age calibration curve (0–55,000 cal BP). *Radiocarbon***,** 1-42.

HINE, A. C. & STEINMETZ, J. C. 1984. Cal Sal Bank, Bahamas: A partially drowned carbonate platform. *Marine Geology,* 59**,** 135-164.

KHAN, N. S., ASHE, E., HORTON, B. P., DUTTON, A., KOPP, R. E., BROCARD, G., ENGELHART, S. E., HILL, D. F., PELTIER, W. & VANE, C. H. 2017.

Drivers of Holocene sea-level change in the Caribbean. *Quaternary Science Reviews,* 155**,** 13-36.

KNAPP, K. R., DIAMOND, H. J., KOSSIN, J. P., KRUK, M. C. & SCHRECK, C. J. 2018. International Best Track Archive for Climate Stewardship (IBTrACS) Project, Version 4, [North Atlantic Subset]. *In:* INFORMATION, N. N. C. F. E. (ed.).

KNAPP, K. R., KRUK, M. C., LEVINSON, D. H., DIAMOND, H. J. & NEUMANN, C. J. 2010. The international best track archive for climate stewardship (IBTrACS) unifying tropical cyclone data. *Bulletin of the American Meteorological Society,* 91**,** 363-376.

KNUTSON, T., CAMARGO, S. J., CHAN, J. C., EMANUEL, K., HO, C.-H., KOSSIN, J., MOHAPATRA, M., SATOH, M., SUGI, M. & WALSH, K. 2020. Tropical cyclones and climate change assessment: Part II. Projected response to anthropogenic warming. *Bulletin of the American Meteorological Society*.

KONDO, Y. 847. BURROWING DEPTH OF INFAUNAL BIVALVES: OBSERVATION OF LIVING SPECIES AND ITS RELATION TO SHELL MORPHOLOGY. Transactions and proceedings of the Paleontological Society of Japan. New series, 1987. Palaeontological Society of Japan, 306-323.

KORTY, R. L., EMANUEL, K. A., HUBER, M. & ZAMORA, R. A. 2017. Tropical cyclones downscaled from simulations with very high carbon dioxide levels. *Journal of Climate,* 30**,** 649-667.

KOSSIN, J. P. 2018. A global slowdown of tropical-cyclone translation speed. *Nature,* 558**,** 104-107.

KOURAFALOU, V. H. & KANG, H. 2012. Florida Current meandering and evolution of cyclonic eddies along the Florida Keys Reef Tract: Are they interconnected? *Journal of Geophysical Research: Oceans,* 117.

LANDSEA, C. W., HARPER, B. A., HOARAU, K. & KNAFF, J. A. 2006. Can we detect trends in extreme tropical cyclones? *Science,* 313**,** 452-454.

LANE, P., DONNELLY, J. P., WOODRUFF, J. D. & HAWKES, A. D. 2011. A decadally-resolved paleohurricane record archived in the late Holocene sediments of a Florida sinkhole. *Marine Geology,* 287**,** 14-30.

LIGHTY, R. G., MACINTYRE, I. G. & STUCKENRATH, R. 1982. Acropora palmata reef framework: a reliable indicator of sea level in the western Atlantic for the past 10,000 years. *Coral reefs,* 1**,** 125-130.

LIN, Y., ZHAO, M. & ZHANG, M. 2015. Tropical cyclone rainfall area controlled by relative sea surface temperature. *Nature Communications,* 6**,** 6591.

LIU, K.-B. & FEARN, M. L. 1993. Lake-sediment record of late Holocene hurricane activities from coastal Alabama. *Geology,* 21**,** 793-796.

LIU, K. & FEARN, M. L. 2000. Reconstruction of prehistoric landfall frequencies of catastrophic hurricanes in NW Florida from lake sediment records. *Quaternary Research,* 52**,** 238-245.

MALLINSON, D. J., SMITH, C. W., MAHAN, S., CULVER, S. J. & MCDOWELL, K. 2011. Barrier island response to late Holocene climate events, North Carolina, USA. *Quaternary Research,* 76**,** 46-57.

MARX, R. F. 1987. *Shipwrecks in the Americas*, Courier Corporation.

MCADIE, C., LANDSEA, C., NEUMANN, C. J., DAVID, J. E. & BLAKE, E. S. 2009. *Tropical Cyclones of the North Atlantic Ocean, 1851-2006: With 2007 and 2008 Track Maps Included*, US Department of Commerce, National Oceanic and Atmospheric Administration.

MILLER, K. G., KOPP, R. E., HORTON, B. P., BROWNING, J. V. & KEMP, A. C. 2013. A geological perspective on sea-level rise and its impacts along the US mid-Atlantic coast. *Earth's Future,* 1**,** 3-18.

OLIVA, F., PEROS, M., VIAU, A., REINHARDT, E., NIXON, F. & MORIN, A. 2018. A multi-proxy reconstruction of tropical cyclone variability during the past 800 years from Robinson Lake, Nova Scotia, Canada. *Marine Geology,* 406**,** 84-97.

OPPENHEIMER, M. & HINKEL, J. 2019. Sea Level Rise and Implications for Low Lying Islands, Coasts and Communities Supplementary Material. *IPCC special report on the ocean and cryosphere in a changing climate*.

PARSONS, T. & GEIST, E. L. 2008. Tsunami probability in the Caribbean region. *Tsunami Science Four Years after the 2004 Indian Ocean Tsunami.* Springer.

PATRICOLA, C. M. & WEHNER, M. F. 2018. Anthropogenic influences on major tropical cyclone events. *Nature,* 563**,** 339-346.

PIELKE JR., R. A., GRATZ, J., LANDSEA, C. W., COLLINS, D., SAUNDERS, M. A. & MUSULIN, R. 2008. Normalized hurricane damage in the United States: 1900-2005. *Natural Hazards Review,* 9**,** 29-42.

PURKIS, S., KERR, J., DEMPSEY, A., CALHOUN, A., METSAMAA, L., RIEGL, B., KOURAFALOU, V., BRUCKNER, A. & RENAUD, P. 2014. Large-scale carbonate platform development of Cay Sal Bank, Bahamas, and implications for associated reef geomorphology. *Geomorphology,* 222**,** 25-38.

RASMUSSEN, K. A., HADDAD, R. I. & NEUMANN, A. C. 1990. Stable-isotope record of organic carbon from an evolving carbonate banktop, Bight of Abaco, Bahamas. *Geology,* 18**,** 790-794.

REIMER, P. J., AUSTIN, W. E., BARD, E., BAYLISS, A., BLACKWELL, P. G., RAMSEY, C. B., BUTZIN, M., CHENG, H., EDWARDS, R. L. & FRIEDRICH, M. 2020. The IntCal20 Northern Hemisphere radiocarbon age calibration curve (0–55 cal kBP). *Radiocarbon***,** 1-33.

REIMER, P. J., BROWN, T. A. & REIMER, R. W. 2004. Discussion: reporting and calibration of post-bomb 14C data. *Radiocarbon,* 46**,** 1299-1304.

SCHMITT, D., GISCHLER, E., ANSELMETTI, F. S. & VOGEL, H. 2020. Caribbean cyclone activity: an annually-resolved Common Era record. *Scientific reports,* 10**,** 1-17.

SMITH, A. B. 2020. U.S. Billion-dollar Weather and Climate Disasters, 1980 - present. *In:* INFORMATION, N. N. C. F. E. (ed.).

SOBEL, A. H., CAMARGO, S. J., HALL, T. M., LEE, C.-Y., TIPPETT, M. K. & WING, A. A. 2016. Human influence on tropical cyclone intensity. *Science,* 353**,** 242-246.

TOTH, L. T., CHENG, H., EDWARDS, R. L., ASHE, E. & RICHEY, J. N. 2017. Millennial-scale variability in the local radiocarbon reservoir age of south Florida during the Holocene. *Quaternary Geochronology,* 42**,** 130-143.

TROUET, V., HARLEY, G. L. & DOMÍNGUEZ-DELMÁS, M. 2016. Shipwreck rates reveal Caribbean tropical cyclone response to past radiative forcing. *Proceedings of the National Academy of Sciences,* 113**,** 3169-3174.

TUKEY, J. W. 1977. *Exploratory data analysis*, Reading, Mass.

ULM, K. 1990. Simple method to calculate the confidence interval of a standardized mortality ratio (SMR). *American journal of epidemiology,* 131**,** 373-375.

VACCHI, M., ENGELHART, S. E., NIKITINA, D., ASHE, E. L., PELTIER, W. R., ROY, K., KOPP, R. E. & HORTON, B. P. 2018. Postglacial relative sea-level histories along the eastern Canadian coastline. *Quaternary Science Reviews,* 201**,** 124-146.

VAN HENGSTUM, P. J., DONNELLY, J. P., FALL, P. L., TOOMEY, M. R., ALBURY, N. A. & KAKUK, B. 2016. The intertropical convergence zone modulates intense hurricane strikes on the western North Atlantic margin. *Scientific reports,* 6.

VECCHI, G. A. & KNUTSON, T. R. 2011. Estimating annual numbers of Atlantic hurricanes missing from the HURDAT database (1878–1965) using ship track density. *Journal of Climate,* 24**,** 1736-1746.

WALLACE, E., DONNELLY, J., VAN HENGSTUM, P., WIMAN, C., SULLIVAN, R., WINKLER, T., D'ENTREMONT, N., TOOMEY, M. & ALBURY, N. 2019. Intense hurricane activity over the past 1500 years at South Andros Island, The Bahamas. *Paleoceanography and Paleoclimatology,* 34.

WALLACE, E. J., COATS, S., EMANUEL, K. & DONNELLY, J. P. 2021a. Centennial-scale shifts in storm frequency captured in paleohurricane records from The Bahamas arise predominantly from random variability. *Geophysical Research Letters,* 48**,** e2020GL091145.

WALLACE, E. J., DONNELLY, J. P., VAN HENGSTUM, P. J., WINKLER, T. S., DIZON, C., LABELLA, A., LOPEZ, I., D'ENTREMONT, N. E., SULLIVAN, R. M., WOODRUFF, J. D., HAWKES, A. D. & MAIO, C. Sub. March 2021. Regional shifts in paleohurricane activity over the last 1500 years derived from blue hole sediments offshore of Middle Caicos Island. *Quaternary Science Reviews*.

WALLACE, E. J., DONNELLY, J. P., VAN HENGSTUM, P. J., WINKLER, T. S., MCKEON, K., MACDONALD, D., D'ENTREMONT, N. E., SULLIVAN, R. M., WOODRUFF, J. D., HAWKES, A. D. & MAIO, C. 2021b. 1050 years of hurricane strikes on Long Island in The Bahamas. *Paleoceanography and Paleoclimatology,* 36**,** e2020PA004156.

WALSH, K. J., CAMARGO, S. J., VECCHI, G. A., DALOZ, A. S., ELSNER, J., EMANUEL, K., HORN, M., LIM, Y.-K., ROBERTS, M. & PATRICOLA, C.

2015. Hurricanes and climate: the US CLIVAR working group on hurricanes. *Bulletin of the American Meteorological Society,* 96**,** 997-1017.

WALSH, K. J., MCBRIDE, J. L., KLOTZBACH, P. J., BALACHANDRAN, S., CAMARGO, S. J., HOLLAND, G., KNUTSON, T. R., KOSSIN, J. P., LEE, T. C. & SOBEL, A. 2016. Tropical cyclones and climate change. *Wiley Interdisciplinary Reviews: Climate Change,* 7**,** 65-89.

WINKLER, T. S., VAN HENGSTUM, P. J., DONNELLY, J. P., WALLACE, E. J., SULLIVAN, R. M., MACDONALD, D. & ALBURY, N. A. 2020. Revising evidence of hurricane strikes on Abaco Island (The Bahamas) over the last 700 years. *Scientific Reports,* 10**,** 1-17.

WONG, P. P., LOSADA, I. J., GATTUSO, J., HINKEL, J., KHATTABI, A., MCINNES, K., SAITO, Y. & SALLENGER, A. 2014. Coastal systems and low-lying areas. *Climate Change***,** 361-409.

WOODRUFF, J. D., DONNELLY, J. P., EMANUEL, K. & LANE, P. 2008. Assessing sedimentary records of paleohurricane activity using modeled hurricane climatology. *Geochemistry, Geophysics, Geosystems,* 9.

WOODRUFF, J. D., IRISH, J. L. & CAMARGO, S. J. 2013. Coastal flooding by tropical cyclones and sea-level rise. *Nature,* 504**,** 44.

YANG, Y., MASELLI, V., NORMANDEAU, A., PIPER, D. J., LI, M. Z., CAMPBELL, D. C., GREGORY, T. & GAO, S. 2020. Latitudinal response of storm activity to abrupt climate change during the last 6,500 years. *Geophysical Research Letters,* 47**,** e2020GL089859.

4. ELEVATED HURRICANE ACTIVITY DURING THE LITTLE ICE AGE

4.1. Introduction

From 1980 to 2020 CE, hurricanes have cost the United States alone an average ~24.6B USD per year (Smith, 2020), with a similar global average of ~$26B USD per year (Mendelsohn et al., 2012). While these numbers are alarming, they fail to demonstrate the disproportional devastation that extreme weather events have on Small Island Developing States, where lower infrastructure and population densities generally result in less perceived financial impact. For example, in 2019, Hurricane Dorian swept across Abaco Island and Grand Bahama at Category 5 strength (sustained winds up to 296 km/hr), killing at least 70 individuals and leaving 282 missing. Dorian caused $3.4B USD in damages, which is equivalent to a quarter of The Bahamas annual Gross Domestic Product (Zegarra et al., 2020). While Caribbean Small Island Developing States only produce <0.4% of global carbon emissions (Shultz et al., 2020), they will likely experience disproportionally severe coastal flooding from hurricanes due to sea-level rise driven by anthropogenic climate change (Woodruff et al., 2013, Pielke Jr et al., 2008). With up to 1 m projected global mean sea-level rise by 2100 CE (Oppenheimer and Hinkel, 2019), The Bahamas may lose up to 11.57% of its total land area which is the highest percentage worldwide (Dasgupta et al., 2009). This means that even weaker hurricanes could produce Dorian level flooding in The Bahamas.

As reviewed by Knutson et al. (2020), Hurricanes are projected to increase in: (i) intensity (Bhatia et al., 2018, Villarini and Vecchi, 2013, Emanuel et al., 2008, Sobel et al., 2016), (ii) delivered precipitation volume (Patricola and Wehner, 2018), and (iii)

storm diameter and rainfall area (Chavas et al., 2016, Lin et al., 2015) in response to anthropogenic climate change throughout the 21st Century. These factors coupled with an observed reduction in hurricane translation speed since 1949 CE will enhance landscape flooding from surge and rainfall globally (Kossin, 2018). However, it remains poorly understood how hurricanes will change at a regional level, especially given the high level of spatial heterogeneity observed in hurricane frequency over the last ~170 years (Fig. 4.1a; Winkler et al., 2020). To anticipate the threat posed by future hurricanes, it is vital to determine the upper limits of long-term hurricane recurrence intervals in The Bahamas, as well as how regional hurricane frequency has been modulated by local and remote ocean/climate variability. Problematically, the instrumental record of hurricane activity compiled by the International Best Track Archive for Climate Stewardship database (IBTrACS; Knapp et al., 2018, Knapp et al., 2010) only extends ~170-years back to 1850 CE. Instrumental hurricane activity records are generally reliable following widespread implementation of satellite observation in the 1960 CE, but measurements of storm conditions (e.g., wind velocity, internal pressure) and even the hurricane tracks themselves are much less complete prior to the use of air-craft monitoring in the 1940s (Vecchi and Knutson, 2011, Landsea and Franklin, 2013, Villarini et al., 2011, McAdie et al., 2009).

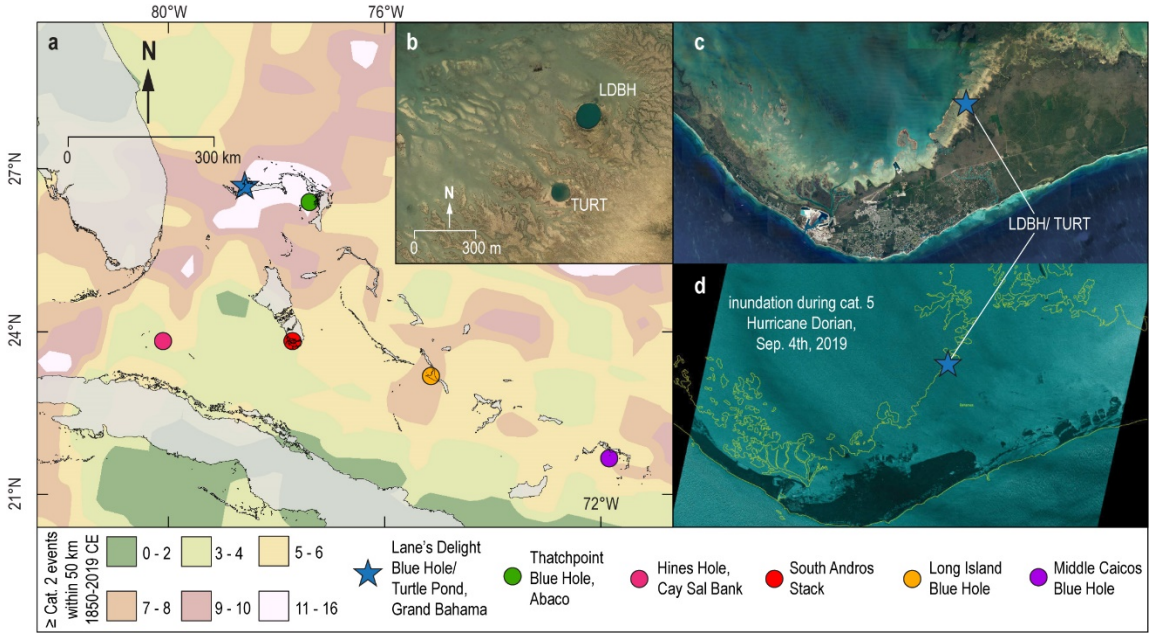

Figure 4.1. (a) Map of ≥Category 2 hurricane frequency within a 50 km radius from 1850 to 2019 CE using storm track and intensity data is from the International Best Track Archive for Climate Stewardship (IBTrACS) v041,2 dataset (map modified from Fig. 1 in Winkler et al. (2020)).
The blue star is the location of Lane's Delight Blue Hole (LDBH) and Turtle Pond (TURT) on Grand Bahama Island in the northern Atlantic, and the colored circles are the locations of high-resolution hurricane reconstructions from the Bahamian Archipelago (colors correspond to Fig. 4.8). Modern hurricane hotspots are pinkish-white in color (11-16 ≥category 2 events within 50 km), and point symbology matches panel a. Basemaps were downloaded from *DIVA-GIS* [73]. (b) *GoogleEarth LandSat* imagery of LDBH and TURT on the northern flank of Grand Bahama. Satellite imagery of Grand Bahama (c) before *[GoogleEarth LandSat]* and (d) during the landfall of category 5 Huricane Dorian on September 4, 2019 *[SAR imaging from ICEYE]*.

Records of Atlantic hurricane impacts have been extended back in time using historical archives (Chenoweth and Divine, 2008, García-Herrera et al., 2005, Trouet et al., 2016) and proxy based reconstructions from the Northeastern Atlantic (Boldt et al., 2010, Brandon et al., 2014, Donnelly et al., 2015, Yang et al., 2020, Mallinson et al., 2011, Castagno et al., 2021, Donnelly et al., 2001a, Donnelly et al., 2001b), the Gulf of Mexico (Brandon et al., 2013, Bregy et al., 2018, Liu and Fearn, 2000, Liu and Fearn,

1993, Rodysill et al., 2020, Toomey et al., 2017, Lane et al., 2011), Yucatan Peninsula (Baldini et al., 2016, Denomee et al., 2014, Gischler et al., 2013, Schmitt et al., 2020, McCloskey and Liu, 2012), and eastern subtropical North Atlantic (Biguenet et al., 2021, Toomey et al., 2013, van Hengstum et al., 2016). However, large gaps remain in spatial coverage across the Atlantic given that most regions lack enough reconstructions to assess record reproducibility. Further, most of these archives only document intense hurricanes (≥Category 3) that pass proximally to the study area, and generally lack the temporal resolution to assess changes in hurricane impacts at a sub-centennial scale.

Shinn et al. (1996) identified the potential for inundated sinkholes known as blue holes to function as natural sediment traps, noting background sedimentation of fine grained aragonitic mud interrupted by skeletal carbonate sand deposited by hurricanes. Since then, Common Era (CE) hurricane activity has been reconstructed at near annual-resolution using sediment core from Lighthouse Blue Hole in Belize (Denomee et al., 2014, Gischler et al., 2013, Schmitt et al., 2020) and a transect of blue holes across the Bahamian Archipelago (Fig. 4.1a; Wallace et al., 2019, Wallace et al., Sub. March 2021, Winkler et al., 2020, Wallace et al., 2021b, Winkler et al., Submitted 2021). These Bahamian records all have nearly linear sedimentation rates of 1-3 cm/yr, and all accumulate carbonate mud during quiescent conditions that is interrupted by coarser sand layers that coincide with known hurricanes since 1850 CE. However, the timing and magnitude of centennial scale hurricane impact frequency archived by each reconstruction demonstrate varying levels of coherence. This suggests that the substantial spatial heterogeneity in hurricane impact frequency since 1850 CE (Fig. 4.1a)

persists in some capacity over the last 1500 years. Based on the methods of Mann et al. (2009a), these high-resolution Bahamian records were statistically synthesized to produce 1500-year long compilation that affords a synoptic understanding of centennial scale variability in regional hurricane activity (Wallace et al., Sub. March 2021, Wallace et al., 2021b). Problematically, this compilation only includes one relatively short record from the northern Bahamas (Thatchpoint Blue Hole-TPBH, Abaco; Winkler et al., 2020) that spans ~700 years. The northern Bahamas has one of the highest rates of hurricane activity of any area in the North Atlantic over the last 170 years, and also experienced periods of elevated hurricane frequency that were coeval with reconstructed activity along the US Eastern Seaboard over the last 700 years (Winkler et al., 2020). As such, it is vital that additional, temporally longer near-annually resolved hurricane reconstructions are included in the Bahamian Compilation to ensure that this record truly depicts a regional signal.

Here we present two near annually resolved paleo-hurricane reconstructions developed using sediment cores collected from two blue holes on the northern shoreline of Grand Bahama. These records combine to produce a coherent 1700-year record that documents four regionally significant periods of heightened hurricane activity from 1825-1925 CE, 1560-1600 CE, 1300-1450 CE, and 420-560 CE. This record fills spatial and temporal gaps in the existing Bahamian Compilation of regional paleo-hurricane frequency (Wallace et al., Sub. March 2021, Wallace et al., 2021b). The two new Bahamian compilations presented here clearly reveal that the northern Caribbean experienced heightened hurricane activity throughout most of the Little Ice Age (LIA)

from ~1300 to 1850 CE (Mann et al., 2009b, Miller et al., 2012, Mann, 2002), with 8.6 ± 3 more hurricanes/century than the other 1000-years (550-1349 CE, 1851-1969 CE). A compilation of paleohurricane records from New England (Wallace et al., Sub. March 2021) as well as lower resolution records of hurricane activity from the U.S. East Coast (Donnelly et al., 2015, Mallinson et al., 2011) and northern Bahamas (Trouet et al., 2016) also suggest a spike in regional hurricane impacts during the LIA. While inherent stochastic variability in hurricane tracks and development can limit the ability of a single record to reflect a regional signal (Wallace et al., 2021a), we now have overwhelming evidence that hurricane frequency was higher across the Bahamian Archipelago during the LIA. While uncertainty remains regarding the precise climate mechanisms that caused this rise in frequency during the LIA, The Bahamas has evidently experienced significantly higher hurricane frequency than relative to observations since 1850 CE.

4.2. Regional Setting and Study Site

Lane's Delight Blue Hole (LDBH; 26.661°N, -78.59°) and Turtle Pond (TURT; 26.658°N, -78.592°W) are located on the northern shore of Grand Bahama, The Bahamas where they are surrounded by carbonate tidal flats (Fig. 4.1). Grand Bahama forms the western portion of the Little Bahama Bank carbonate platform, which likely began accumulating in the Jurassic Period (Mullins and Lynts, 1977). LDBH is 120 m wide and has a depth of ~30 meters below sea level (mbsl, Fig. 4.2), whereas TURT, located ~300 m to the southwest, is 90 m wide and with a depth of ~4 mbsl. Both blue holes are surrounded by a mangroves colonized supratidal periphery that is stabilized by

outcropping limestone along the inland southern rim (Fig. 4.1b, 4.2a). Daily tidal range in this area of The Bahamas is relatively low (<1 m) and tidal flow velocity is restricted by gradually shallowing bank slopes and abundant tidal channels (Rankey et al., 2006).

Based on a qualitative survey of the environment around LDBH and TURT, sediments on the carbonate tidal flats are primarily inorganic calcite and aragonite mud, fragmented organic matter (OM) from surrounding mangroves, and coarser sediment (>63 μm) that is primarily skeletal material and peloids. These lithofacies are consistent with similar environments in Andros (Shinn et al., 1969, Milliman et al., 1993, Maloof and Grotzinger, 2012, Rankey et al., 2004, Rankey, 2002), Crooked Island (Berkeley and Rankey, 2012), and Turks & Caicos (Trower et al., 2019, Wanless et al., 1988b, Trower et al., 2018, Wanless et al., 1988a, Kaczmarek and Hasiuk, 2008, Tedesco and Aller, 1997) and marine carbonate stratigraphy in blue holes surrounded by carbonate tidal flats over the last ~2300 in Abaco (van Hengstum et al., 2020) and South Andros (Wallace et al., 2019). Holocene sediment accumulation on Bahamian carbonate tidal flats is typically <2 m of aragonitic mud that is produced by calcareous green algae such as *Halimeda*, *Penicillus*, and *Udotea* around the bank margin before being transported shoreward by wind and tide driven currents (Maloof and Grotzinger, 2012, Stockman et al., 1967). During stronger storms, these fine-grained sediments are resuspended and swept of the bank top where they are later deposited as periplatform carbonate ooze (Neumann and Land, 1975, Boardman and Neumann, 1984) and contribute ~86% of the fine-grained carbonates found off the northern windward margin of the Little Bahama Bank to the north of LDBH and TURT (Heath and Mullins, 1984). Simultaneously,

coarse-sediment washover fans associated with hurricane surge have been found to extend over the flooding zone in tidal flats (Wanless et al., 1988b). In deeper marine areas near the open ocean, the base of these fans are thick skeletal-peloidal grainstones with a landward fining trend towards peloidal packstones (Wanless et al., 1988b). Topographic lows and *Calliannassa* shrimp burrows act as natural sediment traps that tend to preferentially infill with the coarser sediments (Wanless et al., 1988a).

While storm induced sediment deposits on the carbonate tidal flat surface are frequently reworked, it has been hypothesized that the coarser skeletal grains and peloids observed at the base of modern storm event beds are also deposited into blue holes where they preserve a sedimentary marker of the passage of a specific storm (Wallace et al., 2019, Wallace et al., Sub. March 2021, Wallace et al., 2021b, Winkler et al., 2020, van Hengstum et al., 2014). When Hurricane Dorian passed to the north of Grand Bahama, it inundated much of the northern island with 2-4 m of storm surge (Fig. 4.1d). Dahlgren and Sherman (2020) found that many coral beds north of LDBH and TURT had been buried by silt from the tidal flats during Hurricane Dorian. Further, post Dorian satellite imagery accessed with *Google Earth* shows substantial redistribution of sediment across northern Grand Bahama, so it is likely that sediment was transported into and around LDBH and TURT.

4.3. Methods

4.3.1. Field Methods

A subbottom seismic survey in LDBH was completed with a EdgeTech 3100 Chirp sub-bottom sonar system towed while sweeping at a 4-24 kHz bandwidth (Fig. 4.2a, b). A YSI EXO1 sonde was lowered at 1 cm/second to measure temperature (±0.01 °C), salinity (±0.1 Practical Salinity Units-PSU), dissolved oxygen (±0.01 mg/L), and pH (±0.01 pH units) twice per second (Fig. 4.2c). Sediment cores (7.5 cm diameter) were collected from LDBH in April 2016 using a Rossfelder-P3 submersible vibracorer on the *R/V Arenaria*, with core lengths and locations in APPENDIX D Table S4.1. LDBH-D1 was collected in a 2.4 m long clear polycarbonate barrel to carefully curate the sediment water interface. LDBH-D4 was collected on a drive that penetrated ~14 m into the subsurface, but only 1026 cm was recovered following compaction and potential rodding/sediment loss. Based on visual stratigraphic correlation to LDBH-D1 and LDBH-D3, it is likely that the base of the pipe pushed through the upper 1-2 m of less consolidated stratigraphy in LDBH (Fig. 4.2b) before sediment sampling started (i.e., rodding). In TURT, a single core was collected using a rod driven vibracoring system from the *R/V Arenaria*. Once collected, sediment water interfaces were curated using floral foam and 3 mm diameter holes were drilled ~1.45 m long increments down the core pipe to release interstitial hydrogen-sulfide gas. Following 24 hours of gas release, each core was cut into ~1.45 m sections for transport and cold storage.

4.3.2. Sediment Textural Analysis

In the laboratory, core sections were split lengthwise, photographed, described, and imaged with x-radiography. Cores were wrapped in a thin sheet of polyethylene plastic, secured in a plastic D-tube which was sealed with a piece of saturated floral

foam to limit sediment desiccation, and stored at 4 °C in a refrigerator to promote sediment preservation. Textural variability was analyzed in LDBH cores using a sieve first loss on ignition (LOI) procedure modified from the methods developed by van Hengstum et al. (2016). For Sieve-First LOI, contiguous 2.5 cm^3 sediment subsamples were wet-sieved over a 63 μm mesh stacked on top of a 32 μm mesh to isolate the sand and coarse-silt sediment fractions (Fig. 4.3). Sieved sediments from each size fraction were rinsed into separate pre-weighed ceramic crucibles, and heated at 80 °C for 12 hours or until dry. Crucibles and dried samples were weighed and then placed in a muffle furnace at 550 °C for 4.5 hours to ignite remaining OM in the samples following standard LOI methods (Dean, 1974, Heiri et al., 2001). The crucibles and remaining sediment residues were re-weighed to determine mass of non-organic particles with diameters exceeding >63 and>32 μm per cm^3 (mg/cm^3). The mass of OM lost through ignition also represents the fractional mass of >32 μm sedimentary OM, which provides an estimate of downcore sedimentary OM variability. The sub-section that represents the first ~145 cm of LDBH-D4 was destroyed during the shipping process, so a LDBH composite core was made by combining the first 145 cm of LDBH-D1 to the remaining 1135 cm of LDBH-D4 at a point of stratigraphic correspondence (Fig. 4.3, 4.4d).

Sediment grain size variability in the TURT core was quantified using a Beckman Coulter LS 13 320 laser diffraction particle size analyzer. We identified coarse grain anomalies within the TURT core based on sedimentary characteristics and anomalously high D90 grain size. D90 is the grain size of which 90% of all other sediments in the sample fall below in size, thus identifying the coarsest 10% of the total

sample (Maio et al., 2016). For this method, down core grain size was characterized for contiguous 1 cm subsamples using the lowest grain size that exceeded 90% of particle diameters in the subsample, which is known as D_{90} (Fig. 4.3).

Intervals (i.e., event beds) in LDBH and TURT where coarse-grained sedimentation significantly exceeds background sedimentary conditions were identified using methods modified from (Winkler et al., 2020, Lane et al., 2011). In LDBH, a 41-point moving average of data, excluding those with a coarse fraction value >50 mg/cm^3 (90th percentile of >63 µm mg/cm^3), was subtracted from >63µm sediment (mg/cm^3) for each 1 cm subsample to establish a series of coarse sediment anomalies (CSA; Fig. 4.4d). The 41-point moving average accounts for decadal scale changes in sediment composition (Lane et al., 2011). Deposits in LDBH were deemed significant event beds if the CSA exceeded 24.2 mg/cm^3, which is 1σ (68th percentile) of the cumulative CSA distribution cumulative distribution. If CSA values fell below the 24.2 mg/cm^3 significance threshold but showed a notable spike in >32 µm OM fractional mass (mg/cm^3) and a visibly darker band in the sediment, these beds were identified as Visual-OM event beds (Fig. 4.4c). Similar to LDBH methods, CSAs were identified in TURT by calculating a 41-point moving average D_{90} (upper 10th percentile of particle size in sample) that excludes values >338 µm (upper 1σ value) from the D_{90} of each 1 cm subsample. These CSAs were identified as event beds if they exceeded an anomaly threshold of 68 µm above the 40-point moving average, which is the 90th percentile of TURT CSAs (Fig. 4.4a). Additional Visual event beds were counted if a CSA fell within ~15 µm of the 68 µm threshold AND were in a visually darker, likely OM-rich bed.

4.3.3. Sediment Elemental Analysis

Archived core halves were scanned on the ITRAX X-ray fluorescence (XRF) scanner at Woods Hole Oceanographic Institution (WHOI) to measure elemental chemistry at 1 mm resolution. Mineralogy of granule and pebble sized crystals found within and on top of certain intervals of split LDBH sediment cores was verified using X-ray diffraction (XRD) for two samples from LDBH-D4 (LDBH-D4-2:9 3-18cm and 59-93 cm). XRD was performed using a Bruker-AXS D8 Advanced Bragg–Brentano X-ray powder diffractometer employing standard XRD laboratory protocols at the X-ray Diffraction Laboratory at Texas A&M University. The minerals in each sample were determined by comparing resultant diffractograms with the 2005 International Center for Diffraction Data material identification database (Fawcett et al., 2005).

4.3.4. Age-Control

Downcore radionuclide activity for ^{137}Cs was measured in the upper 150 cm of LDBH-D1 and 105 cm of TURT to better constrain modern chronology (APPENDIX D Fig. S4.3). ^{137}Cs is a man-made radionuclide that can exhibit spikes in activity in sediment that correspond to the onset of hydrogen thermonuclear weapons testing in 1954 CE and the subsequent moratorium in 1963 CE (Pennington et al., 1973, Dunphy and Dibb, 1994). To quantify ^{137}Cs activity, bulk sediment was sampled at 5-15 cm intervals, desiccated, and powdered. Powdered samples were then placed in a Canberra GL2020RS low energy Germanium gamma well detector where gamma decay was measured for 24-hours. In TURT, the onset of an exponential increase in bulk elemental lead (Pb) intensity that corresponds with increased fossil fuel combustion at the onset of

the Industrial Revolution in the late 19th century was utilized as a chronomarker (APPENDIX D Fig. S4.3; (Donnelly et al., 2001b, Maio et al., 2016).

To develop age control for the older part of the record, stratigraphic age-control points were obtained using radiocarbon dating on available mangrove leaves, with 3 dates from LDBH-D1, 6 dates from LDBH-D3, 19 dates from LDBH-D4, and 11 dates from TURT (Table S2). Radiocarbon dated leaves were not sampled from visual or quantifiable coarse sediment beds (see *3.4 Event Attribution and Frequency Calculation*) to limit the possibility of radiocarbon dating older material that was reworked during high-energy events like hurricanes.

Conventional radiocarbon results were calibrated into years before present (cal yrs BP) using the IntCal20 calibration curve to adjust for changes in cosmogenic ^{14}C production in response to solar activity (Reimer et al., 2020). Three radiocarbon dates had a post-date1950 CE fraction of modern carbon value ($F^{14}C$) >1, and were calibrated with the Northern Hemisphere Zone 2 dataset (NHZ2) in CALIbomb (Reimer et al., 2004). Downcore sedimentary age-models with 95% confidence intervals were developed for both LDBH and TURT using Bayesian statistical approaches in the R package Bacon version 2.5.3 (Blaauw and Christen, 2011) (Fig. 4.4b, e). The 19 control points used in the LDBH age-model were the core-top peak in ^{137}Cs associated with the thermonuclear weapons testing peak prior to the 1963 CE moratorium (Pennington et al., 1973) and 17 pre-1950 CE radiocarbon dates (n = 1 from LDBH-D1, n = 16 from LDBH-D4; Fig. 4.3e). The 10 control points used in the TURT age-model included: a core-top age of 1965 CE (based on correlative stratigraphy with LDBH related to the

loss of unsampled stratigraphy during the coring process), the peak in ^{137}Cs around the 1963 CE thermonuclear moratorium, the onset of exponential increase in elemental Pb intensity associated with increased regional fossil fuel combustion between 1850-1890 CE, and 7 radiocarbon dates (Fig. 4.3b). Coarse grained sedimentary layers thicker than 1 cm were assumed to have been deposited instantaneously by a high-energy event, so these coarse layers were treated as geologically instantaneous 1 cm deposits in the downcore age-model.

4.3.5. Event Attribution and Frequency Calculation

While stratigraphic studies indicate that blue hole sediments have demonstrated that coarse sediment beds tend to be associated with hurricane deposition (Denomee et al., 2014, Schmitt et al., 2020, Wallace et al., 2019, Wallace et al., Sub. March 2021, Wallace et al., 2021b, Winkler et al., 2020, Winkler et al., Submitted 2021), significant CSA event beds and Visual-OM event beds from LDBH and TURT were compared to the timing and number of hurricanes that could have impacted these sites during the last 170 years from the IBTrACS observational records of hurricane activity since 1850 CE (Knapp et al., 2018, Knapp et al., 2010) (Fig. 4.5; *4.5.1 Event Bed Drivers and Attribution***)**. No surface drive was collected from TURT that curated the sediment water interface, so this analysis was only performed on the LDBH composite.

Similar to Lane et al. (2011), significant event beds were counted using a 100-yr sliding window to quantify long-term hurricane variability (Fig. 4.6). Two methods were used to compile the event beds from LDBH and TURT into a single record. The first method, which we call the Grand Bahama Total Range and Average (GBAM-TRA) was

to plot the events/century counts from the 3 data sets for LDBH (CSAs, CSAs excluding gypsum, Visual-OM beds; Fig. 4.6a) and the 2 data sets for TURT (CSAs, Visual beds; Fig. 4.6c) on the same temporal axis. From there, we identified the minimum, mean, and maximum counts based on all 5 datasets within each 1-year interval (Fig. 4.7a). The other method, which we call GBAM-Stack, combined all the significant event beds derived from only the CSA data (i.e., no Visual-OM events and no exclusions for gypsum rich deposits; Fig. 4.7b). Following the methods of Wallace et al. (2019), we endeavored to remove redundant counts of the same event recorded by both LDBH and TURT by assessing the timing of CSAs in each core with respect to visual stratigraphic correlation. If event beds in both LDBH and TURT fell within age model uncertainties of each other, only one event was counted in GBAM-Stack (*APPENDIX D Section S4.1.1*). In rare instances where one site would archive more event beds than the other within the same temporal range, the deposits with the most similar median age from each core would be counted as a single deposit while the other event beds found in only one core were counted as their own distinct event bed (see events plotted as dots in Fig. 4.7b). The GBAM-Stack dataset was developed to match the input format required to update the statistical compilation of highly resolved paleohurricane records that we discuss in *4.5.4 North Atlantic Regional Compilations* and *APPENDIX D Section S4.1.2. Methods for Northeast Gulf, New England, and Bahamas Sediment Compilations* (Fig. 4.10c), which was developed by (Wallace et al., 2021b) based on the compilation methods of (Mann et al., 2009a).

Substantial stochastic variability in hurricane frequency can be caused by location of cyclogenesis and impacts of short term local weather patterns on storm tracks (Wallace et al., 2021a), which is independent of modulation driven by ocean conditions or climatic variability. This can naturally create time intervals where hurricane activity at a given locale may diverge from than average conditions. Assuming hurricane frequency at a given location are influenced to some extent by stochastic Poisson processes, upper 90^{th} and lower 10^{th} percentile significance thresholds for hurricane frequency were assigned based on regional frequency estimates derived by Wallace et al. (2019). These estimates were calculated based on expected ≥Category 2 hurricane frequency within 50 km of any given point throughout the entire Bahamian Archipelago region from 1850 CE to 2019 CE (bounding 550 km radius circle centered over 24.08°N and 75.39°W). The expected regional frequency value ≥Category 2 hurricanes passing within 50 km of any given point is 3.7 events/century; this results in upper 90^{th} percentile threshold of 7.3 hurricanes/century and a lower 10^{th} percentile threshold of 1.62 hurricanes/century using methods for Poisson significance threshold calculation described by Ulm (1990). If the number of hurricanes/century exceeds the upper (lower) threshold, there is a 90% probability that this increase (decrease) is not attributed solely to stochastic processes, and can be considered a period of active (quiescent) hurricane activity.

4.4. Results

4.4.1. Geophysics and Hydrography

Due to the shallow depth of TURT, geophysical surveys and hydrographic profiles are only available for LDBH. Based on these surveys, LDBH is a relatively symmetric bowl-shaped depression with a depth of 28-30 mbsl (Fig. 4.2b). This Chirp survey revealed two distinct internal reflectors in the upper 1.4 m of accumulation, one ~0.4 m below a low-density layer at the top of the strata, and another approximately 1 m lower below a denser layer (Fig. 4.2b). No reflectors are observed below 1.4 m from the top of the accumulation, likely due to high levels of interstitial hydrogen sulfide gas that can attenuate acoustic energy during transmission and scatter the return signal. Based on the longest coring drive, there are at least ~14 m of sediment accumulation in LDBH, but the total accumulation depth is unknown.

A hydrographic profile from LDBH on 19 April 2016 showed a stratified water column with tidally-exchanged seawater from 0-15 m, a mixing zone from 15-25 m, and a hypersaline groundwater mass from 25-30 m (Fig. 4.2c). At the base of the tidally-exchanged seawater at 15 m, temperature increased from ~23 °C to ~24 °C, salinity increased from 38.5 practical salinity units (psu) to 40.75 psu, pH dropped from 7.9 to 7.4, and dissolved oxygen (DO) dropped from ~4 mg/L (6 mg/L at surface) to dysoxic conditions at~ 0.4 mg/L. At the base of the mixing zone of the tidally-exchanged seawater and hypersaline groundwater units at ~25 m, temperature decreased from ~24 °C to ~22.2 °C, salinity increased from ~41.7 psu to ~45 psu, pH dropped from 7.4 to

6.8, and DO maintained its steady decrease to < 0.2 ml/L, meaning conditions at the sediment water interface or within the nepheloid layer are suboxic-anoxic.

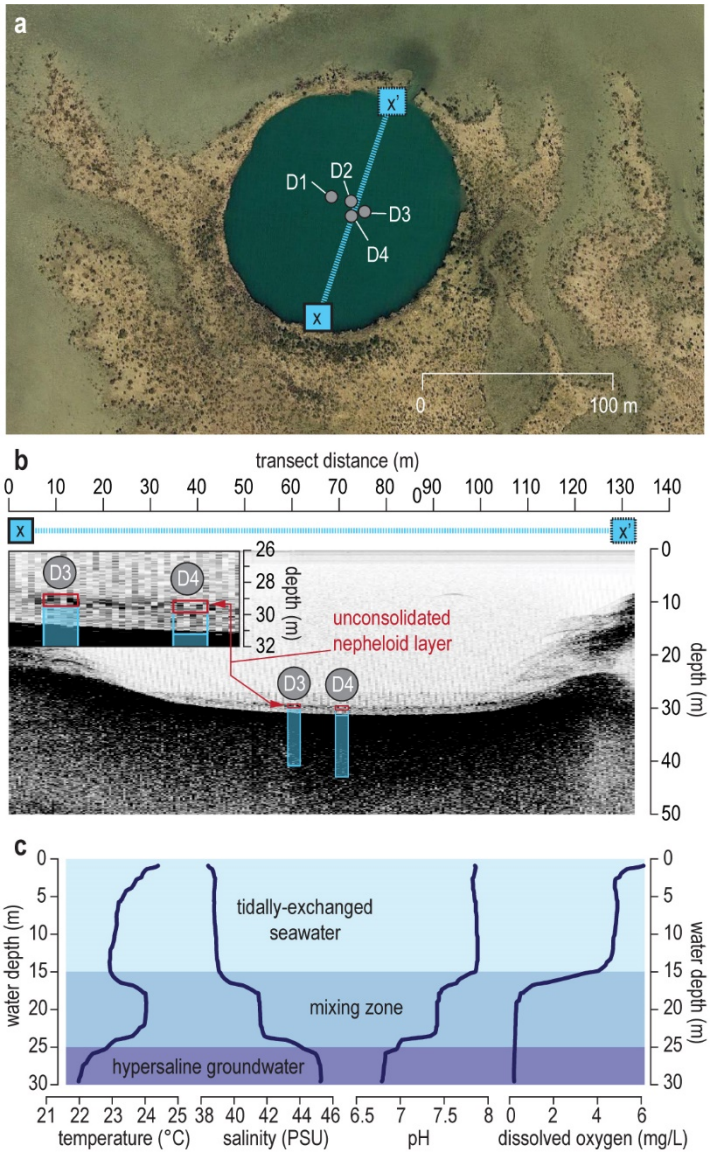

Figure 4.2. LDBH geophysics and hydrography.
(a) Coring locations (grey circles) and the Chirp subbottom seismic transect path in LDBH. (b) Chirp subbottom stratigraphy with the names and coring depths for cores that intersect the survey line. The inset pane shows the upper 2.5 m of the sediment package, with the red box around the upper 30 cm of unconsolidated sediment that was not recovered during the coring process. (c) 30 m water column profile for LDBH measured on 19 April 2016 sampled at 26.66 °N and 78.59 °W.

4.4.2. Sedimentology and Age-Control

The upper 60 cm in LDBH and upper 30cm of TURT are dominated by a black OM rich carbonate mud unit (Munsell color 2.5Y 6/1). Below these layers, sediment is dominated by grey aragonitic mud (Munsell color 2.5Y 6/1) with randomly spaced olive brown (Munsell color 2.5Y 4/4) and olive grey (Munsell color 5YR 4/2) laminations and OM rich beds. These laminations and OM-rich beds vary in thickness from 1-20 cm, and tent to include more terrestrial OM macrofossils (e.g., rootlets, grasses, leaf fragments). Very few salient coarse sediment deposits like the one shown in Figure 4.3 are observable in LDBH cores or TURT. However, textural analysis (i.e., Sieve-first LOI, laser particle size) reveals that there are distinct coarse-sediment beds LDBH and TURT cores, but they are primarily dominated by fine-carbonate sand rich in shallow water benthic foraminifera, fragmented skeletal material from invertebrates, and peloids (Figs. 4.3 and 4.4). Additionally, granule and pebble sized translucent crystals were found within and on top of certain intervals from LDBH but not TURT. XRD analysis of these crystals from 3-18 cm in LDBH-D4-2:9 and 59-93 cm in LDBH-D4-2:9 indicate the minerals are primarily bassanite ($CaSO_4 \cdot 0.5H_2O$) with some gypsum ($CaSO_4 \cdot 2H_2O$) (APPENDIX D Fig. S4.2). However, it is likely that some gypsum crystals were partially dehydrated to precursor mineral bassanite when samples were dried at 80 °C for 24 hours prior to powderization (Van Driessche et al., 2017). Gypsum and bassanite crystals were not noted in the initial description, so it is possible that crystals precipitated from pore water after cores were split.

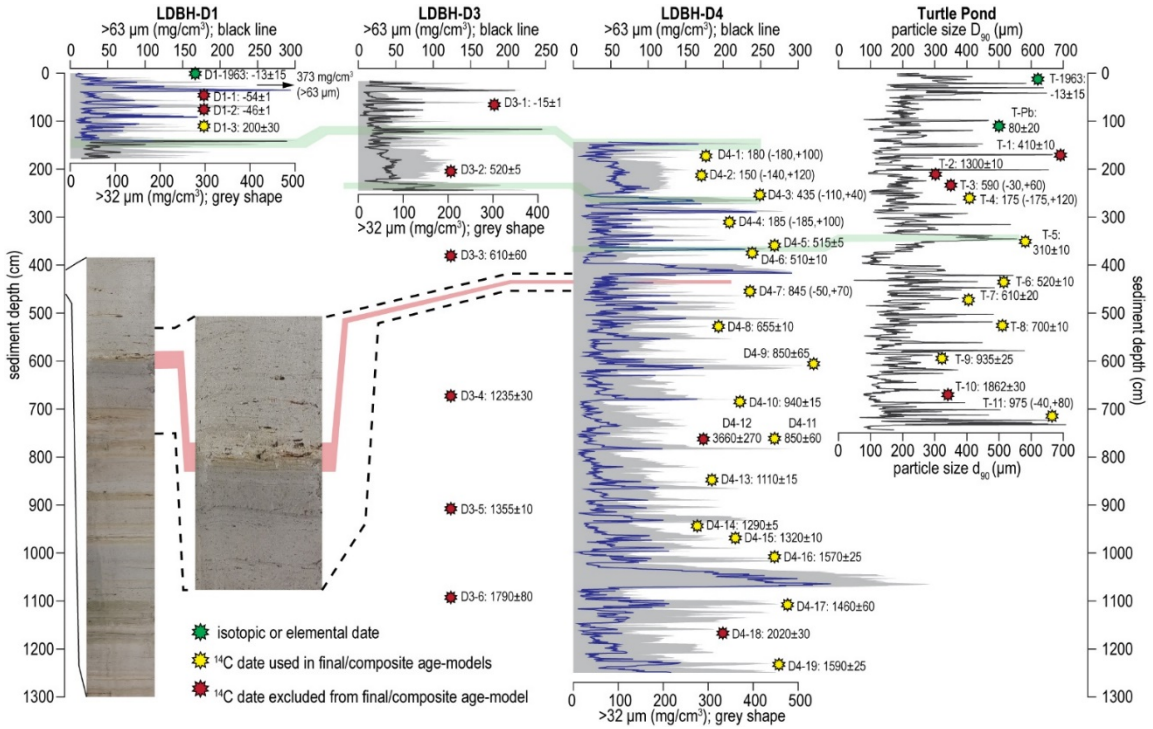

Figure 4.3. Downcore sediment textural data for cores from LDBH and TURT. LDBH cores show the >63 µm mg/cm^3 size fraction (black/blue) and the >32 µm mg/cm^3 size fraction (grey shape) for three of the four cores, with the blue line indicating the portion of LDBH-D1 and D4 used in the LDBH Composite. Downcore d_{90} particle size (µm) is shown for TURT. Coarse sediment layers like the one in the photograph contain weathered karst fragments and abundant shallow water benthic foraminifera and are likely hurricane event deposits. As indicated by the green bars, correlation of peaks is well maintained across the cores in both the >63 µm and >32 µm size fractions. See APPENDIX D Figure S4.1 for more detailed stratigraphic correlation between the LDBH Composite (D1 and D4), LDBH-D3, and TURT. Yellow stars indicate dates that were included in the LDBH Composite and TURT reconstructions sedimentary age-models, while those in yellow were excluded and green stars indicate age-control points interpreted from ^{137}Cs activity or bulk Pb intensity (Appendix D Figure S4.3 and Table S4.2).

Based on stratigraphic correlations developed though visual facies mapping and textural data, the upper 144 cm of LDBH-D1 and LDBH-D4 (1107 cm) were merged to form a single composite record (Figs. 4.3 and 4.4d; *Appendix D Section S4.1.1*). In the 1251 cm long LDBH Composite, 84 >63 µm CSAs exceeded the event bed significance

threshold (41-pt moving average + 24.2 mg/cm^3). Each of these >63 μm event beds showed a corresponding peak in the >32 μm coarse-silt size fraction (Fig. 4.3) as well as >32 μm OM content (Fig. 4.4c). After visual inspection of each of these event beds under a stereomicroscope, it was determined that 5 of these event beds were predominantly >63 μm sulfate mineral crystals, meaning there are 79 non-sulfate mineral rich event beds. Another 17 event beds that fell short of the significance threshold were identified from prominent spikes in >32 μm OM content accompanied darker sediment layers that are coeval with most CSAs, bringing the total number of event beds in the LDBH Composite up to 101 (Fig. 4.4c, d). When all 101 possible event beds are considered, these events account for ~487 cm of sediment, with an average thickness of 4.8 cm and a maximum of 46 cm, and 52 event beds thicker than 1 cm.

In the 744 cm long TURT core, 57 D_{90} CSAs exceeded the significance threshold (41-pt moving average + 68 μm) and were identified as event beds (Fig. 4.4a). While organic matter content was not measured for TURT, an additional 11 visual event beds fell within ~15 μm of the 68 μm threshold and were within a distinct darker bed, bringing the total up to 68 event beds (Fig. 4.4a). The 68 possible TURT event beds account for 211 cm of sediment, with an average thickness of 3.1 cm, a maximum thickness of 20 cm, and 36 event beds thicker than 1 cm.

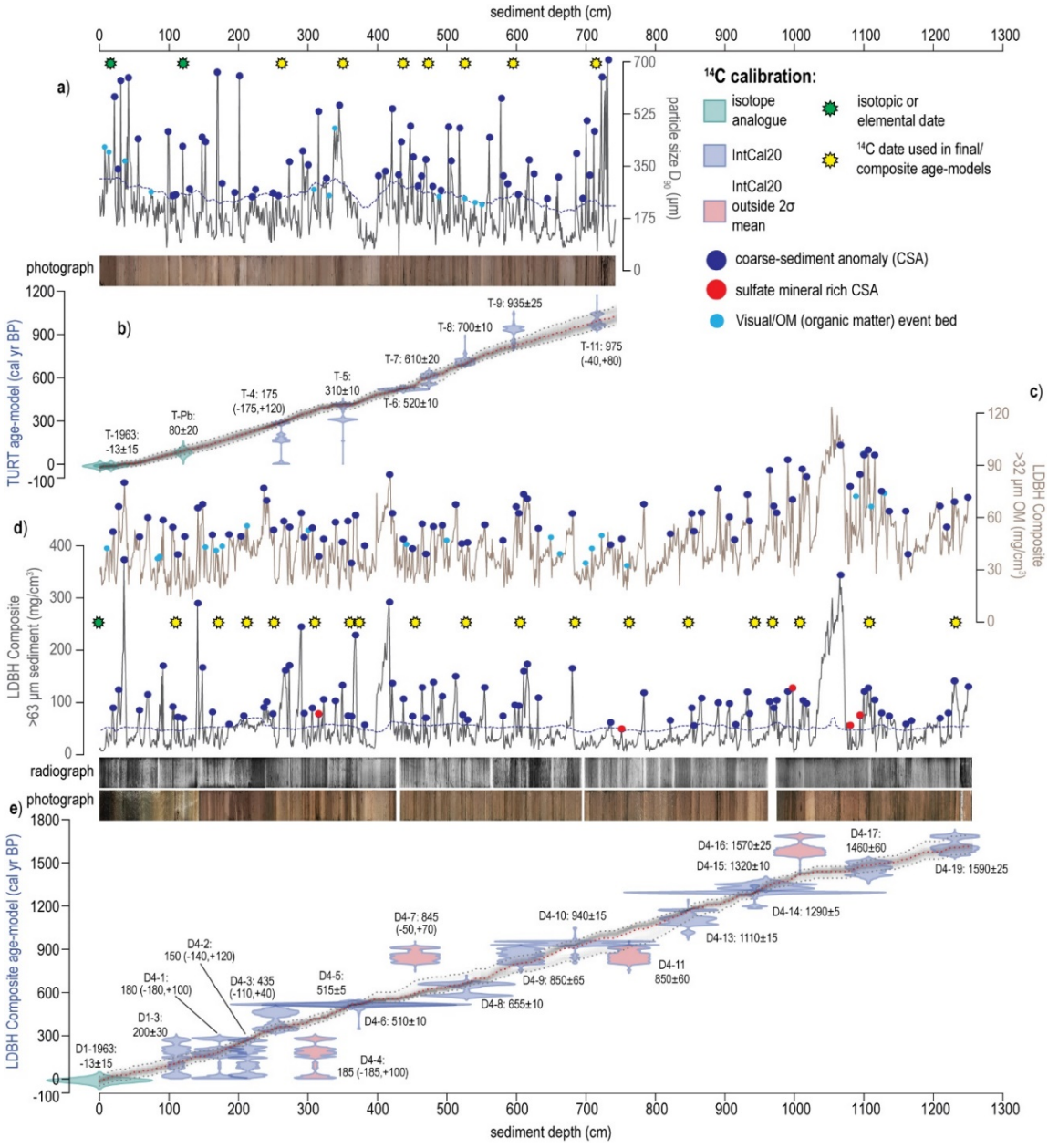

Figure 4.4. LDBH Composite and TURT textural varibility and age-models. (a) TURT D_{90} particle size (µm) with a high-resolution core photograph. The blue dotted line is the sediment anomaly threshold (40-point moving average of D_{90} + 68 µm). Any points above this threshold are coarse-sediment anomalies (dark blue dots). Points within standard deviation of the 40-point moving average that also exhibited visually distinct in the stratigraphy are visual anomalies (light blue dots). Similarly, (c) and (d) respectively show >32 µm bulk organic matter (mg/cm^3) and >63 µm coarse fraction (mg/cm^3) data for the LDBH Composite. The blue dotted line in (d) is the sediment anomaly threshold (40-point moving average of >63 µm coarse fraction + 24 mg/cm^3) and dark blue dots are coarse sediment anomalies

above this threshold while red dots are anomalies that are over 50% gypsum/bassanite crystals. In (c), light blue dots are visual/OM anomalies for coarse peaks that fall within standard deviation of the threshold (from the 40-point moving average) but also show substantial spikes in bulk OM. (b) and (e) are sedimentary age-models for TURT and the LDBH-Composite, where the blue shapes are the probability distribution functions of uncertainty for age-control points derived from radiocarbon dated leaves (TURT: *n=7*; LDBH: *n=18*), and green shapes are control points from ^{137}Cs abundance or Pb intensity. See Appendix D Table S4.2 for details on dated material.

Median age-estimates from the LDBH Composite age-model, including event beds, reveal a consistently linear average sedimentation rate of ~0.8 cm/yr throughout the 1600-year archive (Fig. 4.4e), with a median core-top age of 1968 CE (2σ range: 1936-2001 CE) and a basal age of 341 CE (2σ range: 262-393 CE). Median age-estimates for TURT (including event beds) reveal a 1050-year archive with a slightly lower linear sedimentation rate of ~0.7 cm/yr (Fig. 4.4b), with a median core-top age of 1973 CE (2σ range: 1957-1993 CE) and a basal age of 927 CE (2σ range: 850-981 CE). When significant event beds in each record are counted as an instantaneous 1 cm deposits in the sedimentary age-model, the LDBH Composite length becomes 865 cm, shifting the average sedimentation rate to 0.53 cm/yr. A similar approach in TURT reduces the length to 601 cm, with a lower average sedimentation rate of 0.57 cm/yr. The average age-uncertainty for the LDBH Composite is ±46 yrs compared to ±36 yrs for TURT.

4.5. Discussion

4.5.1. Event Bed Drivers and Attribution

The punctuated nature of the event beds (CSA and Visual-OM) in the LDBH Composite and TURT over the last 1700 years suggests that they were deposited during extreme coastal flooding events driven by heightened currents and waves (Fig. 4.6). Given the number of event beds and the temporal resolution of the LDBH Composite and TURT, these high-resolution sediment records likely archive long-term variability in decadally recurring storm-induced coastal flooding events, meaning that rare tsunami induced coarse-deposit would have negligible impact on reconstructed temporal trends. Further, tectonic sourced events like tsunamis are unlikely to play a major, recurring role in causing extreme waves in the region around The Bahamas over the last 2000 years. Tsunamis that could theoretically impact the northern coast of Grand Bahama are most likely produced at the Azores–Gibraltar plate boundary; however, numerical models of the tsunami caused by the 1755 CE Lisbon Earthquake (strongest recorded event from this fault) predict far-field wave heights of <1 m in the northern Bahamas, (NCEI/WDS Global Historical Tsunami Database; (Barkan et al., 2009, Arcos et al., 2018). Further, the tsunami recurrence interval in The Bahamas is >500 years (Parsons and Geist, 2008), which is insignificant compared to the compared to the sub-decadal recurrence of intense hurricanes impacts in the northern Bahamas since 1850 CE (Winkler et al., 2020).

Long period swell waves from an unnamed extratropical cyclone that stalled off the coast of Massachusetts, USA in March 2018 drove ‘sand to boulder’ sediment transport that produced a coastal washover fan over a 3700 m^2 area in the Gaulding Cay

Quarry of northern Eleuthera, The Bahamas (Wilson and Mohrig, 2021). The sandy tempestite produced by swells from this far-field cyclone are similar in composition to those produced by local storms, and washover events from long period swell waves in this relatively low topographic channel are not uncommon based on local accounts (Wilson and Mohrig, 2021). Based on this, it is also possible that far-field swells produced by storms hundreds to thousands of kilometers away from Grand Bahama could produce sandy event beds in the LDBH and TURT records. However, the extreme flooding that drove sediment transport and produced the washover fan was limited to a relatively narrow area of the northern Eleuthera coastline, and similar impacts in other areas/islands of The Bahamas are not well documented in the literature. It is therefore likely that local coastal geomorphology and slope has an important impact on the flooding potential for these swells, which may cause them to be focused and intensified in specific area like the Gaulding Cay Quarry of Eleuthera rather than producing consistent island-scale coastal impacts. While we cannot rule out the potential for these swells to produce event beds in our records, we remain confident that waves and currents from proximal hurricane passage are the most likely source for most event beds.

To assess hurricane hydrodynamics as a potential depositional mechanism, we compare the stratigraphic age of CSA and Visual-OM event beds from the LDBH Composite to the instrumental record of hurricane activity from 1850-2020 CE (IBTrACS; Knapp et al., 2018, Knapp et al., 2010) (Fig. 4.5). While the upper portion of LDBH Composite and TURT stratigraphy is visually similar (Fig. 4.4 and APPENDIX D Fig. S4.1), we only perform this analysis on the LDBH-Composite as the sediment

water interface in TURT was not preserved. It should be noted that some uncertainty surrounds the core-top ages for LDBH and TURT based on the low detected activity of ^{137}Cs suggesting an age of ~1963 CE at a depth of 0-1 cm in LDBH and 15-16 cm in TURT (APPENDIX D Fig. S4.3). This age conflicts with post-bomb radiocarbon enriched leaves from LDBH-D1 at depths of 44.5 and 75.5 cm in the LDBH Composite that suggest much younger calibrated ages of 2003 CE and 1995 CE, respectively (Fig. 4.3 and APPENDIX D Fig. S4.3). Assuming the average LDBH background sedimentation rate of 0.5 cm/yr (only carbonate mud) and the total accumulation rate of 0.8 cm/yr (mud and event beds) persists between the core-top age of 1970 CE and the collection date in 2016 CE, 24-40 cm of sediment would have accumulated during this time. This accumulation likely corresponds to the ~30-40 cm of unconsolidated strata above a reflector ~2 m below the sediment water interface (Fig. 4.2b). Based on this observation, we believe that the core pipe rodded through a 30-40 cm nepheloid layer that likely accumulated from 1970-2016 CE. It is also possible that stratigraphically higher, younger dated leaves whose ages are out of stratigraphic order (see APPENDIX D Table S4.2) were pushed deeper into the nepheloid layer during the coring process. This may explain why post-1950 CE radiocarbon dates disagree with measured ^{137}Cs activity that suggests an age of 1963 CE within the upper 15 cm of LDBH and TURT.

Based on the sensitivity of other subtidal-intertidal blue holes in the Bahamas to hurricane induced sedimentation (Wallace et al., 2019, Wallace et al., 2021b, Winkler et al., 2020, Wallace et al., Sub. March 2021), hurricanes that passed within 100 km of LDBH during the 2σ age-range of each event bed were considered as potential

depositional mechanisms. During the period from 1850 to 1985 CE when the 2σ age-uncertainty of LDBH Composite event beds overlaps with the instrumental record, 35 ≥Category 1 hurricanes passed within ~100 km of LDBH compared to the 10 event beds during this same time (Fig. 4.5, APPENDIX D Fig. S4.4, APPENDIX D Table S4.3). Starting with the most recent event bed (E1), we isolated which hurricane(s) were most likely to leave a deposit in LDBH based on: (i) the date of the hurricane vs the median age of the event deposit, (ii) hurricane intensity and passage proximity relative to LDBH, and (iii) which side of the island the storm passed on and what quadrant of the storm impacted the site most directly. Attribution of LDBH event beds to observed hurricanes from 1850 CE to 1985 CE (maximum 2σ age-range within the instrumental period) is complicated by the fact that 32 of these 35 hurricanes fall into nine 1-4 years long clusters wherein 2-6 hurricanes pass within 100 km of LDBH in rapid succession. Further, it remains poorly understood how different storm characteristics (e.g., forward translation speed, angle of approach, intensity, proximity, positioning to the north vs south of Grand Bahama, etc.) impact local storm flooding in the remote carbonate tidal flats on the northern coast of Grand Bahama due to lack of firsthand observations or surge and wave modelling studies.

When Hurricane Dorian passed ~30 km to the northeast of LDBH as a Category 4 hurricane on 2-3 September 2019 CE, synthetic-aperture radar imaging showed that the northern half of Grand Bahama was largely inundated, with >4 m of flooding in the tidal flats over LDBH (Fig. 4.1d, ICEYE, 2020). In 2016 CE, Category 4 Hurricane Matthew's front right quadrant passed ~40 km to the west of LDBH on a southeast to

northwest trajectory, causing up to 2.5 m of surge and inundating most coastal areas of western Grand Bahama (Stewart, 2017). However, the strongest counterclockwise winds from the front right quadrant of Matthew would have drawn water away from the northern shoreline of Grand Bahama, making it unlikely that this storm would have produced significant local surge over the LDBH area. In 2004, the front right quadrant of Hurricanes Frances (Category 2) and Jeanne (Category 3) passed ~20 km and 40 km (respectively) to the north of LDBH on generally east to northwest trajectories, producing unquantified but significant storm surge across Grand Bahama that flooded the Freeport airport (Franklin et al., 2006) and devastated pine forests along the northern coast (Winkler and van Hengstum, personal observation in 2014, Fall et al., 2021). Unfortunately, the cores we collected from LDBH and TURT do not capture the last 40 years of accumulation that would allow us to determine if these four hurricanes were archived as event beds in the sediment record. However, they demonstrate that storms passing to the north of Grand Bahama and moving generally westward can produce significant storm surge over LDBH and TURT.

No hurricanes passed within 100 km of LDBH from 1952-1994 CE. Event bed E1 has a median age of 1950 CE and a 2σ age-range from 1912-1985 CE, so the first attributable storm is Category 1 Hurricane Able, which passed 45 km to the north of LDBH in 1951 CE, with the winds from the rear right quadrant directing water onshore toward LDBH (Fig. 4.5, APPENDIX D Fig. S4.4, and APPENDIX D Table S4.3). However, there were 4 other hurricanes from 1947-1949 CE that passed within 100 km of LDBH that could have produced or contributed to event bed E1 given that the

background sedimentation rate of 0.5 cm/yr is likely too low to produce a distinct fine-grained unit in the time between each of these storms. The first of these hurricanes was a Category 4 hurricane that passed ~100 km to the west of LDBH on 26 August 1949 CE, but it is likely that this approach angle pulled water away from the LDBH area rather than inundating it. Two hurricanes passed ~50 km to the north of LDBH on 6 October 1948 CE (Category 2) and on 12 October 1947 CE following a similar southeast to northwest trajectory that would have oriented in the front right quadrant such that the strongest counterclockwise storm winds would have likely drawn water offshore. The final storm in this cluster was a Category 3 hurricane that passed 20 km to the south LDBH on 17 September 1947 CE with the center of the storm moving west to east below the southern shoreline of Grand Bahama. While it is possible that the 17 September 1947 CE storm pushed some water onshore as the front right quadrant passed over LDBH, the strongest winds around the eyewall of this storm would have been dampened by the ~13 km landmass between LDBH and the eyewall (APPENDIX D Fig. S4.3). For these reasons, it is most likely that either Hurricane Able in 1951 CE or the Category 3 hurricane on 17 September 1947 CE deposited E1, but we cannot confidently rule out either of these two events out over one another.

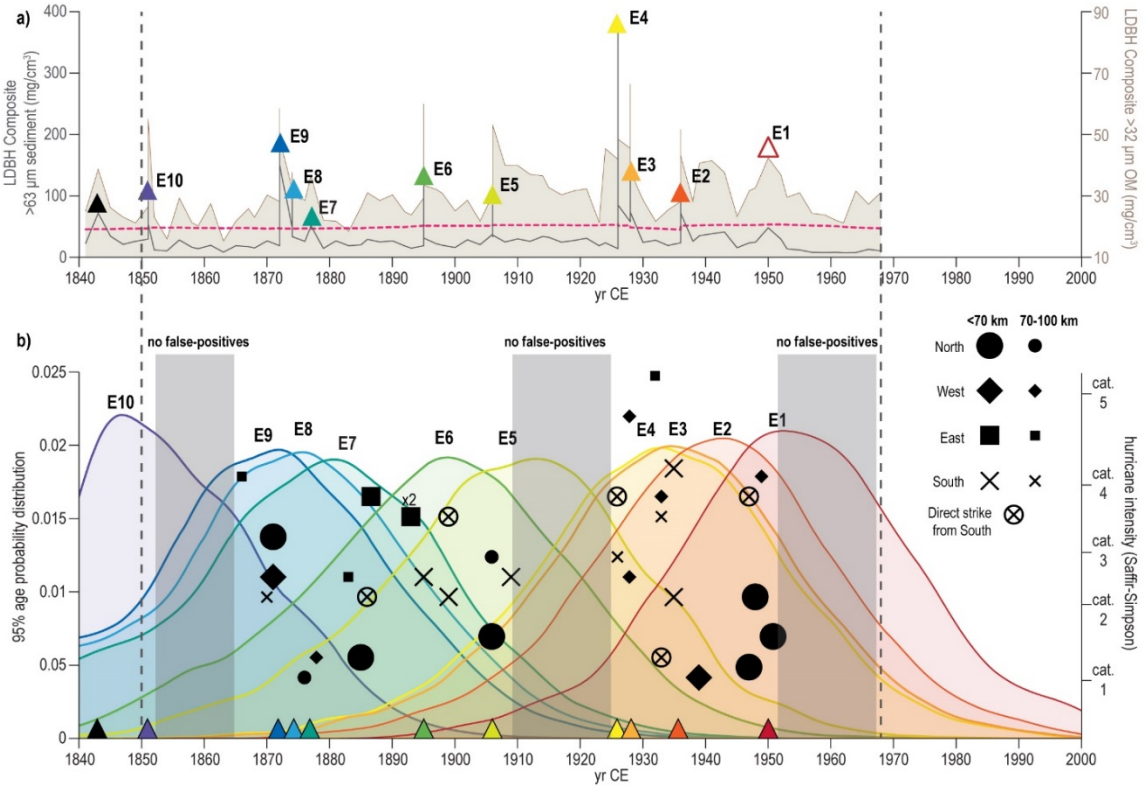

Figure 4.5. LDBH Composite event bed attributions to observed hurricanes. (a) >63 µm coarse fraction data (grey line) and >32 µm bulk OM (brown shape) for the LDBH Composite, with coarse-sediment and OM anomalies E1-E11 indicated respectively by solid and hollow colored triangles that correspond to colors of 95% age probability distribution (95% PDF) plots in (b). Black shapes in (b) correspond to the timing of hurricane events observed within 115 km of LDBH and TURT from 1850 to 2015 CE (*n = 23*), with the direction the storm passed in relation to LDBH and TURT. Shape size is relative to the passage proximity (larger = closer passage), and position of the shape relative to the right y-axis is the intensity of the storm on the Saffir-Simpson hurricane scale.

Event beds E2, E3, and E4 have respective median ages 1936, 1928, and 1926 CE, with a total 2σ age-range from 1885-1971 CE, which are likely derived from some combination of the 11 hurricanes within 100 km of LDBH from 1926-1939 CE. As with the E1 attribution, we cannot be certain which storm(s) produced E2-E4. It is most likely that E2 is either the 17 September 1947 CE Category 3 hurricane described above, or the combined deposit of two hurricanes in 1935 CE that passed across Grand Bahama 38

(24) km to the east of LDBH at Category 2 (4) intensity (Fig. 4.5, APPENDIX D Fig. S4.4, APPENDIX D Table S4.3). A Category 2 hurricane in 1949 CE passed ~100 km to the southwest of LDBH, but the counterclockwise winds in this distal storm likely directed water offshore away from LDBH. Event bed E3 was most likely deposited by the Category 1 hurricane that passed 4 km to the east of LDBH moving south to north across Grand Bahama, but we cannot rule out the possibility that a Category 5 hurricane that moved from south to north ~100 km to the east of LDBH in 1932 CE played a role. Two other Category 3 hurricanes also occurred within 100 km of LDBH in 1933 CE, but were both over 85 km away and passed to the west or south of Grand Bahama and likely had minimal surge near LDBH. Finally, E4 was likely produced by a Category 2 hurricane that passed 15 km to the southeast of LDBH below Grand Bahama moving eastward on 21 October 1926 CE. Three other hurricanes passed over 70 km to the west of LDBH moving northwestward at Category 2 (1928 and 1926 CE) and 4 (1928 CE) intensity, but the orientation and distal nature of these storms likely produced minimal impacts around LDBH.

Following this cluster of 11 hurricanes from 1926-1939 CE, no hurricanes were recorded within 100 km of LDBH until a Category 3 hurricane passed 39 km to the southeast of LDBH below Grand Bahama, and LDBH does not document any event beds until E5 which had a median age of 1906 CE. The lack of false-positive event beds in this 20-year interval with no documented hurricane activity provides further evidence in support of hurricanes as the primary depositional mechanism for these event beds. The median age and 2σ age-range of event beds E5-E10 fall in the most unreliable portion of

the IBTrACS record prior to the implementation of air-craft storm monitoring in the 1940s (Vecchi and Knutson, 2011, McAdie et al., 2009). We attempt to highlight which cluster of storms are most likely to have produced these older event beds in APPENDIX D Figure S4.4 and APPENDIX D Table S4.3, but emphasize that no event bed can be confidently attributed to any single hurricane given: (i) the high number of storms that have impacted this area, (ii) the sedimentation rate of ~0.55 cm/yr into both LDBH and TURT that limits distinction of deposits associated with hurricanes occurring within 2 years of one another, and (iii) average age-model uncertainties of 0.36 to 0.46 cm/yr.

Regardless of the uncertainty regarding the specific types of storms that tend to produce event beds in LDBH, 9 out of 10 event beds in the LDBH Composite with median ages from ~1850-1985 CE can be attributed to one or more hurricanes within 100 km of LDBH within the 2σ age range of each deposit (Fig. 4.5, APPENDIX D Table S4.3). Importantly, there are no false positive event beds with median ages that fall during periods in the instrumental record without hurricanes from 1852-1865 CE, 1910 to 1925 CE, or 1952-1968 CE (Fig. 4.5b). Like Lin et al. (2014) and Wallace et al. (Sub. March 2021), we suggest that orientation of storm passage relative to LDBH and TURT likely plays a more prominent role in producing event beds than storm intensity or proximity alone. In particular, these sites are most likely to document ≥Category 1 hurricanes that pass within 50 km of LDBH and TURT (i.e., the regional average radius of maximum winds estimated by Hsu and Yan, 1998) to the north of Grand Bahama or within 30 km to the east of the blue holes. It is also possible that more intense storms (≥Category 2) that pass >50 km the east and north of the blue holes may leave event

beds, but there is less confidence in these attributions as storm surge direction becomes more difficult to constrain beyond the radius of maximum winds.

4.5.1.1. Other Sedimentary Considerations for Event Beds

Five of the 101 CSA and OM event beds in LDBH were predominantly >63 μm gypsum/bassanite crystals (e.g., hexagonal and rosette), although none of these sulfate mineral rich beds were observed during the last 170 years (Figs. 4.4 and 4.5). As such, it is not clear if these sulfate-mineral crystals are deposited by the same storm induced flooding as CSAs dominated by skeletal material and peloids. Evaporative processes have been previously cited as driving interstitial gypsum and bassanite precipitation on carbonate tidal flats and coastal ponds (Wanless et al., 1988b, Woods and Brown, 1975, Alsharhan and Kendall, 2002, Malaizé et al., 2011). If these crystals formed around the periphery of LDBH during intervals with heightened evaporation (i.e., warmer temperatures or less rainfall), they could be mobilized into LDBH by hurricane flooding as a portion of the coarse sediment signal, and would therefore be indicative of hurricane activity. Gypsum/bassanite crystals were not noted when the LBDH cores were split initially, nor were they found in TURT, thus limiting confidence in surface evaporation as the primary source of gypsum and bassanite crystals in LDBH. Alternatively, Bottrell et al. (1991) found that gypsum is precipitated in situ in the carbonate wall crusts of Stargate Blue Hole on Andros Island, The Bahamas, after hydrogen sulfide (H_2S) produced from bacterial sulfate reduction in the mixing zone is re-oxidized by circulated groundwater. However, dysoxic-suboxic conditions below the tidally-exchanged seawater layer at from 15-18 m (Fig. 4.2c) suggest that saline groundwater in LDBH is

not well circulated. Similar physicochemical properties have been observed in other Bahamian blue holes as well (Bottrell et al., 1991, Gonzalez et al., 2011, Sampson and Guilbeault, 2013).-The drop in dissolved oxygen and pH change are most likely driven by highly-structured microbial communities along the salinity gradient that mediate aerobic and anaerobic microbial respiration processes during the breakdown of organic matter trapped at the pycnocline(s) between water masses. These microbial processes likely include sulfate reduction, resulting in the formation of a brown, H_2S rich water mass within the mixing zone (15-25 m; Fig. 4.2c). Therefore, it is also possible that the sulfide-rich, briny pore water in LDBH cores was oxidized to form sulfate after cores were split and aerially exposed, and that gypsum and bassanite precipitated as the pore water slowly evaporated.

Importantly, occurrence of these crystals is punctuated throughout the core, which implies some type of environmental change either resulted in: (i) the formation of crystals around the periphery that were dissolved after deposition into the blue hole and where then recrystallized from evaporation in split cores, or (ii) higher sulfur concentrations within the saline groundwater achieved by increased OM or sulfate deposition into the LDBH water column. Each of these mechanisms could be related to hurricane induced allochthonous sediment deposition (i.e., coarse sand and sulfate-mineral crystals or increased OM). Further, almost all >63 μm CSAs in the LDBH Composite aside from the five excluded gypsum/bassanite dominated beds are correlated to a spike in 63 μm> x >32 μm sediment fraction that excludes the >63 μm crystals (APPENDIX D Fig. S4.5). However, there is increased uncertainty regarding the source

of these gypsum/bassanite rich deposits relative to other CSAs that are dominated by increased skeletal material, peloids, and karst fragments alone. Based on this, we exclude these 5 gypsum/bassanite crystal dominated deposits from one of three event bed counts for the LDBH Composite to provide a minimum estimate of potential hurricane deposits (Figs. 4.4 and 4.6).

Hurricanes also provide a depositional mechanism for the OM-rich, millimeter-to-centimeter thick laminae found in cores from LDBH and TURT (Fig. 4.4). In LDBH, the darker olive brown and olive grey laminations correspond to an increase in >32 μm OM (mg/cm^3; Fig. 4.4). If we assume that both the suboxic conditions of LDBH bottom water and the sulfate-reducing bacterial colony at the top of the mixing zone (~15 m) persisted throughout the record, it is unlikely that in-situ primary productivity alone could produce these punctuated OM-rich laminae. This observation combined with the fact that these laminae are often above or within CSAs, so it is possible that the abundant *Schizothrix* and *Scytonema* cyanobacterial mats and mangrove OM peats from across the Bahamian tidal flats (Maloof and Grotzinger, 2012, Shinn et al., 1969, Wanless et al., 1988a, Wanless et al., 1988b) are eroded and transported by heightened bottom-currents during hurricanes and deposited into the deeper blue holes. These punctuated laminae from TURT can be visually correlated those in the LDBH Composite (APPENDIX D Fig. S4.1), suggesting a consistent allochthonous source related to hurricane transport. Based on these interpretations, if a spike in coarse sediment from LDBH Composite or TURT records did not meet the significance threshold but was coincident with visual algal-sediment laminae, it was counted as a Visual-OM event bed (Figs. 4.4 and 4.6).

4.5.2. Grand Bahama Hurricane Variability

With hurricane induced waves and currents identified as the most likely source of event beds archived by the LDBH Composite and TURT sediment records, these events beds were counted in a sliding 100-year window to assess centennial scale variability in hurricane frequency (Fig. 4.6). For the LDBH Composite, three sets of event beds were counted: (i) CSAs excluding sulfate-mineral dominated deposits representing a minimum hurricanes/century, (ii) all CSAs, and (iii) Visual-OM event beds that represent a maximum hurricanes/century estimate (Fig. 4.6a, b). From 395-1918 CE, these three datasets respectively archive (i) 4.8 ± 2.4 hurricanes/century, (ii) 5.1 ± 2.5 hurricanes/century, and (iii) 6.1 ± 2.6 hurricanes/century, with an average of 5.3 ± 2.6 hurricanes/century for all counts. Overall, the temporal variability in hurricane frequency from each of these counts reflect the same patterns aside from one interval from ~900-1100 CE, when the Visual-OM counts show a moderate rise in frequency to an average of 4.6 ± 1.1 hurricanes/century while the other 2 counts document <2 hurricanes/century. For TURT, just two sets of event beds were counted: (i) all CSAs, and (ii) Visual event beds that represent a maximum hurricanes/century estimate (Fig. 4.6c, d). From 980-1923 CE, these two datasets respectively archive (i) 5.2 ± 1.6 hurricanes/century and (ii) 6.1 ± 1.5 hurricanes/century, with a total average of 5.6 ± 1.6 hurricanes/century for both datasets. As with the LDBH Composite datasets, the temporal variability in hurricane frequency from the two TURT counts reflect the similar frequency variability trends aside from one interval from ~1530-1590 CE, when the Visual event beds show a

relatively high average frequency of 7.3 ± 1 hurricanes/century while the CSA counts document 4.3 ± 0.9 hurricanes/century.

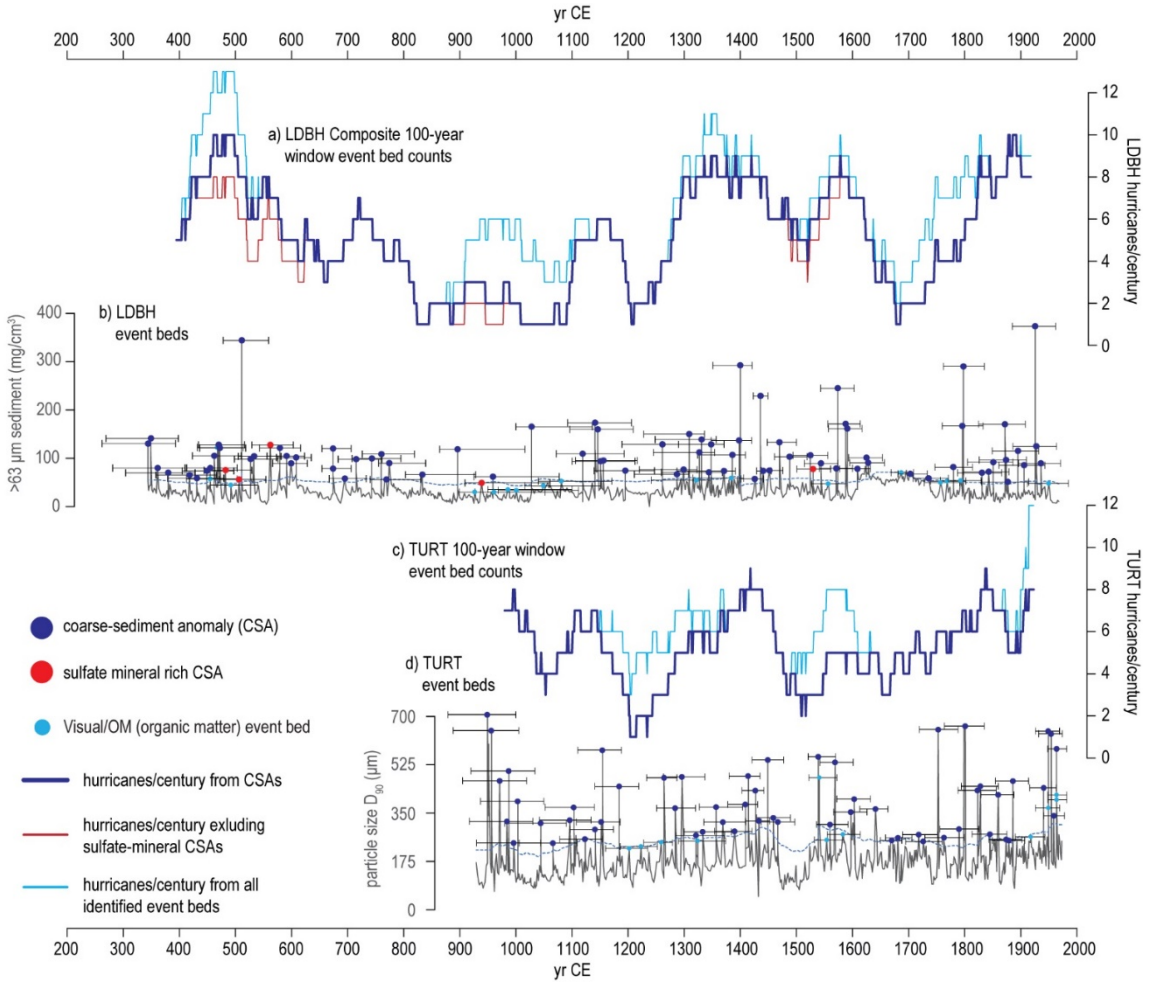

Figure 4.6. Hurricanes/century for LDBH Composite and TURT.
(a) 100-year sliding window counts of hurricane event beds per century from the (b) LDBH Composite. The light blue line is hurricanes/century from all >63 µm coarse sediment and OM anomalies, the dark blue line is hurricanes/century from all >63 µm coarse sediment anomalies, and the red line is hurricanes/century from >63 µm coarse sediment anomalies excluding red dots in (b) that are dominated by sulfate mineral crystals. (c) 100-year sliding window counts of hurricane event beds per century from the (d) TURT Record, with the symbology corresponding to the LDBH record described above. 2σ (95%) age-uncertainty windows for each sediment anomaly are shown by the horizontal black error bars in (b) and (d).

In the ~1040-year period that these two sediment records overlap from 930-1970 CE, the LDBH Composite archives 51-67 event beds, with 57-69 event beds documented by TURT. Given that these two sites are within 300 m of one another at similar elevations in the intertidal zone, it is likely that they have similar archival sensitivity. That said, local sediment supply, textural variability quantification methods (i.e. sieve-first LOI vs laser particle size), blue hole depth, and possible destruction or loss of event beds during core sectioning in the field can result in one record documenting more events than the other during some intervals. As such, these records were compiled into two LDBH-TURT composite records using the two different methods detailed in *4.3.5 Event Attribution and Frequency Calculation*, to best represent the local hurricane variability (Fig. 4.7). GBAM-TRA is the average, minimum, and maximum of the three (two) LDBH Composite (TURT) datasets (Figs. 4.6a and 4.7a) and GBAM-Stack was made by combining the maximum number of non-duplicate CSA event beds from each record (Fig. 4.7b). Overall, the GBAM-TRA (GBAM-Stack) has an average of 5.4 ± 2.1 (5.8 ± 2.2) (hurricanes/century, and average hurricanes/century from GBAM-TRA has a correlation coefficient of R = 0.87 with GBAM-Stack. Given these statistical similarities, we will hereafter refer only to the GBAM-TRA record when discussing the local and regional temporal variations in hurricane frequency as it demonstrates the range in uncertainty for hurricanes/century. However, the CSA derived event beds from GBAM-Stack are used to update the regional Bahamas Compilation discussed in *4.5.4 North Atlantic Regional Compilations* (Fig. 4.10c).

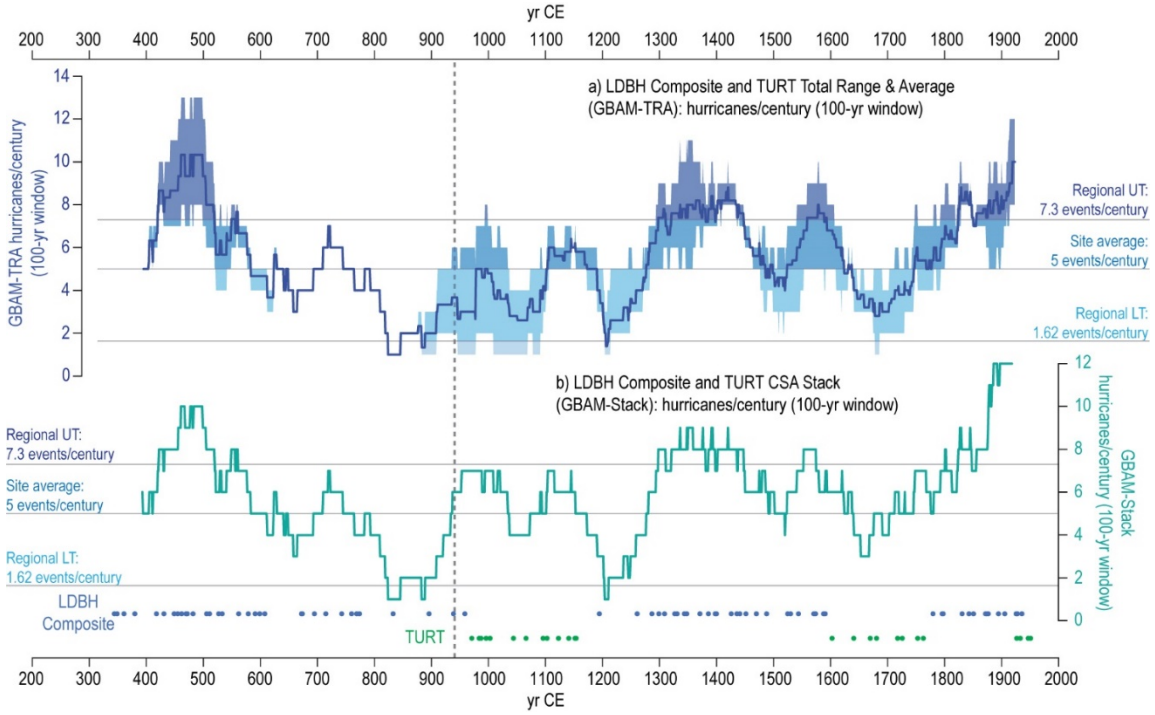

Figure 4.7. Grand Bahama composite records.
(a) Maximum, minimum, and average (dark blue line) hurricane event beds per century across correlated years in each of the hurricanes/century counts from Fig. 7a,c, hereafter referred to as GBAM-TRA. Counts above 7.3 events/century exceed the upper 95% regional hurricane frequency threshold calculated by (Wallace et al., 2019). (b) The teal line in is hurricanes/century based on the combined GBAM-Stack record, which combines all significant LDBH Composite and TURT coarse sediment anomalies into a single record that does not include duplicate events. Event beds from LDBH (TURT) are blue (green) dots.

The GBAM-TRA reconstruction documents 4 active intervals of significantly heightened hurricane frequency with maximum age-ranges from 420-520 CE, 1290-1450 CE, 1540-1610 CE, 1780-1920 CE that exceed the regional upper significance threshold of 7.3 hurricanes/century (≥Category 2 within 50 km; Fig. 4.7a). We acknowledge that this threshold may be too low given the uncertainty regarding the types of storms that impact LDBH and TURT, so this remains an estimate of significance to help differentiate the more vs less active periods. Overall, hurricane

frequency was generally higher than the site-specific reconstruction average of 5.8 hurricanes/century from 400-580 CE, 1270-1610 CE, and 1750-1920 CE, with generally lower than average activity that never exceeds the significance threshold from 580-1270 CE, and 1610-1750 CE.

4.5.3. Bahamian Hurricane Frequency

Substantial spatial heterogeneity is observed in local hurricane frequency across the Bahamian Archipelago from 1850 CE to present, with Grand Bahama and Abaco Island experiencing 11-16 ≥Category 2 hurricanes within 50 km compared to just 3-4 ≥Category 2 hurricanes within 50 km 300 km to the south near South Andros (Fig. 4.1a, Winkler et al., 2020). The LDBH Composite and TURT reconstructions extend and reinforce the understanding of regional paleo-hurricane variability over the last 1500-years that is informed by five other near-annually resolved reconstructions in a northeast to southwest transect across the Bahamian Archipelago (Fig. 4.8; Wallace et al., 2019, Wallace et al., Sub. March 2021, Wallace et al., 2021b, Winkler et al., Submitted 2021, Winkler et al., 2020). Each of these records provide insight to local hurricane patterns and how it may have impacted humans and the landscape (Fall et al., 2021), but the multi-decadal and centennial-scale variations documented by an individual record are not always consistent across the region (Fig. 4.8).

The GBAM-TRA reconstruction documents up to 14 hurricanes/century during the active interval from 420-520 CE, which precedes the temporal extent of the other 5 reconstructions stacked meridionally from north to south in Figure 4.8. This active interval does however coincide with more event beds related to intense hurricane activity

documented by a lower resolution but temporally longer record from an inland sinkhole on Abaco Island (van Hengstum et al., 2016). Reconstructed hurricane frequency is generally consistent across the Bahamian Archipelago until ~1000 CE. GBAM-TRA in the north archives relatively low hurricane frequency near Grand Bahama from 580-1270 CE with <4 hurricanes/century, which is also reflected by a lack of event beds in Blackwood from 600-1500 CE. During this time, GBAM-TRA archives brief spikes in frequency (6-7 hurricanes/century) from 710-745 CE and 935-1035 CE during the Medieval Warm Period (MWP; 950-1250 CE; Mann et al., 2009b). Further to the south, coeval periods of heightened frequency were documented by the South Andros Stack (Fig. 4.8c; Andros Island-central Bahamas; Wallace et al., 2019, Winkler et al., 2020) from 640-815 CE and 920-1035 CE, as well as the Middle Caicos Blue Hole reconstruction (Fig. 4.8g; Turks and Caicos-southernmost site; Wallace et al., Sub. March 2021) from 660-725 CE and 960-1110 CE.

At the onset of the last millennium, GBAM-TRA records a rise in activity to ~6 hurricanes/century from 1090-1190 CE while South Andros, Long Island (Fig. 4.8e; Long Island Blue Hole- central Bahamas; Wallace et al., 2021b), and Middle Caicos all experience relatively low hurricane frequency until 1150 CE, 1200 CE, and 1550 CE (respectively). Punctuated centennial scale periods of substantially heightened hurricane frequency were recorded across the Bahamian Archipelago throughout the LIA (~1300-1850 CE). In the northern Bahamas, GBAM-TRA recorded significant active intervals near Grand Bahama at the onset of the LIA from 1290-1450 CE, 1540-1610 CE, and at the tail end of the LIA from 1780-1920 CE (Fig 4.8a). The ~700-year Thatchpoint Blue

Hole reconstruction from Abaco Island also documents a significant rise in hurricane activity from 1500-1650 CE, with up to 13 hurricanes/century (Fig. 4.8b; Winkler et al., 2020). This coincides with a rise in coarse-sediment deposition and a decline in *Pinus* species pollen documented by sediment from Blackwood Sinkhole in northern Abaco, both of which are likely associated with saltwater inundation and winds from more frequent intense hurricanes (Fall et al., 2021, van Hengstum et al., 2016). Further to the south, South Andros documents active intervals during the LIA from 1150 to 1450 CE and 1600-1800 CE, with a notable drop in hurricanes/century from 1500-1600 CE when all five other near-annually resolved reconstructions from the Bahamian Archipelago record significant active intervals (Fig. 4.8c). The 550-year Hine's Hole reconstruction from Cay Sal Bank (Fig. 4.8d; Winkler et al., Submitted 2021) archives multidecadal active periods with 25-35 >Category 1 hurricanes/century within ~100 km of the blue hole from 1485-1505 CE, 1555-1605 CE, and 1735-1880 CE. Long Island experiences four significant active intervals from 1200-1300 CE, 1350-1500 CE, 1600-1655 CE, and 1775-1840 CE. Following a lull in activity from 1100-1550 CE, Middle Caicos experiences an active interval with 7-11 hurricanes/century for the remainder of the LIA from 1550-1900 CE. At the cease of the LIA, only Abaco (Thatchpoint) and Grand Bahama (GBAM-TRA) in the northern Bahamas document significant active intervals in the mid-1900s through the 20th Century, whereas all sites to south document relatively low hurricane frequency (Fig. 4.8).

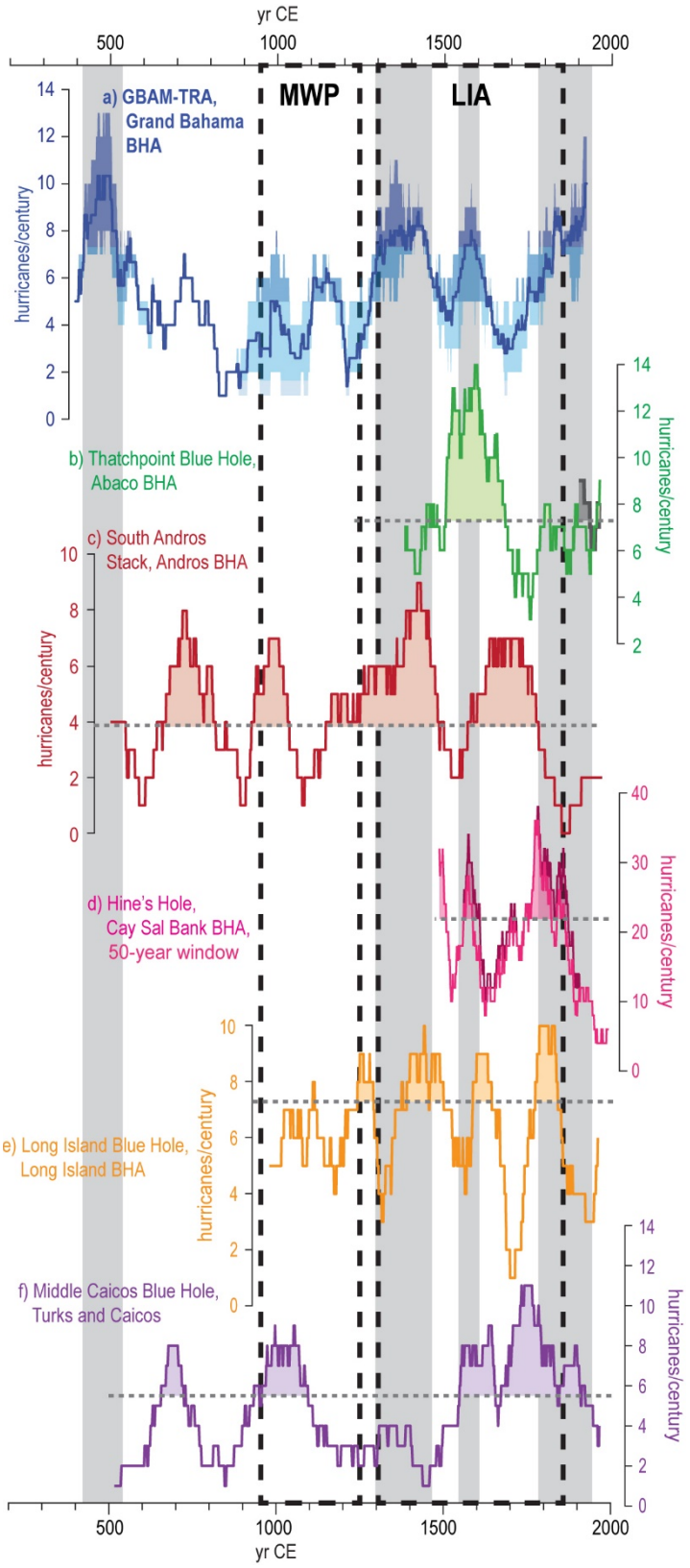
yr CE
500
1000
1500
2000
MWP
LIA
a) GBAM-TRA, Grand Bahama BHA
hurricanes/century
b) Thatchpoint Blue Hole, Abaco BHA
c) South Andros Stack, Andros BHA
d) Hine's Hole, Cay Sal Bank BHA, 50-year window
e) Long Island Blue Hole, Long Island BHA
f) Middle Caicos Blue Hole, Turks and Caicos

Figure 4.8. Hurricanes/century from near annually resolved reconstructions across the Bahamian Archipelago (see Fig. 4.1 for site locations).
Starting from north: (a) Maximum, minimum, and average hurricanes/century from LDBH and TURT (GBAM-TRA) on Grand Bahama; (b) ≥Category 2 (3) hurricanes/century within 50 (75) km of Thatchpoint Blue Hole on Abaco Island (Winkler et al., 2020); (c) ≥Category 3 hurricanes/century within 50 km of the Southern Andros region based on the stacked record from 3 blue holes (Wallace et al., 2019, Winkler et al., 2020); (d) 50-year moving window counts of ≥Category 1 hurricanes/century within 115 km of Hine's Hole on Cay Sal Bank (pink=high-confidence counts, maroon=reduced confidence counts; (Winkler et al., Submitted 2021); (e) ≥Category 2 hurricanes/century within 50 km of Long Island (Wallace et al., 2021b); and (f) ≥Category 2 hurricanes/century within 75 km of Middle Caicos Ocean Hole on Middle Caicos (Wallace et al., Sub. March 2021). Grey bars are LDBH-TURT active intervals exceeding the 7.3 hurricanes/century threshold.

The spatiotemporal variability between the 6 reconstructions in Figure 4.8 suggests that the spatial heterogeneity in regional hurricane frequency since 1850 CE likely persists to some degree over longer time scales. This is likely influenced in part by the slightly different archival sensitivity (i.e., intensity, proximity, orientation) of each blue hole. More importantly, each of these Bahamian hurricane reconstructions likely records a slightly different subset of the broader population of hurricanes that impacts the northern Caribbean, as evidenced by variability in cyclogenesis locations of hurricanes that pass within each site's archival sensitivity threshold from 1850-2019 CE (Fig. 4.9). For example, sites like Thatchpoint Blue Hole from Abaco and Middle Caicos Blue Hole from Turks and Caicos are primarily impacted by hurricanes that form across the Main Development Region from 10° and 20°N (MDR; Goldenberg and Shapiro, 1996), whereas other sites like LDBH-TURT and Long Island Blue Hole are impacted by a more even mixture of hurricanes from both the MDR and Southern Caribbean (Fig. 4.9). While these records do archive significant local frequency variations, Wallace et al. (2021a) demonstrated that inherent stochastic variance in hurricane cyclogenesis and

tracks, independent of broader climate forcing, can produce significant centennial-scale variations in local hurricane activity in the Caribbean. Further, each site's archival sensitivity varies in response to elevation, orientation of the site/island to storm passage, and surrounding coastal landforms. Based on this, a single reconstruction may not always reflect broader changes in regional hurricane climatology.

4.5.4. North Atlantic Regional Compilations

In order to estimate broader trends in paleo-hurricane frequency variability across the North Atlantic, Mann et al. (2009a) statistically compiled eight sediment records of hurricane overwash into a single 1500-year long composite record for the North Atlantic (M09 hereafter). However, this compilation was limited by spatial coverage of available hurricane reconstructions, along with substantial variance in reconstruction resolution and storm-archival sensitivity. More recently Wallace et al. (2021b) and Wallace et al. (Sub. March 2021) modified the methods of Mann et al. (2009a) to develop new regional compilations using only near-annually to decadally-resolved sedimentary reconstructions from the Bahamian Archipelago (Wallace et al., 2019, Wallace et al., Sub. March 2021, Wallace et al., 2021b, Winkler et al., 2020), New England (Boldt et al., 2010, Castagno et al., 2021, Donnelly et al., 2015), and northern Florida Gulf of Mexico (GoM) coast (Brandon et al., 2013, Lane et al., 2011, Rodysill et al., 2020). Using methods detailed by Wallace et al. (2021b) and reviewed in *APPENDIX D Section S4.1.2*, we update the Bahamian Compilation to include the 1700-year GBAM-Stack reconstruction from Grand Bahama (Fig. 4.10c). This updated Bahamian Compilation, which we hereafter refer to as $\text{Bahamas}_{\text{pdf-5}}$, now includes 5 total

records, with 3 from across the Bahamian Archipelago spanning at the last 1500-years: (i) GBAM-Stack (1700-years, northern Bahamas), (ii) South Andros Stack (1500-years, central Bahamas), and (iii) Middle Caicos Blue Hole (1500-years, southernmost site). The only near annually resolved Bahamian blue hole paleo-hurricane record not included in $BHAC_{pdf\text{-}5}$ is Hine's Hole from Cay Sal Bank, which is excluded due to its much higher recording sensitivity (most ≥Category 1 hurricanes within ~100 km) that results in 2-3 times more hurricanes/century recorded on average than any of the other 5 Bahamian records (Fig. 4.10b). We supplement this compilation method with a new compilation of relative variance in regional hurricane frequency hereafter referred to as $BHAC_{stand\text{-}6}$, wherein hurricanes/century based on the median-age estimated for all 6 Bahamian records were standardized to the same scale following then averaged together following the methods in *APPENDIX D Section S4.1.2* (Figs. 4.10c and 4.11a). In addition to updating the $BHAC_{pdf\text{-}5}$, we extend the New England and Florida Gulf Compilations, hereafter NE_{comp} and $FGoM_{comp}$ back to 200 CE following the methods of Wallace et al. (2021b), then standardize the scale of hurricanes/century for these compilations so that they can be averaged with $BHAC_{stand\text{-}6}$ to estimate broader scale Atlantic hurricane frequency variance (Fig. 4.11c,d).

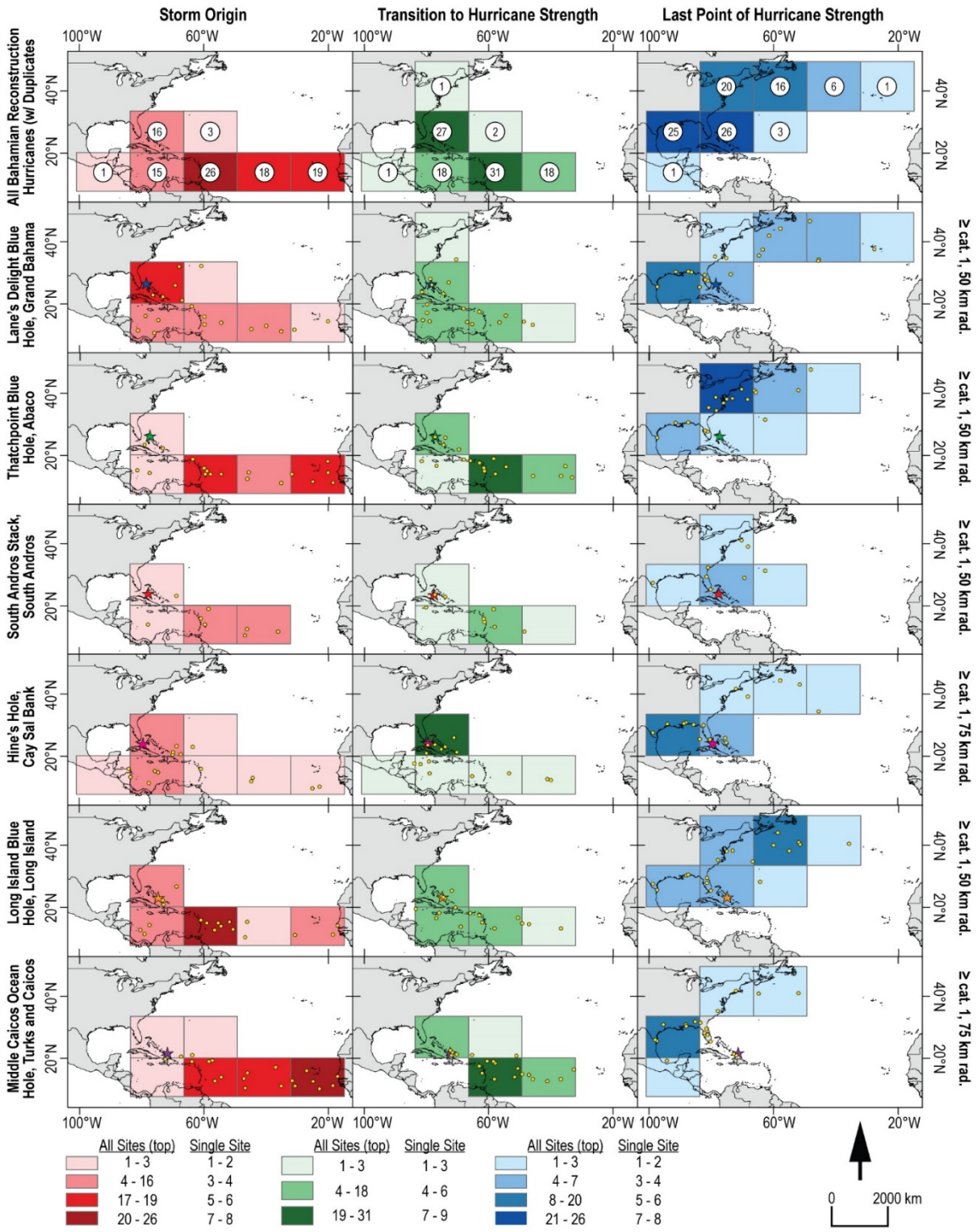

Figure 4.9.Points of origin, transition into hurricane strength, and last location of hurricane strength of all storms that passed within the approximate site-specific sensitivity radius of the six hurricane reconstructions in Fig. 8 from 1850 to 2019 CE as a ≥Category 1 hurricane.

Figure. 4.9 (continued). Site-specific sensitivity radius is based on the values described in the original studies, and the colored stars in each panel show location of the reconstruction that the color corresponds to from Figure 4.1 and 4.8 (also listed on each right y-axis). The color of the cells in the 5x3 grids (add bounds and size) represents the number of points (yellow dots) falling within entirely within the cell, with darker colors associated with more points. The top row includes all points (including duplicates) identified for all six sites.

Based on the instrumental record (Fig. 4.9a), the 5-6 Bahamian paleohurricane records used in the compilations likely reflect changes primarily to MDR sourced storms that go on to impact either the Eastern Seaboard or GoM, most similar to "Cluster 3" storms described by Kossin et al. (2010). The 5 -sites within $BHAC_{pdf\text{-}5}$ and 6 sites in $BHAC_{stand\text{-}6}$ have the potential to respectively document 49% and 59% of the 112 ≥Category 1 hurricanes that pass through the Bahamian Archipelago region from 1950 to 2020 CE (*Appendix D Section S4.1.3***,** APPENDIX D Fig. S4.8). Both new Bahamian compilations document increased hurricane frequency from 670-810 CE, 930-1040 CE, and 1300-1850 CE and have a high correlation coefficient of r = 0.83 (Figs. 4.10c and 4.11a). The $BHAC_{pdf\text{-}5}$ compilation estimates an average 33 ± 3 hurricanes/century across the Bahamian Archipelago from 1350-1850 CE during the LIA. This 500-year span documents 8.6 ± 3 more hurricanes/century than the other 1000-years of the $BHAC_{pdf\text{-}5}$ compilation. While not included in the $BHAC_{pdf\text{-}5}$ compilation, Hine's Hole also documents significant multidecadal-scale active intervals during the LIA from 1485-1505 CE, 1555-1605 CE, and 1735-1870 CE, with ~28 hurricanes/century on average (up to 35 hurricanes/century) during these periods. As discussed by Winkler et al. (Submitted 2021), active periods documented by the Hines Hole Composite are coeval with increased shipwrecks and observed storms in reconstruction based on

historical sailing documents and a suppressed pine tree growth in the Florida Keys from 1550-1650 CE and 1700-1900 CE (Trouet et al., 2016, García-Herrera et al., 2005).

The Bahamian compilations exhibit varying levels of similarity to other regional compilations in the North Atlantic (Figs. 4.10 and 4.11). Overall, the 1800 year long New England and Florida Gulf Compilations document far-fewer hurricanes/century than the $BHAC_{pdf\text{-}5}$, which is to be expected as the areas these compilations represent are impacted by far less ≥Category 2 hurricanes/century during the instrumental record than most of the Bahamian Archipelago (APPENDIX D Fig. S4.6; Winkler et al., 2020). The NE_{comp} (Figs. 4.10d and 4.11c) documents higher than average hurricane frequency (>2.5 hurricanes/century) from 300-600 CE, 1010-1150 CE, 1380-1700 CE, and 1900 CE to the end of the 100-year smoothed record at 1970 CE (includes up to 2020 CE). $FGoM_{comp}$ includes high-threshold (HT; ≥Category 3) and low-threshold (LT; ≥Category 1) composites, but we will only focus on the LT compilation for the sake of discussion as it is more similar to the archival sensitivity of the Bahamian Compilations (Figs. 4.10 and 4.11c). The LT-$FGoM_{comp}$ Compilation shows above average hurricane frequency (>5 hurricanes/century) from 200-300 CE, 750-1300 CE, 1400-1500 CE (not archived in HT), and 1800-1950 CE. Overall, the standardized regional compilations in Figure 4.11 show weak positive correlation between the Bahamian compilations and the NE_{comp}, but the $FGoM_{comp}$ has weak negative correlation with the other regional compilations. The often antiphase nature of $FGoM_{comp}$ to the other regional compilations supports the observations of Donnelly et al. (2015), who noted that many individual proxy records from the Eastern seaboard document elevated hurricane frequency from 1400-1675 CE,

when most records from the GoM suggested lower frequency. Figure 4.11d shows the results of averaging the yearly values for the standardized $BHAC_{stand\text{-}6}$, NE_{comp}, and $LT\text{-}FGoM_{comp}$ regional compilations together, and provides an estimate for broader variance in North Atlantic hurricane frequency (NAT_{comp}) over the last ~1600-years.

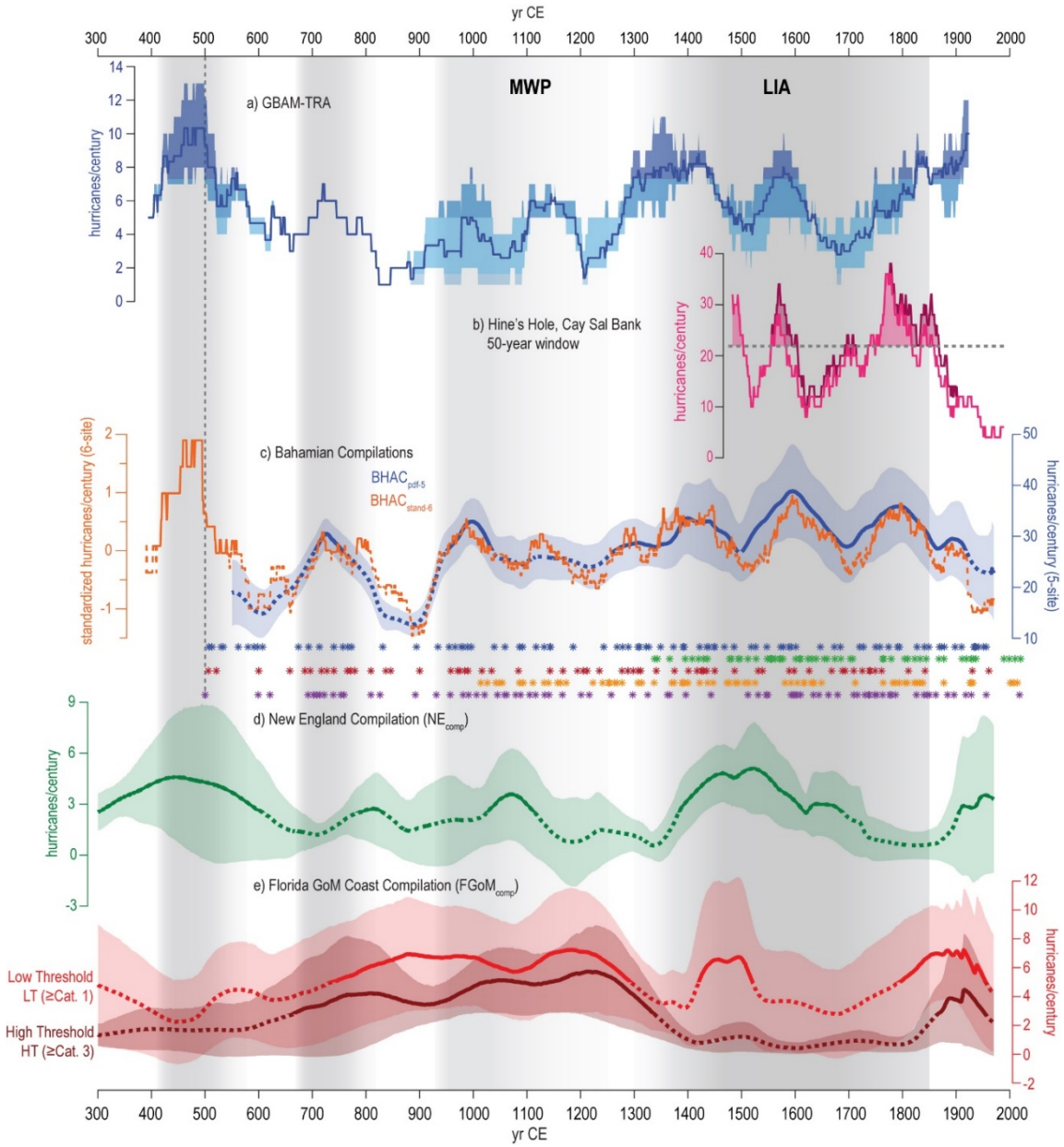

Figure 4.10. Regional paleohurricane compilations.

(a) GBAM-TRA hurricanes/century from LDBH and TURT on Grand Bahama. (b) 50-year moving window counts of most ≥Category 1 hurricanes/century within 115 km of Hine's Hole on Cay Sal Bank (Winkler et al., Submitted 2021). (c-e) 100-year moving window smoothed paleo-hurricane frequency compilations. Shaded confidence intervals for each compilation are calculated from the spread in counts from each record included for the region. window (c) The blue line is a 1500-year compilation of 5 near-annually resolved paleohurricane reconstructions from the Bahamian Archipelago ($BHAC_{pdf\text{-}5}$), which includes the GBAM-Stack from Figure 7b and all studies from Figure 8 aside from Hine's Hole. The dots below are the event beds identified in the studies from Figure 8, and the color of the dot corresponds to the colors used in Figure 8. The orange line is the average all 6 Bahamian reconstructions from Figure 8, wherein hurricanes/century was standardized for each record ($BHAC_{stand\text{-}6}$). 1700-year compilations of storm events from (c) New England (NE_{comp}, green) that includes records from Salt Pond, MA (Donnelly et al., 2015) and Mattapoisett Marsh (Castagno et al., 2021, Boldt et al., 2010), and (d) northwest Florida GoM Coast ($FGoM_{comp}$, red) including records from Mullet Pond, FL (Lane et al., 2011), Spring Creek Pond (Brandon et al., 2013), Shotgun Pond and Basin Bayou (Rodysill et al., 2020). Compilation methods are detailed in (Wallace et al., 2021). The shaded confidence intervals are calculated from the ages produced in Monte Carlo age-simulations run using the Bayesian age-modelling program Bacon (Blaauw and Christen, 2011) for each of the contributing records. All compilations shown were smoothed with a 100-year moving window. The $FGoM_{comp}$ in d) includes a High Threshold (dark red - ≥Category 3) and Low Threshold (red - ≥Category 1) estimates. For all compilations, mean estimated hurricanes/century are solid (dashed) if above (below) the mean hurricanes/century for the region compilation.

Given that $FGoM_{comp}$ is often antiphased with NE_{comp} and $BHAC_{stand\text{-}6}$, NAT_{comp} typically only reflects above average frequency when two or more of the regional compilations document higher frequency. The two longest and highest magnitude active periods in NAT_{comp} are from 950-1200 CE, which was documented by M09 and spans most of the MWP, and 1400-1600 CE, which represents most of the first half of the LIA but was not documented by the M09 compilation (Fig. 4.11d). The MWP and LIA were climatologically distinct, offering a unique opportunity to assess the potential climatological forcing and spatial variance in regional hurricane frequency that produce overall high frequency during these two periods.

4.5.5. Climatic Forcing

Ambient thermodynamic conditions are capable of influencing where cyclogenesis occurs, both in terms of where the storm is initially seeded by a low pressure cell and in the ability for the cyclonic rotation to intensify (Gray, 1968, McBride and Zehr, 1981). Once a tropical cyclone forms, regional ocean/climate conditions exert further influence on storm track and development by modulating upper limits on potential intensity of as the hurricane travels across the ocean (Emanuel, 1986, Kossin et al., 2010, Emanuel, 2000, Holland, 1997, Wing et al., 2007). As reviewed by Korty et al. (2012) and Wallace et al. (Sub. March 2021), the mechanisms that control basin-wide and intra-regional hurricane variability during the Common Era remain an active area of research and likely represent an amalgamation of basin-wide and local climatic control. These factors can include SST variability both locally and at the point of storm origin (Mann et al., 2009a, Donnelly et al., 2015, Kossin, 2017, Kossin et al., 2010), shifting intensity of the North Atlantic Subtropical High (NASH) that can alter the direction of storm tracks (Baldini et al., 2016, Liu and Fearn, 2000, Elsner, 2003, Elsner and Kocher, 2000, Xie et al., 2005, Wallace et al., 2019, Knowles and Leitner, 2007, Yang et al., 2020), localized changes in vertical wind shear that can restrict regional hurricane intensification regardless of conditions throughout the basin (Kossin, 2017, Ting et al., 2019). North Atlantic climatology is largely tied to major basin and global scale climate features including the North Atlantic Oscillation (NAO), El Nino Southern Oscillation (ENSO), position and intensity of the Intertropical Convergence Zone (ITCZ), solar insolation, and Atlantic Meridional Overturing Circulation (AMOC).

However, the expression of these features varies both temporally and spatially. As such, it remains unclear whether hurricane frequency variability documented by the instrumental record (Figs. 4.1a and 4.9; APPENDIX D Fig. S6) and individual paleo-hurricane reconstructions (Figs. 4.8 and 4.11) shifts predictably in response to climate over the last two millennia (Kossin and Camargo, 2009).

Warmer SSTs in the tropical North Atlantic can be associated with a northward shift or expansion of the ITCZ, which can also promote cyclogenesis in the MDR by reducing local vertical wind shear by allowing the ascending branch of Hadley Circulation to shift northward (Kossin and Vimont, 2007, Chang et al., 1997). Based on this, centennial scale migrations in the mean ITCZ position could be influence North Atlantic hurricane variability during the late Holocene (Donnelly et al., 2015, van Hengstum et al., 2016, Baldini et al., 2016). In the millennium prior to ~1100 CE, the ITCZ shifted largely north and became more stable based on increased titanium influx into the Cariaco Basin, Venezuela driven by increased rainfall (Haug et al., 2001) as well as a rise in the Northern to Southern Hemisphere Temperature Anomaly (Schneider et al., 2014; calculated partially using the Cariaco Basin Ti data from Haug et al., 2001). This is consistent with warmer MDR SSTs during the MWP modelled by (Mann et al., 2009a). Conversely, the ITCZ was shifted relatively southward throughout most of the LIA (Schneider et al., 2014, Haug et al., 2001), promoting cooler MDR SSTs and conditions that would typically be unfavorable for cyclogenesis. However, NAT_{comp} shows the highest overall hurricane frequency from 1400-1600 CE, thus suggesting a different mechanism may be responsible. Despite globally cooler LIA SSTs, warmer

local SSTs were documented by an annually resolved coral reconstruction from the northern Great Bahama Bank from the start of the record at ~1550 CE until 1600 CE (Saenger et al., 2009), as well as in the Gulf of Maine at ~1400 CE (Wanamaker et al., 2008). This 200 year span is which is coeval with invigoration of AMOC from 1400-1600 CE (Rahmstorf et al., 2015). Local SST variance can sustain or intensify storms, so it is possible that the rise in frequency from 1400-1650 CE in NE_{comp} and the Bahamian compilations is related to the warmer waters along the Eastern Seaboard sustaining or even intensifying hurricanes (Donnelly et al., 2015). Further, increased breaching of barrier islands on the Outer Banks of North Carolina from 1400-1675 CE (Mallinson et al., 2011) as well as increased hurricane activity in Nova Scotia from 1450-1600 CE (Oliva et al., 2018, Yang et al., 2020) may suggest higher hurricane frequency along much of the Eastern Seaboard during this interval. Interestingly, (Kossin, 2017) and (Ting et al., 2019) observe a dipole pattern over the past 50 years in which the U.S. East Coast has warmer (cooler) SSTs and weaker (stronger) VWS during periods where the MDR has cooler (warmer) and stronger (weaker) VWS. If this dipole persists over time, this could also contribute to higher frequency in the NE_{comp} and Bahamian compilations during the LIA despite generally unfavorable MDR conditions.

As suggested by (Wallace et al., 2021a), it is also possible that the relatively minimal annual variance in mean western tropical North Atlantic SSTs has an insignificant impact on long-term Caribbean hurricane activity. Saenger et al. (2009) demonstrate that summertime SST variance in the northern Bahamas over the last 550 years deviates no more than 1.4 °C lower or 0.2 °C higher than the modern mean of ~26

°C. Notably, the most substantial rise in SST from 1850 CE to present aligns with lower hurricane frequency in the Bahamian compilations. Thus, while warmer SSTs likely have a substantial impact on hurricane activity along the Eastern Seaboard where SSTs are not always conducive for sustaining or intensifying hurricanes, the new GBAM composites and updated Bahamian compilations support previous work that suggests local SSTs have minimal impact on hurricane frequency in tropical regions like The Bahamas (Wallace et al., Sub. March 2021, Wallace et al., 2021b).

The NAO index represents the difference in surface sea-level pressure difference between the NASH and the Subpolar Low. Overall, a negative (positive) NAO index is often associated with weaker (stronger) NASH with a retracted (expanded) western boundary along the Eastern Seaboard (Kossin et al., 2010). The NASH is a semi-permanent high-pressure system centered near Bermuda (Zishka and Smith, 1980) that can affect the steering currents that determine Atlantic hurricane tracks and rainfall delivery (Ortegren and Maxwell, 2014, Kossin et al., 2010). Knaff (1997) also suggests that a positive phase of spring/summer NAO is associated with stronger sea-level pressure anomalies and higher regional VWS in the tropical Atlantic (particularly in the Caribbean) that can restrict tropical cyclone formation and intensification. In the instrumental record, studies finds that a negative NAO results in more storms forming overall, and the compounding effect of eroded western boundary would allow more storms to follow and recurve path and impact Eastern Seaboard (Kossin et al., 2010, Ortegren and Maxwell, 2014). NAO impacts North Atlantic Climate year round, but is most dominant in the Winter months (Barnston and Livezey, 1987).

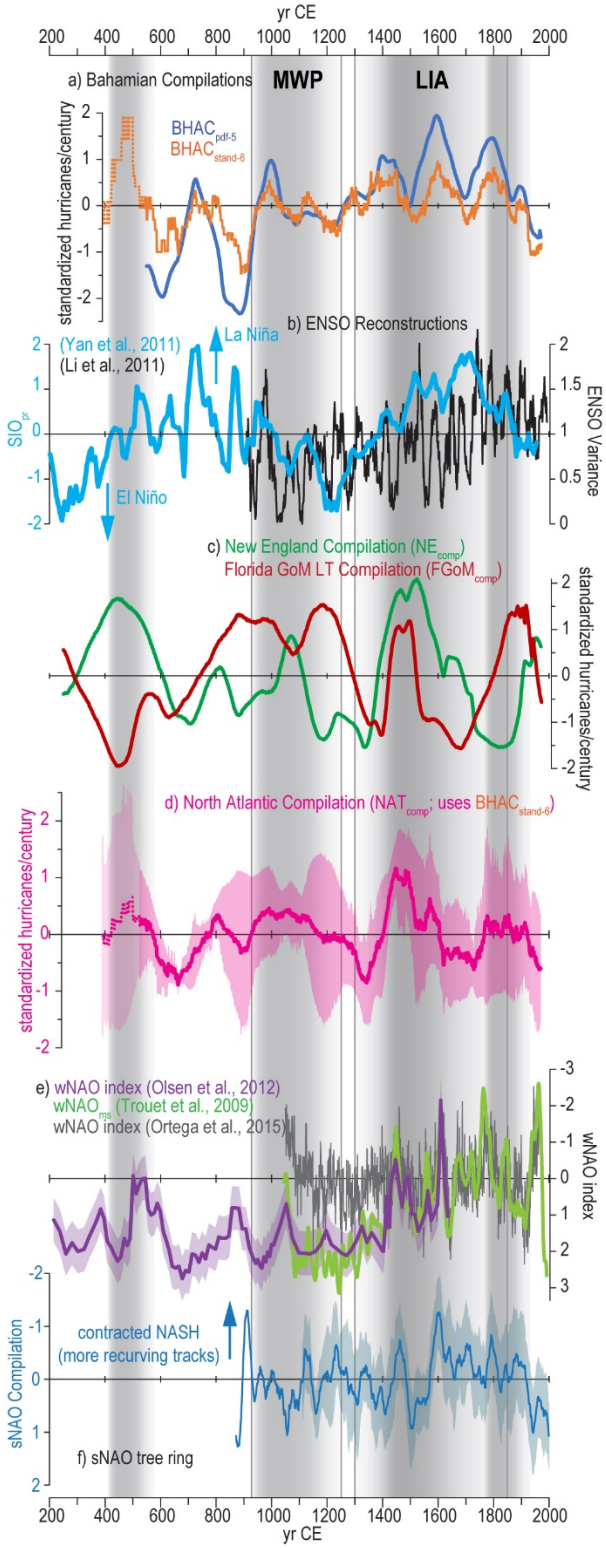

Figure 4.11. Standardized regional paleo-hurricane compilations and climate reconstructions.

(a) **Standardized hurricanes/century for $BHAC_{pdf\text{-}5}$ (blue) and $BHAC_{stand\text{-}6}$ (orange). The Dashed portion of BHACstand-6 prior to ~500 CE only includes GBAM-Stack data, so this portion of the compilation has higher uncertainty. (b) The blue line is a Southern Oscillation Index ($SIO_{pr)}$ proxy from compiled hydroclimate proxy reconstructions that reflect the difference between normalized annual rainfall in the tropical western Pacific and the equatorial eastern and mid-Pacific by Yan et al. (2011), who attributes positive indexes to La Niña like conditions. The black line is variance in ENSO amplitude calculated by Li et al. (2011) based on the North American Drought Atlas (NADA, (Cook et al., 2008, Cook et al., 2004)). (c) Standardized hurricanes/century for the 1700-year compilations of storm events from NE_{comp} (green) and the $LT\text{-}FGoM_{comp}$ (red). (d) Average yearly values for standardized hurricanes/century from $BHAC_{stand\text{-}6}$, NE_{comp}, and $LT\text{-}FGoM_{comp}$ that represent a broader estimate of hurricane frequency variability in the North Atlantic (NAT_{comp}, pink). The pink shading is the ± standard deviation of the averaged values. (e) Proxy reconstructions for winter NAO (wNAO) based on compiled tree ring and speleothem hydroclimate records (Trouet et al., 2009) and Greenland lake sediment record of variations in Mn/Fe ratio wherein higher Mn/Fe ratios indicate oxic lake conditions associated with a negative wNAO (Olsen et al., 2012), and a model tested compilation of a 48-record compilation of wNAO (Ortega et al., 2015). (f) The blue line is compilation of tree-ring records that reflect summer NAO (sNAO) which was produced by averaging the standardized proxy data from (Folland et al., 2009, Linderholm et al., 2015, Rydval et al., 2017, Zhang et al., 2016). Light blue shading is the ± standard deviation of the four averaged records.**

Proxy reconstructions of NAO that span the Common Era are based on hemispheric temperature gradients and variance in compiled North Atlantic hydroclimate proxies and models from high vs low latitudes (Trouet et al., 2009, Olsen et al., 2012, Ortega et al., 2015). However, most records document wintertime variance in NAO (wNAO) that may not be transferable to the more subtle summertime NAO (sNAO) that coincides with Atlantic hurricane season from June-November. During sNAO positive (negative) positive phase, the NASH expands (contracts), deflecting extratropical storm tracks and causing dry/hot (wet/cool) conditions over northwestern Europe (Folland et al., 2009). Folland et al. (2009) were the first to compile tree ring records from northwestern Europe to reconstruct high summer (July-August) sNAO.

Linderholm et al. (2015), Zhang et al. (2016), and Rydval et al. (2017) went further and identified that summer temperatures reconstructed from tree rings can also be indicative of sNAO variability. Based on this, we standardize and compile four records of tree ring growth that were specifically linked to summertime variability in rainfall driven primarily by sNAO (Folland et al., 2009, Rydval et al., 2017, Linderholm et al., 2015, Zhang et al., 2016) by following the same methods used develop to $BHAC_{stand\text{-}6}$ and NA_{comp} (Fig. 4.11f, *Appendix D Section S4.1.2*). Both wNAO and sNAO show substantial a negative index from ~1400-1500 CE when NE_{comp} and NAT_{comp} record most frequent hurricane activity (Fig. 4.11d), which could indicate a contracted NASH that would allow more recurving storm tracks during this time. Both sNAO and wNAO remained in a negative phase for the remainder of the LIA coinciding with higher frequency in the Bahamian compilations and lowest sustained hurricane frequency in the LT- and HT-FGoM compilations. While NAO reconstructions are not necessarily a direct representation, a weakened NASH associated with negative NAO index could drive more recurve tracks along the Eastern Seaboard during LIA that correspond to generally higher hurricane frequency in NE_{comp} and the Bahamian compilations while the $FGoM_{comp}$ generally reflects low hurricane frequency (Fig. 4.11).

El Niño-Southern Oscillation (ENSO) encompasses the coupled effects of east to west shifts in atmospheric pressure alongside Walker Circulation (i.e., Southern Oscillation) and changes in tropical Pacific SST (El Niño). In the North Atlantic, observed ENSO teleconnections are associated with warmer SSTs and lower VWS in the MDR during La Niña phases and cooler SSTs and higher VWS during El Niño phases.

Thereby, La Niña conditions promote more hurricane activity in the tropical North Atlantic (Gray, 1968, Kossin et al., 2010, Shapiro, 1987, Kossin and Vimont, 2007). However, it is unclear if the teleconnections ENSO and Atlantic hurricane activity persist over time.

ENSO indexes derived from variance in regional Pacific SSTs (e.g., Nino 3, Nino 3.4) generally suggest that the MWP was dominated by La Niña like conditions that may have contributed to elevated hurricane activity observed in all three compilations (e.g., Mann et al., 2009a; Fig. 4.11d). However, these same SST based indexes also suggest more El Niño like conditions during the LIA when the Bahamian compilations and NE_{comp} document a rise in regional hurricane frequency. A compilation of tropical Pacific hydroclimate proxy reconstructions that reflects atmospheric changes related to the Southern Oscillation by Yan et al. (2011) alternatively suggests that the LIA may have actually dominated by La Niña conditions from 1400-1800 CE (Fig. 4.11b). The Yan et al. (2011) Southern Oscillation compilation observes the difference between normalized annual rainfall in the tropical western Pacific and the equatorial eastern and central-Pacific, which forms a Southern Oscillation Index (SIO_{pr}) that is likely more indicative of the atmospheric component of ENSO rather than SST changes. It is beyond the scope of this study to reconcile these disagreements; however, some studies have shown that variance in ENSO amplitude and interregional proxy variance (based on the North American Drought Atlas-NADA, Cook et al., 2008, Cook et al., 2004) are both elevated in LIA relative to MWP (Li et al., 2011, Li et al., 2013)(Fig. 4.11b). Still other studies have demonstrated that ENSO index amplitude variance

between the LIA and MWP is insignificant, but that ENSO teleconnections over North America were significantly stronger during the LIA, thus producing more intense El Niño vs La Niña like states (Dee et al., 2020).

Despite lingering uncertainty in the timing, magnitude, and nature of regional impacts of Common Era ENSO variability, existing research broadly indicates substantial ENSO related reorganization of ocean atmospheric conditions during the LIA. While all three-regional paleo-hurricane compilations suggest higher activity at the onset of the LIA, only the two Bahamian compilations document above average hurricane activity throughout the entire LIA coinciding with a sustained positive Southern Oscillation index (SIO_{pr}; Fig. 4.11a). Most records in the Bahamian compilations can document weaker, Category 1 hurricanes, so it is possible that more hurricanes were forming in the tropics throughout LIA, but were dissipated by unfavorable local conditions in GOM and Eastern Seaboard (e.g., higher VWS and cooler SSTs). This suggests that changes variability in ENSO during the LIA may have produced more favorable conditions for hurricanes in tropics (Fig. 4.11a, b), even if conditions do not promote hurricane activity elsewhere in the Atlantic. We do not have the means to confidently determine the exact spatiotemporal impact ENSO variance on North Atlantic SSTs, VWS, and NASH position until more paleo and model records are assimilated. That said, the coeval rise of documented tropical Atlantic hurricane frequency with known shifts in ENSO state is significant, and merits future study.

Finally, changes in the number of tropical cyclones that form in the North Atlantic overall may play a role in hurricane frequency variability documented by the

new Bahamian compilations. African Easterly tropical waves are warmed as they move over the Atlantic Ocean to the west of Africa, thus promoting convection that forms areas of low-pressure that can intensify and develop into hurricanes in MDR if local conditions (e.g., SST, VWS) are conducive (Gray, 1990, Riehl, 1954). Gray (1990) found that more African Easterly tropical waves form during periods with a stronger West African Monsoon, which is also coincident with higher rainfall in the Sahel Region of western Africa. As reviewed by Nash et al. (2016) and further supported by a 1600-year reconstruction of Sahel rainfall based on mollusc shell $\delta^{18}O$ (Carré et al., 2019), Sahel rainfall was higher throughout most of the LIA from 1350-1900 CE relative to dryer conditions documented during most of the MWP. Higher Sahel rainfall during the LIA suggests a stronger West African Monsoon and more African Easterly Waves during this time, which could result in more tropical cyclones forming in the MDR. Hurricanes documented by the records in the Bahamian compilations are primarily sourced from MDR over the last ~170 years (~65%; Fig. 4.9). As such, it is possible that higher MDR sourced hurricane frequency during the LIA could contribute to higher hurricane frequency documented by the Bahamian compilations from 1350-1850 CE (Figs. 4.10 and 4.11), and that multidecadal variance in local VWS and steering related to NASH likely exert further influence on which of these storms impact The Bahamas.

4.6. Conclusions

We develop a 1700-year record of paleo-hurricane frequency in the northern Bahamas using two near-annually resolved sediment records from blue holes on the

northern coast of Grand Bahama (LDBH Composite and TURT; GBAM-TRA and GBAM-Stack). We update an existing four-record compilation of Common Era hurricane frequency variability in the northern Caribbean ($BHAC_{pdf\text{-}5}$) with the new Grand Bahama Composite record (GBAM-Stack), and present a new standardized Bahamian Compilation that includes six near-annually resolved proxy reconstructions of Bahamian Paleohurricane activity ($BHAC_{stand\text{-}6}$). These Bahamian compilations establish with confidence that northern Caribbean hurricane frequency was substantially elevated throughout most of the Little Ice Age (LIA) relative to the rest of the 1500-year record, including most of the Medieval Warm Period (MWP). Temporal uncertainty and variance in proxy interpretation restrict confidence in the precise climatic mechanisms at any given time; however, these Bahamian active intervals are consistently coeval with negative phases of NAO and increased ENSO variability over the last 1500-years. We standardize and compile regional compilations from New England (NE_{comp}) and the Florida Gulf of Mexico ($LT\text{-}FGoM_{comp}$) to form a broad compilation of Common Era hurricane frequency variability in the North Atlantic (NAT_{comp}), which documents above average hurricane frequency during the MWP and LIA from 1400-1600 CE, as well as the 1800s. Regardless of the degree to which climate vs stochasticity influences regional hurricane frequency, these compilations demonstrate with high-confidence that multidecadal to centennial scale hurricane frequency can substantially exceed levels observed since 1850 CE. A return to these levels could have severe consequences for The Bahamas throughout the next century given the projected rise in sea level and changes in hurricane climatology.

4.7. References

ALSHARHAN, A. & KENDALL, C. S. C. 2002. Holocene carbonate/evaporites of Abu Dhabi, and their Jurassic ancient analogs. *Sabkha ecosystems. Kluwer Academic Publishers, Dordrecht, The Netherlands*, 187-202.

ARCOS, N., CHACON-BARRANTES, S., VARNER, J. & LOPEZ, A. 2018. Caribbean and Adjacent Regions Tsunami Sources and Models (CATSAM) Map Viewer.

BALDINI, L. M., BALDINI, J. U., MCELWAINE, J. N., FRAPPIER, A. B., ASMEROM, Y., LIU, K.-B., PRUFER, K. M., RIDLEY, H. E., POLYAK, V. & KENNETT, D. J. 2016. Persistent northward North Atlantic tropical cyclone track migration over the past five centuries. *Scientific reports,* 6**,** 37522.

BARKAN, R., URI, S. & LIN, J. 2009. Far field tsunami simulations of the 1755 Lisbon earthquake: Implications for tsunami hazard to the US East Coast and the Caribbean. *Marine Geology,* 264**,** 109-122.

BARNSTON, A. G. & LIVEZEY, R. E. 1987. Classification, seasonality and persistence of low-frequency atmospheric circulation patterns. *Monthly weather review,* 115**,** 1083-1126.

BERKELEY, A. & RANKEY, E. C. 2012. Progradational Holocene carbonate tidal flats of Crooked Island, south-east Bahamas: An alternative to the humid channelled belt model. *Sedimentology,* 59**,** 1902-1925.

BHATIA, K., VECCHI, G., MURAKAMI, H., UNDERWOOD, S. & KOSSIN, J. 2018. Projected response of tropical cyclone intensity and intensification in a global climate model. *Journal of Climate,* 31**,** 8281-8303.

BIGUENET, M., SABATIER, P., CHAUMILLON, E., CHAGUÉ, C., ARNAUD, F., JORISSEN, F., COULOMBIER, T., GEBA, E., CORDRIE, L. & VACHER, P. 2021. A 1600 year-long sedimentary record of tsunamis and hurricanes in the Lesser Antilles (Scrub Island, Anguilla). *Sedimentary Geology,* 412**,** 105806.

BLAAUW, M. & CHRISTEN, A. 2011. Flexible paleoclimate age-depth models using an autoregressive gamma process. *Bayesian Analysis,* 6**,** 457-474.

BOARDMAN, M. R. & NEUMANN, A. C. 1984. Sources of periplatform carbonates; Northwest Providence Channel, Bahamas. *Journal of Sedimentary Research,* 54**,** 1110-1123.

BOLDT, K. V., LANE, P., WOODRUFF, J. D. & DONNELLY, J. P. 2010. Calibrating a sedimentary record of overwash from Southeastern New England using modeled historic hurricane surges. *Marine Geology,* 275**,** 127-139.

BOTTRELL, S. H., SMART, P. L., WHITAKER, F. & RAISWELL, R. 1991. Geochemistry and isotope systematics of sulphur in the mixing zone of Bahamian blue holes. *Applied Geochemistry,* 6**,** 97-103.

BRANDON, C. M., WOODRUFF, J. D., DONNELLY, J. P. & SULLIVAN, R. M. 2014. How unique was Hurricane Sandy? Sedimentary reconstructions of extreme flooding from New York Harbor. *Scientific reports,* 4**,** 7366.

BRANDON, C. M., WOODRUFF, J. D., LANE, P. & DONNELLY, J. P. 2013. Constraining flooding conditions for prehistoric hurricanes from resultant deposits preserved in Florida sinkholes. *Geochemistry Geophysics Geosystems,* 14**,** 2993-3008.

BREGY, J. C., MAXWELL, J. T., ROBESON, S. M., ORTEGREN, J. T., SOULÉ, P. T. & KNAPP, P. A. 2020. Spatiotemporal Variability of Tropical Cyclone Precipitation Using a High-Resolution, Gridded (0.25°× 0.25°) Dataset for the Eastern United States, 1948–2015. *Journal of Climate,* 33**,** 1803-1819.

BREGY, J. C., WALLACE, D. J., MINZONI, R. T. & CRUZ, V. J. 2018. 2500-year paleotempestological record of intense storms for the northern Gulf of Mexico, United States. *Marine Geology,* 396**,** 26-42.

CARRÉ, M., AZZOUG, M., ZAHARIAS, P., CAMARA, A., CHEDDADI, R., CHEVALIER, M., FIORILLO, D., GAYE, A. T., JANICOT, S. & KHODRI, M. 2019. Modern drought conditions in western Sahel unprecedented in the past 1600 years. Climate Dynamics, 52, 1949-1964.

CASTAGNO, K. A., DONNELLY, J. P. & WOODRUFF, J. D. 2021. Grain-Size Analysis of Hurricane-Induced Event Beds in a New England Salt Marsh, Massachusetts, USA. *Journal of Coastal Research,* 37**,** 326-335.

CHANG, P., JI, L. & LI, H. 1997. A decadal climate variation in the tropical Atlantic Ocean from thermodynamic air-sea interactions. *Nature,* 385**,** 516-518.

CHAVAS, D. R., LIN, N., DONG, W. & LIN, Y. 2016. Observed tropical cyclone size revisited. *Journal of Climate,* 29**,** 2923-2939.

CHENOWETH, M. & DIVINE, D. 2008. A document-based 318-year record of tropical cyclones in the Lesser Antilles, 1690–2007. *Geochemistry, Geophysics, Geosystems,* 9.

COOK, E., LALL, U. & WOODHOUSE, C. 2008. North American summer PDSI reconstructions, version 2a. IGBP PAGES/World Data Center for Paleoclimatology Data Contribution Series# 2008-046. NOAA/NGDC Paleoclimatology Program, Boulder, CO.

COOK, E. R., WOODHOUSE, C. A., EAKIN, C. M., MEKO, D. M. & STAHLE, D. W. 2004. Long-term aridity changes in the western United States. *Science,* 306**,** 1015-1018.

DAHLGREN, C. & SHERMAN, K. 2020. Preliminary assessment of hurricane dorian's impact on coral reefs of abaco and grand bahama. *Perry Institute of Marine Science Report to the Government of The Bahamas*.

DASGUPTA, S., LAPLANTE, B., MEISNER, C., WHEELER, D. & YAN, J. 2009. The impact of sea level rise on developing countries: a comparative analysis. *Climatic change,* 93**,** 379-388.

DEAN, W. E. 1974. Loss on Ignition as a method for estimating organic and carbonate content in sediments: reproducibility and comparability of results. *Journal of Paleolimnology,* 25**,** 101-110.

DEE, S., OKUMURA, Y., STEVENSON, S. & DI NEZIO, P. 2020. Enhanced North American ENSO Teleconnections During the Little Ice Age Revealed by Paleoclimate Data Assimilation. *Geophysical Research Letters,* 47**,** e2020GL087504.

DENOMEE, K. C., BENTLEY, S. J. & DROXLER, A. W. 2014. Climatic control on hurricane patterns: a 1200-y near-annual record from Lighthouse Reef, Belize. *Scientific Reports,* 4**,** 7.

DONNELLY, J. P., HAWKES, A. D., LANE, P., MACDONALD, D., SHUMAN, B. N., TOOMEY, M. R., VAN HENGSTUM, P. J. & WOODRUFF, J. D. 2015. Climate forcing of unprecedented intense-hurricane activity in the last 2000 years. *Earth's Future,* 3**,** 49-65.

DONNELLY, J. P., ROLL, S., WENGREN, M., BUTLER, J., LEDERER, R. & WEBB, T. I. 2001a. Sedimentary evidence of intense hurricane strikes from New Jersey. *Geology,* 29**,** 615-618.

DONNELLY, J. P., SMITH BRYANT, S., BUTLER, J., DOWLING, J., FAN, L., HAUSMANN, N., NEWBY, P., SHUMAN, B., STERN, J., WESTHOVER, K. & WEBB, T. I. 2001b. 700 yr sedimentary record of intense hurricane landfalls in southern New England. *Geological Society of America Bulletin,* 113**,** 715-727.

DUNPHY, P. P. & DIBB, J. E. 1994. 137 Cs gamma-ray detection at Summit, Greenland. *Journal of Glaciology,* 40**,** 87-92.

ELSNER, J. B. 2003. Tracking hurricanes. *Bulletin of the American Meterorological Society,* 84**,** 353-356.

ELSNER, J. B. & KOCHER, B. 2000. Global tropical cyclone activity: A link to the North Atlantic Oscillation. *Geophysical Research Letters,* 27**,** 129-132.

EMANUEL, K. 2000. A statistical analysis of tropical cyclone intensity. *Monthly Weather Review,* 128**,** 1139-1152.

EMANUEL, K., SUNDARARAJAN, R. & WILLIAMS, J. 2008. Hurricanes and global warming: results from downscaling IPCC AR4 simulations. *Bulletin of the American Meterorological Society,* 89**,** 347-367.

EMANUEL, K. A. 1986. An air-sea interaction theory for tropical cyclones. Part I: Steady-state maintenance. *Journal of the Atmospheric Sciences,* 43**,** 585-605.

FALL, P. L., VAN HENGSTUM, P. J., LAVOLD-FOOTE, L., DONNELLY, J. P., ALBURY, N. A. & TAMALAVAGE, A. E. 2021. Human arrival and landscape dynamics in the northern Bahamas. *Proceedings of the National Academy of Sciences,* 118.

FOLLAND, C. K., KNIGHT, J., LINDERHOLM, H. W., FEREDAY, D., INESON, S. & HURRELL, J. W. 2009. The summer North Atlantic Oscillation: past, present, and future. *Journal of Climate,* 22**,** 1082-1103.

FRANKLIN, J. L., PASCH, R. J., AVILA, L. A., BEVEN, J. L., LAWRENCE, M. B., STEWART, S. R. & BLAKE, E. S. 2006. Atlantic hurricane season of 2004. *Monthly Weather Review,* 134**,** 981-1025.

GARCÍA-HERRERA, R., GIMENO, L., RIBERA, P. & HERNÁNDEZ, E. 2005. New records of Atlantic hurricanes from Spanish documentary sources. *Journal of Geophysical Research,* 110**,** 7 p.

GISCHLER, E., ANSELMETTI, F. S. & SHINN, E. A. 2013. Seismic stratigraphy of the Blue Hole (Lighthouse Reef, Belize), a late Holocene climate and storm archive. *Marine Geology,* 344**,** 155-162.

GOLDENBERG, S. B. & SHAPIRO, L. J. 1996. Physical mechanisms for the association of El Niño and West African rainfall with Atlantic major hurricane activity. *Journal of Climate,* 9**,** 1169-1187.

GONZALEZ, B. C., ILIFFE, T. M., MACALADY, J. L., SCHAPERDOTH, I. & KAKUK, B. J. H. 2011. Microbial hotspots in anchialine blue holes: initial discoveries from the Bahamas. 677**,** 149-156.

GRAY, W. M. 1968. Global view of the origin of tropical disturbances and storms. *Monthly Weather Review,* 96**,** 669-700.

GRAY, W. M. 1990. Strong association between West African Rainfall and U.S. landfall of intense hurricanes. Science, 249, 1251-1256.

HAUG, G. H., HUGHEN, K. A., SIGMAN, D. M., PETERSON, L. C. & RÖHL, U. 2001. Southward migration of the intertropical convergence zone through the Holocene. *Science,* 293**,** 1304-1308.

HEATH, K. & MULLINS, H. 1984. Open-ocean, off-bank transport of fine-grained carbonate sediment in the Northern Bahamas. *Geological Society, London, Special Publications,* 15**,** 199-208.

HEIRI, O., LOTTER, A. F. & LEMCKE, G. 2001. Loss on ignition as a method for estimating organic and carbonate content in sediments: reproducibility and comparability of results. *Journal of Paleolimnology,* 25**,** 101-110.

HOLLAND, G. J. 1997. The maximum potential intensity of tropical cyclones. *Journal of the atmospheric sciences,* 54**,** 2519-2541.

HSU, S. & YAN, Z. 1998. A note on the radius of maximum wind for hurricanes. *Journal of coastal research,* 14.

ICEYE 2020. FLOOD IMPACT: GRAND BAHAMA. Espoo, Finland.

KACZMAREK, S. E. & HASIUK, F. J. Mapping surficial sediment distributions on Caicos Platform: A quantitative approach integrating statistical analysis of Landsat spectral data and field observations. Developing models and analogs for isolated carbonate platforms—Holocene and Pleistocene carbonates of Caicos Platform, British West Indies: SEPM Core Workshop, 2008. 57-72.

KNAFF, J. A. 1997. Implications of summertime sea level pressure anomalies in the tropical Atlantic region. *Journal of climate,* 10**,** 789-804.

KNAPP, K. R., DIAMOND, H. J., KOSSIN, J. P., KRUK, M. C. & SCHRECK, C. J. 2018. International Best Track Archive for Climate Stewardship (IBTrACS) Project, Version 4, [North Atlantic Subset]. *In:* INFORMATION, N. N. C. F. E. (ed.).

KNAPP, K. R., KRUK, M. C., LEVINSON, D. H., DIAMOND, H. J. & NEUMANN, C. J. 2010. The international best track archive for climate stewardship (IBTrACS) unifying tropical cyclone data. *Bulletin of the American Meteorological Society,* 91**,** 363-376.

KNOWLES, J. T. & LEITNER, M. 2007. Visual representations of the spatial relationship between Bermuda High strengths and hurricane tracks. *Cartographic Perspectives***,** 37-51.

KNUTSON, T., CAMARGO, S. J., CHAN, J. C., EMANUEL, K., HO, C.-H., KOSSIN, J., MOHAPATRA, M., SATOH, M., SUGI, M. & WALSH, K. 2020. Tropical cyclones and climate change assessment: Part II. Projected response to anthropogenic warming. *Bulletin of the American Meteorological Society*.

KORTY, R. L., CAMARGO, S. J. & GALEWSKY, J. 2012. Variations in tropical cyclone genesis factors in simulations of the Holocene epoch. *Journal of Climate,* 25**,** 8196-8211.

KOSSIN, J. P. 2017. Hurricane intensification along United States coast suppressed during active hurricane periods. *Nature,* 541**,** 390.

KOSSIN, J. P. 2018. A global slowdown of tropical-cyclone translation speed. *Nature,* 558**,** 104-107.

KOSSIN, J. P. & CAMARGO, S. J. 2009. Hurricane track variability and secular potential intensity trends. *Climatic Change,* 97**,** 329-337.

KOSSIN, J. P., CAMARGO, S. J. & SITKOWSKI, M. 2010. Climate modulation of North Atlantic hurricane tracks. *Journal of Climate,* 23**,** 3057-3076.

KOSSIN, J. P. & VIMONT, D. J. 2007. Understanding Altantic Hurricane variability and trends. *Bulletin of American Meteorological Society,* 88**,** 1767-1781.

LANDSEA, C. W. & FRANKLIN, J. L. 2013. Atlantic hurricane database uncertainty and presentation of a new database format. *Monthly Weather Review,* 141**,** 3576-3592.

LANE, P., DONNELLY, J. P., WOODRUFF, J. D. & HAWKES, A. D. 2011. A decadally-resolved paleohurricane record archived in the late Holocene sediments of a Florida sinkhole. *Marine Geology,* 287**,** 14-30.

LI, J., XIE, S.-P., COOK, E. R., HUANG, G., D'ARRIGO, R., LIU, F., MA, J. & ZHENG, X.-T. 2011. Interdecadal modulation of El Niño amplitude during the past millennium. *Nature climate change,* 1**,** 114-118.

LI, J., XIE, S.-P., COOK, E. R., MORALES, M. S., CHRISTIE, D. A., JOHNSON, N. C., CHEN, F., D'ARRIGO, R., FOWLER, A. M. & GOU, X. 2013. El Niño modulations over the past seven centuries. *Nature Climate Change,* 3**,** 822-826.

LIN, N., LANE, P., EMANUEL, K. A., SULLIVAN, R. M. & DONNELLY, J. P. 2014. Heightened hurricane surge risk in northwest Florida revealed from climatological-hydrodynamic modeling and paleorecord reconstruction. *Journal of Geophysical Research: Atmospheres,* 119**,** 8606-8623.

LIN, Y., ZHAO, M. & ZHANG, M. 2015. Tropical cyclone rainfall area controlled by relative sea surface temperature. *Nature Communications,* 6**,** 6591.

LINDERHOLM, H. W., BJÖRKLUND, J., SEFTIGEN, K., GUNNARSON, B. E. & FUENTES, M. 2015. Fennoscandia revisited: a spatially improved tree-ring reconstruction of summer temperatures for the last 900 years. *Climate Dynamics,* 45**,** 933-947.

LIU, K.-B. & FEARN, M. L. 1993. Lake-sediment record of late Holocene hurricane activities from coastal Alabama. *Geology,* 21**,** 793-796.

LIU, K. & FEARN, M. L. 2000. Reconstruction of prehistoric landfall frequencies of catastrophic hurricanes in NW Florida from lake sediment records. *Quaternary Research,* 52**,** 238-245.

MAIO, C. V., DONNELLY, J. P., SULLIVAN, R., MADSEN, S. M., WEIDMAN, C. R., GONTZ, A. M. & SHEREMET, V. A. 2016. Sediment dynamics and hydrographic conditions during storm passage, Waquoit Bay, Massachusetts. *Marine Geology,* 381**,** 67-86.

MALAIZÉ, B., BERTRAN, P., CARBONEL, P., BONNISSENT, D., CHARLIER, K., GALOP, D., IMBERT, D., SERRAND, N., STOUVENOT, C. & PUJOL, C.

2011. Hurricanes and climate in the Caribbean during the past 3700 years BP. *The Holocene,* 21**,** 911-924.

MALLINSON, D. J., SMITH, C. W., MAHAN, S., CULVER, S. J. & MCDOWELL, K. 2011. Barrier island response to late Holocene climate events, North Carolina, USA. *Quaternary Research,* 76**,** 46-57.

MALOOF, A. C. & GROTZINGER, J. P. 2012. The Holocene shallowing-upward parasequence of north-west Andros Island, Bahamas. *Sedimentology,* 59**,** 1375-1407.

MANN, M. E. 2002. Little ice age. *Encyclopedia of global environmental change,* 1**,** 504-509.

MANN, M. E., WOODRUFF, J. D., DONNELLY, J. P. & ZHANG, Z. 2009a. Atlantic hurricanes and climate over the past 1,500 years. *Nature,* 460**,** 880-885.

MANN, M. E., ZHANG, Z., RUTHERFORD, S., BRADLEY, R. S., HUGHES, M. K., SHINDELL, D., AMMANN, C., FALUVEGI, G. & NI, F. 2009b. Global signatures and dynamical origins of the Little Ice Age and Medieval Climate Anomaly. *Science,* 326**,** 1256-1260.

MCADIE, C., LANDSEA, C., NEUMANN, C. J., DAVID, J. E. & BLAKE, E. S. 2009. *Tropical Cyclones of the North Atlantic Ocean, 1851-2006: With 2007 and 2008 Track Maps Included*, US Department of Commerce, National Oceanic and Atmospheric Administration.

MCBRIDE, J. L. & ZEHR, R. 1981. Observational analysis of tropical cyclone formation. Part II: Comparison of non-developing versus developing systems. *Journal of the Atmospheric Sciences,* 38**,** 1132-1151.

MCCLOSKEY, T. A. & LIU, K. B. 2012. *A 7000 year record of paleohurricane activity from a coastal weland in Belize*.

MENDELSOHN, R., EMANUEL, K., CHONABAYASHI, S. & BAKKENSEN, L. 2012. The impact of climate change on global tropical cyclone damage. *Nature climate change,* 2**,** 205-209.

MILLER, G. H., GEIRSDÓTTIR, Á., ZHONG, Y., LARSEN, D. J., OTTO-BLIESNER, B. L., HOLLAND, M. M., BAILEY, D. A., REFSNIDER, K. A., LEHMAN, S. J. & SOUTHON, J. R. 2012. Abrupt onset of the Little Ice Age triggered by volcanism and sustained by sea-ice/ocean feedbacks. *Geophysical Research Letters,* 39.

MILLIMAN, J. D., FREILE, D., STEINEN, R. P. & WILBER, R. J. 1993. Great Bahama Bank aragonitic muds; mostly inorganically precipitated, mostly exported. *Journal of Sedimentary Research,* 63**,** 589-595.

MULLINS, H. T. & LYNTS, G. W. 1977. Origin of the northwestern Bahama Platform: Review and reinterpretation. *Geological Society of America Bulletin,* 88**,** 1447-1461.

NASH, D. J., DE CORT, G., CHASE, B. M., VERSCHUREN, D., NICHOLSON, S. E., SHANAHAN, T. M., ASRAT, A., LÉZINE, A.-M. & GRAB, S. W. 2016. African hydroclimatic variability during the last 2000 years. Quaternary Science Reviews, 154, 1-22.

NEUMANN, C. A. & LAND, L. S. 1975. Lime mud deposition and calcareous algae in the Bight of Abaco, Bahamas; a budget. *Journal of Sedimentary Research,* 45**,** 763-786.

OLIVA, F., PEROS, M., VIAU, A., REINHARDT, E., NIXON, F. & MORIN, A. 2018. A multi-proxy reconstruction of tropical cyclone variability during the past 800 years from Robinson Lake, Nova Scotia, Canada. *Marine Geology,* 406**,** 84-97.

OLSEN, J., ANDERSON, N. J. & KNUDSEN, M. F. 2012. Variability of the North Atlantic Oscillation over the past 5,200 years. *Nature Geoscience,* 5**,** 808-812.

OPPENHEIMER, M. & HINKEL, J. 2019. Sea Level Rise and Implications for Low Lying Islands, Coasts and Communities Supplementary Material. *IPCC special report on the ocean and cryosphere in a changing climate*.

ORTEGA, P., LEHNER, F., SWINGEDOUW, D., MASSON-DELMOTTE, V., RAIBLE, C. C., CASADO, M. & YIOU, P. 2015. A model-tested North Atlantic Oscillation reconstruction for the past millennium. *Nature,* 523**,** 71-74.

ORTEGREN, J. T. & MAXWELL, J. T. 2014. Spatiotemporal Patterns of Drought/Tropical Cyclone Co-occurrence in the Southeastern USA: Linkages to North Atlantic Climate Variability. *Geography Compass,* 8**,** 540-559.

PARSONS, T. & GEIST, E. L. 2008. Tsunami probability in the Caribbean region. *Tsunami Science Four Years after the 2004 Indian Ocean Tsunami.* Springer.

PATRICOLA, C. M. & WEHNER, M. F. 2018. Anthropogenic influences on major tropical cyclone events. *Nature,* 563**,** 339-346.

PENNINGTON, W., CAMBRAY, R. S. & FISHER, E. M. 1973. Observations on lake sediments using fallout 137Cs as a tracer. *Nature,* 242**,** 324-326.

PIELKE JR, R. A., GRATZ, J., LANDSEA, C. W., COLLINS, D., SAUNDERS, M. A. & MUSULIN, R. 2008. Normalized hurricane damage in the United States: 1900–2005. *Natural Hazards Review,* 9**,** 29-42.

RAHMSTORF, S., FEULNER, G., MANN, M. E., ROBINSON, A., RUTHERFORD, S. & SCHAFFERNICHT, E. J. 2015. Exceptional twentieth-century slowdown in Atlantic Ocean overturning circulation. *Nature climate change,* 5**,** 475-480.

RANKEY, E. C. 2002. Spatial patterns of sediment accumulation on a Holocene carbonate tidal flat, northwest Andros Island, Bahamas. *Journal of Sedimentary Research,* 72**,** 591-601.

RANKEY, E. C., ENOS, P., STEFFEN, K. & DRUKE, D. 2004. Lack of impact of Hurricane Michelle on tidal flats, Andros Island, Bahamas: Integrated remote sensing and field observations. *Journal of Sedimentary Research,* 74**,** 654-661.

RANKEY, E. C., RIEGL, B. & STEFFEN, K. 2006. Form, function and feedbacks in a tidally dominated ooid shoal, Bahamas. *Sedimentology,* 53**,** 1191-1210.

REIMER, P. J., AUSTIN, W. E., BARD, E., BAYLISS, A., BLACKWELL, P. G., RAMSEY, C. B., BUTZIN, M., CHENG, H., EDWARDS, R. L. & FRIEDRICH, M. 2020. The IntCal20 Northern Hemisphere radiocarbon age calibration curve (0–55 cal kBP). *Radiocarbon***,** 1-33.

REIMER, P. J., BROWN, T. A. & REIMER, R. W. 2004. Discussion: reporting and calibration of post-bomb 14C data. *Radiocarbon,* 46**,** 1299-1304.

RIEHL, H. 1954. Tropical Meterology, New York, McGraw-Hill Book Co.

RODYSILL, J. R., DONNELLY, J. P., SULLIVAN, R., LANE, P. D., TOOMEY, M., WOODRUFF, J. D., HAWKES, A. D., MACDONALD, D., D'ENTREMONT, N. & MCKEON, K. 2020. Historically unprecedented Northern Gulf of Mexico hurricane activity from 650 to 1250 CE. *Scientific reports,* 10**,** 1-17.

RYDVAL, M., LOADER, N. J., GUNNARSON, B. E., DRUCKENBROD, D. L., LINDERHOLM, H. W., MORETON, S. G., WOOD, C. V. & WILSON, R. 2017. Reconstructing 800 years of summer temperatures in Scotland from tree rings. *Climate Dynamics,* 49**,** 2951-2974.

SAENGER, C., COHEN, A. L., OPPO, D. W., HALLEY, R. B. & CARILLI, J. E. 2009. Surface-temperature trends and variability in the low-latitude North Atlantic since 1552. *Nature Geoscience,* 2**,** 492-495.

SAMPSON, J. & GUILBEAULT, K. 2013. Baseline physicochemical investigations on waters from three blue holes, San Salvador Island, Bahamas. *Studia UBB Geologia,* 58**,** 11-19.

SCHMITT, D., GISCHLER, E., ANSELMETTI, F. S. & VOGEL, H. 2020. Caribbean cyclone activity: an annually-resolved Common Era record. *Scientific reports,* 10**,** 1-17.

SCHNEIDER, T., BISCHOFF, T. & HAUG, G. H. 2014. Migrations and dynamics of the intertropical convergence zone. *Nature,* 513**,** 45-53.

SHAPIRO, L. J. 1987. Month-to-month variability of the Atlantic tropical circulation and its relationship to tropical storm formation. *Monthly Weather Review,* 115**,** 2598-2614.

SHINN, E. A., LLOYD, R. M. & GINSBURG, R. N. 1969. Anatomy of a modern carbonate tidal-flat, Andros Island, Bahamas. *Journal of Sedimentary Research,* 39**,** 1202-1228.

SHINN, E. A., REICH, C. D., LOCKER, S. D. & HINE, A. C. 1996. A giant sediment trap in the Florida Keys. *Journal of Coastal Research,* 12**,** 953-959.

SHULTZ, J. M., SANDS, D. E., KOSSIN, J. P. & GALEA, S. 2020. Double environmental injustice—climate change, Hurricane Dorian, and the Bahamas. *New England Journal of Medicine,* 382**,** 1-3.

SMITH, A. B. 2020. U.S. Billion-dollar Weather and Climate Disasters, 1980 - present. *(NCEI Accession 0209268). [Tropical Cyclone Subset]. NOAA National Centers for Environmental Information. Dataset. https://doi.org/10.25921/stkw-7w73. Accessed [Feb. 4,2021].*

SOBEL, A. H., CAMARGO, S. J., HALL, T. M., LEE, C.-Y., TIPPETT, M. K. & WING, A. A. 2016. Human influence on tropical cyclone intensity. *Science,* 353**,** 242-246.

STEWART, S. R. 2017. National Hurricane Center Tropical Cyclone Report: Hurricane Matthew (AL142016). *National Oceanic and Atmospheric Administration, National Weather Service, National Hurricane Center, Miami, FL.* National Hurricane Center

STOCKMAN, K., GINSBURG, R. & SHINN, E. 1967. The production of lime mud by algae in south Florida. *Journal of Sedimentary Research,* 37**,** 633-648.

TEDESCO, L. P. & ALLER, R. C. 1997. 210 Pb chronology of sequences affected by burrow excavation and infilling; examples from shallow marine carbonate sediment sequences, Holocene South Florida and Caicos Platform, British West Indies. *Journal of Sedimentary Research,* 67**,** 36-46.

TING, M., KOSSIN, J. P., CAMARGO, S. J. & LI, C. 2019. Past and future hurricane intensity change along the US east coast. *Scientific reports,* 9**,** 1-8.

TOOMEY, M. R., CURRY, W. B., DONNELLY, J. P. & VAN HENGSTUM, P. J. 2013. Reconstructing 7000 years of North Atlantic hurricane variability using deep-sea sediment cores from the western Great Bahama Bank. *Paleoceanography,* 28**,** 31-41.

TOOMEY, M. R., KORTY, R. L., DONNELLY, J. P., VAN HENGSTUM, P. J. & CURRY, W. B. 2017. Increased hurricane frequency near Florida during Younger Dryas Atlantic meridional overturning circulation slowdown. *Geology,* 45**,** 1047-1050.

TROUET, V., ESPER, J., GRAHAM, N. E., BAKER, A., SCOURSE, J. D. & FRANK, D. C. 2009. Persistent positive North Atlantic Oscillations mode dominated the medieval climate anomaly. *Science,* 324**,** 78-80.

TROUET, V., HARLEY, G. L. & DOMÍNGUEZ-DELMÁS, M. 2016. Shipwreck rates reveal Caribbean tropical cyclone response to past radiative forcing. *Proceedings of the National Academy of Sciences,* 113**,** 3169-3174.

TROWER, E. J., CANTINE, M. D., GOMES, M. L., GROTZINGER, J. P., KNOLL, A. H., LAMB, M. P., LINGAPPA, U., O'REILLY, S. S., PRESENT, T. M. & STEIN, N. 2018. Active ooid growth driven by sediment transport in a high-energy shoal, Little Ambergris Cay, Turks and Caicos Islands. *Journal of Sedimentary Research,* 88**,** 1132-1151.

TROWER, E. J., LAMB, M. P. & FISCHER, W. W. 2019. The origin of carbonate mud. *Geophysical Research Letters*.

ULM, K. 1990. Simple method to calculate the confidence interval of a standardized mortality ratio (SMR). *American journal of epidemiology,* 131**,** 373-375.

VAN DRIESSCHE, A. E., STAWSKI, T. M., BENNING, L. G. & KELLERMEIER, M. 2017. Calcium sulfate precipitation throughout its phase diagram. *New perspectives on mineral nucleation and growth.* Springer.

VAN HENGSTUM, P. J., DONNELLY, J. P., FALL, P. L., TOOMEY, M. R., ALBURY, N. A. & KAKUK, B. 2016. The intertropical convergence zone modulates intense hurricane strikes on the western North Atlantic margin. *Scientific reports,* 6.

VAN HENGSTUM, P. J., DONNELLY, J. P., TOOMEY, M. R., ALBURY, N. A., LANE, P. & KAKUK, B. 2014. Heightened hurricane activity on the Little Bahama Bank from 1350 to 1650 AD. *Continental Shelf Research,* 86**,** 103-115.

VAN HENGSTUM, P. J., WINKLER, T. S., TAMALAVAGE, A. E., SULLIVAN, R. M., LITTLE, S. N., MACDONALD, D., DONNELLY, J. P. & ALBURY, N. A. 2020. Holocene sedimentation in a blue hole surrounded by carbonate tidal flats in The Bahamas: Autogenic versus allogenic processes. *Marine Geology,* 419**,** 106051.

VECCHI, G. A. & KNUTSON, T. R. 2011. Estimating annual numbers of Atlantic hurricanes missing from the HURDAT database (1878–1965) using ship track density. *Journal of Climate,* 24**,** 1736-1746.

VILLARINI, G. & VECCHI, G. A. 2013. Projected increases in North Atlantic tropical cyclone intensity from CMIP5 models. *Journal of Climate,* 26**,** 3231-3240.

VILLARINI, G., VECCHI, G. A., KNUTSON, T. R. & SMITH, J. A. 2011. Is the recorded increase in short-duration North Atlantic tropical storms spurious? *Journal of Geophysical Research: Atmospheres,* 116.

WALLACE, E., DONNELLY, J., VAN HENGSTUM, P., WIMAN, C., SULLIVAN, R., WINKLER, T., D'ENTREMONT, N., TOOMEY, M. & ALBURY, N. 2019. Intense hurricane activity over the past 1500 years at South Andros Island, The Bahamas. *Paleoceanography and Paleoclimatology,* 34.

WALLACE, E. J., COATS, S., EMANUEL, K. & DONNELLY, J. P. 2021a. Centennial-scale shifts in storm frequency captured in paleohurricane records from The Bahamas arise predominantly from random variability. *Geophysical Research Letters,* 48**,** e2020GL091145.

WALLACE, E. J., DONNELLY, J. P., VAN HENGSTUM, P. J., WINKLER, T. S., DIZON, C., LABELLA, A., LOPEZ, I., D'ENTREMONT, N. E., SULLIVAN, R. M., WOODRUFF, J. D., HAWKES, A. D. & MAIO, C. Sub. March 2021.

Regional shifts in paleohurricane activity over the last 1500 years derived from blue hole sediments offshore of Middle Caicos Island. *Quaternary Science Reviews*.

WALLACE, E. J., DONNELLY, J. P., VAN HENGSTUM, P. J., WINKLER, T. S., MCKEON, K., MACDONALD, D., D'ENTREMONT, N. E., SULLIVAN, R. M., WOODRUFF, J. D., HAWKES, A. D. & MAIO, C. 2021b. 1050 years of hurricane strikes on Long Island in The Bahamas. *Paleoceanography and Paleoclimatology,* 36**,** e2020PA004156.

WANAMAKER, A. D., KREUTZ, K. J., SCHÖNE, B. R., PETTIGREW, N., BORNS, H. W., INTRONE, D. S., BELKNAP, D., MAASCH, K. A. & FEINDEL, S. 2008. Coupled North Atlantic slope water forcing on Gulf of Maine temperatures over the past millennium. *Climate Dynamics,* 31**,** 183-194.

WANLESS, H. R., TEDESCO, L. P. & TYRRELL, K. M. 1988a. Production of subtidal tubular and surficial tempestites by hurricane Kate, Caicos Platform, British West Indies. *Journal of Sedimentary Research,* 58**,** 739-750.

WANLESS, H. R., TYRRELL, K. M., TEDESCO, L. P. & DRAVIS, J. J. 1988b. Tidal-flat sedimentation from Hurricane Kate, Caicos Platform, British West Indies. *Journal of Sedimentary Research,* 58**,** 724-738.

WILSON, K. & MOHRIG, D. 2021. Modern coastal tempestite deposition by a non-local storm: Swell-generated transport of sand and boulders on Eleuthera, The Bahamas. *Sedimentology*.

WING, A. A., SOBEL, A. H. & CAMARGO, S. J. 2007. Relationship between the potential and actual intensities of tropical cyclones on interannual time scales. *Geophysical research letters,* 34.

WINKLER, T. S., HENGSTUM, P. J. V., DONNELLY, J. P., WALLACE, E. J., D'ENTREMONT, N., HAWKES, A. D., SULLIVAN, R. M., WOODRUFF, J. D. & MAIO, C. V. Submitted 2021. Oceanic passage of hurricanes across Cay Sal Bank in The Bahamas over the last 550 years. *Marine Geology*.

WINKLER, T. S., VAN HENGSTUM, P. J., DONNELLY, J. P., WALLACE, E. J., SULLIVAN, R. M., MACDONALD, D. & ALBURY, N. A. 2020. Revising evidence of hurricane strikes on Abaco Island (The Bahamas) over the last 700 years. *Scientific Reports,* 10**,** 1-17.

WOODRUFF, J. D., IRISH, J. L. & CAMARGO, S. J. 2013. Coastal flooding by tropical cyclones and sea-level rise. *Nature,* 504**,** 44.

WOODS, P. J. & BROWN, R. G. 1975. Carbonate sedimentation in an arid zone tidal flat, Nilemah Embayment, Shark Bay, Western Australia. *Tidal deposits.* Springer.

XIE, L., YAN, T., PIETRAFESA, L. J., MORRISON, J. M. & KARL, T. 2005. Climatology and interannual variability of North Atlantic hurricane tracks. *Journal of climate,* 18**,** 5370-5381.

YAN, H., SUN, L., WANG, Y., HUANG, W., QIU, S. & YANG, C. 2011. A record of the Southern Oscillation Index for the past 2,000 years from precipitation proxies. *Nature Geoscience,* 4**,** 611-614.

YANG, Y., MASELLI, V., NORMANDEAU, A., PIPER, D. J., LI, M. Z., CAMPBELL, D. C., GREGORY, T. & GAO, S. 2020. Latitudinal response of storm activity to abrupt climate change during the last 6,500 years. *Geophysical Research Letters,* 47**,** e2020GL089859.

ZEGARRA, M. A., SCHMID, J. P., PALOMINO, L. & SEMINARIO, B. 2020. Impact of Hurricane Dorian in The Bahamas: A View from the Sky. Inter-American Development Bank.

ZHANG, P., LINDERHOLM, H. W., GUNNARSON, B. E., BJÖRKLUND, J. & CHEN, D. 2016. 1200 years of warm-season temperature variability in central Scandinavia inferred from tree-ring density. *Climate of the Past,* 12**,** 1297-1312.

ZISHKA, K. M. & SMITH, P. J. 1980. The climatology of cyclones and anticyclones over North America and surrounding ocean environs for January and July, 1950–77. *Monthly Weather Review,* 108**,** 387-401.

5. DISSERTATION CONCLUSIONS

5.1. Scientific Contributions and Societal Implications

Islands across the Bahamian Archipelago have been devastated by five major hurricanes from 2010-2020 CE, including Category 5 (Saffir-Simpson scale) Hurricane Dorian in 2019 that inundated parts of Abaco and Grand Bahama with up to 4 m of surge, killing at least 70 humans and leaving 282 missing. Up to 1 m relative sea-level rise is estimated for The Bahamas by 2100 CE (Oppenheimer and Hinkel, 2019), which could enhance flooding from weaker storms (<Category 3) in low-lying coastal areas. Problematically, long-term hurricane frequency remains poorly constrained, especially for weaker Category 1-2 events that are less-likely to be detected by most sediment-based paleo-hurricane reconstructions. While Caribbean SIDs produce <0.4% of global carbon emissions (Shultz et al., 2020), they will likely experience disproportionally severe coastal flooding from hurricanes due to sea-level rise driven by Anthropogenic climate change (Woodruff et al., 2013, Pielke Jr et al., 2008). With up to 1 m projected global mean sea-level rise by, The Bahamas may lose up to 11.57% of its total land area which is the highest percentage worldwide (Dasgupta et al., 2009). This means that even weaker hurricanes could produce Dorian level flooding in The Bahamas.

CHAPTERS 2-4 of my PhD dissertation extend the knowledge of North Atlantic paleo-hurricane variability during the Common Era (last 2 millennia) by developing three near-annually resolved regional hurricane reconstructions spanning the last ~1700 years using sediment cores from 3 blue holes in The Bahamas. In CHAPTER 4, I

compile these new records with other regional studies to assess the potential ocean/atmospheric drivers of observed variability. To complete these reconstructions, I employed a multiproxy approach using sedimentology, geochemistry, micropaleontology, and statistical analysis to: (i) identify storm induced sediment deposits, (ii) constrain the deposit ages based on a well-resolved sedimentary age-model, and (iii) determine periods of statistically higher/lower event deposits.

In CHAPTER 2, I demonstrate that the northern Bahamas have experienced more frequent intense-hurricane impacts than almost anywhere else in the Atlantic since 1850 CE and presented a 700-year long, near-annually resolved stratigraphic record of hurricane passage near Thatchpoint Blue Hole (TPBH) on Abaco Island, The Bahamas (Winkler et al., 2020). Using longer sediment cores (888 cm) and more reliable age-control, this study revises and temporally expands a previous study from TPBH that underestimated the sedimentation rate (van Hengstum et al., 2014). TPBH records at least 13 ≥Category 2 hurricanes per century between 1500 to 1670 CE, which exceeds the 9 ≥Category 2 hurricanes per century within 50 km of TPBH since 1850 CE. The eastern United States also experienced frequent hurricanes from 1500 to 1670 CE, but frequency was depressed elsewhere in the Atlantic Ocean including just 300 km to the southwest on South Andros (Wallace et al., 2019a). This suggests that spatial heterogeneity in Atlantic hurricane activity since 1850 CE could have persisted throughout the last millennium. This heterogeneity is impacted by climatic and stochastic forcing, but additional high-resolution paleo-hurricane reconstructions are required to assess the mechanisms that impact regional variability.

In CHAPTER 3, I present a 550-year record of hurricane passage from Hine's Blue Hole on Cay Sal Bank, The Bahamas (Winkler et al., Submitted 2021). Hine's Hole has an accumulation rate of 2.1-3.2 cm/yr, making it among the highest-resolution hurricane reconstructions to date. Unlike many paleo-hurricane reconstruction sites, Hine's Hole is not surrounded by coastal landmasses that can dampen currents and waves produced by hurricanes, so it archives most ≥Category 1 hurricanes passing within 115 km during the 170-year instrumental record (1850 CE-present). Hine's Hole archives an average 8-9 hurricanes/century from 1890-2016 CE, but documents three periods from 1485-1505 CE, 1555-1605 CE, and 1735-1780 CE with an average 27.4 hurricanes/ century. These active periods correspond to other high-resolution reconstructions from the Bahamian Archipelago (Wallace et al., 2019b, Wallace et al., Sub. March 2021) and Florida Keys (Trouet et al., 2016), but the magnitude of the increase is much higher given that Hine's Hole archives evidence of weaker and more distal hurricanes. As such, this reconstruction provides unprecedented insight into the magnitude of hurricane frequency variability within the pre-industrial climate system and demonstrates that recurrence intervals based on the 170-year instrumental record can severely underestimate the threat hurricanes pose certain localities. Based on subbottom seismic surveys I conducted at Hine's Hole during my PhD, Hine's Hole has accumulated at least 40 m more sediment beyond the 18 meters of collected stratigraphy used to develop the 550-year Hine's Hole Composite (i.e., at least 60 m of accumulation). If the average sedimentation rate of ~3.2 cm/yr calculated for the upper 18 m persisted since the bank top flooded ~11,000 to 6000 years ago (Purkis et al.,

2014), then the observable ~60 m could represent ~1900 years of sediment accumulation that has the potential to document multi-decadal hurricane frequency variability far beyond the extent of any other record from this region.

In CHAPTER 4, I present two near annually resolved paleo-hurricane reconstructions from Grand Bahama that were developed using sediment cores collected from Lane's Delight Bluehole (LDBH) and Turtle Pond (TURT). I combine these records to produce 1700-year stacked record for Grand Bahama (GBAM-TRA and GBAM-Stack) that documents four periods of significantly heightened local hurricane activity from 1825-1925 CE, 1560-1600 CE, 1300-1450 CE, and 420-560 CE. This record fills vital spatial and temporal gaps for the northern Bahamas that existed in previous iterations of a 4-site compilation of near-annually resolved records of Bahamian paleo-hurricane frequency (Wallace et al., Sub. March 2021, Wallace et al., 2021b).

The two Bahamian compilations document substantially higher hurricane frequency in the northern Caribbean throughout the Little Ice Age (LIA) from ~1300 to 1850 CE. While inherent stochastic variability in hurricane tracks can produce substantial variability in hurricane frequency documented by a single record that is independent of regional or basin-wide climatic forcing (Wallace et al., 2021a). However, by compiling the three reconstructions I developed into a six site Bahamian compilation (CHAPTER 4), we now have overwhelming evidence that hurricane frequency was higher across the Bahamian Archipelago during the LIA. While uncertainty remains regarding the precise climate mechanisms may have contributed to this increase in

activity during the LIA, The Bahamas has indisputably experienced significantly higher hurricane activity than what has been observed since 1850 CE. A return to these levels could have severe consequences for The Bahamas throughout the next century given the projected rise in sea level and changes in hurricane climatology.

My research demonstrates that climate variability dictates steep regional gradients in Atlantic hurricane susceptibility over the last 2000 years, but more records are needed to fully constrain the timing and spatial extent of these paleotempestological changes. The most significant intellectual contribution of my research is that it provides vital insight into how past/ocean climate conditions influence hurricane activity in The Bahamas and begins to demonstrate broader regional connectivity in storm patterns throughout the Atlantic. In each reconstruction, there were periods of significantly higher/ lower storm activity than what has been observed in the last 170 years, so the regional threats posed by hurricanes are not static over time. Given the widespread and devastating impacts of hurricanes, my dissertation research has relevance to a diverse audience including: climatologists studying long-term interactions between hurricane activity and environmental change, biologists assessing long-term ecosystem stability/vulnerability to hurricanes, archeologists seeking to understand how ancestral humans responded to long-term variability in extreme weather events, and policy makers, health-officials, and economists who rely on understanding long-term susceptibility of an area too hurricanes and how this could change in the future.

5.2. Future Directions

While knowledge of Atlantic paleotempestology has grown immensely in the last 2 decades, significant spatiotemporal gaps remain in our understanding of paleohurricane activity in regions like Atlantic Canada, where sea level and SSTs are rising faster than anywhere else in the world. There is a critical need to develop high-resolution paleotempestological records in areas like the high mid-latitudes of the Northwestern Atlantic, the western Gulf of Mexico, and Central America so that regional paleo-hurricane compilations can be improved/developed for these areas.

While knowledge of Atlantic paleotempestology has grown immensely in the last two decades, significant spatiotemporal gaps remain in our understanding of paleohurricane activity in regions like Atlantic Canada, where sea level and SSTs are rising faster than anywhere else in the world. There is a critical need to develop high-resolution paleotempestological records in areas like the high mid-latitudes of the Northwestern Atlantic, the western Gulf of Mexico, and Central America so that regional paleo-hurricane compilations can be improved/developed for these areas. Further, we need to develop high-resolution elevation and bathymetric grids for The Bahamas to model storm surge magnitude and extent forced by different types of hurricanes (e.g., intensity, proximity, orientation, translation speed) to better understand the sensitivity of these paleo-hurricane records. It is also vital that more local hydroclimate reconstructions in the tropical north Atlantic to better understand the regional expressions of climate feature like the North Atlantic Subtropical High (NASH) which can influence both hurricanes (Kossin et al., 2010, Liu and Fearn, 2000, Olsen et

al., 2012) and regional rainfall patterns (Gamble and Curtis, 2008). Finally, it is time to vital to expand effort to integrate the pale-hurricane records into high-resolution tropical cyclone models to better understand the regional climatic forcing that could contribute to the high-confidence patterns in regional paleo-hurricane frequency presented in this dissertation.

5.3. References

DASGUPTA, S., LAPLANTE, B., MEISNER, C., WHEELER, D. & YAN, J. 2009. The impact of sea level rise on developing countries: a comparative analysis. *Climatic change,* 93**,** 379-388.

GAMBLE, D. W. & CURTIS, S. 2008. Caribbean precipitation: a review, model and prospect. *Progress in Physical Geography,* 32**,** 265-276.

KOSSIN, J. P., CAMARGO, S. J. & SITKOWSKI, M. 2010. Climate modulation of North Atlantic hurricane tracks. *Journal of Climate,* 23**,** 3057-3076.

LIU, K. & FEARN, M. L. 2000. Reconstruction of prehistoric landfall frequencies of catastrophic hurricanes in NW Florida from lake sediment records. *Quaternary Research,* 52**,** 238-245.

OLSEN, J., ANDERSON, N. J. & KNUDSEN, M. F. 2012. Variability of the North Atlantic Oscillation over the past 5,200 years. *Nature Geoscience,* 5**,** 808-812.

OPPENHEIMER, M. & HINKEL, J. 2019. Sea Level Rise and Implications for Low Lying Islands, Coasts and Communities Supplementary Material. *IPCC special report on the ocean and cryosphere in a changing climate*.

PIELKE JR, R. A., GRATZ, J., LANDSEA, C. W., COLLINS, D., SAUNDERS, M. A. & MUSULIN, R. 2008. Normalized hurricane damage in the United States: 1900–2005. *Natural Hazards Review,* 9**,** 29-42.

PURKIS, S., KERR, J., DEMPSEY, A., CALHOUN, A., METSAMAA, L., RIEGL, B., KOURAFALOU, V., BRUCKNER, A. & RENAUD, P. 2014. Large-scale carbonate platform development of Cay Sal Bank, Bahamas, and implications for associated reef geomorphology. *Geomorphology,* 222**,** 25-38.

SHULTZ, J. M., SANDS, D. E., KOSSIN, J. P. & GALEA, S. 2020. Double environmental injustice—climate change, Hurricane Dorian, and the Bahamas. *New England Journal of Medicine,* 382**,** 1-3.

TROUET, V., HARLEY, G. L. & DOMÍNGUEZ-DELMÁS, M. 2016. Shipwreck rates reveal Caribbean tropical cyclone response to past radiative forcing. *Proceedings of the National Academy of Sciences,* 113**,** 3169-3174.

VAN HENGSTUM, P. J., DONNELLY, J. P., TOOMEY, M. R., ALBURY, N. A., LANE, P. & KAKUK, B. 2014. Heightened hurricane activity on the Little Bahama Bank from 1350 to 1650 AD. *Continental Shelf Research,* 86**,** 103-115.

WALLACE, E., DONNELLY, J., VAN HENGSTUM, P., WIMAN, C., SULLIVAN, R., WINKLER, T., D'ENTREMONT, N., TOOMEY, M. & ALBURY, N. 2019a. Intense hurricane activity over the past 1500 years at South Andros Island, The Bahamas. *Paleoceanography and Paleoclimatology,* 34.

WALLACE, E. J., COATS, S., EMANUEL, K. & DONNELLY, J. P. Investigating the significance of centennial timescale paleohurricane activity using modeled hurricane climatology over the past millennium. AGU Fall Meeting 2019, 2019b. AGU.

WALLACE, E. J., COATS, S., EMANUEL, K. & DONNELLY, J. P. 2021a. Centennial-scale shifts in storm frequency captured in paleohurricane records from The Bahamas arise predominantly from random variability. *Geophysical Research Letters,* 48**,** e2020GL091145.

WALLACE, E. J., DONNELLY, J. P., VAN HENGSTUM, P. J., WINKLER, T. S., DIZON, C., LABELLA, A., LOPEZ, I., D'ENTREMONT, N. E., SULLIVAN, R. M., WOODRUFF, J. D., HAWKES, A. D. & MAIO, C. Sub. March 2021. Regional shifts in paleohurricane activity over the last 1500 years derived from blue hole sediments offshore of Middle Caicos Island. *Quaternary Science Reviews*.

WALLACE, E. J., DONNELLY, J. P., VAN HENGSTUM, P. J., WINKLER, T. S., MCKEON, K., MACDONALD, D., D'ENTREMONT, N. E., SULLIVAN, R. M., WOODRUFF, J. D., HAWKES, A. D. & MAIO, C. 2021b. 1050 years of hurricane strikes on Long Island in The Bahamas. *Paleoceanography and Paleoclimatology,* 36**,** e2020PA004156.

WINKLER, T. S., HENGSTUM, P. J. V., DONNELLY, J. P., WALLACE, E. J., D'ENTREMONT, N., HAWKES, A. D., SULLIVAN, R. M., WOODRUFF, J. D. & MAIO, C. V. Submitted 2021. Oceanic passage of hurricanes across Cay Sal Bank in The Bahamas over the last 550 years. *Marine Geology*.

WINKLER, T. S., VAN HENGSTUM, P. J., DONNELLY, J. P., WALLACE, E. J., SULLIVAN, R. M., MACDONALD, D. & ALBURY, N. A. 2020. Revising evidence of hurricane strikes on Abaco Island (The Bahamas) over the last 700 years. *Scientific Reports,* 10**,** 1-17.

WOODRUFF, J. D., IRISH, J. L. & CAMARGO, S. J. 2013. Coastal flooding by tropical cyclones and sea-level rise. *Nature,* 504**,** 44.

APPENDIX A

BLUE HOLE DISTRIBUTION METHODS AND DETAILS

APPENDIX A Section S1.1 Introduction

I have had the opportunity to explore over 50 blue holes on 6 different islands of the The Bahamas throughout the course of my PhD research,. Interestingly, it appeared that some islands such as Andros and Long Island have more blue holes than islands to the north like Grand Bahama. Motivated by this, I identified over 5000 sinkholes and blue holes across the Bahamian Archipelago sing satellite imagery to test the hypothesis that blue holes are more abundant (relative to land area) in the south-central Bahamian Archipelago. As discussed in CHAPTER 1 section *1.1.1. Caribbean Blue Holes and Sinkholes*, this analysis revealed a meridional gradient in landform density, which was indeed highest in the southern Bahamas. It is likely that a southward shift of Caribbean rain belts during glacial periods enhanced carbonate dissolution in the southern Bahamas, resulting in more blue holes to the south. The methods for this analysis, which is a part of an in preparation study (Winkler et al., In prep., 2021) are detailed below.

APPENDIX A Section S1.2. Methods

Inland and nearshore karst landforms that are flooded by fresh, marine, or mixed (anchialine) water will be referred to as blue holes or BHFs hereafter in accordance with Mylroie et al. (1995). BHFs were identified by scanning *Google Earth Pro* imagery with the satellite eye altitude at ~2.5 km at using a 400 m x 400 m grid overlay to ensure that

all areas were assessed. Separate high- and reduced-confidence datasets were developed to address uncertainty related to variance in the quality of satellite imagery as well as marine inundation that obscured some features (>3 m; marsh or offshore). A "High Confidence" (HC) BHF: (i) has a near-perfect circle opening at the terrestrial or shallow-flooded surface, (ii) has a diameter >10 m, (iii) is distinguishable from other surrounding features or a marsh complex, and (iv) is flooded with water in all available satellite imagery (most recent and historical). Any other BHFs that did not meet HC definition criteria were designated as "Reduced Confidence" (RC).

Blue hole density across the Lucayan Archipelago assessed in *ArcMap 10.7.1* using a processing extent from 20.77 to 27.42° N and 70.73 to 80.58° W (processing area = 266,588 km^2), which was subdivided into a grid of 10 equivalent latitudinal zones (1 row ~0.67° lat). The HC (*n=893 points*) and RC (n=*5805 points*) features in each latitudinal band was calculated using a spatial join. These bands were then projected into the USA Contiguous Albers Equal Area coordinate system so that land area within each band could be accurately measured. In the "*Total_Area*" analysis, the number of BHFs per band in each dataset were divided by the entire terrestrial surface area within the band to determine land-area normalized BHF density (BHF per 100 km^2) for the (Fig. 1.2). This process was repeated for a subset of the data that only included features within a 3 km inland buffer zone along modern shoreline boundaries to account for bias related to the exceptionally large land area of northerly islands like Andros, Grand Bahama, and Abaco ("*3km_Buffer*" analysis, Fig. 1d,e,f). This 3 km buffer represents the zone in

which 85% of all BHFs (RC dataset) occur is the approximate width of many narrow islands in the southern archipelago (e.g., Long Island, Crooked Island, Exuma).

Assuming blue hole formation in a region follows a Poisson process in which regional event formation events occur discretely, we calculate cumulative Poisson probability (P) of regional BHF density equaling value (k) based on average values (λ) as follows in Eq. S1.1:

$$P(k,\lambda) = 1 - \sum_{k=0}^{k} \frac{\lambda^k e^{-\lambda}}{k!} \qquad \textbf{Eq. S1.1}$$

Values for expected land area normalized BHF density (λ) across the entire Bahamian Archipelago (Fig. 1.2a-c) as well as in the 3 km shoreline buffer zone (Fig. 1.2d-f) were calculated by dividing total BHF counts in each dataset (HC and RC) by the total land area being considered. Following the methods of Ulm (1990), upper 95th and lower 5th percentile thresholds were calculated based on the λ value of each data set to determine if BHF density significantly exceeds/falls-below the estimated variance exerted by stochastic forcing alone (Fig. 1.2).

APPENDIX A Section S1.3 Results

In total, 5085 RC BHF were identified across the Bahamian Archipelago, and 893 of these features were sub-designated as HC BHFs. In both datasets, blue holes are most common along the windward flanks of the islands, and 85% of RC blue holes occurred within 3 km of the modern shoreline (Figs. 1.2). Blue hole density in both the HC and RC datasets reveal density bias across the Bahamian Archipelago when

evaluated across the entire modern island areas (Fig. 1a) and within the 3 km shoreline buffer zone (Fig. 1.2b).

In the *Total_Area* evaluation of the HC dataset (area = 14,380 km^2), mean area normalized BHF density is 6.21 HC BHF per 100 km^2 across the Bahamian Archipelago, with Poisson significance thresholds of 13.1 HC BHF per 100 km^2 (95th percentile upper limit) and 2.2 HC BHF per 100 km^2 (5th percentile lower limit). Normalized density for the HC data exceeds the mean BHF per km^2 in meridional rows *R1* (27.42 - 26.75° N), *R6-R8* (24.09 - 22.1° N), and *R10* (21.43 – 20.77° N), and *R7* (27.5 BHF per 100 km^2; 23.43 – 22.77° N) exceeds the upper 95% threshold (Fig. 1.2a-c). In the RC dataset, there is an average 40.4 BHF per 100 km^2, with upper 95th (lower 5th) percentile thresholds of 55 (29) RC BHF per km^2. Rows *R6-R8* (24.09 - 21.43° N) all exceed the RC upper 95% Poison threshold with normalized density exceeding 55.1 BHF per 100 km^2. Except for *R4*, rows *R1-R5* (27.41 – 24.09° N) in the *Total_Area* RC analysis fall below the lower 5% Poisson significance threshold of 29 BHF per 100 km^2.

Similar spatial bias is observed in the *3km_Buffer* evaluations, which accounts for BHFs within a 3 km inland buffer along modern shoreline boundaries (area = 9490 km^2) (Fig. 1.2d-f). Average normalized *3km_Buffer* BHF density is 6.59 HC BHF per 100 km^2 across the Bahamian Archipelago, with Poisson significance thresholds of 13.74 HC BHF per 100 km^2 (95th percentile upper limit) and 2.5 HC BHF per 100 km^2 (5th percentile lower limit). Bands *R6-R8* all exceeded the average BHF per 100 km^2, but only *R7* exceed the upper 95% significance threshold with 27.2 HC BHF per 100 km^2. Bands *R1-R5* all fell below the mean HC BHF per km^2, and R2-R3 fell below the lower

5% significance threshold meaning that BHF density is significantly lower than expected in these bands. In the RC dataset, there is an average 50.5 BHF per 100 km2, with upper 95th (lower 5th) percentile thresholds of 68.8 (37.5) RC BHF per km^2. Rows *R6* and *R9* exceed the RC upper 95% Poison threshold, and aside from *R4*, rows R1-R5 all fall below the lower 5% Poisson significance threshold.

APPENDIX A Section S1.4 Discussion

The results of this study demonstrate that the majority of identified BHFs are located 3-7 km from the approximate LGM shoreline and may not have been "coastal" landforms at the time of formation. Overall, the *Total_Area* and *3km_Buffer* evaluations each reveal that *R6-R8* (24.09 - 22.1° N) tend to have the highest sustained BHF density in both the HC and RC datasets, and that bands *R1-R5* (27.41 – 24.09° N) tend to have the lowest BHF density. This demonstrates significantly lower BHF density in the higher latitudes with a bias toward the higher densities at the lower mid-archipelago. It is therefore unlikely that blue hole development is exclusively driven by groundwater mixing dissolution at the coastal zone, which is the predominant mechanism of the Flank Margin Model for Dissolution Development (Mylroie and Carew, 1990). Numerous geologic and geographic mechanisms could drive this spatial bias at an island scale, but it likely that long term hydroclimate plays a substantial role at a broader regional scale.

In the Bahamas, studies have shown that karst dissolution rates in the freshwater lens vary in response to seasonal rainfall in (Whitaker and Smart, 1997a) and are higher after sustained rainfall events (Whitaker and Smart, 2007a). Rainfall events have also

been found to ventilate the subsurface, thus promoting microbial respiration and DOC oxidation in the upper portion of the water table (Gulley et al., 2020). Based on this, significant regional variability in rainfall likely influence the long-term rate of karstification across the Bahamian Archipelago.

A north-south annual precipitation gradient is observed across the Bahamian Archipelago over the last 70 years, with the northern Bahamas receiving nearly twice the annual precipitation of the southern islands due to a zone of arid subsidence that is situated from 70° to 80° W in the Caribbean (Jury et al., 2007, Magaña and Caetano, 2005). Records demonstrate that regional hydroclimate can vary substantially throughout the Holocene in response to ocean/climate forcing (Sullivan et al., Submitted, Tamalavage et al., 2020, Kjellmark, 1996), so it possible that long-term variability in regional hydroclimate contributes to the spatial density bias in BHFs.

As reviewed by Schneider et al. (2014), the position of the ITCZ has a substantial meridional influence on rainfall in the tropical North Atlantic. Broadly speaking, warm-moist air convected at the ITCZ advects poleward, delivering precipitation until the air mass descends at the subtropical extent of the North Atlantic Hadley Cell. In the Atlantic, mean ITCZ position migrates between extents of ~9° N in boreal summer and ~2° N in boreal winter; however, overall annual mean ITCZ position can migrate or expand meridionally by up to ±7° in response to centennial and millennial scale variability in hemispheric temperature gradients and oceanic circulation (Arbuszewski et al., 2013, Schneider et al., 2014). During the LGM, the ITCZ experienced as much as a 7° southward migration (Arbuszewski et al., 2013). It is likely that the persistent rainbelt

over the northern Bahamas migrated south alongside the ITCZ during Quaternary glacial periods, thereby reducing rainfall in the northern archipelago and enhancing it over the islands in R6-R8 (24.09 - 22.1° N, Fig. 1.2). Indeed, speleothem records from Abaco Island in the Northern Bahamas record more negative $\delta^{18}O$ migrations that are related to air temperature decreases and aridity during periods of Northern Hemispheric cooling like (e.g., Heinrich Stadials and the LGM) (Arienzo et al., 2015, Arienzo et al., 2017). Over the last 20,000 years, more depleted $\delta^{18}O$ values in northern Bahamian speleothems are anticorrelated with enhanced rainfall noted by decreasing surface salinity and $\delta^{18}O_{seawater}$ in deep marine cores from the equatorial Atlantic (Arbuszewski et al., 2013).

Conduit cave development is enhanced on larger, circular carbonate islands where a higher area/perimeter ratios restrict diffuse discharge of the meteoric lens (Larson and Mylroie, 2018). Enhanced regional rainfall in the southern archipelago during glacial periods coupled with up to 120 m lower sea level would result in expanded island areas with extensive meteoric lenses that could have persisted until 8-9 KYA when sea-level was within ~10 m of current levels (Larson and Mylroie, 2018, Khan et al., 2017). The change to accommodation space would have been dramatic on narrow islands on the eastern Great Bahama Bank (i.e., Eleuthra, Exuma, Long Island) and Crooked Island/Aklins (Fig. 1.2). This sustained dissolution conduit development in these southern islands would have resulted in more BHFs while enhancing bedrock porosity overall in these limestones. Indeed, the Lucayan limestone bedrock in the southern Bahamas tends to have higher matrix porosity than similar strata to the north

(Cant and Weech, 1986). Higher aquifer porosity is also conducive to fast flow meteoric injection which can deliver more DOC into the meteoric lens while and enhancing mixing and tidal ventilation, thus fueling processes that further enhancing dissolution rates on these islands (Gulley et al., 2020, Gulley et al., 2015, Whitaker and Smart, 2007).

Smaller islands in the southeastern Bahamas receive less rain and typically have thinner freshwater lens(es) based on observations from the last 30 years (Cant and Weech, 1986, Roebuck et al., 2004, Jury et al., 2007). Holocene sea-level rise inundated the majority of Bahamian platforms around 8-9 KYA (Khan et al., 2017, Larson and Mylroie, 2018), following this, the meteoric lens(es) have split by on islands with (i) evaporation rates in excess of meteoric recharge and (ii) higher limestone porosity that promotes rapid diffuse or conduit flow (Gulley et al., 2016). It is possible that during Quaternary interglacials, more zones of shallow dissolution exist at the distal extents of fractured meteoric lenses where dissolution is promoted by high specific discharge rates.

APPENDIX A Section S1.5. Conclusions

This study provides evidence of a significant spatial bias in BHF density across the Bahamian Archipelago, wherein BHF density (normalized to land area) is highest between meridional bands between 24.09 - 22.1° N (Fig. 1.2). In light of these results, we hypothesize that higher rates of carbonate dissolution in the southern Bahamian Archipelago are driven in large part by long-term shifts in regional hydroclimate. In particular, increased rainfall during Quaternary glacial sea-level lowstands when the

ITCZ shifts southward due to hemispheric cooling enhances dissolution and results in higher bedrock porosity on these southern islands. Coupling this geologic change with interglacial sea-level rise and lower rainfall driven by a northward shift of the ITCZ creates a thin, divided meteoric lens across many of these southern islands where stratigraphically shallow carbonate dissolution continues. Together, these mechanisms can create a positive feedback loop in which the southern islands are continually experiencing enhanced dissolution, with rainfall consistently being a key variable. Further studies that improve our understanding the age, depth/elevation, and surrounding geology of BHFs as well as the long-term hydroclimate variability and groundwater flow patterns for specific islands and platform areas will help improve interpretations this study's results.

APPENDIX A Section S1.6. References

ARBUSZEWSKI, J. A., DEMENOCAL, P. B., CLÉROUX, C., BRADTMILLER, L. & MIX, A. J. N. G. 2013. Meridional shifts of the Atlantic intertropical convergence zone since the Last Glacial Maximum. 6**,** 959-962.

ARIENZO, M. M., SWART, P. K., BROAD, K., CLEMENT, A. C., POURMAND, A. & KAKUK, B. 2017. Multi-proxy evidence of millennial climate variability from multiple Bahamian speleothems. *Quaternary Science Reviews,* 161**,** 18-29.

ARIENZO, M. M., SWART, P. K., POURMAND, A., BROAD, K., CLEMENT, A. C., MURPHY, L. N., VONHOF, H. B. & KAKUK, B. 2015. Bahamian speleothem reveals temperature decrease associated with Heinrich stadials. *Earth and Planetary Science Letters,* 430**,** 377-386.

CANT, R. V. & WEECH, P. S. 1986. A review of the factors affecting the development of Ghyben-Hertzberg lenses in the Bahamas. *Journal of Hydrology,* 84**,** 333-343.

GULLEY, J., BREECKER, D., COVINGTON, M., COOPERDOCK, S., BANNER, J., MOORE, P., NORONHA, A., BREITHAUPT, C., MARTIN, J. & JENSON, J.

2020. Tidal pumping and biogeochemical processes: dissolution within the tidal capillary fringe of eogenetic coastal carbonates. *Earth Surface Processes and Landforms*.

GULLEY, J., MAYER, A., MARTIN, J. & BEDEKAR, V. 2016. Sea level rise and inundation of island interiors: Assessing impacts of lake formation and evaporation on water resources in arid climates. *Geophysical Research Letters,* 43**,** 9712-9719.

GULLEY, J. D., MARTIN, J. B., MOORE, P. J., BROWN, A., SPELLMAN, P. D. & EZELL, J. 2015. Heterogeneous distributions of CO2 may be more important for dissolution and karstification in coastal eogenetic limestone than mixing dissolution. *Earth Surface Processes and Landforms,* 40**,** 1057-1071.

JURY, M., MALMGREN, B. A. & WINTER, A. 2007. Subregional precipication climate of the Caribbean and relationships with ENSO and NAO. *Journal of Geophysical Research,* 112**,** 11.

KHAN, N. S., ASHE, E., HORTON, B. P., DUTTON, A., KOPP, R. E., BROCARD, G., ENGELHART, S. E., HILL, D. F., PELTIER, W. & VANE, C. H. 2017. Drivers of Holocene sea-level change in the Caribbean. *Quaternary Science Reviews,* 155**,** 13-36.

KJELLMARK, E. 1996. Late Holocene climate change and human disturbance on Andros Island, Bahamas. *Journal of Paleolimnology,* 15**,** 133-145.

LARSON, E. B. & MYLROIE, J. E. 2018. Diffuse Versus Conduit Flow in Coastal Karst Aquifers: The Consequences of Island Area and Perimeter Relationships. *Geosciences,* 8**,** 268.

MAGAÑA, V. & CAETANO, E. 2005. Temporal evolution of summer convective activity over the Americas warm pools. *Geophysical Research Letters,* 32**,** L02803.

MYLROIE, J. E. & CAREW, J. L. 1990. The flank margin model for dissolution cave development in carbonate platforms. *Earth Surface Process Landforms,* 15**,** 413-424.

MYLROIE, J. E., CAREW, J. L. & MOORE, A. I. 1995. Blue holes: definitions and genesis. *Carbonates and Evaporites,* 10**,** 225-233.

ROEBUCK, L., POCHATILA, J. & ORTIZ, T. 2004. *Water resources assessment of the Bahamas*, US Army Corps of Engineers, Mobile District & Topographic Engineering Center.

SCHNEIDER, T., BISCHOFF, T. & HAUG, G. H. 2014. Migrations and dynamics of the intertropical convergence zone. *Nature,* 513**,** 45-53.

SULLIVAN, R. M., VAN HENGSTUM, P. J., COATS, S. J., DONNELLY, J. P., TAMALAVAGE, A. E., WINKLER, T. S. & ALBURY, N. A. Submitted. Hydroclimate Dipole drive multi-centennial variability in the western Tropical North Atlantic Margin during the Middle and Late Holocene. *Paleoceanography and Paleoclimatology*.

TAMALAVAGE, A. E., VAN HENGSTUM, P. J., LOUCHOUARN, P., FALL, P. L., DONNELLY, J. P., ALBURY, N. A., COATS, S. & FEAKINS, S. J. 2020. Plant wax evidence for precipitation and vegetation change from a coastal sinkhole lake in the Bahamas spanning the last 3000 years. *Organic Geochemistry,* 150**,** 104120.

ULM, K. 1990. Simple method to calculate the confidence interval of a standardized mortality ratio (SMR). *American journal of epidemiology,* 131**,** 373-375.

WHITAKER, F. F. & SMART, P. L. 2007. Geochemistry of meteoric diagenesis in carbonate islands of the northern Bahamas: 1. Evidence from field studies. *Hydrological Processes: An International Journal,* 21**,** 949-966.

WINKLER, T. S., VAN HENGSTUM, P. J., CAVAZOS, O., HIGHFIELD, W., DONNELLY, J. P. & COATS, S. In prep., 2021. Latitudinal rainfall mediates karst landform density across the Bahamian Archipelago. Texas A&M University.

APPENDIX B

CHAPTER 2 SUPPLEMENTAL INFORMATION

Revising evidence of hurricane strikes on Abaco Island (The Bahamas) over the last 700 years

APPENDIX B Section S2.1. Hurricane track density distribution map methods

The map of hurricane track density distribution was based on International Best Track Archive for Climate Stewardship (*IBTrACS) v04* hurricane track segments from 1851 to 2019 CE (Knapp et al., 2018, Knapp et al., 2010). Hurricane intensity (Saffir-Simpson scale) at each segment is from the IBTrACS v4 subset USA_Agency_SSHS, which is derived from HURDAT_ATL maximum wind speed data. The *USA_Agency* subset is a hierarchical composite of multiple meteorological organizations measured maximum wind speed data, but is primarily populated by HURDAT2 data. For more information on how data from the *USA_Agency* subset was compiled, see Knapp et al. (2010) and Knapp et al. (2018).

To create this map, a grid of 50x50 km cells was overlaid across the North Atlantic Basin (including the GOM and Caribbean) in *ArcMap v10.7.1* software. *IBTrACS v04* storm tracks were then filtered to exclude any storm track segments that were not ≥Category 2 hurricanes (or ≥Category 3 in APPENDIX B Fig. S2.1), meaning that segments of storms with maximum wind speeds <154 km hr^{-1} were not counted at any point, even if the storm reached ≥Category 2 intensity at other points along its track. Once the data was filtered, the storm-tracks were "dissolved" (i.e., merged) into a single track for each qualifying storm using the Storm Identification number (SID) as a

qualifier. This left 566 individual storms that qualified as ≥Category. 2 hurricanes. These 566 hurricane tracks were then spatially joined to the 50x50 km grid cells so that the number of segments that fell within each could be summed. These grid cells were then spatially joined to points located at the center of each cell so that the point could be assigned the z-value of the sum of ≥Category 2 or 3 storm tracks within the grid cell.

We utilized Inverse Distance Weighted (IDW) interpolation with the ArcMap *Geostatiscal Analyst* toolbox to spatially characterize the gradients in storm counts throughout the basin. This interpolation method allows the user to specify the degree to which surrounding point values influence one another. We utilized a power factor of 8, meaning that the IDW interpolation weighted proximal value points far more heavily that distal points. This is an appropriate method given that hurricanes strikes are relatively localized events and each grid cell, and the point with event count values were richly and evenly disturbed across the north Atlantic. Given that storm tracks are geographically stochastic (albeit, not necessarily climatologically), IDW interpolation using a higher power factor of 8 will better preserve extremes and spatial count gradients in data values that are evenly spaced and relatively abundant.

The resulting interpolated output was visualized using six in event frequency bins. We acknowledge increased levels of uncertainty in the track and measured intensity of storms that occurred prior to the satellite era of hurricane observation in the 1960s, assuming that observational error was consistent from region to region over time, we can be confident in the results of this spatial analysis as a metric of relative geographic variability in hurricane track density.

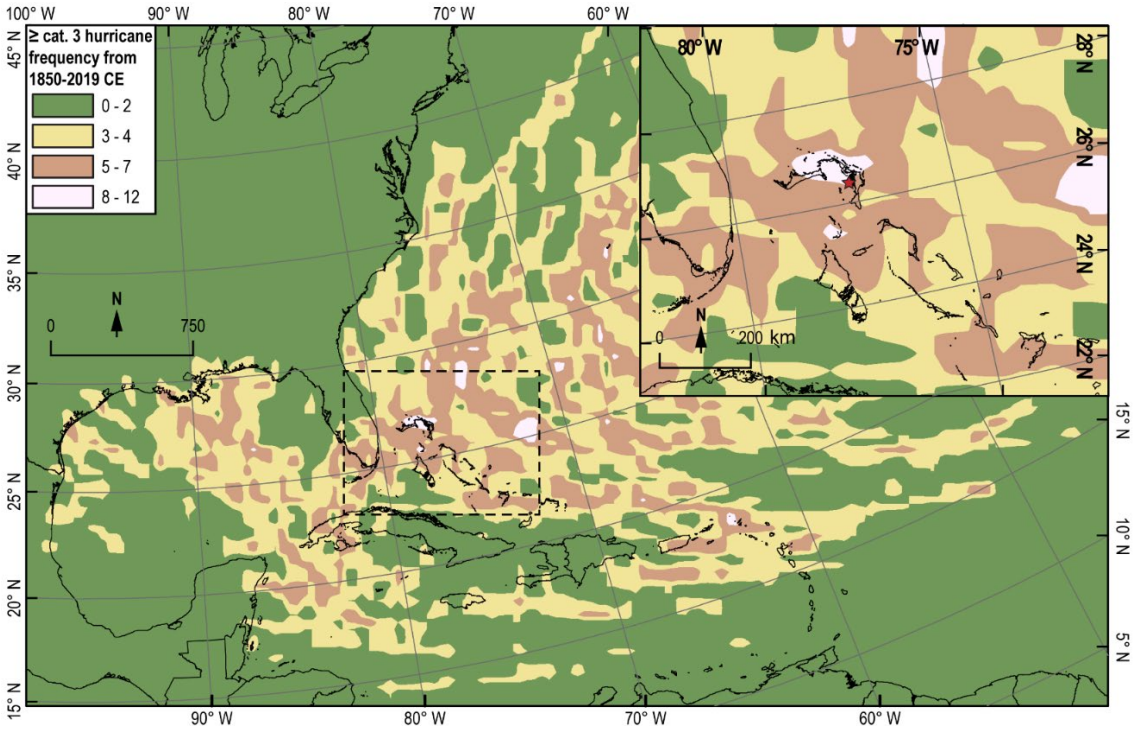

APPENDIX B Figure S2.1. Frequency of exposure to ≥Category 3 hurricane winds a 50 km radius from 1850 to 2019 CE throughout the North Atlantic. As with Fig. 2.1 from CHAPTER 2 and described above, but a density map of higher intensity >Category 3 events. Storm track and intensity data is from the IBTrACS dataset v04 (Knapp et al., 2018, Knapp et al., 2010). Saffir-Simpson storm intensity is specifically derived from the IBTrACS v4 subset USA_Agency_SSHS, which is derived from HURDAT_ATL maximum wind speed data. Thatchpoint Blue Hole is indicated with a red star. The regions that we refer to as modern hurricane hotspots are pinkish white in color (11-16 ≥category 2 events within 50 km s). Basemaps were downloaded from *DIVA-GIS* (Hijmans et al., 2005). Map and assciated spatial calculations were performed in ArcMap 10.7.1 software using North America Albers Equal Conic Area projected coordinate system (Snyder, 1978).

APPENDIX B Section S2.2. Coring locations in Thatchpoint Blue Hole

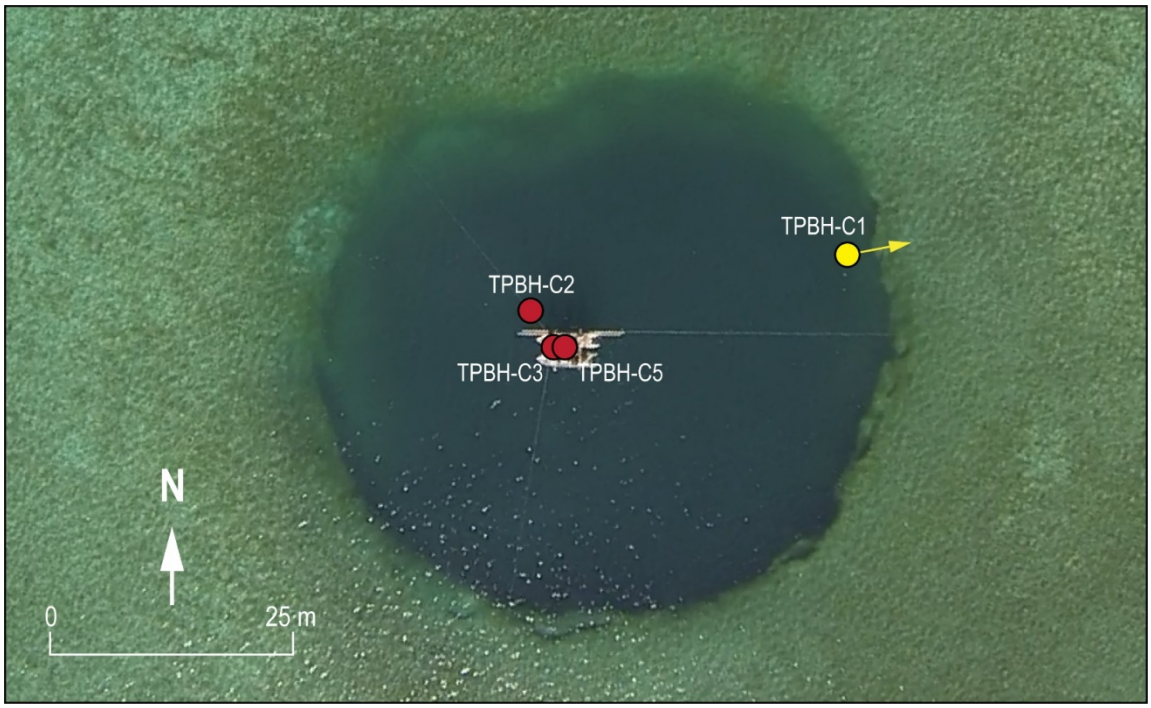

APPENDIX B Figure S2.2. Coring locations in TPBH. The three cores collected in January 2015 (red circles) were TPBH-C2 (26.32342° N, -77.29345° W, 615 cm), TPBH-C3 (26.323390° N, -77.29342° W; recovered length of 836 cm), and TPBH-C5 (26.32339° N, -77.29343° W; 194 cm). These cores were collected using a Rossfelder P3 submersible vibracoring system from the inflatable raft seen in the image. The yellow circle for TPBH-C1 (26.32346° N, -77.29315° W; recovered length of 164 cm) marks the location in which the scientific divers boat was anchored as published by (van Hengstum et al., 2014); however, it is now thought that the is a push core collected on SCUBA in August, 2011 was collected from underneath the wall that overhangs to the east of the yellow circle as marked by the yellow arrow. Aerial imagery was collected by Pete van Hengstum in January 2015 using a DJI Phantom 3 with a mounted GoPro Hero3 digital camera.

APPENDIX B Section 2.3. Age-control points from Thatchpoint Blue Hole composite record.

APPENDIX B Table S2.1. Radiocarbon results from TPBH. Of the 16 samples from TPBH-C3 that were radiocarbon dated, 11 were included in the Bayesian statistical age model as 5 samples had measured ages older than stratigraphically deeper dates. This suggests that these samples were reworked from older sediments before being redeposited in to TPBH. Both dates from TPBH-C2 were included in the age-model. Radiocarbon dates were calibrated using IntCal13 or MarineCal13 (Reimer et al., 2013) as described in section 2.3. Methods in CHAPTER 2. The text "NaN ± NaN" in the "Conventional ^{14}C age" column of sample 1 denotes that the sample is younger than 1950 CE, and was therefore calibrated using the Northern Hemisphere Zone 2 (NHZ2) post-comb calibration data set in CALIbomb (Reimer et al., 2004). All possible 1σ and 2σ age calibrations are provided for each submitted date.

	Index No.	Accession number	Core	Section depth (cm)	Total core depth (cm)	Material	$F^{14}C$	Conventional ^{14}C age	$d^{13}C$ (‰)	1σ calendar ages in yrs. B_{1950} (probability)	2σ calendar ages in yrs. B_{1950} (probability)	Highest probability 1σ age (cal yrs B_{1950})	Median probabilit age (cal y B_{1950})
TPBH-C3	1	OS-128341	TPBH-C3-1:6	46.5	61.5	Leaf	1.1774 ± 0.0028	NaN ± (NaN)	-26	-39.14 to -37.84 (0.964	-39.84 to -37.77 (0.802	-38.48 ± 1	-38.48
										-37.25 to -37.18 (0.036	-37.46 to -36.94 (0.095		
											-36.36 to -36.24 (0.014		
											-35.93 to -35.83 (0.011		
											-9.13 to -8.50 (0.078)		
	2	OS-137779	TPBH-C3-3:6	37.5	315.5	Unidentifiable Organics	0.922 ± 0.0018	655 ± (15)	-17.04	307-271 (1.000)	364-257 (1.000)	290 ± 20	290
	3	OS-124637	TPBH-C3-3:6	38.5	316.5	Leaf	0.9727 ± 0.0022	225 ± (20)	-25.32	297-284 (0.52)	305-275 (0.504)	290 ± 5	190
										166-154 (0.48)	181-180 (0.004)		
											172-151 (0.417)		
											8-0* (0.075)		
	4	OS-124753	TPBH-C3-3:6	87.5	365.5	Leaf	0.9649 ± 0.0031	285 ± (25)	-25.3	426-392 (0.586)	435-352 (0.613)	410 ± 15	380
										318-298 (0.414)	333-288 (0.387)		
	5	OS-147817	TPBH-C3-4:6	1.5	464.5	Leaf	0.9695 ± 0.002	250 ± (15)	NM	303-291 (1.000)	307-285 (0.926)	295 ± 5	295
											165-157 (0.074)		
	6	OS-127186	TPBH-C3-4:6	100.5	502.5	Leaf	0.9621 ± 0.0019	310 ± (15)	-26.86	426-391 (0.684)	433-355 (0.772)	410 ± 20	395
										387-379 (0.122)	332-306 (0.228)		
										319-309 (0.194)			
	7	OS-124752	TPBH-C3-5:6	22.5	629.5	Unidentifiable Organics	0.9022 ± 0.0019	825 ± (15)	-8.79	486-450 (1.000)	499-428 (1.000)	470 ± 20	465
	8	OS-124638	TPBH-C3-5:6	95.5	702.5	Leaf	0.9525 ± 0.0019	390 ± (15)	-25.75	498-468 (1.000)	503-451 (0.889)	485 ± 15	480
											443-440 (0.011)		
											348-335 (0.1)		
	9	OS-127185	TPBH-C3-6:6	7.5	762.5	Leaf	0.9527 ± 0.002	390 ± (15)	-24.53	498-468 (1.000)	503-451 (0.889)	485 ± 15	480
											443-440 (0.011)		
											348-335 (0.1)		
	10	OS-137463	TPBH-C3-6:6	90.5	845.5	Mollusc	0.8995 ± 0.0017	850 ± (15)	0.01	582-568 (0.253)	603-560 (0.353)	640 ± 25	635
										657-628 (0.747)	664-617 (0.647)		
	11	OS-121213	TPBH-C3-6:6	94.5	849.5	Mollusc	0.8982 ± 0.002	860 ± (20)	1.51	579-570 (0.137)	602-560 (0.274)	645 ± 25	640
										663-630 (0.863)	670-618 (0.726)		
TPBH-C2	12	OS-147909	TPBH-C2-4:6	53.5	390.5	Leaf	0.9294 ± 0.0019	590 ± (15)	-8.79	279-228 (0.961)	282-172 (0.907)	255 ± 25	245
										158-153 (0.039)	168-145 (0.093)		
	13	OS-147910	TPBH-C2-6:6	34.5	560.5	Leaf	0.958 ± 0.0018	345 ± (15)	-26.17	459-429 (0.418)	477-424 (0.401)	445 ± 15	380
										376-348 (0.369)	396-317 (0.599)		
										339-323 (0.213)			
Unused dates	14	OS-128299	TPBH-C3-2:6	56.5	201.5	Mollusc	0.9397 ± 0.0019	500 ± (15)	2.03	186-165 (0.119)	233-47 (0.923)	105 ± 45	115
										146-59 (0.846)	25-0* (0.077)		
										5-0* (0.036)			
	15	OS-137462	TPBH-C3-2:6	88.5	233.5	Mollusc	0.9034 ± 0.0018	815 ± (15)	1.69	481-442 (1.000)	495-421 (1.000)	460 ± 20	460
	16	OS-137762	TPBH-C3-3:6	34.5	312.5	Fish Bone	0.8683 ± 0.0021	1130 ± (20)	-11.23	697-655 (1.000)	726-641 (1.000)	680 ± 20	680
	17	OS-121212	TPBH-C3-3:6	85.5	363.5	Mollusc	0.886 ± 0.0023	975 ± (20)	1.46	570-534 (0.656)	622-518 (1.000)	565 ± 30	565
										597-575 (0.344)			
	18	OS-137780	TPBH-C3-5:6	94.5	701.5	Unidentifiable Organics	0.9303 ± 0.0023	580 ± (20)	-18.67	271-224 (0.702)	278-139 (1.000)	250 ± 25	225
										214-194 (0.181)			
										161-149 (0.118)			

APPENDIX B Table S2.2. Pollen and Opaque Spherule abundance in TPBH. Pollen recorded in percentages. Nomenclature follows Correll and Correll (1982).

	Core	TPBH-C3-1:6	TPBH-C3-1:6	TPBH-C3-2:6	TPBH-C3-2:6	TPBH-C3-3:6	TPBH-C3-3:6	TPBH-C3-4:6
	Section depth (cm)	**51.5**	**124.5**	**61.5**	**130.5**	**58.5**	**127.5**	**44.5**
	Total core depth (cm)	**66.5**	**139.5**	**206.5**	**275.5**	**336.5**	**405.5**	**507.5**
	Age-model median age (yr CE)	**1976**	**1926**	**1871**	**1814**	**1769**	**1709**	**1622**
Fossil Pollen Concentration	Exotic pollen added (#grains/2.5cm³)	27,000	27,000	27,000	27,000	27,000	27,000	27,000
	Fossil pollen counted (#grains/2.5cm³)	103	102	107	102	105	77	101
	Exotic pollen counted (#grains/2.5cm³)	69	68	102	127	70	147	93
	Fossil pollen concentration (#grains/cm³)	16121.73913	16200	11329.41176	8674.015748	16200	5657.142857	11729.03226
Opaque Spherules	Raw counts opaque spherules (#spherules/2.5cm³)	360	925	222	148	34	124	19
	Opaque spherules (#spherules/cm³)	144	370	88.8	59.2	13.6	49.6	7.6
Mangroves	*Conocarpus erectus* L.	0	0	0	1.92	2.33	6.06	0
	Rhizophora mangle L.	1.19	1.15	0	0	2.33	3.03	3.23
	Avecennia germinans (L.)L.	1.19	0	0	0	0	0	0
Trees & Shrubs	Whole Grains *Pinus caribaea* Morelet	33.33	25.29	37.78	23.86	30.23	22.73	19.35
	1/3 Grains *Pinus caribaea* Morelet	19.05	34.48	33.33	27.27	23.26	22.73	34.41
	Total *Pinus caribaea* Morelet	52.38	59.77	71.11	51.13	53.49	45.46	53.76
	Arecaceae Bercht. and J.Presl, nom. cons.	2.38	10.34	2.22	2.27	3.49	9.09	10.75
	Acacia Mill.	2.38	0	2.2	0	5.81	1.52	1.08
	Metopium toxiferum (L.) Krug and Erb.	0	1.15	0	0	0	3.03	1.08
	Bursera Jacq. ex L.	1.19	0	0	0	0	0	0
	Buxus bahamensis Baker	3.57	0	2.22	4.55	3.49	0	1.08
	Caesalpinoideae D C.	3.57	4.6	2.22	7.95	1.16	4.55	14.58
	Capparis L.	0	0	1.11	1.14	0	0	0
	Coccoloba P. Br. Ex L. nom. cons.; Howard	0	1.15	2.22	0	0	1.52	0
	Cordia L.	0	2.3	2.22	0	0	3.03	0
	Cupressaceae Bartl.	0	1.15	1.11	1.14	0	0	2.15
	Euphorbiaceae Juss.	2.38	0	0	0	0	0	0
	Fabaceae Lindley	0	3.11	1.11	0	1.16	0	0
	Myrica cerifera L.	5.95	2.3	1.11	6.82	0	9.09	1.08
	Myrtaceae Juss.	1.19	1.15	0	1.14	0	0	0
	Picrodendron baccatum (L.) Krug. And Erb	0	0	0	0	3.49	0	3.23
	Randia aculeata L.	3.57	2.3	0	1.14	0	0	1.08
	Swietenia mahogani (L.) Jacq.	0	1.15	0	0	0	0	0
	Tabebuia DC.; Gentry	0	1.96	0	0	0	1.52	0
Herbs & Pteridophytes	*Asteraceae* Dum., nom. cons.	0	0	1.11	1.14	0	0	1.08
	Bromeliaceae Juss.	0	0	0.93	0	0	0	0
	Amarthaceae Juss.	0	0	0	4.55	0	0	0
	Convolvulaceae Juss.	2.38	0	0	0	1.16	0	2.15
	Poaceae Barnhart	3.51	1.15	6.67	7.95	2.33	3.03	4.3
	Batis maritima L.	0	0	0	0	0	0	0.99
	Heliotropium L.	0	1.15	0	0	0	1.52	2.15
	Salicornia L.	0	2.3	1.11	2.27	0	0	0
	Sesuvium L.	0	1.15	0	1.14	0	0	0
	Pteridium (L.) Kuhn	6.8	3.92	12.5	4.9	11.43	5.19	0
	Trilete Spore	0	0	0	0	0	0	5.94
Indeterminates & Unknowns	Indeterminates and Unknowns	23.5	13.42	5.02	13.37	11.43	16.67	7.1

APPENDIX B Figure S2.3. Imagery of opaque spherules from 139-140 cm in the TPBH composite record (TPBH-C3-1:6_124.5 cm). The large spherule near the center of the frame is exactly 10 um in diameter, well within the range of opaque spherule size range) found by Clark and Patterson (1984) (5-25 um), and the broader range of sizes) from Griffin and Goldberg (1975)(approximately 4-50 um). The image was taken on an Olympus BH-2 OM with a Cannon DS126201 digital camera in the Hartshorn Quaternary Laboratory at UMASS Amherst.

Total fossil pollen was counted to over 100 grains per level except for TPBH-C3-3:6_127.5 cm, and total fossil pollen concentrations ranged from 16,200 to 5,657 grains/cm^3. At level TPBH-C3-3:6_127.5 cm (400.5 cm total core depth), the lower 5,657 grain concentration counts limited the total counts to 77 grains. Total fossil pollen concentrations were calculated using the method of Bennett and Willis (2001). As discussed in **CHAPTER 2** section *2.3.2. Age Control*, the sharp peak in opaque spherules at 140 cm (TPBH-C3-1:6_124.5 cm) is interpreted as an artifact of the "Wilson City" logging settlement from 1906 to 1916 CE (due east of TPBH), and possibly a regional increase in economic activity including shipping around the turn of century before late WWI (Craton and Saunders, 2002).

APPENDIX B Section S2.3.2. Gamma Dating: Methods and Results.

Downcore radionuclide activity for ^{137}Cs and ^{210}Pb was measured to better constrain the modern chronology of the upper portion of TPBH-C3. ^{137}Cs is a manmade radionuclide that is useful for identifying the onset of hydrogen thermonuclear weapons testing in 1954 and its moratorium in 1963 (Pennington et al., 1973). To quantify ^{137}Cs activity, bulk sediment was sampled at 5-15 cm intervals, desiccated, and powdered. Powdered samples were then placed on a Canberra GL2020RS low energy Germanium gamma well detector where the gamma decay of the sample was measured for a 24-hour period.

The peak in ^{137}Cs activity associated with 1963 CE moratorium on nuclear weapons testing falls at 80-81 cm. Independent of this constraint, the sedimentary age-model predicts as median age of 1963 CE at 79-80 cm (APPENDIX B Fig. S2.4). Further, the onset of detectable levels of ^{137}Cs around 1954 CE occurs between 115 to 100 cm in the composite TPBH record. This is within the age and depth error range of the Bayesian age-model (Fig. 2.3), where 1954 CE occurs at a minimum depth of 69 cm, a median depth of 89-90 cm, and maximum depth of 124 cm. Altogether, measure ^{137}Cs provides a useful independent assessment the veracity of the TPBH age-model during the instrumental record and of the TPBH composite record sedimentary age-model that was derived from radiocarbon dates and an opaque spherule chronohorizon.

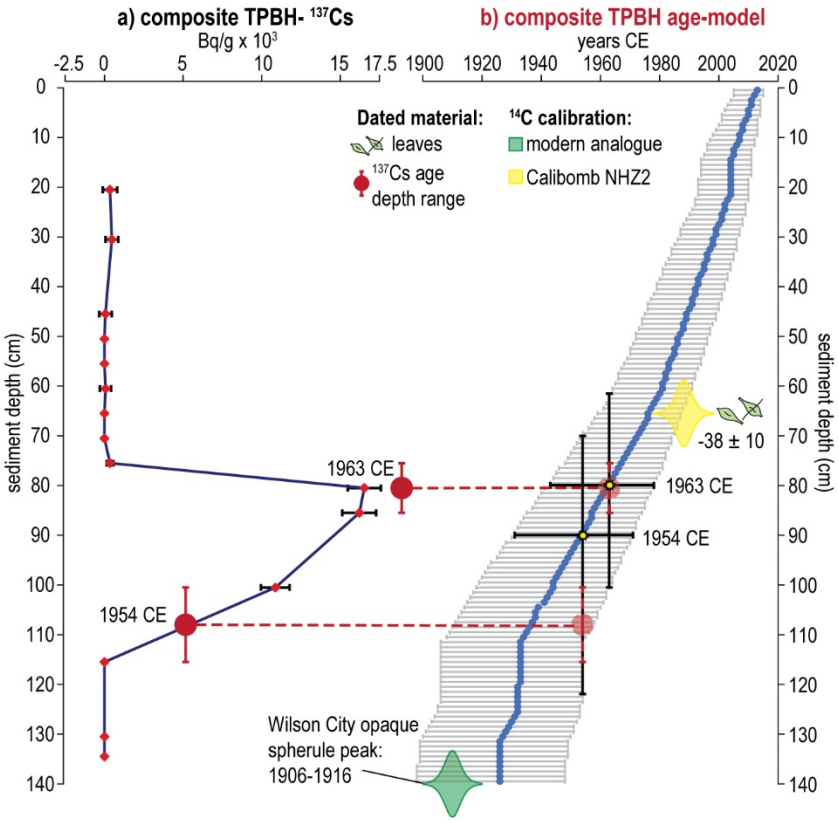

APPENDIX B Figure S2.4. 137Cs activity compared to the radiocarbon-based Bayesian sedimentary age-model. a) Red diamonds represent the sampling locations and measured ^{137}Cs activity in 1000 Becquerels per gram (Bq -g^{-1} x 10^{3}). The black bars on each diamond show the uncertainty in measured ^{137}Cs activity. Red circles show the estimated 1954 and 1963 CE chronohorizon depths based on the 137Cs activity, and the red error bars show the depth uncertainty on where that peak could have occurred (±5 cm for 1963 CE, ±7.5 cm for 1954 CE onset). b) The blue dots represent the median age at each cm interval for the first 140 cm of the TPBH composite record, and the grey error bars represent the 2σ age uncertainty at each interval. The yellow stars represent the depth that the radiocarbon age-model predicts to have median ages of 1954 and 1963 CE, and the black bars show the uncertainty for age (horizontal) and depth at each point.

APPENDIX B Section S2.4. Event Attributions

APPENDIX B Table S2.3. Event attributions for event beds with median dates from 1940 to 2015 CE. This table lists all hurricane events within 50 and 115 km of TPBH from 1940 to 2015 CE based on IBTrACS[1,2] and supplements the CHAPTER 2 section 2.5.1. Historical Hurricane Strikes: Calibrating the Record and Figure 2.4. This portion of the instrumental record has higher confidence due to aircraft monitoring of meteorological events beginning in the 1940s, and the eventual development of satellite monitoring in the 1960s (McAdie et al., 2009, Vecchi and Knutson, 2011). The hurricane(s) that is most likely attributed to the event bed is in bold text. Grey text is used for events that violate the Principle of Superposition if we assume prior attributions are correct, and stars are used to denote hurricanes that are attributed to stratigraphically higher (shallower) event beds.

Event Bed	*Median Age (year CE)*	*2σ Age-Range (year CE)*	*Historical Events within 50 km*	*Passage Details*	*Historical Events within 115 km*	*Passage Details*	*Most Probable Event(s)*
E1	2013	2005-2015	Sandy, 2012 (cat. 1)	45 km E	Noel, 2007 (cat. 1)	80 km E	**Irene, 2011 (cat. 2)**, most intense and proximal of possible events
			Irene, 2011 (cat. 2)	**15 km east**			
E2	2004	1995-2011	*Irene, 2011 (cat. 2)	*15 km E	Noel, 2007 (cat. 1)	80 km E	**Jeanne, 2004 (cat. 3), Frances, 2004 (cat. 2)**; high coarse sediment % likely combined result of two events in the same year
			Jeanne, 2004 (cat. 2)	**50 km N**	Dennis, 1999 (cat. 1)	60 km NE	
			Frances, 2004 (cat. 3)	**40 km S**			
			Floyd, 1999 (cat. 3)	15 km E			
			Erin, 1995 (cat. 1)	25 km S			
E3	1995	1982-2004	*Jeanne, 2004 (cat. 2)	*50 km N	Dennis, 1999 (cat. 1)	60 km NE	**Floyd, 1999 (cat. 3)**; storm surge from this storm had profound impacts across Abaco due to intensity and proximity of this storm
			*Frances, 2004 (cat. 3)	*40 km S	Andrew, 1992 (cat. 4-5)	112 km S	
			Floyd, 1999 (cat. 3)	**15 km S**			
			Erin, 1995 (cat. 1)	25 km S			
E4	1986	1972-1996	Erin, 1995 (cat. 1)	25 km S	**Andrew, 1992 (cat. 4-5)**	**112 km S**	**Andrew, 1992 (cat. 4-5)**; in passing NE→SW southward of TPBH, the peak winds from front right quadrant directed water from Atlantic toward TPBH
No event beds	1951-1990				Betsy, 1965 (cat. 3)	70 km E	No significant event beds
					Janice, 1958 (cat. 1)	100 km E	
					Betsy, 1956 (cat. 3)	84 km E	
					Able, 1951 (cat. 1)	90 km NE	
E5	1941	1915-1961	**21 Sep. 1947 (cat. 3)**	**43 km NE**	Janice, 1958 (cat. 1)	100 km E	**21 Sep. 1947 (cat. 3), 12 Sep 1946 (cat. 1)**; First ≥cat. 2 events within 50 km of TPBH prior the lull in activity from 1950 to 1990 CE
			12 Sep. 1946 (cat. 1)	**30 km SW**	Betsy, 1956 (cat. 3)	84 km E	
			5 Sep. 1933 (cat. 3)	15 km W	Able, 1951 (cat. 1)	90 km NE	
			29 Jul. 1933 (cat. 1)	4 km N	11 Aug. 1939 (cat. 1)	65-100 km S	
			6 Sep. 1932 (cat. 5)	Direct strike	4 Nov. 1935 (cat. 2)	55 km NW	
					29 Sep. 1935 (cat. 4)	95 km NW	
					6 Sep. 1934 (cat. 1)	80 km NE	
					3 Sep. 1933 (cat. 4)	75 km S	
					25 Sep. 1929 (cat. 4)	105 km SE	
					16 Sep. 1928 (cat. 4)	115 km SW	
					26 Jul. 1926 (cat. 3)	115 km SW	
					21 Oct. 1926 (cat. 3)	90 km NW	
					27 Sep. 1923 (cat. 1)	100 km E	

APPENDIX B Table S2.4. Event attributions for event beds with median dates from 1850 to 1940 CE. This table lists all hurricane events within 50 and 115 km of TPBH from 1850 to 1940 CE based on IBTrACS and supplements the attribution text below and Fig. 2.4. This portion of the instrumental record has lower confidence regarding observations of storm intensity, track, translation speed, size, etc. (McAdie et al., 2009, Vecchi and Knutson, 2011). The hurricane(s) that is most likely attributed to the event bed is in bold text. Grey text is used for events that violate the Principle of Superposition if we assume prior attributions are correct, and stars are used to denote hurricanes that are attributed to stratigraphically higher (shallower) event beds.

Event Bed	Median Age (year CE)	2σ Age-Range (year CE)	Historical Events within 50 km	Passage Details	Historical Events within 115 km	Passage Details	Most Probable Event(s)
E6	1936	1910-1957	*21 Sep. 1947 (cat. 3)	*43 km NE	Betsy, 1956 (cat. 3)	84 km E	**29 Sep. 1935 (cat. 4)**
			*12 Sep. 1946 (cat. 1)	*30 km SW	Able, 1951 (cat. 1)	90 km NE	
			5 Sep. 1933 (cat. 3)	15 km W	11 Aug. 1939 (cat. 1)	65-100 km S	
			29 Jul. 1933 (cat. 1)	4 km N	4 Nov. 1935 (cat. 2)	55 km NW	
			6 Sep. 1932 (cat. 5)	Direct strike	**29 Sep. 1935 (cat. 4)**	**95 km NW**	
					6 Sep. 1934 (cat. 1)	80 km NE	
					3 Sep. 1933 (cat. 4)	75 km S	
					25 Sep. 1929 (cat. 4)	105 km SE	
					16 Sep. 1928 (cat. 4)	115 km SW	
					26 Jul. 1926 (cat. 3)	115 km SW	
					21 Oct. 1926 (cat. 3)	90 km NW	
					27 Sep. 1923 (cat. 1)	100 km E	
E7	1933	1906-1954	*21 Sep. 1947 (cat. 3)	*43 km NE	Betsy, 1956 (cat. 3)	84 km E	**6 Sep. 1932 (cat. 5)**
			*12 Sep. 1946 (cat. 1)	*30 km SW	Able, 1951 (cat. 1)	90 km NE	
			5 Sep. 1933 (cat. 3)	15 km W	11 Aug. 1939 (cat. 1)	65-100 km S	
			29 Jul. 1933 (cat. 1)	4 km N	4 Nov. 1935 (cat. 2)	55 km NW	
			6 Sep. 1932 (cat. 5)	**Direct strike**	*29 Sep. 1935 (cat. 4)	95 km NW	
					6 Sep. 1934 (cat. 1)	80 km NE	
					3 Sep. 1933 (cat. 4)	75 km S	
					25 Sep. 1929 (cat. 4)	105 km SE	
					16 Sep. 1928 (cat. 4)	115 km SW	
					26 Jul. 1926 (cat. 3)	115 km SW	
					21 Oct. 1926 (cat. 3)	90 km NW	
					27 Sep. 1923 (cat. 1)	100 km E	
E8	1926	1898-1948	*21 Sep. 1947 (cat. 3)	*43 km NE	11 Aug. 1939 (cat. 1)	65-100 km S	**25 Sep. 1929 (cat. 4), 16 Sep. 1928 (cat. 4)**
			*12 Sep. 1946 (cat. 1)	*30 km SW	4 Nov. 1935 (cat. 2)	55 km NW	
			5 Sep. 1933 (cat. 3)	15 km W	*29 Sep. 1935 (cat. 4)	95 km NW	
			29 Jul. 1933 (cat. 1)	4 km N	6 Sep. 1934 (cat. 1)	80 km NE	
			*6 Sep. 1932 (cat. 5)	Direct strike	3 Sep. 1933 (cat. 4)	75 km S	
			1 Oct. 1908 (cat. 2)	5 km west	**25 Sep. 1929 (cat. 4)**	**105 km SE**	
					16 Sep. 1928 (cat. 4)	**115 km SW**	
					27 Jul. 1926 (cat. 3)	115 km SW	
					21 Oct. 1926 (cat. 3)	90 km NW	
					27 Sep. 1923 (cat. 1)	100 km E	
					12 Oct. 1909 (cat. 2)	75 km W	
					7 Sep. 1906 (cat. 3)	105 km NE	
					1899 (cat. 3)	115 km W	
					1899 (cat. 1)	115 km W	

APPENDIX B Table S2.4. Attributions for event beds with median dates from 1850 to 1940 CE (continued).

Event Bed	Median Age (year CE)	2σ Age-Range (year CE)	Historical Events within 50 km	Passage Details	Historical Events within 115 km	Passage Details	Most Probable Event(s)
			5 Sep. 1933 (cat. 3)	15 km west	11 Aug. 1939 (cat. 1)	65-100 km S	
			29 Jul. 1933 (cat. 1)	4 km north	4 Nov. 1935 (cat. 2)	55 km NW	
			*6 Sep. 1932 (cat. 5)	*Direct strike	*29 Sep. 1935 (cat. 4)	95 km NW	
			1 Oct. 1908 (cat. 2)	**5 km W**	6 Sep. 1934 (cat. 1)	80 km NE	
			6 Sep. 1896 (cat. 3)	10 km W	3 Sep. 1933 (cat. 4)	75 km S	
			12 Oct. 1893 (cat. 3)	40 km N	*25 Sep. 1929 (cat. 4)	*105 km SE	
			26 Aug. 1893 (cat. 3)	20 km SW	*16 Sep. 1928 (cat. 4)	*115 km SW	
E9	1918	1890-1942			26 Jul. 1926 (cat. 3)	115 km SW	**1 Oct. 1908 (cat. 2)**
					21 Oct. 1926 (cat. 3)	90 km NW	
					27 Sep. 1923 (cat. 1)	100 km E	
					12 Oct. 1909 (cat. 2)	75 km W	
					7 Sep. 1906 (cat. 3)	105 km NE	
					30 Oct. 1899 (cat. 1)	115 km W	
					13 Aug. 1899 (cat. 3)	115 km W	
					22 Oct. 1896 (cat. 2)	75 km NW	
			*1 Oct. 1908 (cat. 2)	*5 km W	12 Oct. 1909 (cat. 2)	75 km W	
			6 Sep. 1896 (cat. 3)	10 km W	7 Sep. 1906 (cat. 3)	105 km NE	
			12 Oct. 1893 (cat. 3)	40 km N	30 Oct. 1899 (cat. 1)	115 km W	
			26 Aug. 1893 (cat. 3)	**20 km SW**	13 Aug. 1899 (cat. 3)	115 km W	
E10	1883	1851-1909	22 Aug. 1887 (cat. 3)	25 km N	22 Oct. 1895 (cat. 2)	75 km NW	**26 Aug. 1893 (cat. 3)**
			9 Sep. 1883 (cat. 2)	40 km W	17 Aug. 1879 (cat. 1)	55 km E	
			2 Oct. 1866 (cat. 4)	30 km W	24 Aug. 1871 (cat. 2)	110 km S	
					15 Aug. 1871 (cat. 3)	55 km N	
					12 Oct. 1870 (cat. 1-2)	60 km W	
			6 Sep. 1896 (cat. 3)	10 km W	30 Oct. 1899 (cat. 1)	115 km W	
			12 Oct. 1893 (cat. 3)	40 km N	13 Aug. 1899 (cat. 3)	115 km W	
			*26 Aug. 1893 (cat. 3)	*20 km SW	22 Oct. 1895 (cat. 2)	75 km NW	
E11	1873	1841-1900	22 Aug. 1887 (cat. 3)	25 km N	17 Aug. 1879 (cat. 1)	55 km E	**2 Oct. 1866 (cat. 4)**
			9 Sep. 1883 (cat. 2)	40 km W	24 Aug. 1871 (cat. 2)	110 km S	
			2 Oct. 1866 (cat. 4)	**30 km W**	15 Aug. 1871 (cat. 3)	55 km N	
					12 Oct. 1870 (cat. 1-2)	60 km W	

APPENDIX B Section S2.5 References

BENNETT, K. D. & WILLIS, K. J. 2001. Pollen. *In:* SMOL, J. P., BIRKS, H. J. & LAST, W. M. (eds.) *Tracking Environmental Change Using lake Sediments. Volume 3: Terrestrial, Algal, and Siliceous Indicators.* Dordrecht, The Netherlands: Kluwer Academic Publishers.

CLARK, J. S. & PATTERSON, W. A. 1984. Pollen, Pb-210, and opaque spherules; an integrated approach to dating and sedimentation in the intertidal environment. *Journal of Sedimentary Research,* 54**,** 1251-1265.

CORRELL, D. S. & CORRELL, H. B. 1982. Flora of the Bahama archipelago. *Flora of the Bahama Archipelago.*

CRATON, M. & SAUNDERS, G. 2002. *Islanders in the Stream: A History of the Bahamian People. Volume Two: From the Ending of Slavery to the Twenty-First Century*, JSTOR.

GRIFFIN, J. J. & GOLDBERG, E. D. 1975. The fluxes of elemental carbon in coastal marine sediments. *Limnology and Oceanography,* 20**,** 456-463.

HIJMANS, R. J., CAMERON, S. E., PARRA, J. L., JONES, P. G. & JARVIS, A. 2005. Very high resolution interpolated climate surfaces for global land areas. *International journal of climatology,* 25**,** 1965-1978.

KNAPP, K. R., DIAMOND, H. J., KOSSIN, J. P., KRUK, M. C. & SCHRECK, C. J. 2018. International Best Track Archive for Climate Stewardship (IBTrACS) Project, Version 4, [North Atlantic Subset]. *In:* INFORMATION, N. N. C. F. E. (ed.).

KNAPP, K. R., KRUK, M. C., LEVINSON, D. H., DIAMOND, H. J. & NEUMANN, C. J. 2010. The international best track archive for climate stewardship (IBTrACS) unifying tropical cyclone data. *Bulletin of the American Meteorological Society,* 91**,** 363-376.

MCADIE, C., LANDSEA, C., NEUMANN, C. J., DAVID, J. E. & BLAKE, E. S. 2009. *Tropical Cyclones of the North Atlantic Ocean, 1851-2006: With 2007 and 2008 Track Maps Included*, US Department of Commerce, National Oceanic and Atmospheric Administration.

PENNINGTON, W., CAMBRAY, R. S. & FISHER, E. M. 1973. Observations on lake sediments using fallout 137Cs as a tracer. *Nature,* 242**,** 324-326.

REIMER, P. J., BARD, E., BAYLISS, A., BECK, J. W., BLACKWELL, P. G., RAMSEY, C. B., BUCK, C. E., CHENG, H., EDWARDS, R. L. & FRIEDRICH, M. 2013. IntCal13 and Marine13 radiocarbon age calibration curves 0–50,000 years cal BP. *Radiocarbon,* 55**,** 1869-1887.

REIMER, P. J., BROWN, T. A. & REIMER, R. W. 2004. Discussion: reporting and calibration of post-bomb 14C data. *Radiocarbon,* 46**,** 1299-1304.

SNYDER, J. P. 1978. Equidistant conic map projections. *Annals of the Association of American Geographers,* 68**,** 373-383.

VAN HENGSTUM, P. J., DONNELLY, J. P., TOOMEY, M. R., ALBURY, N. A., LANE, P. & KAKUK, B. 2014. Heightened hurricane activity on the Little Bahama Bank from 1350 to 1650 AD. *Continental Shelf Research,* 86**,** 103-115.

VECCHI, G. A. & KNUTSON, T. R. 2011. Estimating annual numbers of Atlantic hurricanes missing from the HURDAT database (1878–1965) using ship track density. *Journal of Climate,* 24**,** 1736-1746.

APPENDIX C

CHAPTER 3 SUPPLEMENTAL INFORMATION

Oceanic passage of hurricanes across Cay Sal Bank in The Bahamas over the last 550 years

APPENDIX C Section S3.1. Additional Hine's Hole Subbottom, Photos, and Coring Locations

APPENDIX C Table S3.1. Coring drive lengths and locations

Core	Latitude °N	Longitude °W	Water depth (m)	Pipe length (cm)	Drive length (cm)	Recovery length (cm)	Intact sediment/ water interface
Core-4	23.8662	79.8063	75	244	240	202	No
Core-7	23.8658	79.8052	87.5	1800	1800	1627	No
Core-8	23.8659	79.8047	86.5	244	200	162	Yes
Core-9	23.866	79.805	88	2100	1300	1240	Yes

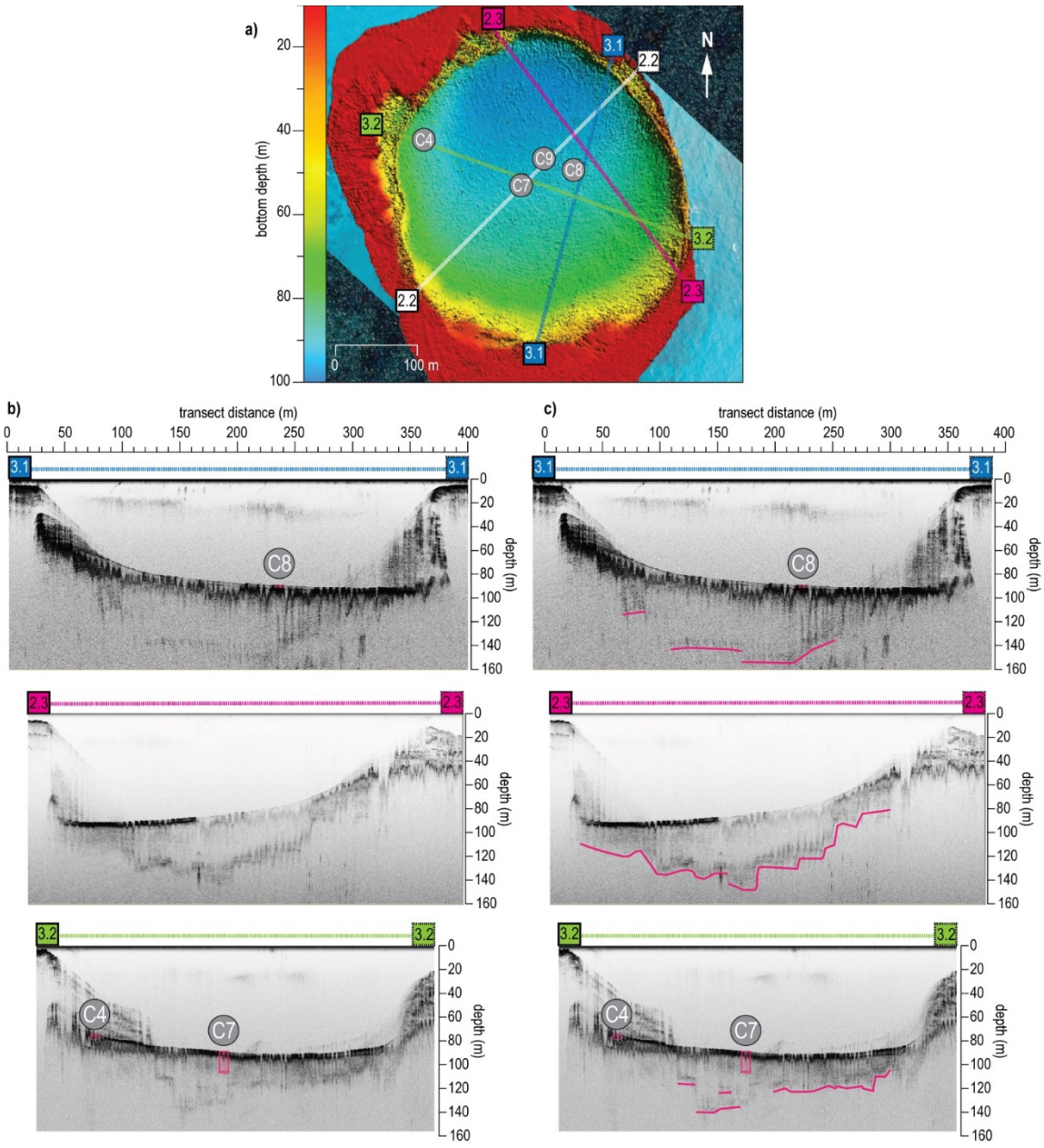

APPENDIX C Figure S3.1. 2D depiction of multibeam bathymetry of Hine's Hole from along with coring locations noted by grey circles and 3 Chirp subbottom seismic transect paths. Images from each transect are shown below the map panel, with raw output to the left and interpreted subbottom features noted in pink in the identical images to the right. Core names and depths are added to each image where the transect line intersects core sampling location.

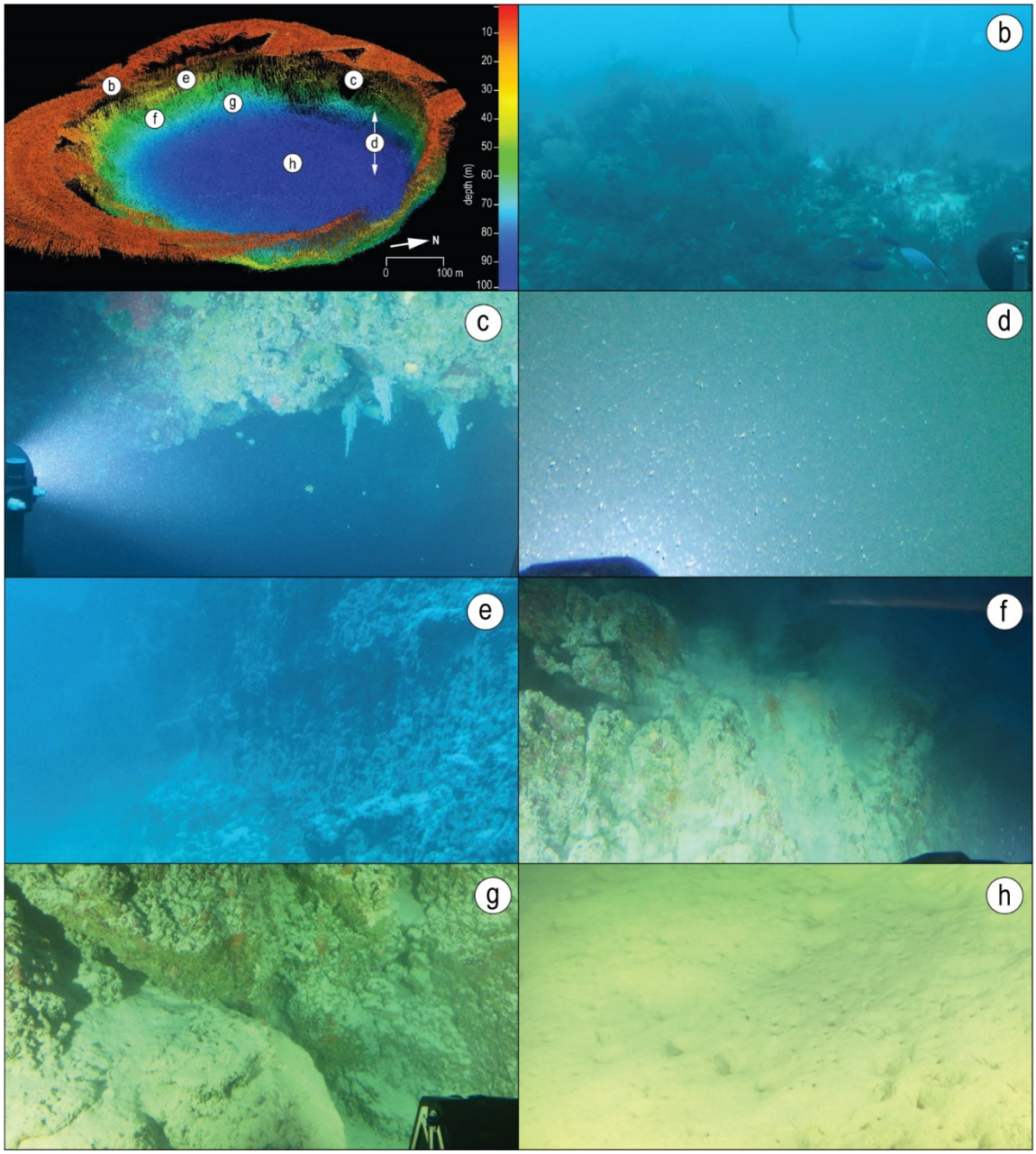

APPENDIX C Figure S3.2. a) 3D multibeam bathymetry of Hine's Hole with photograph locations noted by white circles. b) Soft corals and seagrass along the rim of Hine's Hole; c) overhanging wall below the rim of Hine's Hole wherein fine grained carbonate sediments in water column are illuminated by light from *HOV Nadir*; d) fine grained carbonate sediments raining out through water column in the center of Hine's Hole; e) sheer wall with carbonate mud accumulating; f-g) carbonate mud accumulation along wall thickens as slope diminishes with water depth; h) scattered invertebrate burrows in fine-grained carbonate sediment accumulated in Hine's Hole near the location of Core-7.

APPENDIX C Section 3.2. Stratigraphic Correlation

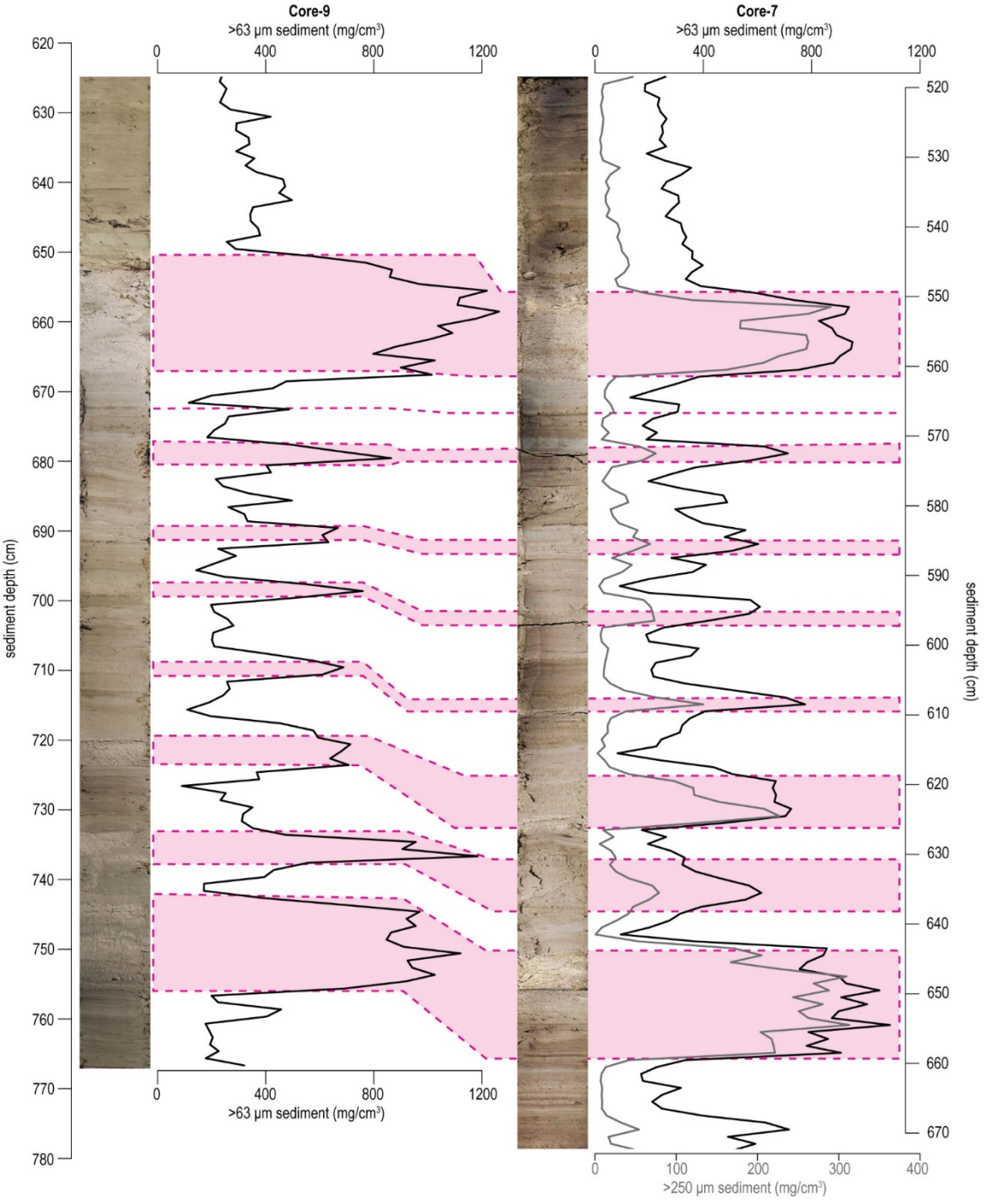

APPENDIX C Figure S3.3. Example stratigraphic correlation between Cores-9 and -7.

APPENDIX C Section 3.3. Age-control points from Hine's Hole Cores

APPENDIX C Table S3.2. Radiocarbon results from Hine's Hole. Of the 26 samples from Hine's Hole Cores-7 (11) and 9 (4) that were radiocarbon dated, only the 15 dates sampled from core sections included in the Hine's Hole Composite were included in the Bayesian statistical age model (i.e., upper 280 cm of Core 9 and lower 1447 cm of Core 7). To produce the sedimentary age model (CHAPTER 3 Fig. 3.5a; APPENDIX C Fig. S4), radiocarbon dates were calibrated with Marine20 calibration curve (Heaton et al., 2020) as described in the *3.2 Age-Control* in CHAPTER 3. The text ">Modern" in the "Conventional ^{14}C age" column of samples C7-1,2 and C9-1,2 denotes that these samples are rich in radiocarbon produced by thermonuclear weapons testing, meaning that they are younger than 1950 CE. As such, these dates were calibrated using the Northern Hemisphere Zone 2 (NHZ2) post-comb calibration data set in CALIbomb (Reimer et al., 2004). In the column "Hine's Hole Composite Depth", which is the adjusted stratigraphic depth of the sample in the Hine's Hole Composite that was used to generate the age model, "N/A" is used for samples from sections not included in the composite. The symbol "N/M" is used to denote that that a value was not measured for certain samples.

Accession Number	Core and Section	Section Depth (cm)	Core Depth (cm)	Hine's Hole Composite Depth (cm)	Material Dated	Δ14C	Conventional ^{14}C age	Conventional ^{14}C age error	$F^{14}C$	$F^{14}C$ Error	$\delta^{13}C$ (‰)
OS-154216	CSAL1-D7-1:14	44	44.5	N/A	bivalve shell	82.27	>Modern		1.0909	0.0022	-0.58
OS-154217	CSAL1-D7-1:14	121.5	121.5	N/A	bivalve shell	-60.03	435	15	0.9475	0.0018	0.86
OS-154218	CSAL1-D7-2:14	51.5	179.5	280.5	bivalve shell	-58.1	415	15	0.9495	0.0019	1.92
OS-154219	CSAL1-D7-3:14	53.5	310.5	412.5	bivalve shell	-66.58	490	15	0.9409	0.0018	2.14
OS-154220	CSAL1-D7-4:14	96.5	392.5	494.5	bivalve shell	-72.76	545	15	0.9347	0.0018	1.08
OS-154221	CSAL1-D7-8:14	9.5	484.5	586.5	bivalve shell	-89.79	690	15	0.9175	0.0019	0.99
OS-150279	CSAL1-D7-4:14	4.5	697.5	798.5	bivalve shell	-68.01	500	15	0.9395	0.0018	0.78
OS-150280	CSAL1-D7-6:14	50.5	828.5	929.5	bivalve shell	-81.16	615	15	0.9262	0.0018	2.61
OS-150281	CSAL1-D7-8:14	69.5	888.5	989.5	bivalve shell	-92.93	720	15	0.9143	0.0018	1.15
OS-150282	CSAL1-D7-10:14	102	1160.5	1260.5	bivalve shell	-101.13	790	15	0.9061	0.0019	1.53
OS-150283	CSAL1-D7-11:14	97.5	1280.5	1381.5	bivalve shell	-109.61	870	15	0.8975	0.0017	N/M
OS-150284	CSAL1-D7-12:14	104.5	1428.5	1529.5	bivalve shell	-117.78	940	15	0.8893	0.0019	0.9
OS-135569	CSAL1-D7-14:14	65.5	1626.5	1727.5	gorgonian coral	N/M	1,060	16	0.8767	0.0018	-11.65
OS-154210	CSAL1-D9-1:12	16.5	16.5	16.5	bivalve shell	70.59	>Modern		1.0792	0.0022	0.08
OS-154211	CSAL1-D9-1:12	95.5	95.5	95.5	bivalve shell	119.18	>Modern		1.1281	0.0023	0.54
OS-154222	CSAL1-D9-2:12	70	186.5	186.5	bivalve shell	-64.41	470	15	0.9431	0.0019	0.83
OS-154223	CSAL1-D9-3:12	48	273.5	273.5	bivalve shell	-60.22	435	15	0.9473	0.0018	1.73
OS-154224	CSAL1-D9-7:12	22.5	372.5	N/A	bivalve shell	-70.54	525	15	0.9369	0.002	1.45
OS-154225	CSAL1-D9-10:12	29.5	456.5	N/A	bivalve shell	-89.88	690	15	0.9174	0.0019	0.64
OS-154226	CSAL1-D9-11:12	16.5	586.5	N/A	bivalve shell	-88.25	680	15	0.9191	0.0018	0.68
OS-150285	CSAL1-D9-4:12	42.5	634.5	N/A	bivalve shell	-63.02	460	15	0.9445	0.0019	1.03
OS-150286	CSAL1-D9-5:12	125.5	781.5	N/A	bivalve shell	-65.27	480	15	0.9422	0.0019	1.8
OS-150287	CSAL1-D9-7:12	70.5	894.5	N/A	bivalve shell	-77.72	585	15	0.9297	0.0018	1.9
OS-150288	CSAL1-D9-9:12	14	930.5	N/A	bivalve shell	-74.2	555	15	0.9332	0.0019	0.68
OS-150289	CSAL1-D9-10:12	65.5	1000.5	N/A	bivalve shell	-90.62	700	15	0.9167	0.0018	0.6
OS-150290	CSAL1-D9-12:12	71	1173	N/A	bivalve shell	-93.76	725	15	0.9135	0.0018	1.03

APPENDIX C Section 3.4. ΔR Considerations and Alternate Age models

An alternate age model was developed using the same depths and control points as the age model used for the Hine's Hole Composite record to assess the potential impact that ΔR correction calculated from a mix of regional values in the literature (APPENDIX C Fig. S3.4). The weighted mean of the 40 closest literature values, derived from various corals, bivalves, and gastropods, suggest a correction of ΔR=-92 ± 111 (Diaz et al., 2017, Druffel, 1997, Druffel and Linick, 1978, DiNapoli et al., 2021, Hadden and Schwadron, 2019, Lighty et al., 1982, Broecker and Olson, 1961). The ΔR correction value of -92 years is exceeded by the uncertainty in this estimate, which is expected given the high intra- and inter-island variability in local marine reservoir offsets throughout The Caribbean described by DiNapoli et al. (2021). This reservoir correction of ΔR (2σ) = -92 ± 111 only shifts the median projected age older by an average 19.6 cal yrs BP ±8.8. Further, based on the work of Kondo (1987), the pallial sinus index of the Tellinidae bivalve specimens we dated (~0.3) suggests that these organisms burrow their approximate body length into the sediment, meaning that dated organisms are likely to be stratigraphically young. As such, we feel that adding any additional ΔR correction presents greater uncertainty than correcting to the global marine reservoir value alone and remain confident in the age model used for this study in which a default ΔR value of 0 was applied.

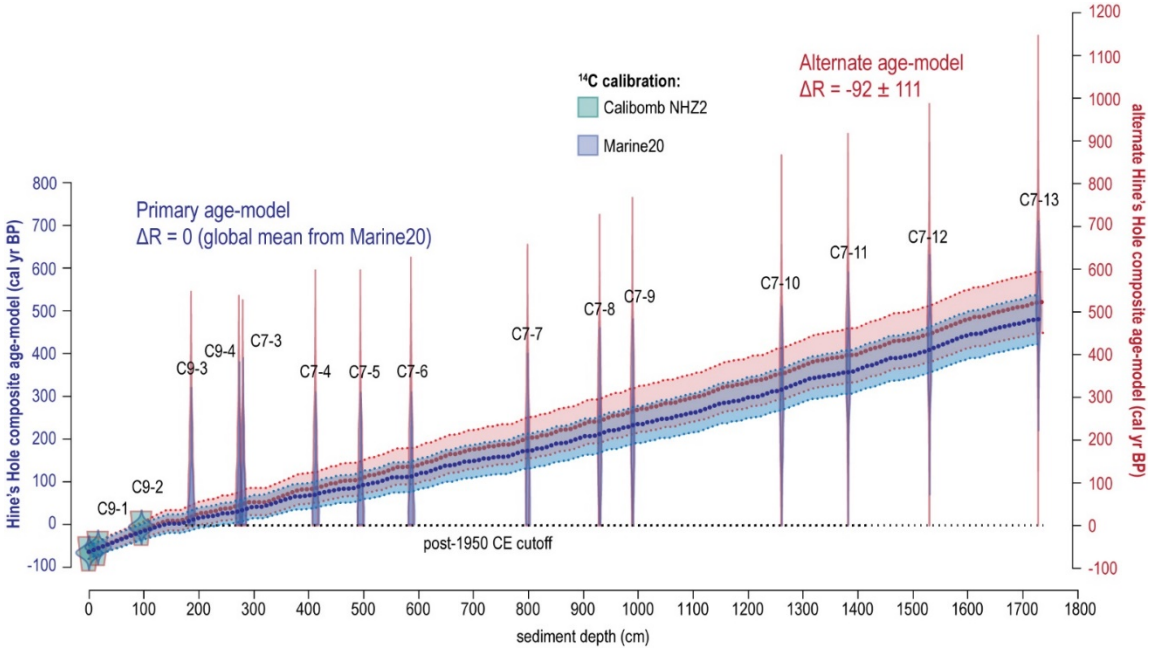

APPENDIX C Figure S3.4. Potential age models for Hine's Hole Composite record made using BACON (Blaauw and Christen, 2011) and Marine20 (Heaton et al., 2020). In blue is the primary age model used for this study where no additional ΔR correction was added to account for local variance in the marine radiocarbon reservoir and had a median age range of -64 to 491 cal yrs BP (average uncertainty -32.5 yrs or +30 yrs). In red is an alternative age model developed for this study using an additional regional reservoir correction of ΔR= -92 ± 111 based on an average of the 40 most proximal literature values and had a median age range of -62 to 525 cal yrs BP (average uncertainty -47.6 or +44). Overall, the ΔR= -92 ± 111 correction resulted in slightly older age-estimates, with an average shift of 19.6 cal yrs BP older (±8.8) with the largest impacts toward the base of the core.

APPENDIX C Section 3.5. IBtRACS Hurricane Track Analysis (1850-2019 CE)

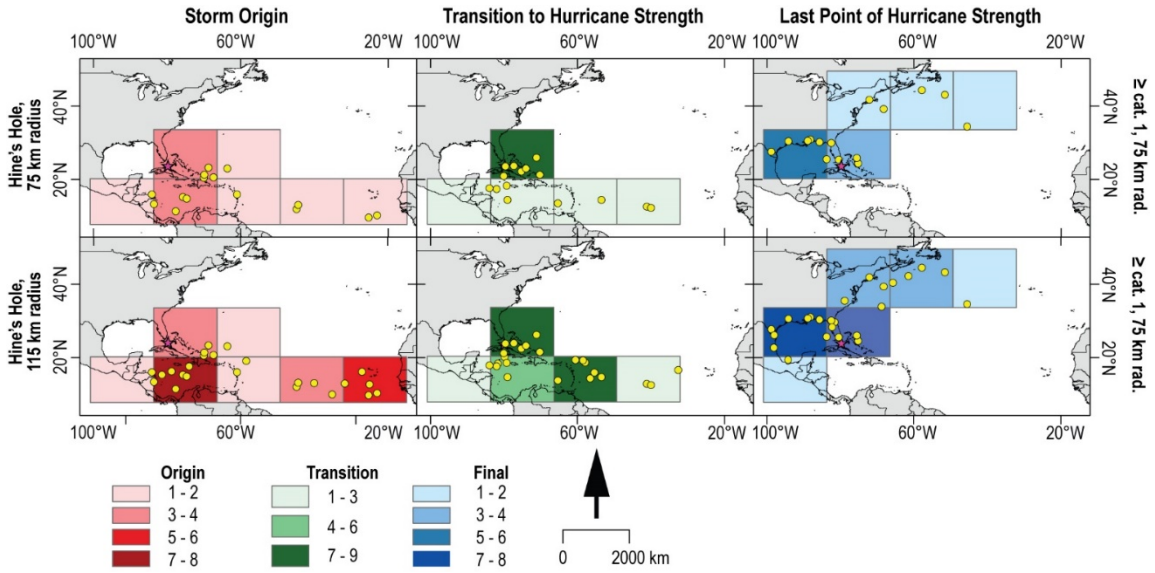

APPENDIX C Figure S3.5. Locations of storm origin (column 1, red), point of transition into hurricane strength storm (column 2, green), and the last point of hurricane strength winds before dissipation (column 3, blue) of all ≥Category 1 hurricanes passing with a 75 km radius (row 1, 15 events) or a 115 km radius (row 2, 23 events) of Hine's Hole (pink star). All data is from the International Best Track Archive for Climate Stewardship (IBTrACS) v04 (Knapp et al., 2018, Knapp et al., 2010) dataset spanning the period from 1850 to 2016 CE. The ~1500 km x ~1800 km grids count the number of track points within each grid, with darker colors corresponding to more points within the grid cell. This shows that hurricanes that are most likely to impact the area around Hine's Hole tend to form in the Main Development Region just off the western coast of Africa near Cape Verde or in central Southern Caribbean between Cuba and northern South America. These events tend to intensify to hurricane strength east of Cay Sal Bank near the Bahamian Archipelago or the Lesser Antilles, and highest rates of final landfall are observed throughout the northern Gulf of Mexico.

APPENDIX C Table S3.3. Event attributions for >250 µm coarse sediment anomalies with median dates from 1900 to 2015 CE. This table lists all hurricane events within 75 and 115 km of Hine's Hole from 1900 to 2015 CE based on IBTrACS and supplements the CHAPTER 3 section *5.2 Calibrating the Record to Historical Hurricanes* and Figure 3.6. The hurricane(s) that is most likely attributed to the event bed is in bold text. Grey text is used for events that violate the Principle of Superposition if we assume prior attributions are correct.

Event Bed	*2σ Age-Range (CE)*	*Median Age (CE)*	*Historical Events within 75 km*	*Passage Details*	*Historical Events within 115 km*	*Passage Details*	*Most Probable Event(s)*
E1	1993-2022	2007	Rita, 2005 (Cat. 1)	71 km, RR			Michelle, 2001 (Cat. 1)
			Michelle, 2001 (Cat. 1)	**74 km, FL**			
			Georges, 1998 (Cat. 1-2)	65 km, FR			
E2	1976-2007	1991	Rita, 2005 (Cat. 1)	26 km, RR			Georges, 1998 (Cat. 1-2)
			Michelle, 2001 (Cat. 1)	74 km, FL			
			Georges, 1998 (Cat. 1-2)	**65 km, FR**			
E3	1961-1994	1977	**Greta, 1970 (TS)**	**30 km, FL**	Inez, 1966, (Cat. 1)	85 km, FL	**Greta, 1970 (TS)**
			Cleo, 1964 (Cat. 1)	21 km, FL			
			Donna, 1960 (Cat. 3)	11 km, FL			
E4	1929-1966	1947	Cleo, 1964 (Cat. 1)	21 km, FL	Inez, 1966, (Cat. 1)	85 km, FL	**Donna, 1960 (Cat. 3)**
			Donna, 1960 (Cat. 3)	**11 km, FL**	15 Sep. 1945 (Cat. 4)	100 km, FL	
			Fox, 1952 (Cat. 1)	30 km, FR	1 Sep. 1933 (Cat. 3)	89 km, FR	
			King, 1950 (Cat. 2)	34 km, RL	5 Oct. 1933 (Cat. 2)	86 km, FR	
			2 Sep. 1935 (Cat. 4)	8 km, FL			
			28 Sep. 1935 (Cat. 3)	43 km, FR			
			27 Sep. 1929 (Cat. 3)	63 km, FL			
E5	1911-1951	1930	**King, 1950 (Cat. 2)**	**34 km, RL**	15 Sep. 1945 (Cat. 4)	100 km, FL	**King, 1950 (Cat. 2)**
			2 Sep. 1935 (Cat. 4)	8 km, FL	1 Sep. 1933 (Cat. 3)	89 km, FR	
			28 Sep. 1935 (Cat. 3)	43 km, FR	5 Oct. 1933 (Cat. 2)	86 km, FR	
			27 Sep. 1929 (Cat. 3)	63 km, FL			
			9 Sep. 1919 (Cat. 4)	15 km, FL			
E6	1906-1947	1926	2 Sep. 1935 (Cat. 4)	8 km, FL	**15 Sep. 1945 (Cat. 4)**	**100 km, FL**	**15 Sep. 1945 (Cat. 4)**
			28 Sep. 1935 (Cat. 3)	43 km, FR	1 Sep. 1933 (Cat. 3)	89 km, FR	
			27 Sep. 1929 (Cat. 3)	63 km, FL	5 Oct. 1933 (Cat. 2)	86 km, FR	
			9 Sep. 1919 (Cat. 4)	15 km, FL			
E7	1901-1942	1921	**2 Sep. 1935 (Cat. 4)**	**8 km, FL**	**1 Sep. 1933 (Cat. 3)**	**89 km, FR**	**Multiple events from 1933 to 1935 CE**
			28 Sep. 1935 (Cat. 3)	**43 km, FR**	**5 Oct. 1933 (Cat. 2)**	**86 km, FR**	
			27 Sep. 1929 (Cat. 3)	63 km, FL			
			9 Sep. 1919 (Cat. 4)	15 km, FL			
			17 Oct. 1904 (Cat. 1)	38 km, RR			
E8	1896-1938	1916	2 Sep. 1935 (Cat. 4)	8 km, FL	1 Sep. 1933 (Cat. 3)	89 km, FR	**27 Sep. 1929 (Cat. 3)**
			28 Sep. 1935 (Cat. 3)	43 km, FR	5 Oct. 1933 (Cat. 2)	86 km, FR	
			27 Sep. 1929 (Cat. 3)	**63 km, FL**	29 Oct. 1899 (Cat. 1)	82 km, RL	
			9 Sep. 1919 (Cat. 4)	15 km, FL			
			17 Oct. 1904 (Cat. 1)	38 km, RR			
E9	1883-1927	1904	27 Sep. 1929 (Cat. 3)	63 km, FL	29 Oct. 1899 (Cat. 1)	82 km, RL	**9 Sep. 1919 (Cat. 4)**
			9 Sep. 1919 (Cat. 4)	**15 km, FL**	04 Sep. 1888 (Cat. 3)	105 km, FR	
			17 Oct. 1904 (Cat. 1)	38 km, RR	22 Aug. 1886 (Cat. 1)	84 km, FL	
			22 Oct. 1895 (Cat. 2)	21 km, FL			
E10	1866-1923	1889	9 Sep. 1919 (Cat. 4)	15 km, FL	29 Oct. 1899 (Cat. 1)	82 km, RL	**17 Oct. 1904 (Cat. 1)**
			17 Oct. 1904 (Cat. 1)	**38 km, RR**	04 Sep. 1888 (Cat. 3)	105 km, FR	
			22 Oct. 1895 (Cat. 2)	21 km, FL	22 Aug. 1886 (Cat. 1)	84 km, FL	
					10 Oct. 1870 (Cat. 2)	100 km, FR	

APPENDIX C Table S3.4. Lower confidence event attributions for >250 µm coarse sediment anomalies with median dates from 1850 to 1899 CE. This table lists all hurricane events within 75 and 115 km of Hine's Hole from 1850 to 1899 CE based on IBTrACS and supplements CHAPTER 3 section *55.2 Calibrating the record to historical hurricanes* and Figure 3.6. Due to technological limitations and limited observational capabilities prion to 1900 CE, there is increased uncertainty in track location and intensity measurements during this time. The hurricane(s) that is most likely attributed to the event bed is in bold text. Grey text is used for events that violate the Principle of Superposition if we assume prior attributions are correct.

Event Bed	*2σ Age-Range (CE)*	*Median Age (CE)*	*Historical Events within 75 km*	*Passage Details*	*Historical Events within 115 km*	*Passage Details*	*Most Probable Event(s)*
E11	1854-1903	1878	22 Oct. 1895 (Cat. 2)	21 km, FL	**29 Oct. 1899 (Cat. 1)**	**82 km, RL**	**29 Oct. 1899 (Cat. 1)**
			15 Aug. 1861 (Cat. 1)	42 km, FR	04 Sep. 1888 (Cat. 3)	105 km, FR	
					22 Aug. 1886 (Cat. 1)	84 km, FL	
					10 Oct. 1870 (Cat. 2)	100 km, FR	
E12	1853-1902	1877	**22 Oct. 1895 (Cat. 2)**	**21 km, FL**	29 Oct. 1899 (Cat. 1)	82 km, RL	**22 Oct. 1895 (Cat. 2)**
			15 Aug. 1861 (Cat. 1)	42 km, FR	04 Sep. 1888 (Cat. 3)	105 km, FR	
					22 Aug. 1886 (Cat. 1)	84 km, FL	
					10 Oct. 1870 (Cat. 2)	100 km, FR	
*E13**	1851-1900	1875	22 Oct. 1895 (Cat. 2)	21 km, FL	29 Oct. 1899 (Cat. 1)	82 km, RL	***Aug. 24 1891 (Cat. 1), 175 km, FL**
			15 Aug. 1861 (Cat. 1)	42 km, FR	04 Sep. 1888 (Cat. 3)	105 km, FR	
			22 Aug. 1852 (Cat. 2)	52 km, FR	22 Aug. 1886 (Cat. 1)	84 km, FL	
					10 Oct. 1870 (Cat. 2)	100 km, FR	
E14	1845-1895	1869	22 Oct. 1895 (Cat. 2)	21 km, FL	**04 Sep. 1888 (Cat. 3)**	**105 km, FR**	**04 Sep. 1888 (Cat. 3)**
			15 Aug. 1861 (Cat. 1)	42 km, FR	22 Aug. 1886 (Cat. 1)	84 km, FL	
			22 Aug. 1852 (Cat. 2)	52 km, FR	10 Oct. 1870 (Cat. 2)	100 km, FR	
E15	1841-1891	1865	15 Aug. 1861 (Cat. 1)	42 km, FR	04 Sep. 1888 (Cat. 3)	105 km, FR	**22 Aug. 1886 (Cat. 1)**
			22 Aug. 1852 (Cat. 2)	52 km, FR	**22 Aug. 1886 (Cat. 1)**	**84 km, FL**	
					10 Oct. 1870 (Cat. 2)	100 km, FR	
E16	1835-1887	1860	15 Aug. 1861 (Cat. 1)	42 km, FR	22 Aug. 1886 (Cat. 1)	84 km, FL	**10 Oct. 1870 (Cat. 2)**
			22 Aug. 1852 (Cat. 2)	52 km, FR	**10 Oct. 1870 (Cat. 2)**	**100 km, FR**	
*E17**	1834-1885	1859	15 Aug. 1861 (Cat. 1)	42 km, FR	10 Oct. 1870 (Cat. 2)	100 km, FR	***No clear analogue**
			22 Aug. 1852 (Cat. 2)	52 km, FR			
E18	1833-1885	1859	**15 Aug. 1861 (Cat. 1)**	**42 km, FR**	22 Aug. 1886 (Cat. 1)	84 km, FL	**15 Aug. 1861 (Cat. 1)**
			22 Aug. 1852 (Cat. 2)	52 km, FR	10 Oct. 1870 (Cat. 2)	100 km, FR	
E19	1822-1874	1848	15 Aug. 1861 (Cat. 1)	42 km, FR	10 Oct. 1870 (Cat. 2)	100 km, FR	**22 Aug. 1852 (Cat. 2)**
			22 Aug. 1852 (Cat. 2)	**52 km, FR**			

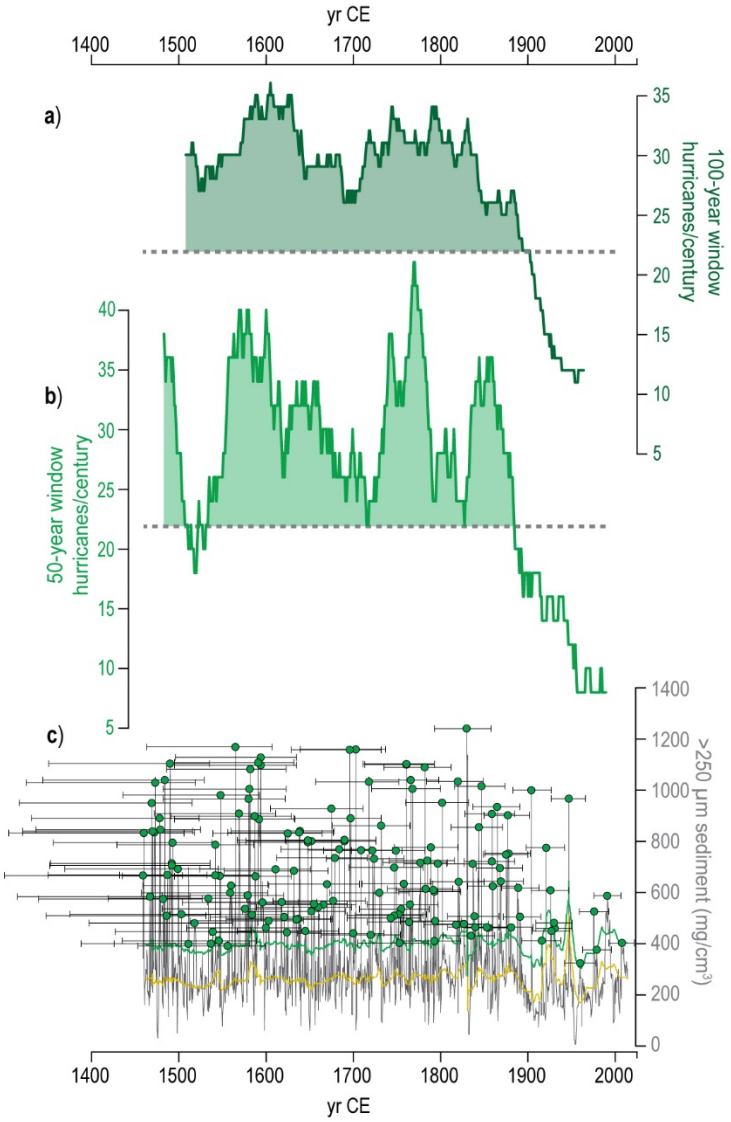

APPENDIX C Figure S3.6. a) The dark green line represents 100-year moving window counts for >63 µm hurricanes/century in the Hine's Hole Composite. The regionally derived statistical active interval threshold, >21.8 hurricanes/century (≥Category 1 within 115 km), is marked by a dashed black line. Temporal windows where hurricanes/century exceed this limit are shaded dark green. b) Same as a), but light green lines represent the 50-year window counts which were doubled to normalize to hurricanes/century, with light green shading highlighting periods that exceed the significance threshold. c) >63 µm coarse sediment anomalies (grey line) from Hine's Hole Composite from 1460 to 2016 CE. The lower gold dashed line is the 40-pt moving average of the >63 µm fractional mass data (mg/cm^3), and the green dashed line above it is the moving average plus 135 mg/cm^3 anomaly threshold. Coarse sediment beds that exceed this threshold are marked with green circles that have black horizontal error-bars denoting 2σ (95%) age-uncertainty.

APPENDIX C Section 3.5. References

BLAAUW, M. & CHRISTEN, A. 2011. Flexible paleoclimate age-depth models using an autoregressive gamma process. *Bayesian Analysis,* 6**,** 457-474.

BROECKER, W. S. & OLSON, E. A. 1961. Lamont radiocarbon measurements VIII. *Radiocarbon,* 3**,** 176-204.

DIAZ, M., MACARIO, K., GOMES, P., ÁLVAREZ-LAJONCHERE, L., AGUILERA, O. & ALVES, E. 2017. Radiocarbon marine reservoir effect on the northwestern coast of Cuba. *Radiocarbon,* 59**,** 333.

DINAPOLI, R. J., FITZPATRICK, S. M., NAPOLITANO, M. F., RICK, T. C., STONE, J. H. & JEW, N. P. 2021. Marine reservoir corrections for the Caribbean demonstrate high intra-and inter-island variability in local reservoir offsets. *Quaternary Geochronology,* 61**,** 101126.

DRUFFEL, E. M. & LINICK, T. W. 1978. Radiocarbon in annual coral rings of Florida. *Geophysical Research Letters,* 5**,** 913-916.

DRUFFEL, E. R. 1997. Pulses of rapid ventilation in the North Atlantic surface ocean during the past century. *Science,* 275**,** 1454-1457.

HADDEN, C. S. & SCHWADRON, M. 2019. Marine reservoir effects in eastern oyster (Crassostrea virginica) from southwestern Florida, USA. *Radiocarbon,* 61**,** 1501-1510.

HEATON, T. J., KÖHLER, P., BUTZIN, M., BARD, E., REIMER, R. W., AUSTIN, W. E., RAMSEY, C. B., GROOTES, P. M., HUGHEN, K. A. & KROMER, B. 2020. Marine20—the marine radiocarbon age calibration curve (0–55,000 cal BP). *Radiocarbon***,** 1-42.

KNAPP, K. R., DIAMOND, H. J., KOSSIN, J. P., KRUK, M. C. & SCHRECK, C. J. 2018. International Best Track Archive for Climate Stewardship (IBTrACS) Project, Version 4, [North Atlantic Subset]. *In:* INFORMATION, N. N. C. F. E. (ed.).

KNAPP, K. R., KRUK, M. C., LEVINSON, D. H., DIAMOND, H. J. & NEUMANN, C. J. 2010. The international best track archive for climate stewardship (IBTrACS) unifying tropical cyclone data. *Bulletin of the American Meteorological Society,* 91**,** 363-376.

KONDO, Y. 847. BURROWING DEPTH OF INFAUNAL BIVALVES: OBSERVATION OF LIVING SPECIES AND ITS RELATION TO SHELL MORPHOLOGY. Transactions and proceedings of the Paleontological Society of Japan. New series, 1987. Palaeontological Society of Japan, 306-323.

LIGHTY, R. G., MACINTYRE, I. G. & STUCKENRATH, R. 1982. Acropora palmata reef framework: a reliable indicator of sea level in the western Atlantic for the past 10,000 years. *Coral reefs,* 1**,** 125-130.

REIMER, P. J., BROWN, T. A. & REIMER, R. W. 2004. Discussion: reporting and calibration of post-bomb 14C data. *Radiocarbon,* 46**,** 1299-1304.

APPENDIX D

CHAPTER 4 SUPPLEMENTAL INFORMATION

Elevated Hurricane Activity During the Little Ice Age

APPENDIX D Section S4.1. CHAPTER 4 Supplemental Methods and Text.

APPENDIX D Section S4.1.1. Methods for GBAM-Stack Development

GBAM-Stack was compiled from the coarse sediment anomalies (CSAs) in the Lane's Delight Blue Hole (LDBH) Composite and Turtle Pond (TURT) records following the methods Winkler et al. (2020) used to develop the South Andros Stack. To summarize these methods, if multiple event beds on an island occurred within age model uncertainties, we counted them as a single event-bed given that LDBH and TURT were likely impacted by the same hurricane strikes over time. When there was more than one event in a blue hole record falling within the age uncertainties of an event from another blue hole record, we consolidated the event to the age defined by LDBH as the LDBH sedimentary age-model was resolved with more age-control points. While most event beds could be correlated between the LDBH-Composite and TURT, we always counted the maximum number of CSAs possible between visual stratigraphic correlation. For instance, TURT had 8 CSA event beds from ~1450-1600 CE, whereas the LDBH-Composite had 14 (see Fig. 4.7). This interval was constrained by visual stratigraphic correlation (Appendix D Fig. S4.1), so it likely represented the same depositional

window that was either better archived by LDBH or the sediment textural methods (sieving vs laser particle size) were more suited for documenting those event beds.

APPENDIX D Section S4.1.2. Methods for Northeast Gulf, New England, and Bahamas Sediment Compilations

We created compilations of sedimentary records from the Bahamian Archipelago ($BHAC_{pdf\text{-}5}$ and $BHAC_{stand\text{-}6}$), New England (NE_{comp}), and northern Florida Gulf of Mexico Coast ($FGoM_{comp}$). The Bahamian compilations span the last 1500 years (500-2019 CE) with at least 3 overlapping reconstructions at any point. $BHAC_{stand\text{-}6}$ extends an additional ~200 years to ~1300 CE, but there is limited confidence in this interval being reflective of regional hurricane frequency as it is only represented by the GBAM-Stack record from Grand Bahama. As detailed by Wallace et al. (2021), sedimentary paleohurricane reconstructions were selected for use in the compilation if they have: (i) consistent near-annual or multi-decadal resolution spanning at least 500 years, (ii) clearly defined statistical criteria for what constitutes a storm event bed that is supported by attribution to hurricanes in the instrumental record, and (iii) accessible information about each record's age model to allow for estimating age uncertainties of event layers including uncalibrated dates and detailed methods used for age-model development in the original study, iv) more than one site from the region that meets these criteria as a single site may not be indicative of broader regional patterns.

Two separate Bahamian Archipelago compilations were made given the variable archival sensitivity of the records. $BHAC_{pdf\text{-}5}$ includes events from Grand Bahama

(LDBH and TURT in GBAM-Stack; this study), Abaco Island (Thatchpoint Blue Hole; Winkler et al., 2020), South Andros Island (South Andros Stack; Wallace et al., 2019, Winkler et al., 2020), Long Island (Long Island Blue Hole; Wallace et al., 2021), and Middle Caicos Island in Turks and Caicos (Middle Caicos Blue Hole; Wallace et al., Sub. March 2021). $BHAC_{stand\text{-}6}$ was developed using separate methods that we detail below, but it also includes a particularly high resolution (~3 cm/yr sedimentation rate), 550 year reconstruction from an oceanic blue hole on Cay Sal Bank (Hine's Hole ; Winkler et al., Submitted 2021). NE_{comp} uses reconstructions from Salt Pond (Donnelly et al., 2015) and Mattapoisett Marsh (Boldt et al., 2010, Castagno et al., 2021). The $FGoM_{comp}$ includes records from Apalachee Bay (Spring Creek Pond (Brandon et al., 2013), Mullet Pond (Lane et al., 2011), Shotgun Pond (Rodysill et al., 2020), and Choctawhatchee Bay (Basin Bayou: Rodysill et al., 2020). Each of the events captured in the Florida records were sorted by intensity in the original publications, wherein High Threshold (HT) events were created by intense hurricanes (≥ Category 3 on the Saffir Simpson scale) and Low Threshold (LT) events were created by ≥Category 1 hurricanes. We create both a HT and LT compilation for $FGoM_{comp}$.

The compilation methods used to create NE_{comp}, $FGoM_{comp}$, and $BHAC_{pdf\text{-}5}$ are detailed in Wallace et al (2021). First, we reproduce the age model for each record using BACON v2.5.2 software (Blaauw and Christen, 2011) using IntCal20 (Reimer et al., 2020) or Marine20 (Heaton et al., 2020) reservoir corrections and age-model parameters (e.g., slumps, depths, age-limits, etc.) as specified in the original publication. For regions/islands with multiple contributing records (New England, Apalachee Bay, Grand

Bahama, South Andros Island), we remove redundant counts of the same events and use the age model from the record with the smallest age uncertainty (see APPENDIX D Fig. S4.7a). We create age probability distributions functions (pdfs) for each event bed in each record, which are derived from 1000 age-estimate ensembles generated in BACON. Overlapping age pdf values for each reconstruction are summed to create our island/site composites shown in APPENDIX D Figure S4.7a. The final regional composites (APPENDIX D Fig. S4.7b) are formed by summing all the contributing island/site composites within a region together, then weighting each interval of time based on the number of overlapping records included for that time (i.e., sum/(x/5)) We calculate confidence intervals as the spread among all contributing records in each region. Finally, we apply a 100-year smooth to the compilations.

$BHAC_{stand\text{-}6}$ was created following different methods in order to include the Hine's Hole reconstruction from Cay Sal Bank, which documents more than twice as many hurricanes/century on average than the other Bahamian reconstructions due to its higher archival sensitivity. First, age-models were reproduced for each site using BACON v2.5.2 (as described above). For all sites but Hine's Hole, a 100-year sliding window was used to calculate hurricanes/century for each reconstruction based on the median-age estimate. Due to the exceptionally high sedimentation rate in Hine's Hole, a 50-year sliding window along median-age estimate was used to count event beds, which were then doubled to normalize to hurricanes/century (see Winkler et al. (Submitted 2021) for further explanation). Hurricanes/century were standardized for each site by subtracting average hurricanes/century for the entire record from each 1-year interval,

then dividing this by the standard deviation hurricanes/century through the entire record. Standardized hurricane frequency from all 6 records were averaged at corresponding 1-year intervals, and uncertainty was estimated based on the standard deviation values for each averaged interval. Following the same methods, we standardized the average hurricanes/century from $BHAC_{pdf\text{-}5}$, NE_{comp}, and $FGoM_{comp}$ compilations. Following this, we averaged NE_{comp}, $BHAC_{stand\text{-}6}$, and LT-$FGoM_{comp}$ together to produce a 3-region, 1400-1500 year North Atlantic Compilation (NAT_{comp}).

APPENDIX D Section S4.1.3. IBTrACS Assessment of Variance

From 1850-2020 CE, 112 ≥Category 1 hurricanes pass within a boundary shown around the Bahamian Archipelago in APPENDIX D Figure S4.8. We created buffers around each of the 6 study sites from in the Bahamian Compilations (Figs. 4.1, 4.8, S4.6) based on the literature derived sensitivity radii for each reconstruction: Grand Bahama (LDBH-TURT, ≥Category 2 within a 75 km radius), Abaco Island (Thatchpoint Blue Hole, ≥Category 2 within a 75 km radius; (Winkler et al., 2020)), South Andros Island (South Andros Stack, ≥Category 3 within a 50 km radius; (Wallace et al., 2019)), Cay Sal Bank (Hine's Hole, ≥Category 1 within a 100 km radius; (Winkler et al., Submitted 2021), Long Island (≥Category 2 within a 75 km radius; (Wallace et al., 2021)), and Middle Caicos Island (≥Category 1 within a 75 km radius; (Wallace et al., Sub. March 2021)). The number of these hurricanes that could theoretically be captured in the $BHAC_{pdf\text{-}5}$ compilation (red lines) is 54, or 49% of the 112 possible hurricanes since 1950 CE. The number of these hurricanes that could theoretically be captured in the

$BHAC_{stand\text{-}6}$ compilation (green and red lines) is 65, or 59% of the 112 possible hurricanes since 1850 CE (APPENDIX D Fig. S4.8).

APPENDIX D Section S4.2. CHAPTER 4 Supplemental Figures.

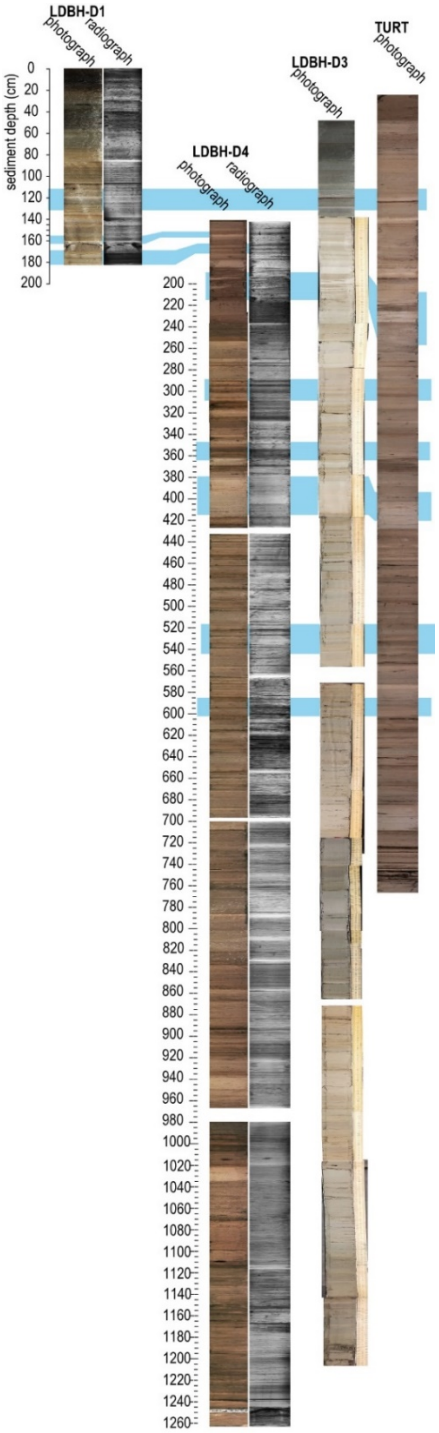

APPENDIX D Figure S4.1. Core photographs and stratigraphic correlations figure.

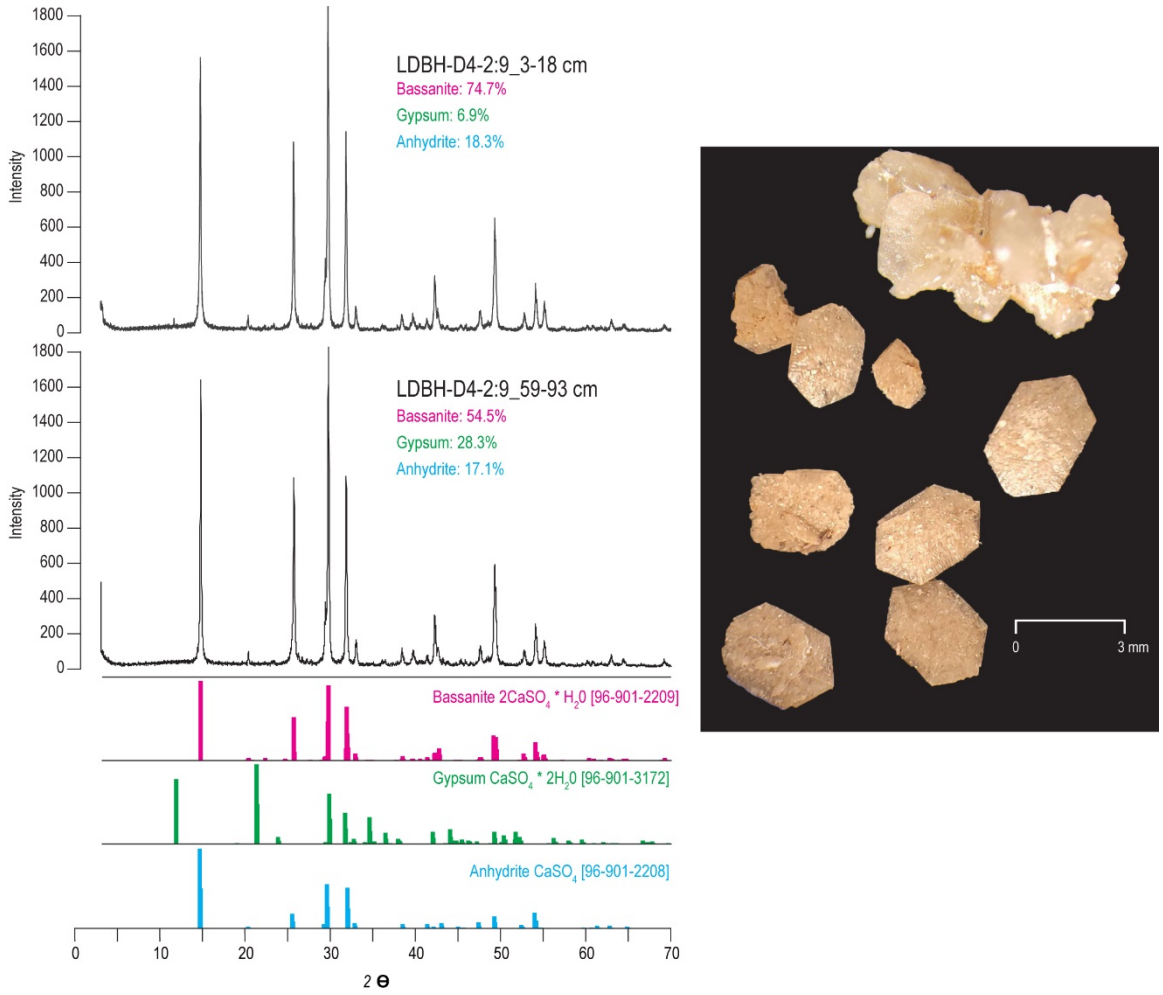

APPENDIX D Figure S4.2. LDBH XRD plots from LDBH-D4-2:9_3-18 cm (240-255 cm in LDBH-Composite) and LDBH-D4-2:9_59-93 cm (296-330 cm in LDBH-Composite). Peaks were identified and matched using Match! version 3.11.5 software. The percentage match for each mineral is listed next to the mineral name for each panel. Reference peaks for minerals are identified below (bar graphs: bassanite-pink and anhydrite-blue (Bezou et al., 1995), gypsum-green (Comodi et al., 2008)). Scaled photographs of the observed crystals in the sampled intervals are in the right panel.

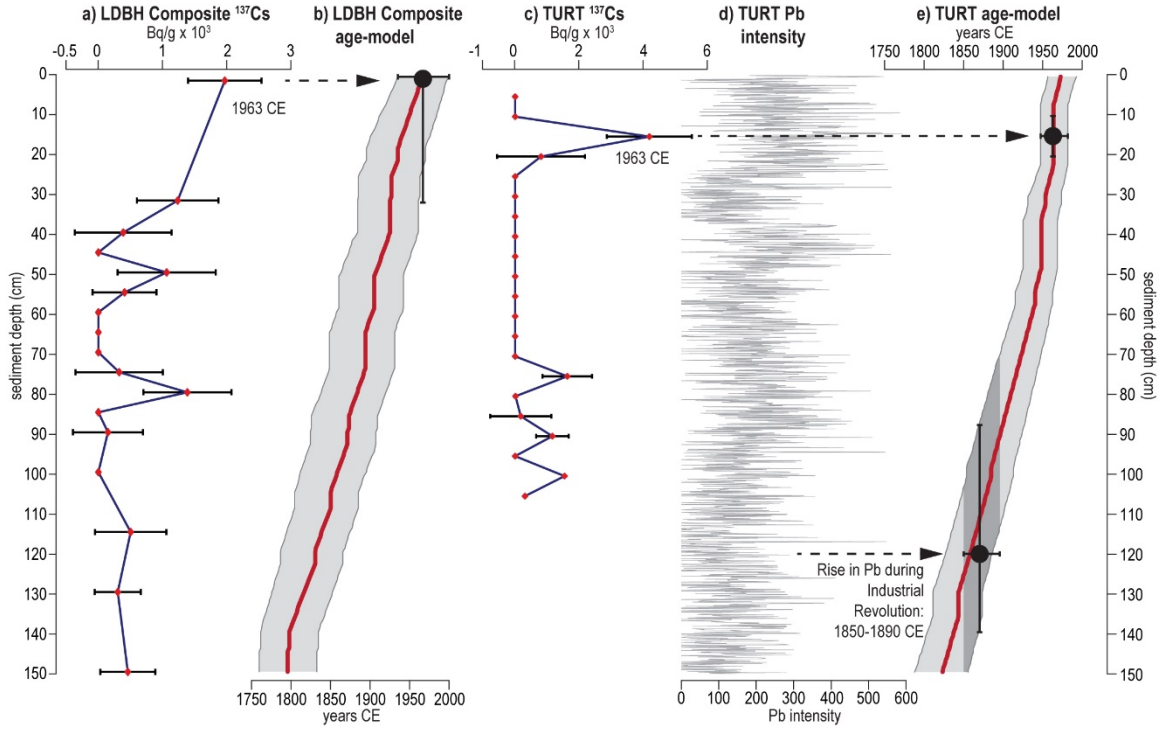

APPENDIX D Figure S4.3. (a, c) ^{137}Cs abundance for LDBH and TURT labelled with the 1963 CE peak in ^{137}Cs associated with a spike in thermonuclear weapons testing prior to the moratorium in 1963 CE. These ^{137}Cs peaks have horizontal bars showing temporal uncertainty based on the sedimentary age-models produced for each record using BACON (Blaauw and Christen, 2011; b, c). (d) Bulk elemental lead (Pb) intensity results from x-ray fluorescence scans of TURT that show a Pb intensity that corresponds with increased fossil fuel combustion at the onset of the Industrial Revolution in the late 19th century (Donnelly et al., 2001, Maio et al., 2016)

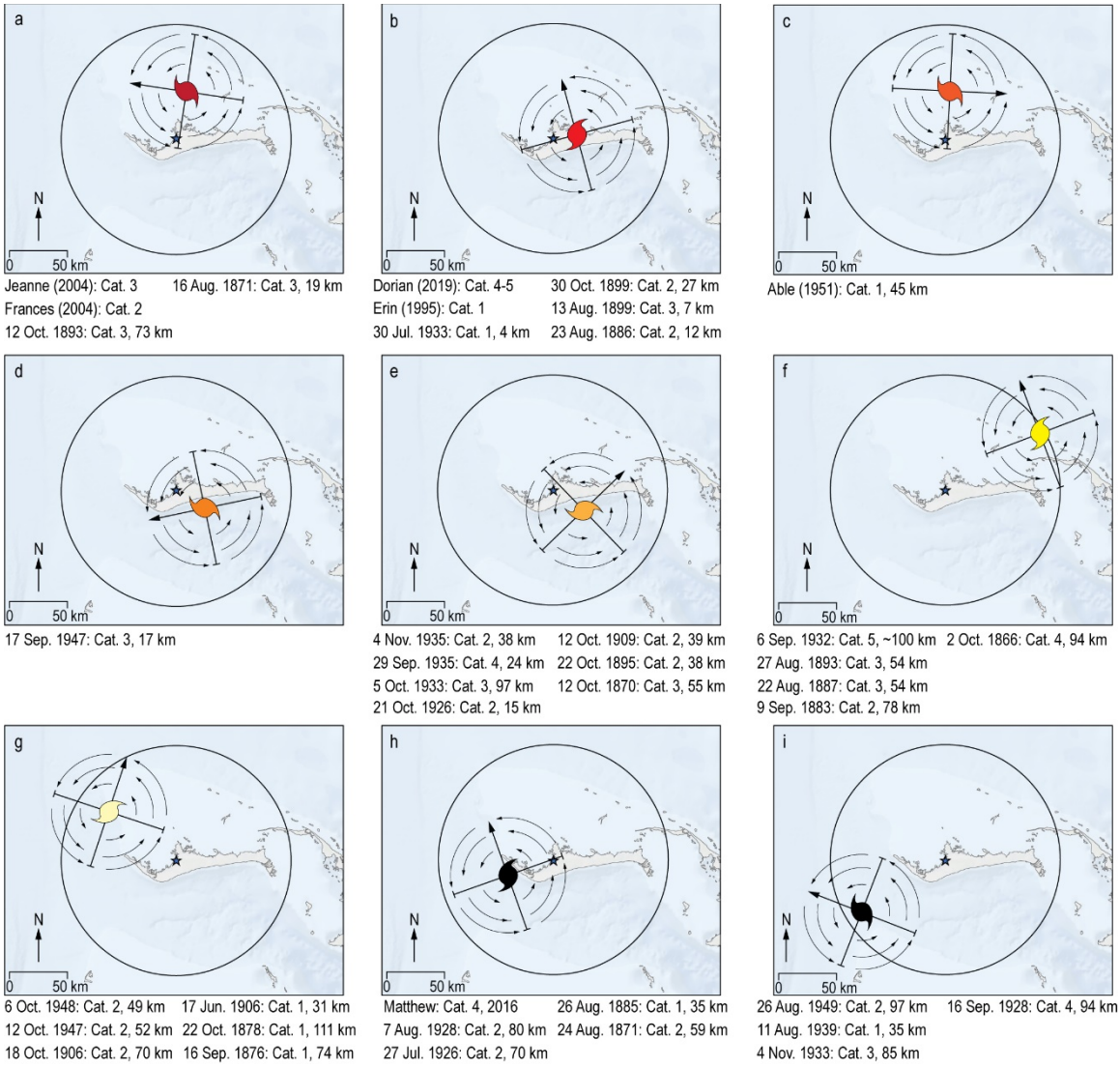

APPENDIX D Figure S4.4. Common hurricane path orientations relative to LDBH and TURT (blue star) based on storm tracks from 1850-2019 CE. Hurricanes from 1850-2019 CE are listed below the orientation that most closely matches the observed storm path. These orientations are arranged in alphabetic order, from most to least likely to leave a deposit in LDBH or TURT based on the direction that the 50 km average radius of maximum winds (Hsu and Yan, 1998) would direct waves and currents as well as the which quadrant of the storm the winds were from. This was used to inform the modern calibration/event-attribution analysis (CHAPTER 4 section *4.5.1 Event Bed Drivers and Attribution*, Fig. 4.5). Color of the storm reflect alphabetical order regarding likelihood of leaving a deposit from red (most-likely) to yellow (least-likely) and black being hurricanes that almost certainly did not leave a deposit as they would have pulled water away from LDBH-TURT.

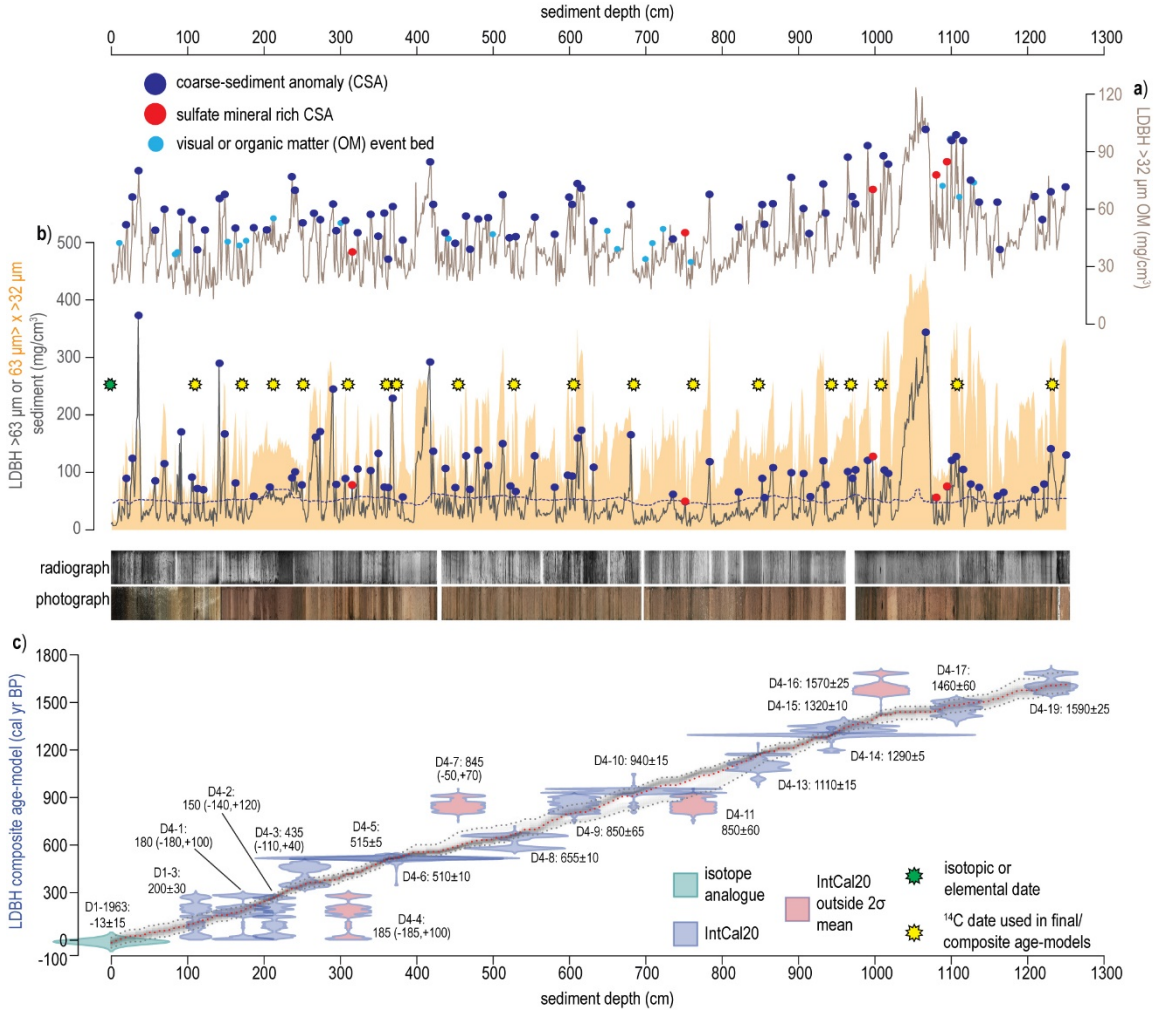

APPENDIX D Figure S4.5. (a) and (b) respectively show >32 µm bulk organic matter (mg/cm^3) and >63 µm coarse fraction (mg/cm^3) data for the LDBH Composite (black line). The orange shape in (b) is the 32 µm < x < 63 µm data, which shows >32 µm mg/cm^3 data minus >32 µm mg/cm^3 data. The blue dotted line in (b) is the sediment anomaly threshold (40-point moving average of >63 µm coarse fraction + 24 mg/cm^3) and dark blue dots are coarse sediment anomalies above this threshold while red dots are anomalies that are over 50% gypsum/bassanite crystals. Overall, only gypsum rich peaks indicated by the red do not show a peak in 32 µm < x < 63 µm data corresponding to the >63 µm CSA. In (a), light blue dots are visual/OM anomalies for coarse peaks that fall within standard deviation of the threshold (from the 40-point moving average) but also show substantial spikes in bulk OM. (c) The sedimentary age-model for the LDBH Composite, where the blue shapes are the probability distribution functions of uncertainty for age-control points derived from radiocarbon dated leaves (LDBH:

***n=18*), and green shapes age-control points interpreted from ^{137}Cs abundance. See APPENDIX D Table S4.2 for details on dated material.**

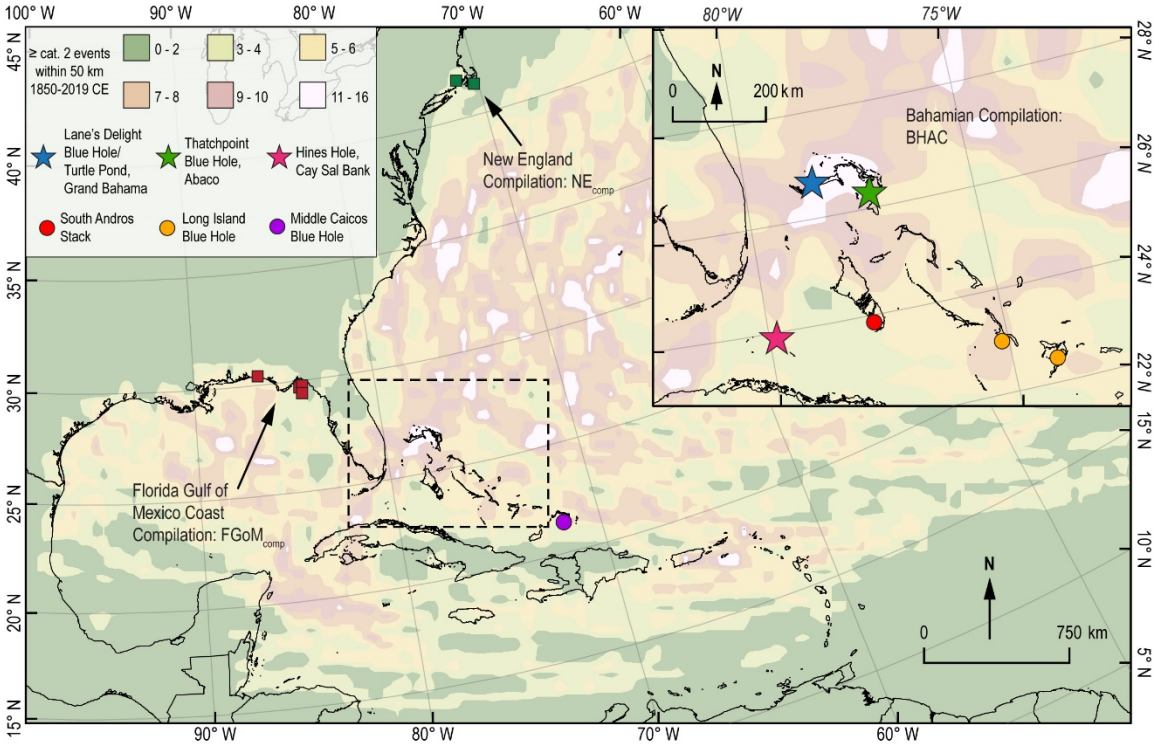

APPENDIX D Figure S4.6. Frequency of ≥Category 2 hurricanes passing with 50 km from 1850-2019 CE and study site locations in the North Atlantic (adapted from (Winkler et al., 2020) Fig. 1). Storm track and intensity data is from the International Best Track Archive for Climate Stewardship (IBTrACS) v04 dataset (Knapp et al., 2018, Knapp et al., 2010). Stars indicate location of paleo-hurricane records developed for this dissertation, and circles represent other similar near-annually resolved reconstructions from the Bahamina Archipelago. Red (green) squares are the locations of paleo-hurricane records from the Florida- FGoM$_{comp}$ (New England-NE$_{comp}$) regional compilations.

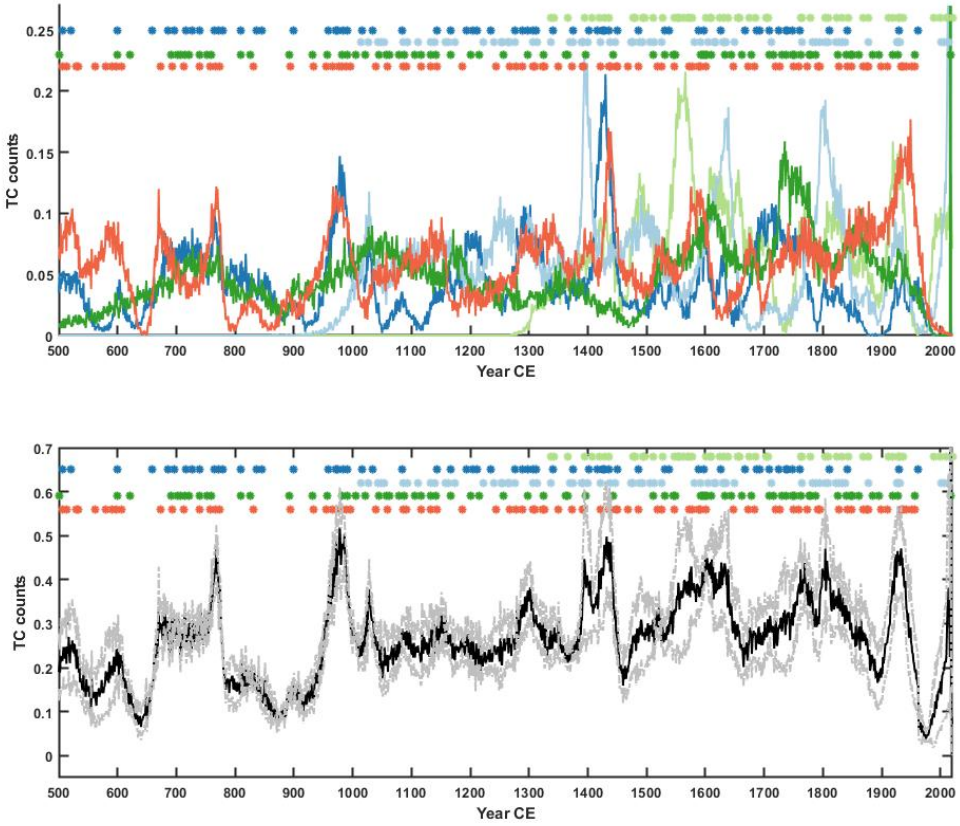

APPENDIX D Figure S4.7. (top panel) Components of the BHAC regional compilations 500-2019 CE which include: Abaco (Winkler et al., 2020; light green), South Andros (Wallace et al., 2019, Winkler et al., 2020; dark blue), Middle Caicos (Wallace et al., Sub. March 2021; dark green), Long Island (Wallace et al., 2021; light blue). South Andros includes events from the AM5, AM4 and AM2 records (Wallace et al., 2019). The compilations are the sum of the age probability distributions of each of these events. (b) Unsmoothed $BHAC_{pdf\text{-}5}$ generated by summing the time series in APPENDIX D Figure S4.7a. Standard errors are shaded in grey around the black mean estimate and are calculated as the spread among the estimates in APPENDIX D Figure S4.8a. The dots at the top of each panel indicate the median age of each event used in the compilation.

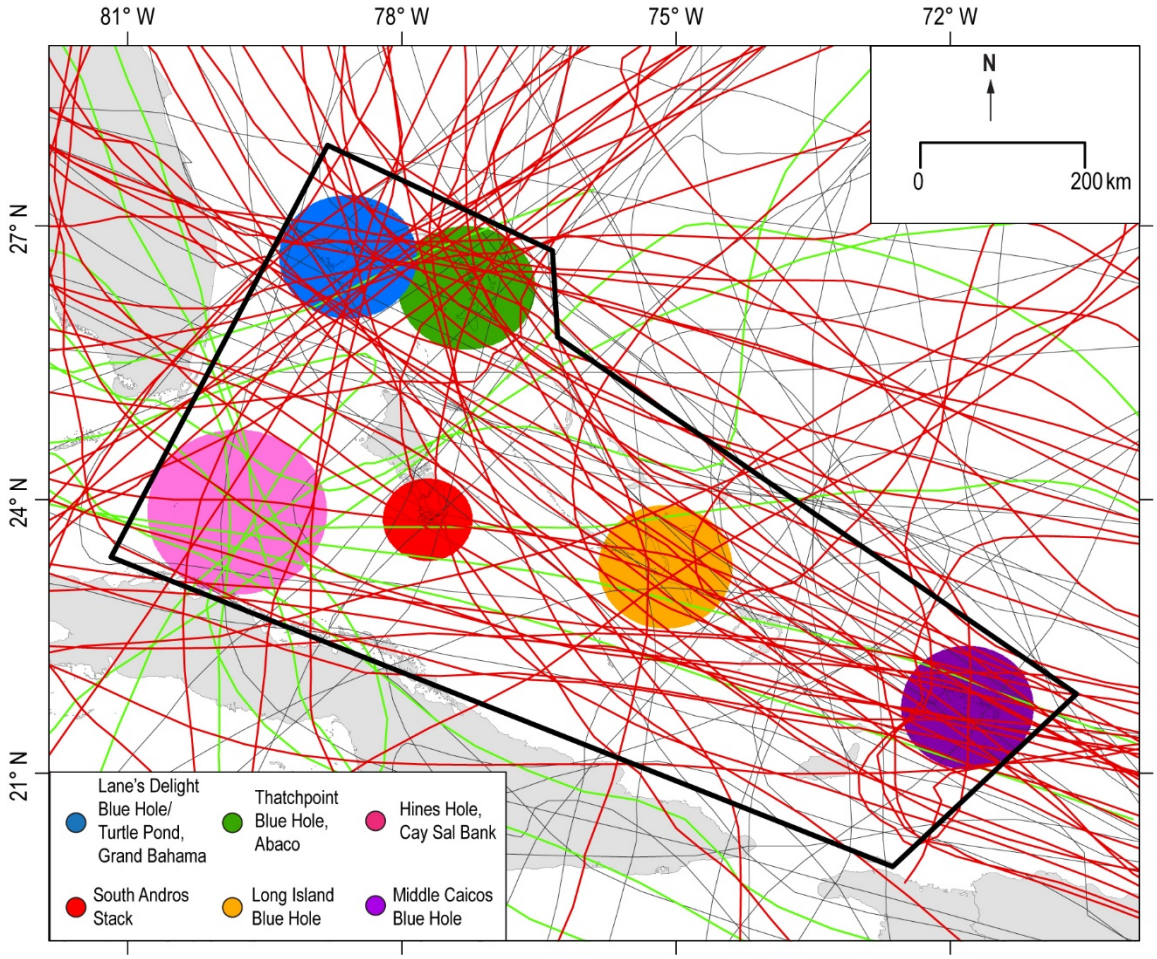

APPENDIX D Figure S4.8. ≥Category 1 hurricanes pass within a boundary shown around the Bahamian Archipelago (black lines). Sensitivity radii buffers around each of the 6 study sites from in the Bahamian Compilations correspond to the colors in Figures 4.1 and 4.8 (see Appendix D Section S3). The number hurricanes since 1850 CE that could be captured in the $BHAC_{pdf\text{-}5}$ compilation (red lines) is 54, or 49% of the 112 possible hurricanes since 1950 CE. The number hurricanes that could be captured in the $BHAC_{stand\text{-}6}$ compilation (green and red lines) is 65, or 59% of the 112 possible hurricanes since 1950 CE (APPENDIX D Fig. S4.6).

APPENDIX D Section S4.3. CHAPTER 4 Supplemental Tables.

APPENDIX D Table S4.1. Coring Locations and drive lengths.

Drive	Latitude °N	Longitude °W	Water depth (m)	Pipe length (cm)	Drive length (cm)	Recovery length (cm)	Intact sediment/ water interface
LDBH-D1	26.6618	78.5902	29	240	200	193	yes
LDBH-D3	26.6617	78.5901	29	1200	1150	1124	uncertain
LDBH-D4	26.6617	78.5902	29	2100	1400	1106-1251	no
TURT-D1	26.6584	78.5917	3.5	900	750	744	uncertain

APPENDIX D Table S4.2. Radiocarbon results from leaf and plant matter in LDBH and TURT. Dates in red text were not included in the sedimentary age models. The leaves in upper 75 cm of LDBH-D1 and D3 were excluded as they were likely pushed deeper into the core during the coring process. The 2 dates exclude from LDBH-D4 and 3 dates excluded from TURT violated the Principle of Superposition, returning calibrated dates older than samples below them. All radiocarbon dates were calibrated with IntCal20 (Reimer et al., 2020) in Bacon version 2.5.3 (Blaauw and Christen, 2011).

Accession Number	Core and Section	Name	Drive Depth (cm)	Composite Record Depth (cm)	Material Dated	Δ14C	Conv.^{14}C age	Conv.^{14}C age error	$F^{14}C$	$F^{14}C$ Error	$\delta^{13}C$ (‰)
OS-154096	LDBH-D1_1:2	D1-1	44.5	N/A	Leaf	66.11	>Modern		1.0747	0.0023	-26.49
OS-154097	LDBH-D1_1:2	D1-2	75.5	N/A	Leaf	105.54	>Modern		1.1144	0.0023	-26.71
OS-154125	LDBH-D1_2:2	D1-3	110.5	110.5	Leaf	-27.44	160	25	0.9804	0.0033	-26.66
OS-154128	LDBH-D3_1:9	D3-1	64.5	N/A	Leaf	722.61	>Modern		1.7364	0.0048	-28.04
OS-154214	LDBH-D3_2:9	D3-2	204.5	N/A	Leaf	-66.87	490	15	0.9406	0.0019	-25.72
OS-154475	LDBH-D3_4:9	D3-3	380.5	N/A	Leaf	-85.13	650	70	0.9222	0.0083	-26.59
OS-154478	LDBH-D3_6:9	D3-4	672.5	N/A	Leaf	-153.11	1,270	20	0.8537	0.0019	-25.59
OS-154215	LDBH-D3_7:9	D3-5	907.5	N/A	Leaf	-173.79	1,470	15	0.8328	0.0017	-28.7
OS-154476	LDBH-D3_9:9	D3-6	1087.5	N/A	Leaf	-205.89	1,790	75	0.8005	0.0072	-24.86
OS-154209	LDBH-D4_1:9	D4-1	28.5	172.5	Leaf	-31.25	190	15	0.9765	0.0019	-23.68
OS-137775	LDBH-D4_1:9	D4-2	69.5	213.5	Leaf		150	15	0.9816	0.0020	-28.85
OS-137776	LDBH-D4_2:9	D4-3	109.5	253.5	Leaf		365	20	0.9555	0.0025	-26.39
OS-128337	LDBH-D4_2:9	D4-4	166.5	310.5	Leaf		185	20	0.9771	0.0027	-26.35
OS-137777	LDBH-D4_3:9	D4-5	217.5	361.5	Leaf		475	15	0.9424	0.0019	-24.58
OS-133768	LDBH-D4_3:9	D4-6	229.5	373.5	Leaf	-63.94	465	20	0.9436	0.0024	-25.29
OS-154212	LDBH-D4_4:9	D4-7	310.5	454.5	Leaf	-119.22	955	15	0.8878	0.0018	-25.49
OS-128338	LDBH-D4_4:9	D4-8	384.5	528.5	Leaf		675	25	0.9194	0.0026	-27.4
OS-133769	LDBH-D4_5:9	D4-9	462.5	606.5	Leaf	-116.86	935	15	0.8902	0.0018	-25.93
OS-139793	LDBH-D4_5:9	D4-10	540.5	684.5	Leaf		1020	15	0.8806	0.0018	-25.58
OS-133770	LDBH-D4_6:9	D4-11	618.5	762.5	Leaf	-118.82	950	20	0.8882	0.0023	-26.96
OS-154474	LDBH-D4_6:9	D4-12	622.5	N/A	Leaf	-350.54	3400	220	0.6547	0.0179	
OS-139792	LDBH-D4_7:9	D4-13	703.5	847.5	Leaf		1180	15	0.8632	0.0018	-25.29
OS-128339	LDBH-D4_7:9	D4-14	799.5	943.5	Leaf		1360	15	0.844	0.0018	-25.87
OS-137778	LDBH-D4_7:9	D4-15	815.5	959.5	Leaf		1460	15	0.8336	0.0017	-27.51
OS-154477	LDBH-D4_8:9	D4-16	864.5	1008.5	Leaf	-197.04	1700	20	0.8094	0.0019	-23.43
OS-133771	LDBH-D4_8:9	D4-17	963.5	1107.5	Leaf	-183.93	1570	20	0.8226	0.0018	-26.34
OS-154213	LDBH-D4_9:9	D4-18	1024.5	N/A	Leaf	-232.97	2070	20	0.7732	0.0017	-26.22
OS-128340	LDBH-D4_9:9	D4-19	1087.5	1231.5	Leaf		1720	20	0.8069	0.0018	-23.86
OS-137108	TURT_2:6	T-1	171	N/A	Leaf	-167.7	290	15	0.8391	0.0016	-26.49
OS-137109	TURT_2:6	T-2	212	N/A	Leaf	-43.15	1,410	15	0.9646	0.0019	-26.71
OS-137767	TURT_2:6	T-3	235	N/A	Leaf		640	15	0.9236	0.0018	-26.66
OS-137276	TURT_3:6	T-4	261	N/A	Leaf		205	15	0.9748	0.0019	-28.04
OS-128457	TURT_3:6	T-5	350	N/A	Leaf	-103.3	280	15	0.9657	0.0019	-25.72
OS-134124	TURT_4:6	T-6	437	N/A	Leaf		485	15	0.9413	0.0018	-26.59
OS-128458	TURT_4:6	T-7	474	N/A	Leaf	-220.36	590	20	0.9290	0.0021	-25.59
OS-134062	TURT_5:6	T-8	526	N/A	Leaf		810	20	0.9039	0.0021	-28.7
OS-128459	TURT_5:6	T-9	596	N/A	Leaf	-66.14	1,020	25	0.8809	0.0025	-24.86
OS-134063	TURT_6:6	T-10	670	N/A	Leaf		1,940	15	0.7859	0.0016	-23.68
OS-128482	TURT_6:6	T-11	716	N/A	Leaf		1,080	20	0.8744	0.0020	-28.85

APPENDIX D Table S4.3. Attributions for LDBH-Composite event beds with median dates from 1850-1970 CE. Hurricanes within 100 km of LDBH from 1850-1970 CE are listed. Hurricanes that are likely attributed to the event bed are highlighted in grey. Grey text is used for events that violate the Principle of Superposition if prior attributions are correct. Storms with highly variable track estimates between IBtRACS datasets are in orange.

Event Bed	*2σ Age-Range (CE)*	*Median Age (CE)*	*Hurricanes within 100 km*	*Saffir-Simpson*	*Wind Velocity (km/hr)*	*Passage Proximity (km)*	*Direction*	*Quadrant*
N/A		1952-1970						
E1	1912-1985	1950	**Able, 1951**	**1**	**124**	**45**	**NW to SE to NE; N of GB**	**FR**
			26 Aug. 1949	**4**	**204**	**97**	**SE to NW; SW of GB**	**FR**
			6 Oct. 1948	**2**	**157**	**49**	**SW to NE; N of GB**	**FR**
			12 Oct. 1947	**1**	**124**	**52**	**SW to NE; N of GB**	**FR**
			17 Sep. 1947	**3**	**204**	**17**	**W to E; S of GB**	**FR**
			11 Aug. 1939	1	120	35	SE to NW; SW of GB	FR
			4 Nov. 1935	2	157	38	NE to SW; S of GB	FR
			29 Sep. 1935	4	217	24	SE to NW; directly over LDBH	FL
			5 Oct. 1933	3	194	97	SW to NE; S of LDBH	FL
			4 Nov. 1933	3	204	85	SE to NW; SW of GB	FR
			30 Jul. 1933	1	130	4	SE to NW; directly over LDBH	FL
			6 Sep. 1932	5	259	103	S to N; E of GB	FL
			16 Sep. 1928	4	241	94	SE to NW; SW of GB	FR
			7 Aug. 1928	2	167	80	SE to NW; SW of GB	FR
			21 Oct. 1926	3	204	15	SE to NW; across GB	FL
			27 Jul. 1926	2	176	70	SE to NW; SW below GB	FR
E2	1896-1971	1936	Able, 1951	1	124	45	NW to SE to NE; N of GB	FR
			26 Aug. 1949	4	204	97	SE to NW; SW of GB	FR
			6 Oct. 1948	2	157	49	SW to NE; N of GB	FR
			12 Oct. 1947	1	124	52	SW to NE; N of GB	FR
			17 Sep. 1947	3	204	17	W to E; S of GB	FR
			11 Aug. 1939	**1**	**120**	**35**	**SE to NW; SW of GB**	**FR**
			4 Nov. 1935	**2**	**157**	**38**	**NE to SW; S of GB**	**FR**
			29 Sep. 1935	**4**	**217**	**24**	**SE to NW; directly over LDBH**	**FL**
			5 Oct. 1933	3	194	97	SW to NE; S of LDBH	FL
			4 Nov. 1933	3	204	85	SE to NW; SW of GB	FR
			30 Jul. 1933	1	130	4	SE to NW; directly over LDBH	FL
			6 Sep. 1932	5	259	103	S to N; E of GB	FL
			16 Sep. 1928	4	241	94	SE to NW; SW of GB	FR
			7 Aug. 1928	2	167	80	SE to NW; SW of GB	FR
			21 Oct. 1926	3	204	15	SE to NW; across GB	FL
			27 Jul. 1926	2	176	70	SE to NW; SW below GB	FR
			12 Oct. 1909	2	167	39	SW to NE; S of GB	FL
			18 Oct. 1906	2	176	70	SW to NE; N of GB	FR
			17 Jun. 1906	1	139	31	SW to NE; N of GB	FR
			30 Oct. 1899	2	157	27	S to NE; E of LDBH across GB	FL
			13 Aug. 1899	3	194	7	N to S; directly over LDBH	FL

Event Bed	*2σ Age-Range (CE)*	*Median Age (CE)*	*Hurricanes within 100 km*	*Saffir-Simpson*	*Wind Velocity (km/hr)*	*Passage Proximity (km)*	*Direction*	*Quadrant*
E3	1886-1964	1928	Able, 1951	1	124	45	NW to SE to NE; N of GB	FR
			26 Aug. 1949	4	204	97	SE to NW; SW of GB	FR
			6 Oct. 1948	2	157	49	SW to NE; N of GB	FR
			12 Oct. 1947	1	124	52	SW to NE; N of GB	FR
			17 Sep. 1947	3	204	17	W to E; S of GB	FR
			11 Aug. 1939	1	120	35	SE to NW; SW of GB	FR
			4 Nov. 1935	2	157	38	NE to SW; S of GB	FR
			29 Sep. 1935	4	217	24	SE to NW; directly over LDBH	FL
			5 Oct. 1933	**3**	**194**	**97**	**SW to NE; S of LDBH**	**FL**
			4 Nov. 1933	**3**	**204**	**85**	**SE to NW; SW of GB**	**FR**
			30 Jul. 1933	**1**	**130**	**4**	**SE to NW; directly over LDBH**	**FL**
			6 Sep. 1932	**5**	**259**	**103**	**S to N; E of GB**	**FL**
			16 Sep. 1928	4	241	94	SE to NW; SW of GB	FR
			7 Aug. 1928	2	167	80	SE to NW; SW of GB	FR
			21 Oct. 1926	3	204	15	SE to NW; across GB	FL
			27 Jul. 1926	2	176	70	SE to NW; SW below GB	FR
			12 Oct. 1909	2	167	39	SW to NE; S of GB	FL
			18 Oct. 1906	2	176	70	SW to NE; N of GB	FR
			17 Jun. 1906	1	139	31	SW to NE; N of GB	FR
			30 Oct. 1899	2	157	27	S to NE; E of LDBH across GB	FL
			13 Aug. 1899	3	194	7	N to S; directly over LDBH	FL
			22 Oct. 1895	2	167	38	SW to NE; S of GB	FL
			12 Oct. 1893	3	194	73	SE to NW; N of GB	FL
			27 Aug. 1893	3	194	54	SE to N; directly over LDBH	FL
			22 Aug. 1887	3	204	54	SE to N; NE of LDBH	FL
			23 Aug. 1886	2	157	12	S to N; directly over LDBH	FL

Event Bed	*2σ Age-Range (CE)*	*Median Age (CE)*	*Hurricanes within 100 km*	*Saffir-Simpson*	*Wind Velocity (km/hr)*	*Passage Proximity (km)*	*Direction*	*Quadrant*
			Able, 1951	1	124	45	NW to SE to NE; N of GB	FR
			26 Aug. 1949	4	204	97	SE to NW; SW of GB	FR
			6 Oct. 1948	2	157	49	SW to NE; N of GB	FR
			12 Oct. 1947	1	124	52	SW to NE; N of GB	FR
			17 Sep. 1947	3	204	17	W to E; S of GB	FR
			11 Aug. 1939	1	120	35	SE to NW; SW of GB	FR
			4 Nov. 1935	2	157	38	NE to SW; S of GB	FR
			29 Sep. 1935	4	217	24	SE to NW; directly over LDBH	FL
			5 Oct. 1933	3	194	97	SW to NE; S of LDBH	FL
			4 Nov. 1933	3	204	85	SE to NW; SW of GB	FR
			30 Jul. 1933	1	130	4	SE to NW; directly over LDBH	FL
			6 Sep. 1932	5	259	103	S to N; E of GB	FL
			16 Sep. 1928	**4**	**241**	**94**	**SE to NW; SW of GB**	**FR**
E4	1885-1962	1926	**7 Aug. 1928**	**2**	**167**	**80**	**SE to NW; SW of GB**	**FR**
			21 Oct. 1926	**3**	**204**	**15**	**SE to NW; across GB**	**FL**
			27 Jul. 1926	**2**	**176**	**70**	**SE to NW; SW below GB**	**FR**
			12 Oct. 1909	2	167	39	SW to NE; S of GB	FL
			18 Oct. 1906	2	176	70	SW to NE; N of GB	FR
			17 Jun. 1906	1	139	31	SW to NE; N of GB	FR
			30 Oct. 1899	2	157	27	S to NE; E of LDBH across GB	FL
			13 Aug. 1899	3	194	7	N to S; directly over LDBH	FL
			22 Oct. 1895	2	167	38	SW to NE; S of GB	FL
			12 Oct. 1893	3	194	73	SE to NW; N of GB	FL
			27 Aug. 1893	3	194	54	SE to N; directly over LDBH	FL
			22 Aug. 1887	3	204	54	SE to N; NE of LDBH	FL
			23 Aug. 1886	2	157	12	S to N; directly over LDBH	FL
			26 Aug. 1885	1	130	35	S to N; W of GB	FR

Event Bed	*2σ Age-Range (CE)*	*Median Age (CE)*	*Hurricanes within 100 km*	*Saffir-Simpson*	*Wind Velocity (km/hr)*	*Passage Proximity (km)*	*Direction*	*Quadrant*
			11 Aug. 1939	1	120	35	SE to NW; SW of GB	FR
			4 Nov. 1935	2	157	38	NE to SW; S of GB	FR
			29 Sep. 1935	4	217	24	SE to NW; directly over LDBH	FL
			5 Oct. 1933	3	194	97	SW to NE; S of LDBH	FL
			4 Nov. 1933	3	204	85	SE to NW; SW of GB	FR
			30 Jul. 1933	1	130	4	SE to NW; directly over LDBH	FL
			6 Sep. 1932	5	259	103	S to N; E of GB	FL
			16 Sep. 1928	4	241	94	SE to NW; SW of GB	FR
			7 Aug. 1928	2	167	80	SE to NW; SW of GB	FR
			21 Oct. 1926	3	204	15	SE to NW; across GB	FL
			27 Jul. 1926	2	176	70	SE to NW; SW below GB	FR
			12 Oct. 1909	**2**	**167**	**39**	**SW to NE; S of GB**	**FL**
			18 Oct. 1906	**2**	**176**	**70**	**SW to NE; N of GB**	**FR**
			17 Jun. 1906	**1**	**139**	**31**	**SW to NE; N of GB**	**FR**
E5	1861-1943	1906	30 Oct. 1899	2	157	27	S to NE; E of LDBH across GB	FL
			13 Aug. 1899	3	194	7	N to S; directly over LDBH	FL
			22 Oct. 1895	2	167	38	SW to NE; S of GB	FL
			12 Oct. 1893	3	194	73	SE to NW; N of GB	FL
			27 Aug. 1893	3	194	54	SE to N; directly over LDBH	FL
			22 Aug. 1887	3	204	54	SE to N; NE of LDBH	FL
			23 Aug. 1886	2	157	12	S to N; directly over LDBH	FL
			26 Aug. 1885	1	130	35	S to N; W of GB	FR
			9 Sep. 1883	2	167	78	S to N; E of GB	FL
			16 Sep. 1876	1	120	76	S to N; forms N of GB	RR
			24 Aug. 1871	2	167	59	SE to NW; SW of GB	FR
			16 Aug. 1871	3	185	19	E to W; N of GB	FL
			12 Oct. 1870	2	157	55	SW to NE; S of GB	FL
			2 Oct. 1866	4	213	94	N to S, E of GB	RL

Event Bed	*2σ Age-Range (CE)*	*Median Age (CE)*	*Hurricanes within 100 km*	*Saffir-Simpson*	*Wind Velocity (km/hr)*	*Passage Proximity (km)*	*Direction*	*Quadrant*
E6	1849-1932	1895	6 Sep. 1932	5	259	103	S to N; E of GB	FL
			16 Sep. 1928	4	241	94	SE to NW; SW of GB	FR
			7 Aug. 1928	2	167	80	SE to NW; SW of GB	FR
			21 Oct. 1926	3	204	15	SE to NW; across GB	FL
			27 Jul. 1926	2	176	70	SE to NW; SW below GB	FR
			12 Oct. 1909	2	167	39	SW to NE; S of GB	FL
			18 Oct. 1906	2	176	70	SW to NE; N of GB	FR
			17 Jun. 1906	1	139	31	SW to NE; N of GB	FR
			30 Oct. 1899	**2**	**157**	**27**	**S to NE; E of LDBH across GB**	**FL**
			13 Aug. 1899	**3**	**194**	**7**	**N to S; directly over LDBH**	**FL**
			22 Oct. 1895	**2**	**167**	**38**	**SW to NE; S of GB**	**FL**
			12 Oct. 1893	**3**	**194**	**73**	**SE to NW; N of GB**	**FL**
			27 Aug. 1893	**3**	**194**	**54**	**SE to N; directly over LDBH**	**FL**
			22 Aug. 1887	3	204	54	SE to N; NE of LDBH	FL
			23 Aug. 1886	2	157	12	S to N; directly over LDBH	FL
			26 Aug. 1885	1	130	35	S to N; W of GB	FR
			9 Sep. 1883	2	167	78	S to N; E of GB	FL
			22 Oct. 1878	1	130	111	SW to NE; W of GB	FR
			16 Sep. 1876	1	120	76	S to N; forms N of GB	RR
			24 Aug. 1871	2	167	59	SE to NW; SW of GB	FR
			16 Aug. 1871	3	185	19	E to W; N of GB	FL
			12 Oct. 1870	2	157	55	SW to NE; S of GB	FL
			2 Oct. 1866	4	213	94	N to S, E of GB	RL
E7	1830-1914	1877	12 Oct. 1909	2	167	39	SW to NE; S of GB	FL
			18 Oct. 1906	2	176	70	SW to NE; N of GB	FR
			17 Jun. 1906	1	139	31	SW to NE; N of GB	FR
			30 Oct. 1899	2	157	27	S to NE; E of LDBH across GB	FL
			13 Aug. 1899	3	194	7	N to S; directly over LDBH	FL
			22 Oct. 1895	2	167	38	SW to NE; S of GB	FL
			12 Oct. 1893	3	194	73	SE to NW; N of GB	FL
			27 Aug. 1893	3	194	54	SE to N; directly over LDBH	FL
			22 Aug. 1887	**3**	**204**	**54**	**SE to N; NE of LDBH**	**FL**
			23 Aug. 1886	**2**	**157**	**12**	**S to N; directly over LDBH**	**FL**
			26 Aug. 1885	**1**	**130**	**35**	**S to N; W of GB**	**FR**
			9 Sep. 1883	**2**	**167**	**78**	**S to N; E of GB**	**FL**
			22 Oct. 1878	**1**	**130**	**111**	**SW to NE; W of GB**	**FR**
			16 Sep. 1876	**1**	**120**	**76**	**S to N; forms N of GB**	**RR**
			24 Aug. 1871	2	167	59	SE to NW; SW of GB	FR
			16 Aug. 1871	3	185	19	E to W; N of GB	FL
			12 Oct. 1870	2	157	55	SW to NE; S of GB	FL
			2 Oct. 1866	4	213	94	N to S, E of GB	RL

Event Bed	2σ Age-Range (CE)	Median Age (CE)	Hurricanes within 100 km	Saffir-Simpson	Wind Velocity (km/hr)	Passage Proximity (km)	Direction	Quadrant
E8	1826-1910	1874	12 Oct. 1909	2	167	39	SW to NE; S of GB	FL
			18 Oct. 1906	2	176	70	SW to NE; N of GB	FR
			17 Jun. 1906	1	139	31	SW to NE; N of GB	FR
			30 Oct. 1899	2	157	27	S to NE; E of LDBH across GB	FL
			13 Aug. 1899	3	194	7	N to S; directly over LDBH	FL
			22 Oct. 1895	2	167	38	SW to NE; S of GB	FL
			12 Oct. 1893	3	194	73	SE to NW; N of GB	FL
			27 Aug. 1893	3	194	54	SE to N; directly over LDBH	FL
			22 Aug. 1887	3	204	54	SE to N; NE of LDBH	FL
			23 Aug. 1886	2	157	12	S to N; directly over LDBH	FL
			26 Aug. 1885	1	130	35	S to N; W of GB	FR
			9 Sep. 1883	2	167	78	S to N; E of GB	FL
			22 Oct. 1878	1	130	111	SW to NE; W of GB	FR
			16 Sep. 1876	1	120	76	S to N; forms N of GB	RR
			24 Aug. 1871	**2**	**167**	**59**	**SE to NW; SW of GB**	**FR**
			16 Aug. 1871	**3**	**185**	**19**	**E to W; N of GB**	**FL**
			12 Oct. 1870	**2**	**157**	**55**	**SW to NE; S of GB**	**FL**
			2 Oct. 1866	4	213	94	N to S, E of GB	RL
E9	1825-1908	1872	12 Oct. 1909	2	167	39	SW to NE; S of GB	FL
			18 Oct. 1906	2	176	70	SW to NE; N of GB	FR
			17 Jun. 1906	1	139	31	SW to NE; N of GB	FR
			30 Oct. 1899	2	157	27	S to NE; E of LDBH across GB	FL
			13 Aug. 1899	3	194	7	N to S; directly over LDBH	FL
			22 Oct. 1895	2	167	38	SW to NE; S of GB	FL
			12 Oct. 1893	3	194	73	SE to NW; N of GB	FL
			27 Aug. 1893	3	194	54	SE to N; directly over LDBH	FL
			22 Aug. 1887	3	204	54	SE to N; NE of LDBH	FL
			23 Aug. 1886	2	157	12	S to N; directly over LDBH	FL
			26 Aug. 1885	1	130	35	S to N; W of GB	FR
			9 Sep. 1883	2	167	78	S to N; E of GB	FL
			22 Oct. 1878	1	130	111	SW to NE; W of GB	FR
			16 Sep. 1876	1	120	76	S to N; forms N of GB	RR
			24 Aug. 1871	2	167	59	SE to NW; SW of GB	FR
			16 Aug. 1871	3	185	19	E to W; N of GB	FL
			12 Oct. 1870	2	157	55	SW to NE; S of GB	FL
			2 Oct. 1866	**4**	**213**	**94**	**N to S, E of GB**	**RL**
E10	1805-1886	1851	26 Aug. 1885	1	130	35	S to N; W of GB	FR
			9 Sep. 1883	2	167	78	S to N; E of GB	FL
			22 Oct. 1878	1	130	111	SW to NE; W of GB	FR
			16 Sep. 1876	1	120	76	S to N; forms N of GB	RR
			24 Aug. 1871	2	167	59	SE to NW; SW of GB	FR
			16 Aug. 1871	3	185	19	E to W; N of GB	FL
			12 Oct. 1870	2	157	55	SW to NE; S of GB	FL
			2 Oct. 1866	4	213	94	N to S, E of GB	RL

APPENDIX D Section S4.4. References

BEZOU, C., NONAT, A., MUTIN, J.-C., CHRISTENSEN, A. N. & LEHMANN, M. 1995. Investigation of the crystal structure of γ-CaSO4, CaSO4· 0.5 H2O, and CaSO4· 0.6 H2O by powder diffraction methods. *Journal of Solid State Chemistry,* 117**,** 165-176.

BLAAUW, M. & CHRISTEN, A. 2011. Flexible paleoclimate age-depth models using an autoregressive gamma process. *Bayesian Analysis,* 6**,** 457-474.

BOLDT, K. V., LANE, P., WOODRUFF, J. D. & DONNELLY, J. P. 2010. Calibrating a sedimentary record of overwash from Southeastern New England using modeled historic hurricane surges. *Marine Geology,* 275**,** 127-139.

BRANDON, C. M., WOODRUFF, J. D., LANE, P. & DONNELLY, J. P. 2013. Constraining flooding conditions for prehistoric hurricanes from resultant deposits preserved in Florida sinkholes. *Geochemistry Geophysics Geosystems,* 14**,** 2993-3008.

CASTAGNO, K. A., DONNELLY, J. P. & WOODRUFF, J. D. 2021. Grain-Size Analysis of Hurricane-Induced Event Beds in a New England Salt Marsh, Massachusetts, USA. *Journal of Coastal Research,* 37**,** 326-335.

COMODI, P., NAZZARENI, S., ZANAZZI, P. F. & SPEZIALE, S. 2008. High-pressure behavior of gypsum: A single-crystal X-ray study. *American Mineralogist,* 93**,** 1530-1537.

DONNELLY, J. P., HAWKES, A. D., LANE, P., MACDONALD, D., SHUMAN, B. N., TOOMEY, M. R., VAN HENGSTUM, P. J. & WOODRUFF, J. D. 2015. Climate forcing of unprecedented intense-hurricane activity in the last 2000 years. *Earth's Future,* 3**,** 49-65.

DONNELLY, J. P., SMITH BRYANT, S., BUTLER, J., DOWLING, J., FAN, L., HAUSMANN, N., NEWBY, P., SHUMAN, B., STERN, J., WESTHOVER, K. & WEBB, T. I. 2001. 700 yr sedimentary record of intense hurricane landfalls in southern New England. *Geological Society of America Bulletin,* 113**,** 715-727.

HEATON, T. J., KÖHLER, P., BUTZIN, M., BARD, E., REIMER, R. W., AUSTIN, W. E., RAMSEY, C. B., GROOTES, P. M., HUGHEN, K. A. & KROMER, B. 2020. Marine20—the marine radiocarbon age calibration curve (0–55,000 cal BP). *Radiocarbon***,** 1-42.

HSU, S. & YAN, Z. 1998. A note on the radius of maximum wind for hurricanes. *Journal of coastal research,* 14.

KNAPP, K. R., DIAMOND, H. J., KOSSIN, J. P., KRUK, M. C. & SCHRECK, C. J. 2018. International Best Track Archive for Climate Stewardship (IBTrACS) Project, V. 4, [North Atlantic Subset]. *In:* INFORMATION, N. N. C. F. E. (ed.).

KNAPP, K. R., KRUK, M. C., LEVINSON, D. H., DIAMOND, H. J. & NEUMANN, C. J. 2010. The international best track archive for climate stewardship

(IBTrACS) unifying tropical cyclone data. *Bulletin of the American Meteorological Society,* 91**,** 363-376.

LANE, P., DONNELLY, J. P., WOODRUFF, J. D. & HAWKES, A. D. 2011. A decadally-resolved paleohurricane record archived in the late Holocene sediments of a Florida sinkhole. *Marine Geology,* 287**,** 14-30.

MAIO, C. V., DONNELLY, J. P., SULLIVAN, R., MADSEN, S. M., WEIDMAN, C. R., GONTZ, A. M. & SHEREMET, V. A. 2016. Sediment dynamics and hydrographic conditions during storm passage, Waquoit Bay, Massachusetts. *Marine Geology,* 381**,** 67-86.

REIMER, P. J., AUSTIN, W. E., BARD, E., BAYLISS, A., BLACKWELL, P. G., RAMSEY, C. B., BUTZIN, M., CHENG, H., EDWARDS, R. L. & FRIEDRICH, M. 2020. The IntCal20 Northern Hemisphere radiocarbon age calibration curve (0–55 cal kBP). *Radiocarbon***,** 1-33.

RODYSILL, J. R., DONNELLY, J. P., SULLIVAN, R., LANE, P. D., TOOMEY, M., WOODRUFF, J. D., HAWKES, A. D., MACDONALD, D., D'ENTREMONT, N. & MCKEON, K. 2020. Historically unprecedented Northern Gulf of Mexico hurricane activity from 650 to 1250 CE. *Scientific reports,* 10**,** 1-17.

WALLACE, E., DONNELLY, J., VAN HENGSTUM, P., WIMAN, C., SULLIVAN, R., WINKLER, T., D'ENTREMONT, N., TOOMEY, M. & ALBURY, N. 2019. Intense hurricane activity over the past 1500 years at South Andros Island, The Bahamas. *Paleoceanography and Paleoclimatology,* 34.

WALLACE, E. J., DONNELLY, J. P., VAN HENGSTUM, P. J., WINKLER, T. S., DIZON, C., LABELLA, A., LOPEZ, I., D'ENTREMONT, N. E., SULLIVAN, R. M., WOODRUFF, J. D., HAWKES, A. D. & MAIO, C. Sub. March 2021. Regional shifts in paleohurricane activity over the last 1500 years derived from blue hole sediments offshore of Middle Caicos Island. *Quaternary Science Reviews*.

WALLACE, E. J., DONNELLY, J. P., VAN HENGSTUM, P. J., WINKLER, T. S., MCKEON, K., MACDONALD, D., D'ENTREMONT, N. E., SULLIVAN, R. M., WOODRUFF, J. D., HAWKES, A. D. & MAIO, C. 2021. 1050 years of hurricane strikes on Long Island in The Bahamas. *Paleoceanography and Paleoclimatology,* 36**,** e2020PA004156.

WINKLER, T. S., HENGSTUM, P. J. V., DONNELLY, J. P., WALLACE, E. J., D'ENTREMONT, N., HAWKES, A. D., SULLIVAN, R. M., WOODRUFF, J. D. & MAIO, C. V. Submitted 2021. Oceanic passage of hurricanes across Cay Sal Bank in The Bahamas over the last 550 years. *Marine Geology*.

WINKLER, T. S., VAN HENGSTUM, P. J., DONNELLY, J. P., WALLACE, E. J., SULLIVAN, R. M., MACDONALD, D. & ALBURY, N. A. 2020. Revising evidence of hurricane strikes on Abaco Island (The Bahamas) over the last 700 years. *Scientific Reports,* 10**,** 1-17.